

UNDERSTANDING PHOTO-INITIATED DYNAMICS
USING PROGRAMMABLE SHAPED PULSES

By

Muath Nairat

A DISSERTATION

Submitted to
Michigan State University
in partial fulfillment of the requirements
for the degree of

Chemistry—Doctor of Philosophy

2018

ABSTRACT

UNDERSTANDING PHOTO-INITIATED DYNAMICS USING PROGRAMMABLE SHAPED PULSES

By

Muath Nairat

This dissertation outlines the implementation of shaped femtosecond laser pulses to understand molecular dynamics as well as control their response with a temporally shaped electric field. The opening work focuses on using conventional time-resolved spectroscopic methods to understand excited state proton transfer dynamics using a Schiff base chromophore. The later studies describe the implementation of single beam based methods utilizing shaped femtosecond pulses to retrieve dynamical information from several cyanine dyes within the first 200 fs after the absorption of photons. The approach of shaping femtosecond pulses is applied to understand the dynamics of a set of cyanine dyes with various molecular polar responses as well as understanding the role a cyanine dye plays once placed inside human serum albumin protein. Lastly, the shaped pulses approach is applied to control both internal conversion from higher excited states in cyanines as well as the multiphoton ionization process of aromatic molecules.

The first chapter provides a brief introduction on femtosecond laser spectroscopy and pulse shaping along with their use in understanding and controlling molecular dynamics on the ultrafast timescale. The second chapter focuses on using steady state and time-resolved spectroscopic methods to disentangle the dynamical steps during an excited state proton transfer from protic solvents to a Schiff base acting as a photobase. It was realized from steady state spectroscopic data that the Schiff base undergoes an increase in 14 pK_a units upon excitation, which is the largest change in pK_a units that has been reported for a photobase. The time-resolved studies reveal that

the proton transfer process is initiated through the formation of a highly-polarized hydrogen bonding intermediate state within a timescale that is limited by the dielectric solvation constant.

The third and fourth chapters discuss the application of programmable shaped femtosecond pulses to reveal dynamical information about the intramolecular response of substituted cyanines dyes. Changes in the molecular response, tracked through fluorescence or stimulated emission as a function of time delay between the spectral components of the excitation field, are related to the role of the substituent and its effect on the initial intramolecular energy relaxation soon after excitation. The role of binding indocyanine green inside the pocket of human serum albumin protein has been also investigated using the same approach in which it was revealed that the protein mitigates triplet state formation through hindering the twisting motion.

The following two chapters expand on utilizing shaped pulses to control dynamical processes. In chapter 5, emission from the higher excited state, S_2 , is enhanced at the cost of suppressing internal conversion to the S_1 state. This enhancement is achieved under strongly coupled excitation conditions using transform-limited pulses and can be tuned when excitation is carried out using chirped pulses. Lastly, chapter 6 summarizes the role of high order dispersion which results in the appearance of pre- and post-pulse pedestals that enhances the multiphoton ionization of toluene and *p*-nitrotoluene.

In the final chapter a summary of the overall work is provided along with a future outlook and proposed experiments to be carried out are also discussed.

*To the joy of my life...
my wife and my two sons*

ACKNOWLEDGEMENTS

First and foremost, I offer my sincerest gratitude to my PhD advisor Prof. Marcos Dantus for his ongoing guidance, munificent support & endless motivation throughout my PhD. Not only did his valuable criticisms along with his substantial knowledge shape my current scientific character, but also his endless lessons in management, resourcefulness and parenting shape my character in general.

I would also like to express my sincere thanks to the members of the thesis committee, Prof. Warren F. Beck, Prof. Gary Blanchard and Prof. Benjamin Levine with whom I had the chance to work and make use of their expertise.

My appreciation & thanks for the accomplishment of my PhD work are proudly directed to all the former Dantus research group members whom with all patience shared their time and knowledge, Dr. Vadim V. Lozovoy, Dr. Nagitha Ekanayake, Dr. Arkaprabha Konar, Dr. Gennady Rasskazov, Dr. Anton Ryabtsev, Dr. Ilyas Saytashev, Dr. Christopher Mancuso, Dr. Rachel Glenn, Dr. Alexander van Rhijn, Morgan Webb, Marie Kaniecki, and Elizabeth Mroczka. I also thank the current group members with whom I had all the pleasure to work and share the experience, Patrick Pawlaczyk, Gabrielle Murashova, Jurick Lahiri, Matthew Michie, Diego Sierra, Maryann Laboe, Benjamin Farris, Nicholas Weigartz, Jacob Stamm, and Jessica Kline.

I also would like to thank many of our collaborators from the Department of Chemistry at MSU as well as other institutions, Prof. Piotr Piecuch, Prof. Babak Borhan, Prof. James H. Geiger, Prof. James Jackson, Prof. Ehud Pines, Prof. Itzik Ben-Itzhak, and Dr. Artem Rudenko as well as their students.

Lastly & most importantly, my special thanks & gratitude are expressed to those who encouraged me throughout the years, supported me with smile and tears, & aided me to overcome my fears ... to my family. My wife, for being there for me throughout those years, my two sons who brought me joy with their smiles, my parents and siblings for all the courage they gave me to pursue my PhD.

TABLE OF CONTENTS

LIST OF TABLES	ix
LIST OF FIGURES	x
KEY TO ABBREVIATIONS.....	xvii
Chapter 1 Introduction.....	1
1.1 Femtosecond Laser Spectroscopy	3
1.2 Pulse Shaping and Phase Control.....	8
1.3 Understanding and Controlling Dynamics Using Shaped Pulses	13
Chapter 2 Dynamics of a Super Photobase	16
2.1 Introduction and Background.....	17
2.2 Experimental Methods	20
2.3 Results and Discussion.....	21
2.4 Conclusion.....	35
Chapter 3 Intramolecular Response of Cyanine Dyes.....	36
3.1 Introduction and Background.....	37
3.2 Experimental Methods	40
3.2.1 Synthesis	40
3.2.2 Steady State Spectroscopy	41
3.2.3 Laser Experiments.....	42
3.2.4 Computational Methods.....	43
3.3 Results	46
3.3.1 Steady State Spectroscopy	46
3.3.2 Chirp and Time Delay Measurements.....	48
3.4 Quantum Chemical Calculations & Discussion.....	53
3.5 Conclusion.....	65
Chapter 4 Cyanine Dynamics Inside Protein Pocket.....	66
4.1 Introduction and Background.....	67
4.2 Experimental Methods	71
4.3 Results and Discussion.....	75
4.3.1 Molecular Modeling & Docking.....	75
4.3.2 Fluorescence Behavior with Shaped Laser Pulses	76
4.4 Conclusion.....	82
Chapter 5 Controlling Energy Transfer in Cyanines.....	83
5.1 Introduction and Background.....	84
5.2 Experimental Methods	87
5.2.1 Laser and pulse shaper	87
5.2.2 Fluorescence Excitation and Detection.....	88

5.2.3	Samples	88
5.3	Results	90
5.3.1	Steady State Spectroscopy	90
5.3.2	Chirp studies on the S ₂ state of IR144 and mPi-IR806	97
5.3.3	Theoretical Modeling	103
5.4	Discussion	108
5.5	Conclusion.....	110
Chapter 6	Role of High-Order Dispersion on the Ionization of Molecules.....	111
6.1	Introduction and Background.....	112
6.2	Experimental Methods	115
6.3	Results	120
6.4	Discussion	129
6.5	Conclusion.....	133
Chapter 7	Summary and Future Outlook.....	134
7.1	Photobases and Proton Transfer Dynamics.....	135
7.2	Controlling Energy Transfer in Cyanines	136
APPENDIX	137
BIBLIOGRAPHY	140

LIST OF TABLES

Table 3.1 Absorption maxima, fluorescence maxima, Stokes shifts and fwhm of the absorption and the emission spectra of the first excited state (S1) for IR806, mTF-IR806, mAn-IR806, and mPi-IR806. S1-S0 Stokes shift measured as the difference between the absorption and fluorescence spectra maxima	48
Table 3.2 The cyanine dyes' TDDFT vertical excitation energies, error relative to the experimental absorption maxima, NBO charge on the central carbon, and the average dihedral angles for the ground state structures	56
Table 3.3 Ground and excited state energies at the FC and S1 minima for the three cyanine models	63
Table 5.1 Absorption maxima, fluorescence maxima, Stokes shifts and FWHM of the absorption and the emission spectra of the S ₁ state for IR806, IR144 and <i>mPi</i> -IR806. S ₁ -S ₀ Stokes shift measured as the difference between the absorption and fluorescence spectra maxima.	92
Table 5.2 Fitting parameters for the lifetime decay curves of <i>mPi</i> -IR806.....	97

LIST OF FIGURES

- Figure 1.1** Ultrafast molecular processes occurring on a fast timescale after the absorption of photons. Obtained with from ref⁸ with permission. 3
- Figure 1.2** A typical transient absorption setup in which the white light probe is dispersed on a spectrometer and the change in absorption is analyzed as a function of time delay between the pump and the probe. The obtained transient absorption on the right trace would contain contributions from ground state bleaching (dashed line), stimulated emission (dotted line), and excited state absorption (light line) to produce the overall (bold line) spectrum. Obtained from ref⁷ with permission. 5
- Figure 1.3** Various femtosecond spectroscopic approaches using a sequence of pulses to extract different orders of molecular light-matter interaction susceptibilities. Obtained from ref²¹ with permission. 6
- Figure 1.4** Gaussian laser spectrum (black on the left column) with a) flat spectral phase (red on the left column) leading to a TL pulse in the time domain (right column). b) linear spectral phase leading to a time delay of the pulse (red relative to original black on the right column). And c) quadratic phase leading to elongation of the pulse in the time domain (red relative to original black on the right column). 9
- Figure 1.5** Contour plots showing the spectral components arrival time within the femtosecond pulse for a) quadratic phase with a negative sign, b) flat phase producing a TL pulse, and c) quadratic phase with the exact value as (a) while having a positive sign and hence the inversed spectral components arrival order. 10
- Figure 1.6** Typical layout of a 4f pulse shaper in which the input beam is diffracted and controlled using an mask located in the Fourier plane of the 4f geometry. Obtained from ref²³ with permission. 10
- Figure 2.1** Photoacids are prevalent in a variety of applications, as they offer control of function via a light prompt. **FR0-SB** is one of few photobases known, formed in a modular manner from the reaction of **FR0** aldehyde with an amine. 18
- Figure 2.2** Absorption (solid line) and emission (shaded area) spectra of **FR0-SB** in (a) ACN (blue), (b) EtOH (black) and acidified EtOH (red). 21
- Figure 2.3** Absorption and emission spectra of **FR0-SB** in (a) MeOH and (b) BuOH. The absorption (black) has a maximum at 373 nm. The dual fluorescence emission (red) has a maximum at around 457 nm from the non-protonated form and a maximum at around 635 nm in MeOH and 620 nm in BuOH from the protonated form. 22
- Figure 2.4** Life-time traces with single exponential fits for **FR0-SB** near the emission maxima when dissolved in ACN (blue) and EtOH (black and red). Inset shows that the red emission trace at 650 nm of **FR0-SB** is identical to the **FR0-PSB** emission with 400 nm excitation. 23

Figure 2.5 TCSPC traces obtained using 400 nm excitation wavelength and detecting the emission from FR0-SB at 460 nm. A biexponential decay fit is included for all except MeOH that fit with a single exponential that closely corresponds to the instrument response function (dashed line). (b) TCSPC traces obtained using 400 nm excitation wavelength and detecting the emission from the protonated FR0-PSB at 650 nm. The data is fit by an exponential rise (τ_1) and an exponential decay (τ_2), $\langle\tau\rangle$ is the weighted average decay constant. The observed rise time at 650 nm is longer than the decay at 460 nm, the difference is attributed to the presence of an intermediate during the proton transfer process. 24

Figure 2.6 Calculated electron density difference between the excited state and ground state of FR0-SB. With optical excitation, the increase in electron density or negative charge is shown in purple while the decrease in electron density is shown in yellow. Overall electron density migrates from the yellow regions to the blue regions upon excitation. We notice a decrease in electron density at the diethyl amine side (left) and a net increase in negative charge on the imine nitrogen, which favors proton abstraction. The optimized ground state structure and its SCF electron density was obtained at the PBE/6-31G* level of theory while the excited state CI electron density was obtained using the same functional and basis set with the TD-DFT formalism. 26

Figure 2.7 Fluorescence spectra of FR0-SB in (a) MeOH, (b) EtOH, and (c) BuOH with multiple Gaussians fit used to estimate the relative emission between the protonated FR0-PSB to the nonprotonated FR0-SB. 27

Figure 2.8 Estimation of the relative fluorescence quantum yield between **FR0-SB** and **FR0-PSB**. The fluorescence spectrum in acetonitrile was obtained and then the sample was acidified with diluted HClO₄ in acetonitrile to produce the protonated iminium (**FR0-PSB**). Acidification was carried out until no emission was observed from **FR0-SB**. Each sample was excited at the absorption maxima. The experiments were repeated (two trials) in samples with different concentration. The measured quantum yield from both trials was in close agreement. 27

Figure 2.9 (a) Transient absorption spectra of FR0-SB at various time intervals after excitation in EtOH. Labeled arrows show the steps during the ESPT process. (b) Energy progression during the proton transfer process. 28

Figure 2.10 Transient absorption data of FR0-SB in acetonitrile. (a) Energy progression in ACN showing the long-lived ESA (b) and SE (c) signals from the non-protonated form along with biexponential fits at certain frequencies corresponding to each signal. 29

Figure 2.11 Stimulated emission decay of FR0-PSB in ethanol (acidified with HClO₄). Two decay components can be observed, a fast component corresponding to an intramolecular response from FR0-SB and a slow component corresponding to the excited state lifetime. 30

Figure 2.12 Pictorial model for the observed intermolecular ESPT dynamics in EtOH along with the associated time constants for the steps as obtained from global analysis (black) and the TCSPC data (colored). 31

Figure 2.13 Transient absorption of FR0-SB in methanol. The plot shows the energy progression during the course of proton transfer from MeOH to FR0-SB. 32

Figure 2.14 Transient absorption traces at (a) 570 nm where SE from the intermediate formation is observed, and (b) 650 nm where SE from the protonated FR0-SB can be seen while dissolved in EtOH (black) and EtOD (red). Biexponential decay constants are given in the inset along with the pre-exponential factors in parentheses. An isotope effect of 1.5 is observed during the formation of the partially-transferred proton intermediate while an isotope effect of 2 is observed during the final protonated form formation. Note, as the result of its apparent long-lived nature, lifetime of the 650 nm decay for the EtOD experiment could not be determined.....	33
Figure 2.15 Transient absorption traces of FR0-SB in fully deuterated methanol. TA traces at (a) 580 nm where SE from the intermediate formation is observed, and (b) 660 nm where SE from the protonated FR0-SB can be seen while dissolved in MeOH (black) and fully deuterated methanol (red). Biexponential decay constants are given in the inset with the pre-exponential factors in parentheses. An isotope effect of 2 is observed during the formation of the intermediate as well as in the formation of the final protonated form	34
Figure 3.1 Schematic representation for the intermolecular solvation potentials of a cyanine dye where the surrounding solvent responds to the change in the cyanine dipole moment associated with photoexcitation. Relaxation across the intermolecular coordinate is coupled with changes in the multidimensional intramolecular coordinate.	39
Figure 3.2 Chemical structures of the prepared cyanine dyes.	40
Figure 3.3 The chemical structures for the three model cyanine dyes used in the CASSCF calculations.	45
Figure 3.4 Steady state absorption (black) and fluorescence (red) spectra for the cyanine dyes (a) IR806, (b) mTF-IR806, (c) mAn-IR806, and (d) mPi-IR806. The used solvent with each dye is indicated in parentheses.	47
Figure 3.5 Total fluorescence signal as a function of linear chirp for (a) IR806, (b) mTF-IR806, (c) mAn-IR806, and (d) mPi-IR806. Top axis shows the duration of the chirped pulse.....	49
Figure 3.6 Stimulated emission signal as a function of linear chirp for (a) IR806, (b) mTF-IR806, (c) mAn-IR806, and (d) mPi-IR806. The traces are inversely correlated with fluorescence signal as a function of linear chirp.	50
Figure 3.7 Total fluorescence signal using two color pump-probe pulses for the four cyanine dyes when (a) the high frequency pulse precedes the lower frequency one and when (b) the arrival order is reversed.	52
Figure 3.8 Bond length across the conjugated polymethine chain for the optimized ground state structures of the four cyanine dyes. Terminal nitrogens are indexed as -5 and 5.....	54
Figure 3.9 Electron density difference between the ground and first excited states for (a) IR806 and (b) mPi-IR806. Upon excitation, the electron density migrates from the yellow to the blue regions.....	58

Figure 3.10 The minimum energy path on the first excited state potential from the FC region up to the S1 minima using CASSCF for the three cyanine models.	60
Figure 3.11 CASSCF MEP on the S1 potential (filled black) for (a) CN11N and (b) CN11NC2 from the FC region to the emissive S1 minima. Right y axis shows the change in the dihedral angles (open colored) compared to the FC geometry.	61
Figure 3.12 Optimized S1 CASSCF and CASPT2//CASSCF potential for (a & b) CN11N and (c & d) CN11NC2 as a function of the two dihedral angles that represent the substituent. The dihedral angles are measured as departure from the FC geometry dihedral angles.	63
Figure 4.1 Normalized ICG (black) and ICG-HSA (red) absorbance spectra showing ICG red shift after binding inside HSA site IIA pocket.	69
Figure 4.2 (a) TL pulse spectrum (red) with positive chirp phase mask (blue) and positive delay time phase mask (black). (b) Experimental setup, note the laser was not focused on the cuvette. (c) Schematic representation of a positively chirped pulse in the time domain, and of a (d) pump-probe type pair of pulses with positive delay time having frequency arrival ordering such that the red portion of the pulse arrives before the blue portion.	72
Figure 4.3 Molecular modeling showing the most favored binding site of ICG within site IIA of the HSA protein. HSA was colored according to its chains and ICG elements were colored in grey (C), blue (N), yellow (S) and red (O).	75
Figure 4.4 Normalized integrated fluorescence intensity as a function of spectral chirp for (a) ICG solution and (b) ICG-HSA solution at different repetition rates.	77
Figure 4.5 Integrated fluorescence intensity as a function of spectral chirp at a repetition rate of 200 Hz for ICG (black) and ICG-HSA (red) normalized (a) from 0 to 1 and (b) according to integrated fluorescence using TL pulses.	78
Figure 4.6 Normalized integrated fluorescence intensity as a function of chirp for ICG solution in the presence and absence of O ₂ at 1 kHz repetition rate.	79
Figure 4.7 Normalized integrated fluorescence intensity as a function of chirp for ICG-HSA solution in the presence and absence of O ₂ at 1 kHz repetition rate.	79
Figure 4.8 Normalized integrated fluorescence intensity as a function of delay time between the pump and probe pulses for (a) ICG solution and (b) ICG-HSA solution at repetition rates of 1 kHz (black) and 200 Hz (red).	80
Figure 4.9 Integrated fluorescence intensity as a function of delay time between pump and probe pulses for ICG-HSA. The ~290 fs oscillations in the negative delay time side and the ~175 fs oscillations in the positive delay time were fitted using a cosine function with $115 \pm 15 \text{ cm}^{-1}$ and $190 \pm 15 \text{ cm}^{-1}$ oscillation respectively and are vertically zoomed in the insets.	81
Figure 5.1 Experimental Setup. The output of the NOPA was phase and amplitude shaped using MIIPS femtoJock pulse shaper and then was focused on the cyanine dye in a 2 mm path length	

cuvette, the fluorescence signal was detected directly at a right angle using a fiber-coupled compact spectrometer. 87

Figure 5.2 Chemical structures of (a) IR806, (b) IR144 and (c) *m*Pi-IR806. 89

Figure 5.3 (a) Absorption spectra for the three cyanine-dyes in scheme 1. Two-dimensional fluorescence excitation–emission spectra for (b) IR806, (c) IR144 and (d) *m*Pi-IR806. Contour lines are plotted on a logarithmic scale. The absorption spectrum (black line) for each dye is superimposed on the excitation axis. 91

Figure 5.4 Absorption spectrum for IR806 along with the excitation spectra for the emission with maxima at 637 nm (determined with detection at 640 nm) and the emission with maxima at 700 nm (determined with detection at 710 nm). 93

Figure 5.5 IR806 fluorescence from both TICT's and the S_1 state bottom was depleted while increasing the solvent viscosity, indicating that the nature of these emissions as twisting along the polyene conjugation backbone from the planar Franck-Condon region to the S_1 bottom within the S_1 surface. MeOH: methanol. EtGly: ethylene glycol. 93

Figure 5.6 (a) IR144 and (b) *m*Pi-IR806 absorption spectra along with the excitation spectra for S_2 fluorescence with maxima at 588 nm and 557 nm, respectively. 94

Figure 5.7 (a) IR144 and (b) *m*Pi-IR806 fluorescence spectra showing an increase in the S_2 fluorescence yield while increasing the solvent viscosity. MeOH: methanol. EtGly: ethylene glycol. 95

Figure 5.8 TCSPC decay curves along with biexponential fit constants for the S_1 (red) and S_2 (green) fluorescence for (a) IR144 when excited at 540 nm and (b) *m*Pi-IR806 when excited at 505 nm. 96

Figure 5.9 Fluorescence lifetime decay curves for *m*Pi-IR806 upon excitation at 505 nm showing three different emissions at different wavelengths. 96

Figure 5.10 (a) IR144 and (b) *m*Pi-IR806 fluorescence spectra using direct excitation to the S_2 state for each dye. 98

Figure 5.11 Integrated fluorescence intensity from S_1 (red) and S_2 (black) states as a function of linear chirp for (a) IR144 and (b) *m*Pi-IR806, top axis shows the corresponding chirped pulse duration. TL pulses lead to greater S_2 fluorescence, while chirped pulses lead to greater S_1 fluorescence. A greater degree of asymmetry between positive and negative chirp values is observed for *m*Pi-IR806. Inset: S_1 and S_2 emission spectra when excited by TL (blue) and chirped (red) pulses. 99

Figure 5.12 (a) IR144 S_2 (solid lines) and S_1 (dashed lines) fluorescence yield as a function of chirp at various laser fluence values. Fluorescence intensity dependence as a function of laser fluence for IR144 from (b) S_2 and (a) S_1 states using TL (black), negatively (red) and positively (blue) chirped 1000 fs² pulses. Fluorescence intensity dependence as a function of laser fluence for *m*Pi-IR806 from (d) S_2 and (e) S_1 states using TL (black), negatively (red) and positively (blue)

chirped 1000 fs² pulses. The vertical lines indicate the laser fluence values at which the chirp scans were carried out. Linear fitting for the fluorescence yield at low laser fluence (0.1-0.25 mJ/cm²) is shown as a guide to discern where nonlinear fluence dependence becomes important. 101

Figure 5.13 (a) Total fluorescence intensity for the emission with maxima at 637 nm as a function of chirp on the 540 nm centered pulses. (b) IR806 emission when excited using 540 nm centered pulses at different chirp values showing that the change is only associated with 637 nm emission. 102

Figure 5.14 Simplified schematic of S₀, S₁, and S₂ energy levels considered in our model. (Left) Four level model used for our calculations, consists of the ground state and 3 levels in the S₂ excited state. ω_0 is the laser frequency, ω_1 and ω_2 are frequencies of the two levels in S₂ that interact with the laser. n_f is the population reaching the bottom of S₂, note this state is outside the laser spectrum, V is the transition dipole dependent laser interaction, Γ is the relaxation rate, γ is the dephasing rate. (Right) Schematic representation of the three lower singlet states of cyanine molecules plotted as a function of spatial coordinates involving twisting from the planar ground state configuration and bond lengthening. Internal conversion (IC) to S₁ requires twisting. The IC from S₁ to S₀ expected at a torsion angle of 90° is not indicated. 104

Figure 5.15 Theoretical simulations for S₂ state (black) and S₁ state (red) population as a function chirp for (a) IR144 and (b) mPi-IR806. 107

Figure 6.1 Interferrometric AC for (a) TL, (b) -3×10^4 fs³ TOD, (c) 3×10^4 fs³ TOD, and (d) 3×10^6 fs⁴ FOD pulses. The TOD traces are cross-correlations with TL pulses to show the asymmetric time profiles. 117

Figure 6.2 Cross-correlation for -3×10^4 fs³ TOD (black, bottom axis) and 3×10^4 fs³ TOD (red, top axis) with a TL pulse. 118

Figure 6.3 Theoretical simulation for the intensity of TL pulses compared to that of (a) -3×10^4 fs³ TOD and (b) 3×10^6 fs⁴ FOD pulses. The insets show same pulses on a linear scale. Positive TOD (not shown) resembles the negative TOD shown in (a) except that the pedestal appears after the main pulse. 119

Figure 6.4 TOF mass spectrum for toluene. The inset in the spectrum shows magnified region over the small m/z fragments. 120

Figure 6.5 TOF mass spectrum for *o*-nitrotoluene. The inset shows magnified region over the small m/z fragments. 121

Figure 6.6 Spider plots on a logarithmic scale for the observed toluene fragment ions using FOD (blue), negative (red), and positive (green) TOD pulses compared to TL (black) pulses at (a) 1.7, (b) 3.4, (c) 5.1, and (d) 6.8×10^{14} W/cm² peak intensity. The ion yield enhancements indicated by the black arrows using FOD are: in (a) for C₄H₄⁺=12.5±1.0, C₃H₃⁺=18.4±1.6, C₂H₂⁺=14.6±1.9, and H⁺=20±2. In (c) for C²⁺=13.7±0.8. In (d) for C³⁺=16±1. 122

Figure 6.7 Spider plots on a logarithmic scale for the observed *o*-nitrotoluene fragment ions using FOD (blue), negative (red) and positive (green), TOD pulses compared to TL (black) pulses at (a) 1.7, (b) 3.4, (c) 5.1, and (d) 6.8×10^{14} W/cm² peak intensity. The ion yield enhancements indicated by the black arrows using FOD in (a) for $H^+ = 15.9 \pm 1.0$ 124

Figure 6.8 Spider plots on a logarithmic scale for the observed acetylene fragment ions using FOD (blue), negative (red), and positive (green) TOD pulses compared to TL (black) pulses at (a) 3.4, (b) 5.1, and (c) 6.8×10^{14} W/cm² peak intensity. The ion yield enhancements indicated by the black arrows using FOD are: in (a) for $C_2H_2^+ = 12.2 \pm 0.8$. In (b) for $C_2H_2^{2+} = 10.2 \pm 0.9$. In (c) for $C_2H_2^{2+} = 12.2 \pm 0.7$, and for $C^{2+} = 16.5 \pm 1.2$ 125

Figure 6.9 KER from (a-c) toluene and (d-f) *o*-nitrotoluene using TL (black), positive (green) and negative (red) TOD, and FOD (blue) pulses at 6.8×10^{14} W/cm² peak intensity. 127

Figure 6.10 KER from acetylene using TL (black), positive (green) and negative (red) TOD, and FOD (blue) pulses at 6.8×10^{14} W/cm² peak intensity. 128

Figure 6.11 (a) Ion yield enhancement from toluene at 5.1×10^{14} W/cm² normalized with respect to the yield of 36 fs TL pulses (black unity circle at 1) when using negative TOD (red) and FOD (blue). (b) The same normalized comparison with respect to 36 fs TL pulses when using 48 fs TL pulses (red) and 64 fs TL pulses (blue). 130

Figure 6.12 Ion yield as a function of peak intensity for (a) toluene and (b) *o*-nitrotoluene on a double-log scale. Vertical lines indicate the peak intensities at which the HOD pulses were used. 131

KEY TO ABBREVIATIONS

ACN	Acetonitrile
β -BBO	Beta Barium Borate
BLA	Bond Length Alternation
BuOH	<i>n</i> -Butanol
CI	Conical Intersection
CASPT2	Complete Active-Space Second Order Perturbation Theory
CASSCF	Complete Active-Space Self-Consistent Field
DFT	Density Functional Theory
GGA	Generalized Gradient Approximation
EAS	Evolution Associated Spectra
ESA	Excited State Absorption
ESPT	Excited State Proton Transfer
EtOH	Ethanol
FC	Franck-Condon
FDA	Food and Drug Administration
FOD	Fourth Order Dispersion
FROG	Frequency Resolved Optical Gating
FWHM	Full Width at Half Maxima
HOD	High Order Dispersion
HSA	Human Serum Albumin
IC	Internal Conversion

ICG	Indocyanine Green
ISC	Intersystem Crossing
IEF-PCM	Integral Equation Formalism Polarizable Continuum Model
KER	Kinetic Energy Release
MeOH	Methanol
MIIPS	Multiphoton Intrapulse Interference Phase Scan
NBO	Natural Bonding Orbitals
NOPA	Non-Collinear Optical Parametric Amplifier
PES	Potential Energy Surface
PrOH	<i>n</i> -Propanol
SB	Schiff base
SE	Stimulated Emission
SHG	Second Harmonic Generation
SLM	Spatial Light Modulator
SOD	Second Order Dispersion
SPIDER	Spectral Phase Interferometry for Direct Electric-Field Reconstruction
TCSPC	Time Correlated Single Photon Counting
TDDFT	Time Dependent Density Functional Theory
TICT	Twisted Intramolecular Charge Transfer
TL	Transform Limited
TOD	Third Order Dispersion
TOF-MS	Time of Flight-Mass Spectrometer
YAG	Yttrium Aluminum Garnet

Chapter 1 Introduction

Since the early experimental work on molecular dynamics in the gas and condensed phases,^{1,2} femtosecond lasers have emerged as indispensable tools in multidisciplinary research fields. The advent of femtosecond lasers in molecular dynamics studies has allowed their implementation in various ongoing research fields that can be generalized into two main areas (i) understanding molecular dynamics processes on a femtosecond timescale and (ii) controlling the molecular response with femtosecond laser pulses.

On the side of understanding molecular dynamics and the ability to observe the ongoing processes in real time at the atomic level, it has been realized that the speed of atomic motion is about 1 km/s, therefore an atomic motion of about 1 Angstrom would require a temporal resolution of ~ 100 fs ($1 \text{ fs} = 10^{-15} \text{ s}$).³ This realization was piloted by Zewail in 1987 after his first observation of a bond-breaking transition state in real time.¹ Zewail's technique⁴ to observe the transition state was achieved by making use of a femtosecond laser pulse called a pump that creates a wave packet on an the excited state potential energy surface (PES). After the molecule is allowed to evolve, another femtosecond pulse, called the probe, is sent to create further excitation to a higher excited state on the PES. By varying the time delay between the pump and the probe pulses, Zewail was able to capture the wave packet motion in real time. The pump-probe technique has been exploited in various areas of research to understand the real-times dynamics of molecules, for which an immense amount of reviews can be found.^{3,5-9}

The other aspect of using femtosecond lasers with molecules is utilizing the phase of laser pulses to exploit constructive interference between multiple pathways to achieve enhancement in the desired state. This approach can be traced back to Brumer and Shapiro¹⁰ through which the constructive interference within a multiphoton transition can control the outcome of the final state.

Their approach has been made feasible with the advent and development of modern pulse shapers that allow precise and accurate control over the phase of broadband femtosecond pulses.¹¹

The studies presented in this dissertation start with using conventional time-resolved transient absorption to study the dynamics of proton transfer. Later on, the use of single beam methods based on programmable shaped pulses to understand excited state dynamics is presented in order to compare the advantages of shaped pulses relative to multiple beams methods. Lastly, the use of shaped femtosecond pulses to control the dynamics of molecules is explored.

1.1 Femtosecond Laser Spectroscopy

Molecules are represented in an ensemble of equilibrium along their multidimensional nuclear degrees of freedom as well as their surrounding environment. This state can be described as a low energy point on their ground state PES. When molecules are provided with energy in the form of light, the electronic population is transferred to an excited state and is no longer considered in equilibrium with the nuclear coordinates and the surroundings. The new electronic configuration allows the molecules to evolve on the excited state PES on a fast timescale that can range from few femtoseconds such as the inertial solvation response and up to several nanoseconds as in diffusional solvent transport. Such dynamical processes are illustrated in **Figure 1.1**. Tremendous effort, both by experimentalists and theoreticians has been devoted to understand the early dynamical response of molecules soon after the absorption of photons.^{3,5-9}

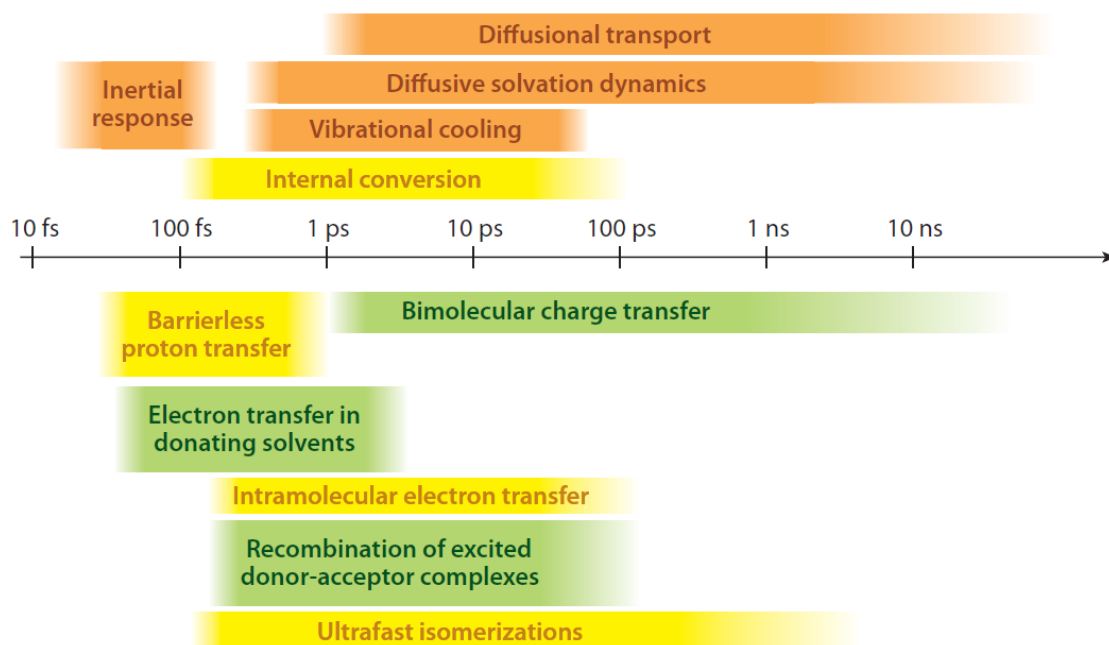


Figure 1.1 Ultrafast molecular processes occurring on a fast timescale after the absorption of photons. Obtained with from ref⁸ with permission.

Over the past three decades, femtosecond lasers have been the workhorse to study and understand the ultrafast dynamics of molecules upon excitation. The early approach relied on using two femtosecond laser pulses termed the pump and the probe. The pump pulse creates a new electronic population on the excited state that is allowed to evolve with the progress of time. Later on, a probe pulse with precise and controlled time delay is sent to interact with the excited molecules. Based on the probe pulse frequency, the probe can either create further excitation to higher excited state or stimulate down the excited state population. The obtained signal as a function of time delay between the two pulses is then related to dynamics: *e.g.* transition state prior a dissociative channel,¹ wavepacket motion within an excited state PES,¹² or molecular vibrations and rotations,¹³ to name a few.

Progress and development has been made on how pump-probe and ultrafast spectroscopy in general are implemented.^{7,14-18} One such example is transient absorption spectroscopy which is a pump-probe technique in its essence while having a broad bandwidth probe pulse. The probe pulse is usually white light that is generated from focusing the femtosecond pulse on various crystalline media such as Sapphire, CaF₂ or YAG. This focusing induces a process called super-continuum generation through which new spectral components are introduced to the bandwidth of the original femtosecond pulse. The generated super-continuum is much weaker than the femtosecond pulse itself and only serves the purpose of probing changes in the absorption of molecules after excitation. In an approach that is similar to pump-probe spectroscopy, the pump pulse excites a fraction of the molecules while the white light probe measures changes in the absorption (ΔA). This is usually carried out while modulating the pump pulse using a chopper and tracking the transmitted probe in the presence and absence of the pump. Changes in the absorption of molecules after being excited generally appear as: (i) ground state bleaching and recovery: in

which the excited molecules no longer absorb the probe pulse at particular wavelengths and the signal appears as negative ΔA in bleaching and positive ΔA in recovery. (ii) Stimulated emission: in which electronic population from the excited molecules is stimulated back to the ground state through which more light arrives at the detector and the signal appears as negative ΔA . (iii) Excited state absorption: through which excited molecules further absorb light from the probe to reach a higher excited state. The overall obtained transient absorption signal would appear as a cumulative sum of all or part of the contributing signals as shown in **Figure 1.2** requiring further comprehensive analysis schemes such as global and target analysis.¹⁹ While tracking the transient absorption signal in time as a function of delay between the two pulses, one can assess the dynamics that are associated with the molecular processes occurring after the absorption of light, such as excited state energy migration, charge transfer, electron or proton transfer, isomerization, internal conversion, and intersystem crossing. In Chapter 2, transient absorption spectroscopy is used to understand the excited state proton transfer dynamics of a photobase.

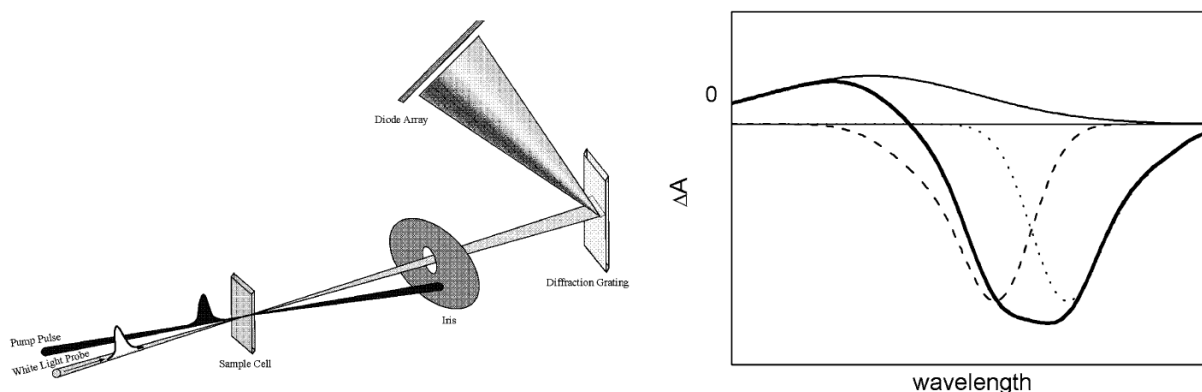


Figure 1.2 A typical transient absorption setup in which the white light probe is dispersed on a spectrometer and the change in absorption is analyzed as a function of time delay between the pump and the probe. The obtained transient absorption on the right trace would contain contributions from ground state bleaching (dashed line), stimulated emission (dotted line), and excited state absorption (light line) to produce the overall (bold line) spectrum. Obtained from ref⁷ with permission.

The transient absorption signal results from light-matter interaction through the third order nonlinear susceptibility $\chi^{(3)}$ that is due to the two beams interaction with the molecules.²⁰ There have been several developments in femtosecond spectroscopic approaches to extract molecular responses with short laser pulses from higher order light-matter interaction susceptibilities using a sequence of multiple pulses as summarized in **Figure 1.3**.

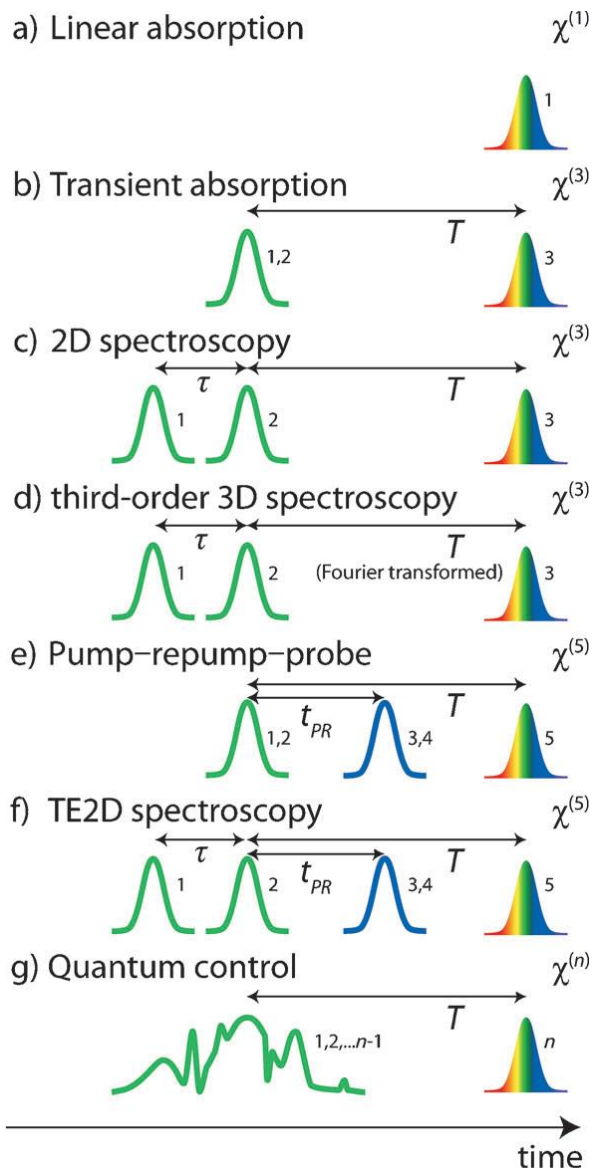


Figure 1.3 Various femtosecond spectroscopic approaches using a sequence of pulses to extract different orders of molecular light-matter interaction susceptibilities. Obtained from ref²¹ with permission.

With an increased number of pulses used in the femtosecond experiment, one would be able to extract and separate further information from a highly congested signal. However, this is at the cost of increasing the experimental complexity and the requirement to precisely control the spatial and temporal profiles of the femtosecond pulses and the ability to analyze the produced data while extracting useful information that is related to molecular dynamics. There has been another approach termed as quantum control (**Figure 1.3g**). The quantum control approach utilizes a single femtosecond pulse that results in multiple interactions with molecules. The multiple interactions are highly dependent on the temporal profile of the femtosecond pulse itself and the ability to control and deliver the desired temporal profile to the molecular system. This control has been made feasible with recent advances and development in pulse shapers that made such an approach reachable.^{11,22} In the next section, pulse shapers and their use in compressing and shaping femtosecond pulses are going to be described.

1.2 Pulse Shaping and Phase Control

A femtosecond pulse can be described as a pulse of an oscillating electric field in the time domain $E(t)$ that is represented by a Fourier integral of the complex spectrum $E(\omega)$,

$$\tilde{E}(t) \propto E(t) + c.c. = \int E(\omega) e^{-i\omega t} d\omega + c.c. \quad (1.1)$$

the spectral phase $\varphi(\omega)$ among the spectral components within the spectral amplitude $|E(\omega)|$ controls the time dependence of the field in the time domain as can be illustrated with

$$E(t) = \int |E(\omega)| e^{i\varphi(\omega)} e^{-i\omega t} d\omega \quad (1.2)$$

$\varphi(\omega)$ can be described using any arbitrary form such as a Taylor expansion:

$$\varphi(\omega) = \varphi_0 + \varphi'(\omega - \omega_0) + \frac{\varphi''}{2}(\omega - \omega_0)^2 + \dots \quad (1.3)$$

a spectral phase value of 0 among all the spectral components within spectral amplitude $|E(\omega)|$ would imply the shortest Fourier integral $E(t)$ in the time domain and corresponds to the shortest pulse that can be obtained from a particular laser pulse bandwidth and is usually termed as a Transform-Limited (TL) pulse (**Figure 1.4a**). Any other spectral phase value would affect the contracted pulse in the time domain as illustrated using: (i) a linear phase with the first order in the Taylor expansion $\varphi'(\omega)$ leading to a delay of the pulse in time while preserving the pulse duration as shown in **Figure 1.4b**. (ii) Quadratic phase using the second order in the Taylor expansion $\varphi''(\omega)$ that leads to elongation of the pulse in the time domain as shown in **Figure 1.4c**. It is also worth noting that the sign of the phase reflects the order at which different spectral components are represented in the time domain. For instance, an absolute value of quadratic phase would stretch the pulse in time by the same magnitude regardless of the sign; however, the arrival order of frequencies would be inversed based on the sign as shown in **Figure 1.5**.

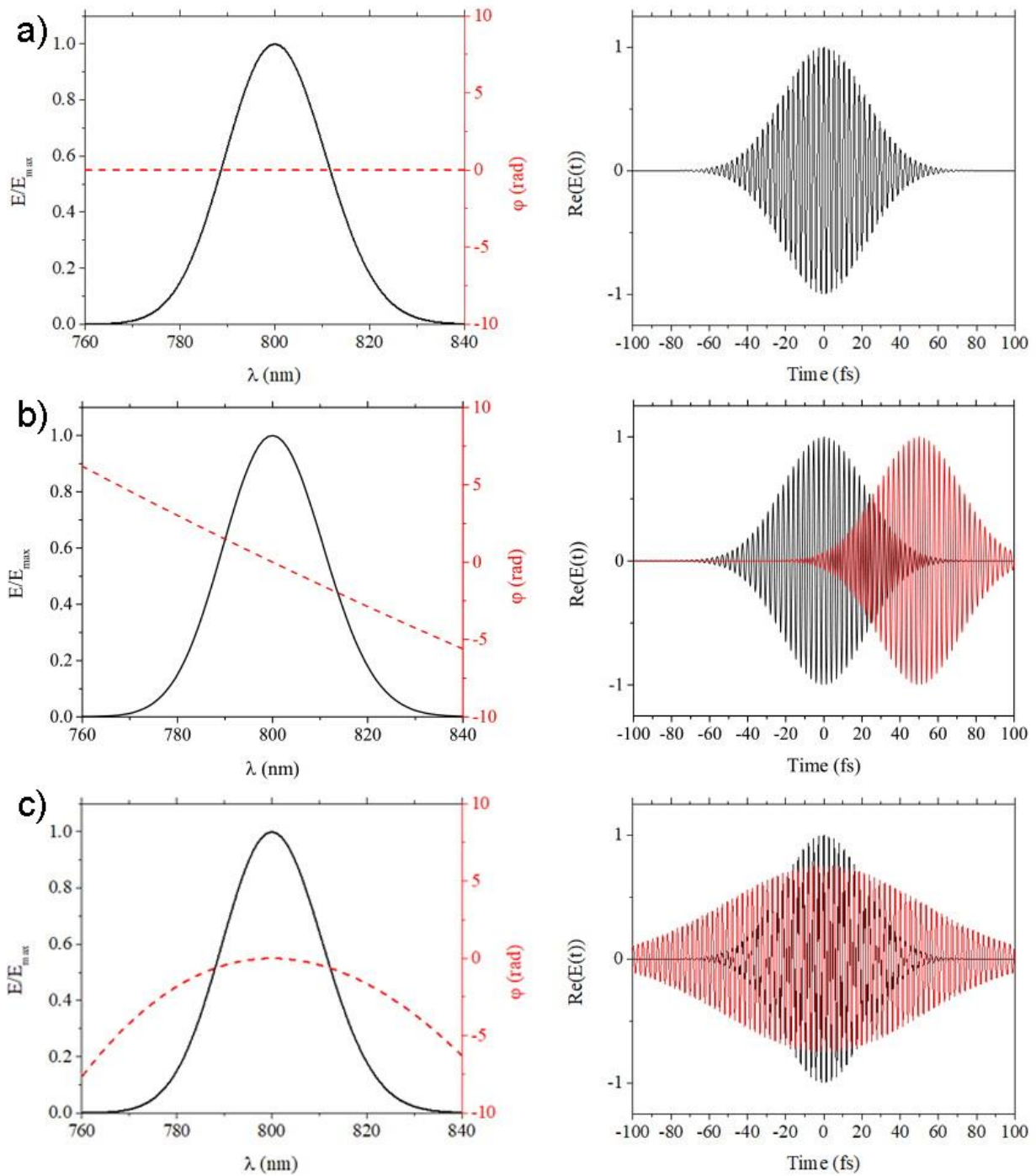


Figure 1.4 Gaussian laser spectrum (black on the left column) with a) flat spectral phase (red on the left column) leading to a TL pulse in the time domain (right column). b) linear spectral phase leading to a time delay of the pulse (red relative to original black on the right column). And c) quadratic phase leading to elongation of the pulse in the time domain (red relative to original black on the right column).

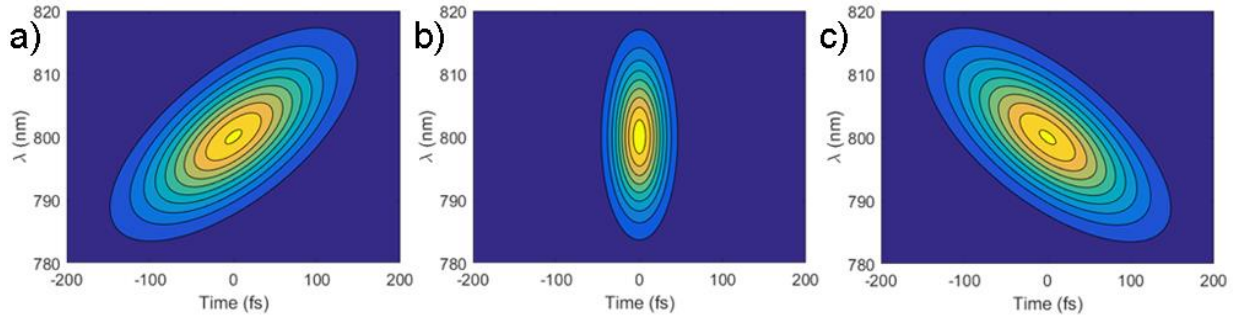


Figure 1.5 Contour plots showing the spectral components arrival time within the femtosecond pulse for a) quadratic phase with a negative sign, b) flat phase producing a TL pulse, and c) quadratic phase with the exact value as (a) while having a positive sign and hence the inversed spectral components arrival order.

Control over $\varphi(\omega)$ is achieved using devices called pulse shapers that bring the ability to separately control the individual spectral components of the femtosecond pulse.²³ A typical pulse shaper layout is shown in **Figure 1.6** and known as a 4f pulse shaper which is a zero dispersion configuration compressor with a mask that controls the individual spectral components. The f stands for the focal length of the lens that is used to collimate and focus the diffracted beam.

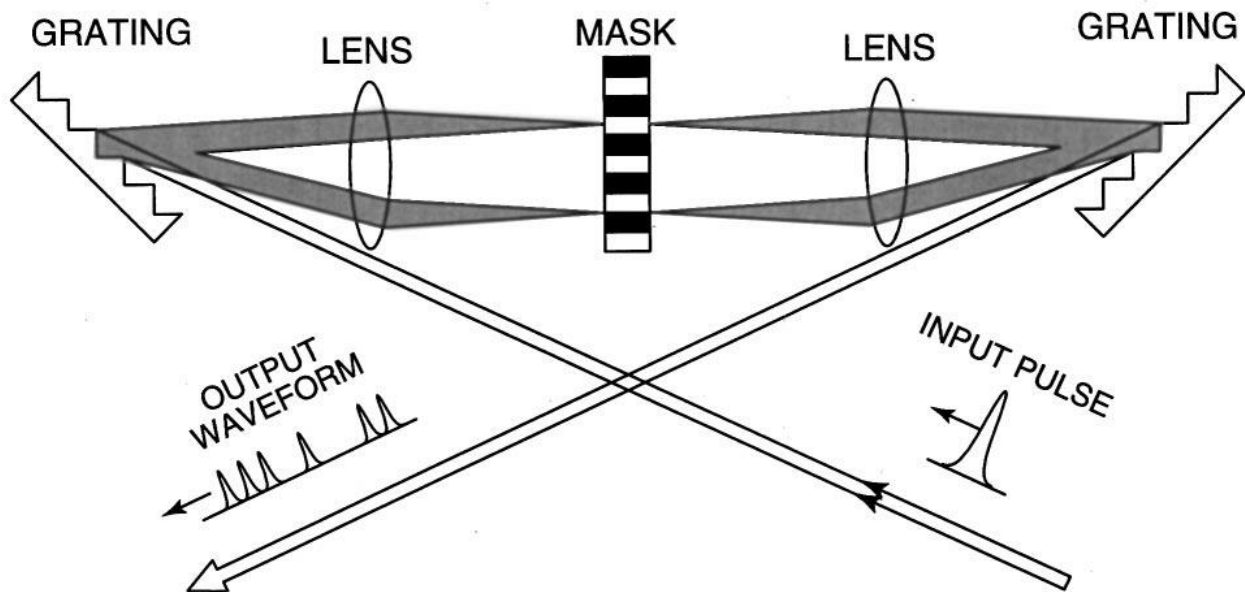


Figure 1.6 Typical layout of a 4f pulse shaper in which the input beam is diffracted and controlled using an mask located in the Fourier plane of the 4f geometry. Obtained from ref²³ with permission.

In the 4f pulse shaper, the input femtosecond pulse is diffracted using a grating and then collimated using a lens that sends the diffracted beam to a mask that is placed in the Fourier plane and has the ability to control the retardation of each individual spectral component in the spatially dispersed spectrum of the pulse. The output from the mask is then focused and combined using another grating. Practical improvement on the pulse shaper can be introduced by using a folded design through which a mirror is placed behind the mask which reflects the beam back to the original lens and grating at a slightly different height.

The most common masks that are used to control the spatially dispersed spectrum of the laser are called spatial light modulators (SLM's) that are based on liquid crystal. There are other types of phase controllers that are based on acoustic-optics modulators, deformable mirrors, and micromechanical mirrors. The research that has been carried out throughout this thesis was limited to the most common type, the liquid crystal SLM. The liquid crystal SLM is a thin layer of nematic liquid crystal placed between two layers of glass windows that are covered from the inside with a transparent electrical conducting layer. The liquid crystal is separated into different regions called pixels through which different voltage can be applied to each pixel separately. The application of an electric field on these pixels causes the liquid crystals to tilt and change their refractive index which allows the introduction of phase retardation to the incoming light with respect to the liquid crystals axis. Since the light that is sent to the SLM is spectrally dispersed onto different pixels, the phase retardation of each spectral component can be controlled with the voltage of each pixel separately to manipulate the phase of the output laser pulse. The right amount of voltage to introduce the desired phase has to be programmed in order to produce the desired phase.

Pulse shapers are generally operated under open loop or adaptive feedback control. In the open loop approach the user sets the desired phase mask and monitors the output using some

known pulse characterization methods such as autocorrelation, frequency resolved optical gating (FROG),²⁴ or spectral phase interferometry for direct electric-field reconstruction (SPIDER).²⁵ However, this approach requires some knowledge about the original phase of the femtosecond pulses and a well programmed and calibrated shaper to introduce the desired phase. The adaptive control approach depends on the outcome of a desired process to change the phase accordingly. There have been several demonstrations on the implications of the adaptive approach to control the phase of femtosecond pulses.²⁶⁻²⁸ Throughout this thesis, pulse shaping is carried out using an adaptive approach that is named the multiphoton intrapulse interference scan (MIIPS).²⁹⁻³¹

MIIPS relies on the phase influence on nonlinear optical properties at specific frequencies, namely, the second harmonic generation (SHG) spectrum of the femtosecond pulse. MIIPS has the advantage of not only characterizing the phase of femtosecond laser pulses, but also has the ability to compress any distorted pulses to their TL duration as well as the introduction of any desired phase mask to produce precisely phase-shaped pulses. The exploitation of MIIPS has led to successful implementation in various avenues such as multiphoton microscopy,³² control of physiochemical processes,³³⁻³⁴ systematic chemical recognition,³⁵ stand-off chemical detection,³⁶ and understanding excited state dynamics.³⁷⁻³⁸

1.3 Understanding and Controlling Dynamics Using Shaped Pulses

The development of computer controlled and programmable pulse shapers³⁹⁻⁴⁰ has enabled their implementation to solve many chemical problems, this is in terms of using shaped femtosecond pulses to understand excited state dynamics through their nonlinear interaction with matter^{37,41-42} as well as controlling the response of molecules using shaped pulses.⁴³⁻⁴⁴

The principle of using shaped femtosecond pulses that carry a well-defined and structured temporal resolution relies on the nonlinear response of molecules to the shaped pulses as shown earlier in **Figure 1.3g**. The temporal moments of such synthesized pulses are distributed in a versatile way in which one pulse can produce a sequence of interactions that eliminates the need for multiple beams and delay stages. This has allowed ultrafast dynamics to be studied on a single molecule owing the applicability to deliver a single beam with the desired pulse sequence through the objective of the microscope while detecting the fluorescence.⁴⁵⁻⁴⁷ A common approach of using shaped pulses to understand dynamics is to scan the second order dispersion (SOD), also known as chirp.⁴⁸⁻⁴⁹ A negatively chirped pulse allows multiple intrapulse interactions through which the high to low frequencies arrangement creates a pump and dump in the excited state population while positively chirped pulses with an inverse frequencies ordering don't permit such process to occur. Having this information in hand has enabled distinguishing between multiple competing excited state pathways such as relaxation, photoisomerization and ionization.⁵⁰⁻⁵¹ Positively chirped pulses have also been used as spectroscopic tools to reveal the early solvation response of cyanines.³⁸ The implication of using shaped pulses to understand excited state dynamics is discussed in Chapter 3 which shows how negatively chirped pulses can be used to reveal differences in the intramolecular response of various substituted cyanines. Also in Chapter 4 which investigates how human serum albumin (HSA) protein mitigates triplet state formation in the excited state of Indocyanine green.

Pulse shapers also have been used to simplify the way multidimensional spectroscopic experiments are carried out by the introduction of finely controlled pump pulses in the same arm with well-known phase in a two arm pump-probe geometry.^{41,52} This eliminates the complexity of multiple arm setups that are typically used in multidimensional spectroscopy experiments.

The phase information that is preserved within the femtosecond pulse can exploit constructive interference at certain frequencies which has been effectively demonstrated in nonlinear multiphoton processes.⁵³⁻⁵⁴ This approach was initially proposed from a theoretical point of view¹⁰ and later on was experimentally realized in the gas phase.⁵⁵ The ability to control chemical processes with light seemed as a promising tool to solve many problems and that field is known as coherent control or quantum control. Later on it was realized that the amount of search space for the optimal phase to drive the chemical reaction towards the point of interest is immensely large, therefore many researches followed an approach that utilizes Genetic Algorithms with optimal phase control based on the experimental outcome.⁵⁶ Unfortunately, the Genetic Algorithms approach failed to deliver many of its promises owing to the lack of uniqueness in any of the obtained phases for many chemical problems and the failure to relate any of the obtained phases to the chemical property of interest.

Despite the introduced drawbacks with the use of Genetic Algorithms in the field of quantum control, there have been elegant approaches in the field relying systematically on the phase itself and how it is connected to the enhanced molecular property of interest.⁴⁴ Such experiments are carried out using a sinusoidal spectral phase to specifically induce large changes in the multiphoton laser-induced fluorescence of large organic molecules in solutions,^{33,57} a π step across the phase to invert the excited state population⁵⁸ or enhance the two-photon transition,⁵³

third order dispersion to pre-align molecules and enhance their ionization,⁵⁹ and selectively excite Raman transitions.⁶⁰

In this thesis the systematic approach of using shaped pulses to control chemical processes is followed. Chapter 5 shows how intense TL pulses can couple the electronic transition between the resonant higher excited state and the ground state while suppressing internal conversion to the lower excited state; this is relative to chirped pulses through which higher population transfer from the higher to the lower excited states were observed. In Chapter 6 the quantum control approach is followed by utilizing pulses with high order dispersion (HOD) to enhance the ionization of molecules due to pre-alignment and bond softening that is introduced from the pedestal in the HOD pulse.

Chapter 2 Dynamics of a Super Photobase

This Chapter discusses excited state proton transfer (ESPT) in a modular system (Schiff base formed from an aldehyde and an amine) that upon photoexcitation yields a more basic imine capable of intermolecular proton transfer from organic protic solvents. The steady state spectroscopy showed that the Schiff base acquires a 14-unit increase in pK_a upon excitation. Lifetime measurements and time-resolved studies using transient absorption revealed that the proton transfer process is initiated through an intermediate formation that is ascribed to a highly polarized H-bonding state. It was also found that the intermediate formation timescale is limited by the dielectric solvation constant. A primary isotope effect was also observed in the ESPT reaction.

This chapter has been adapted with permission from (*Angew. Chem. Int. Ed.* **2018**, 57, 14742-14746)
Copyright © 2018, John Wiley and Sons.

2.1 Introduction and Background

Transfer of the hydrogen atom or the hydrogen cation (proton) are undoubtedly one of the most crucial and fundamental steps in many chemical and biological processes.⁶¹ The later reactions involve proton transfer from a proton donor (acid) to an acceptor (base). Due to the dynamic nature of the dissociation-association equilibrium between the acid and the base, it has been difficult to assess the steps that are involved in proton transfer while in the ground state. However, since the early work on excited state proton transfer (ESPT) processes by Förster and Weller⁶² and their realization that some weak acids and bases exhibit an increase in their acidity ($pK_a^* < pK_a$) or basicity ($pK_a^* > pK_a$) with photo excitation; tremendous progress has been achieved in understanding proton transfer steps in which the proton transfer event is triggered with light. Such compounds that undergo ESPT are named as photoacids and photobases (**Figure 2.1**) for which there has been a large number of experimental and theoretical studies that have investigated the underlying ESPT dynamics and principles.^{8,63-69} This stems from both the fundamental interest in understanding ESPT dynamics and the exploitation of photoacids as a functional tool in areas such as triggering protein folding⁷⁰ and pH jumps,⁷¹ as well as probing microsolvation⁷² and regulating enzymatic reactions using light,⁷³ to name a few. Recently, photoacids have found more extensive applications in chemical sensors, proton-transfer lasers, organic light-emitting diodes,⁷⁴ dye-sensitized ion exchange membranes,⁷⁵ and large Stokes shift fluorescent proteins.⁷⁶ A recent example highlights photoacids in the enantioselective protonation of silyl enol ethers leading to enantioenriched α -substituted carbonyls.⁷⁷ In contrast, the literature on photobases is scarce and limited to heterocyclic amines such as acridines,⁷⁸ 3-styrylpyridines,⁷⁹ aminoanthraquinones,⁸⁰ Schiff bases,⁸¹ and quinolines.⁸² Curcumin,⁸³ xanthone,⁸⁴ and other bifunctional photoacids have been sporadically reported to show certain photobasic features.⁸⁵ These photobases are different

from photobase generators, which are bases that are generated from their salts with the use of light and have the drawback of being irreversible and having slow proton transfer rates.⁸⁶

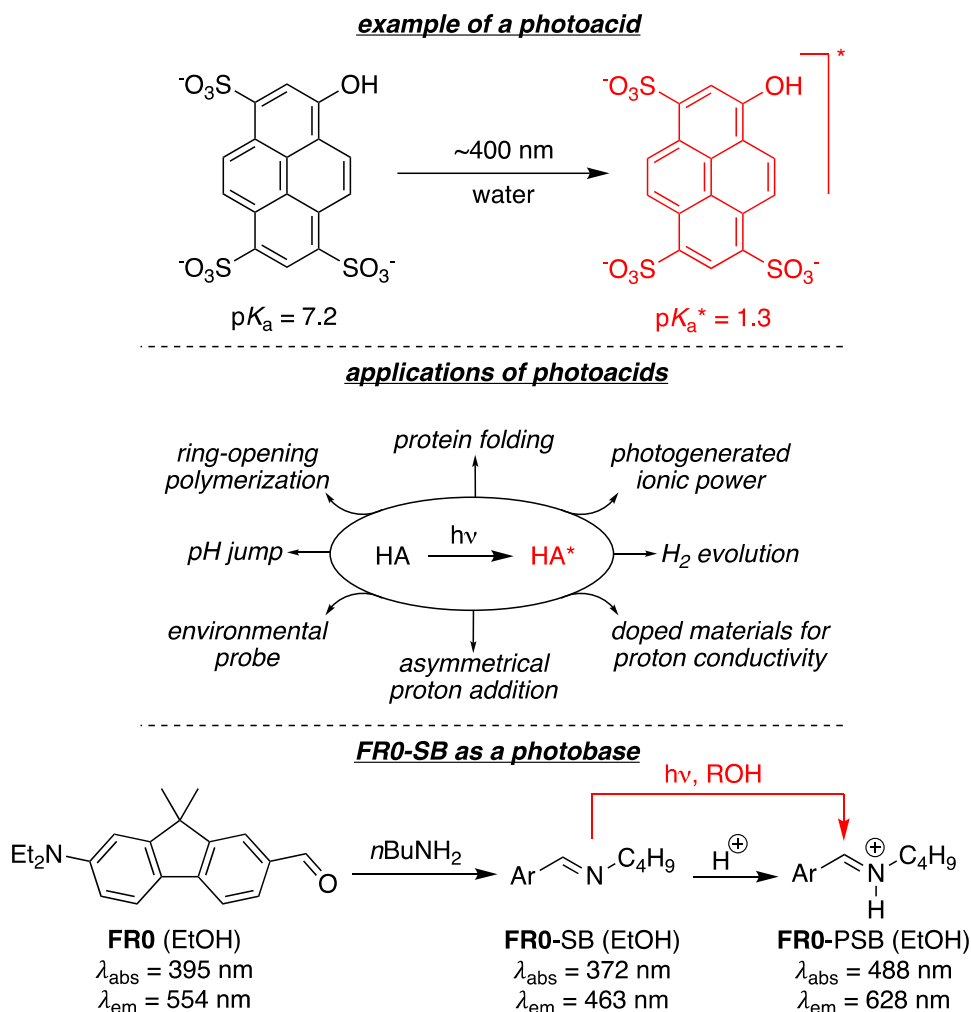


Figure 2.1 Photoacids are prevalent in a variety of applications, as they offer control of function via a light prompt. **FR0-SB** is one of few photobases known, formed in a modular manner from the reaction of **FR0** aldehyde with an amine.

The prevalence of photoacids has led to their exploitation in a number of avenues, however, the paucity of photobases has hampered investigations into their utility. Nonetheless, the ability to control the basicity of an agent via photoexcitation can be as important as those demonstrated with photoacids; to expand upon the repertoire of light-gated transformations and actions. The term

super-photoacidity was coined by Tolbert and coworkers for photoacids that are strong enough to photo-dissociate in non-aqueous solutions.⁸⁷ The term stemmed from work by Carmeli et al,⁸⁸ and Huppert, Tolbert and coworkers.⁸⁹ Similarly, one may formally introduce the term super-photobasicity for photobases which are strong enough to abstract protons from non-aqueous solvents such as alcohols. This definition is general and does not depend on an arbitrary pK_a value or change in pK_a value upon photoexcitation. Here, we show the photobasic properties and proton transfer dynamics of **FR0-SB**, a conjugated Schiff base (SB) obtained via the imine formation between the strong solvatochromic dye **FR0** (a fluorene based aldehyde) with n-butylamine (**Figure 2.1**), a system that is featured in being modular with versatile aldehydes and amines.⁹⁰ Upon photoexcitation of **FR0-SB** in ethanol, fluorescence of the protonated Schiff base (PSB) is observed, which warrants the consideration of **FR0-SB** as a super photobase.

This chapter discusses the optical properties of **FR0-SB** and the underlying ESPT dynamics in different solvents and their deuterated isotopologues, leading to the elucidation of the steps that are involved in the proton transfer event.

2.2 Experimental Methods

Fluorescence lifetime data was obtained using the second harmonic of a femtosecond Ti:Sapphire oscillator detecting the fluorescence at right angles with a spectrometer that collected both parallel and perpendicular emissions. The lifetime was obtained from the isotropic contribution ($I_{\text{parallel}} + 2I_{\text{perpendicular}}$). The instrument response function was measured by collecting laser scatter near 400 nm. For the data comparing the lifetimes in methanol and ethanol with their fully deuterated isotopologues we used the third harmonic of a femtosecond Yb fiber laser at 353 nm as the excitation wavelength, which is closer to the absorption maximum.

The transient absorption setup consists of a regeneratively amplified Ti:Sapphire laser (Legend, Coherent, Santa Clara, CA) producing femtosecond pulses at a repetition rate of 1 kHz. The pulses were compressed to their transform-limit duration with a pulse shaper utilizing the Multiphoton Intrapulse Interference Phase Scan (MIIPS) approach.^{33,57} The output was centered at 800 nm with a duration of 40 fs. The pulses were split using a beam splitter into an arm that was used to generate the second harmonic signal centered at 400 nm using a BBO crystal which served as the pump. The probe arm was sent into an optical delay line and was focused on a 2 mm YAG crystal to generate a white light continuum that extends from 450 to 900 nm. A 680 nm short pass filter was used to filter the continuum probe pulses. Half-wave plate on one of the arms was used to set the relative polarization to magic angle (54.7°). The two arms were non-collinearly combined and focused using a 25.0 cm lens into a 1 mm quartz cuvette. The probe signal was collected using a compact CCD (QE65000, Ocean Optics). Temporal dispersion of the probe pulse was measured by cross correlation and the observed chirp was used to correct the transient absorption data during global analysis. Global analysis of the results was carried out using Glotaran software.⁹¹

2.3 Results and Discussion

FR0-SB in acetonitrile (ACN) has an absorption centered at 369 nm and an emission maximum at 479 nm (**Figure 2.2a**). When **FR0-SB** is dissolved in protic solvents, dual emission bands are observed with maxima at 463 nm and 628 nm for EtOH (**Figure 2.2b**, see **Figure 2.3** for spectra in MeOH and *n*-BuOH). The emergence of the red emission in protic solvents is ascribed to the protonated Schiff base (PSB) of **FR0** that forms upon excitation. To confirm, the **FR0-SB** was acidified by addition of dilute HClO₄ to protonate the imine in EtOH, leading to a large red shift in the absorption spectrum (from 372 nm to 488 nm, **Figure 2.2b**). Accordingly, the fluorescence becomes limited to the low energy emission with a 630 nm maximum which confirms the assignment of the protonated form of **FR0-SB** (**FR0-PSB**).

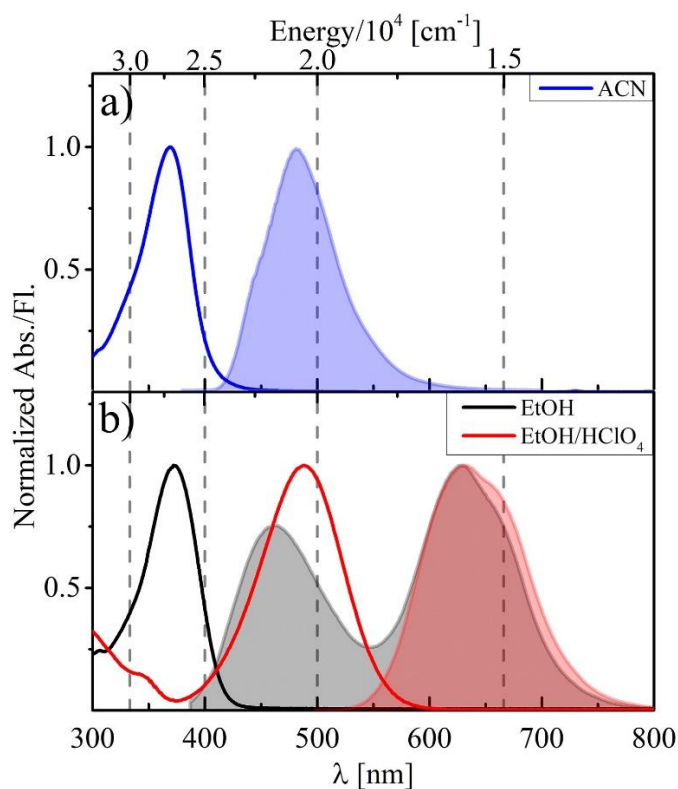


Figure 2.2 Absorption (solid line) and emission (shaded area) spectra of **FR0-SB** in (a) ACN (blue), (b) EtOH (black) and acidified EtOH (red).

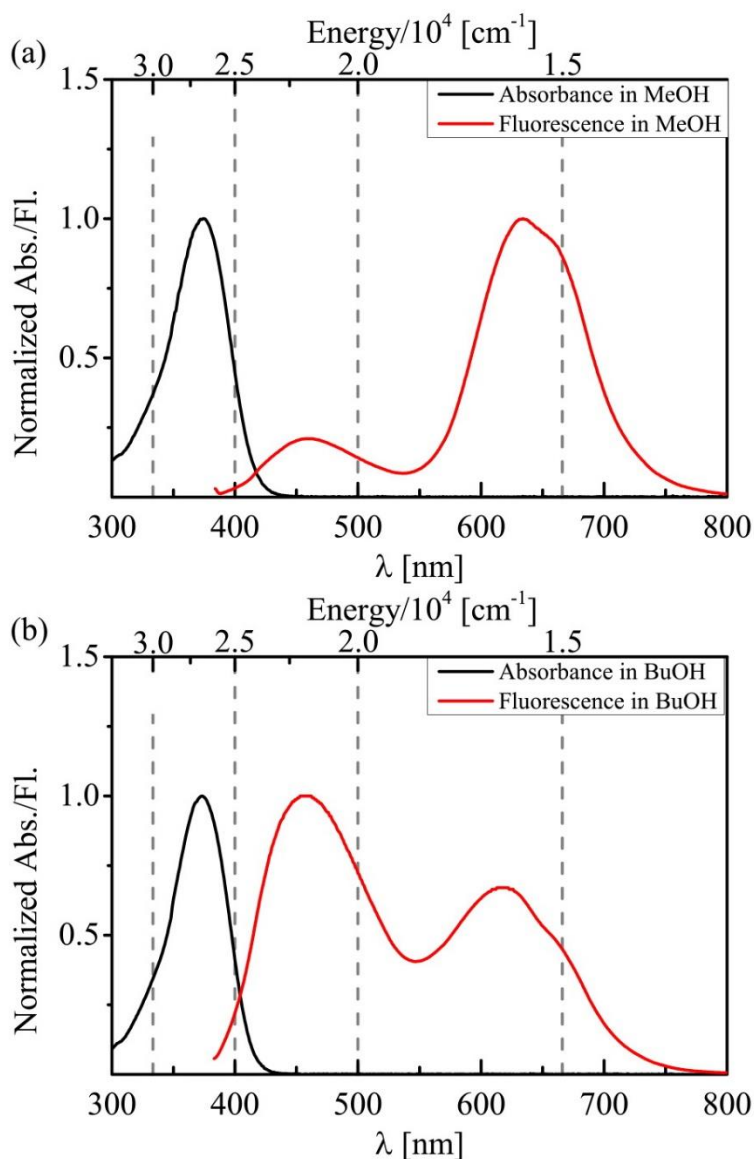


Figure 2.3 Absorption and emission spectra of FR0-SB in (a) MeOH and (b) BuOH. The absorption (black) has a maximum at 373 nm. The dual fluorescence emission (red) has a maximum at around 457 nm from the non-protonated form and a maximum at around 635 nm in MeOH and 620 nm in BuOH from the protonated form.

Due to the rapid decay of the excited state that leads to the rapid protonation of **FR0-SB**, time-resolved fluorescence measurements were carried out by picosecond time-correlated single photon counting (TCSPC) to further confirm the nature of the red emission (**Figure 2.4**). The

emission in ACN exhibits a single exponential decay with a 2.11 ns lifetime, whereas in EtOH, the blue emission lifetime decreases sharply to ca. 89 ps. The decrease in the blue-emission lifetime can be explained by the competing intermolecular proton transfer from the solvent to **FR0**-SB in the excited state, a process that is not possible in ACN. The excited **FR0**-SB acts as a photobase that readily abstracts a proton from EtOH to form the iminium, which has an emission maximum at 628 nm. The red emission of **FR0**-SB in EtOH displays an identical decay trace to that of the iminium formed in EtOH/HClO₄ solution with a lifetime of 1.31 ns (**Figure 2.4** inset). Further detailed TCSPC traces in MeOH and BuOH are provided in **Figure 2.5**.

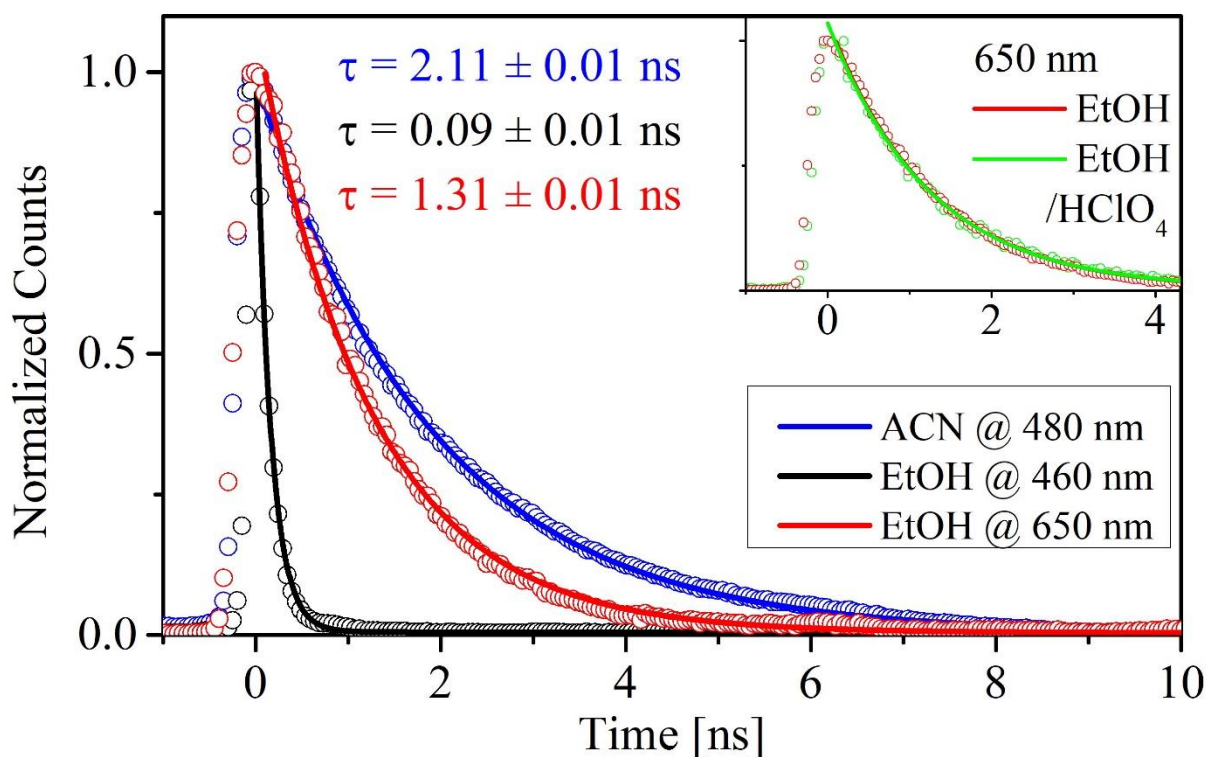


Figure 2.4 Life-time traces with single exponential fits for **FR0**-SB near the emission maxima when dissolved in ACN (blue) and EtOH (black and red). Inset shows that the red emission trace at 650 nm of **FR0**-SB is identical to the **FR0**-PSB emission with 400 nm excitation.

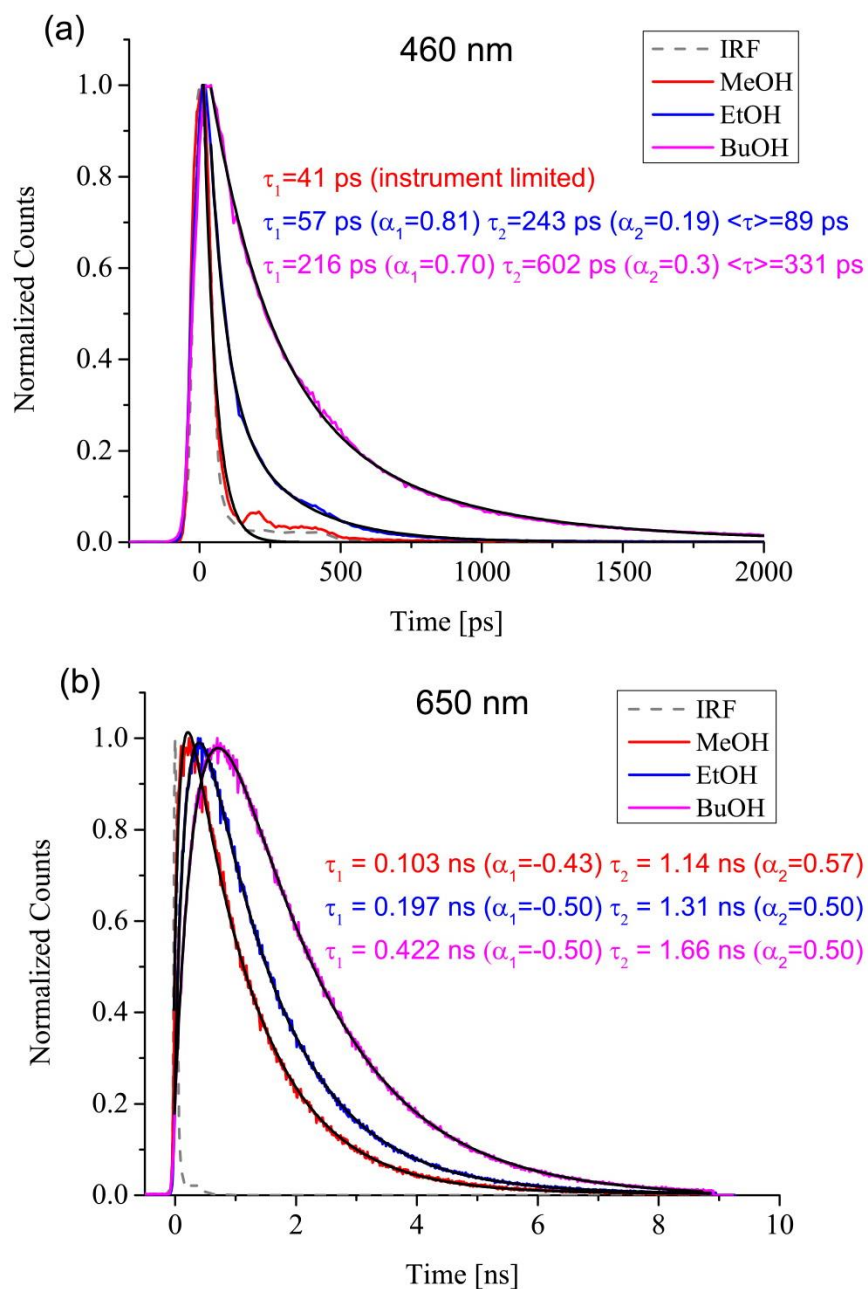


Figure 2.5 TCSPC traces obtained using 400 nm excitation wavelength and detecting the emission from FR0-SB at 460 nm. A biexponential decay fit is included for all except MeOH that fit with a single exponential that closely corresponds to the instrument response function (dashed line). (b) TCSPC traces obtained using 400 nm excitation wavelength and detecting the emission from the protonated FR0-PSB at 650 nm. The data is fit by an exponential rise (τ_1) and an exponential decay (τ_2), $\langle \tau \rangle$ is the weighted average decay constant. The observed rise time at 650 nm is longer than the decay at 460 nm, the difference is attributed to the presence of an intermediate during the proton transfer process.

The change in pK_a upon excitation is determined using the Förster equation,^{67,92}

$$pk_a^* - pk_a = (hv_1 - hv_2) / 2.3RT \quad (2.1)$$

where pK_a^* and pK_a are the excited state and ground state logarithmic acidity constants, respectively; $h\nu$ is the energy of the 0-0 electronic transition of the base and its conjugate acid. The 0-0 transition energies were estimated as 24,450 cm^{-1} and 17,890 cm^{-1} from the corresponding crossing points of the absorption and emission spectra for both **FR0-SB** and **FR0-PSB**, respectively (**Figure 2.2**).⁹³ The calculated increase in pK_a is 13.8 units. While pK_a changes up to 14 units have been reported for photoacids,⁸⁵ to the best of our knowledge the largest pK_a change reported for a photobase is 10.8 for 5-aminoquinoline.⁹⁴

With the ΔpK_a in hand, calculation of the excited state pK_a^* requires an estimate for the ground state pK_a of **FR0-PSB**. Although a good estimate for the pK_a in EtOH can be derived from the pK_a of the imine in water this was hampered by the insoluble nature of **FR0-SB** in water. Note that the pK_a of ammonium salt is generally elevated by ~ 3 units when dissolved in EtOH instead of water.⁹⁵⁻⁹⁶ Therefore, we resorted to an indirect measurement of the pK_a via quantifying the mole fraction of each species by multi-variant linear regression with known extinction coefficients as a function of wavelengths (UV-vis analysis), generated between the acid-base reaction of **FR0-SB** with α -naphthylammonium in EtOH as described in a previously reported procedure.⁹⁷ **FR0-PSB** shows a 0.23 unit lower pK_a than that of α -naphthylammonium in EtOH. The pK_a of α -naphthylammonium in water is 3.9, thus its pK_a in EtOH is estimated at 6.9. Considering the difference in pK_a values for α -naphthylammonium and **FR0-PSB**, the pK_a of the latter in EtOH is estimated to be 6.7. This results in an estimated excited state pK_a^* of 21 for **FR0-SB**. The large change in pK_a , occurring upon excitation, is ascribed to the increased electron density, and thus an

amplified negative polarity on the imine nitrogen atom in the excited state as shown in the electron density difference between the excited and ground states in **Figure 2.6**.

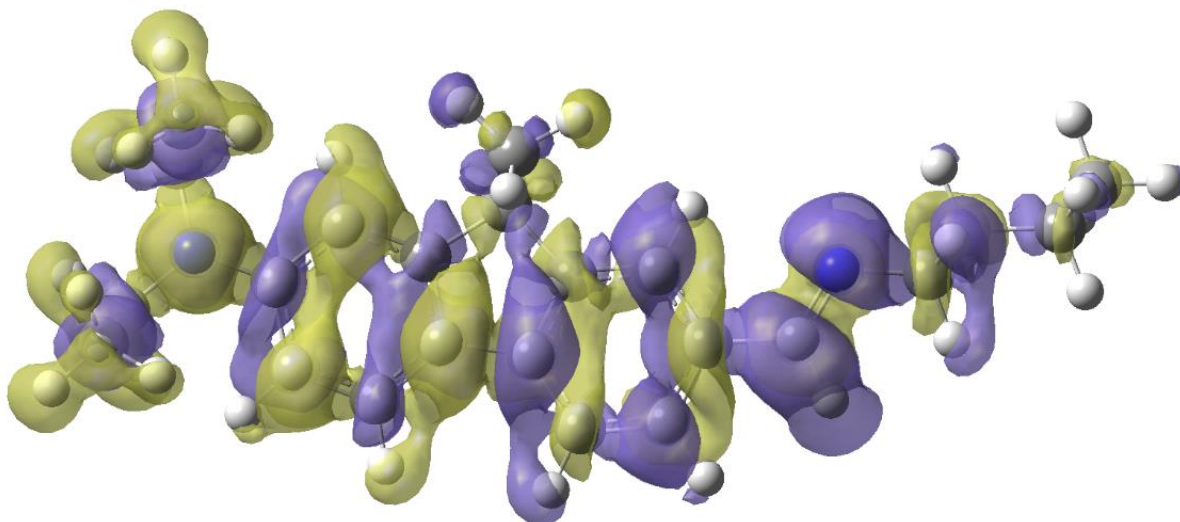


Figure 2.6 Calculated electron density difference between the excited state and ground state of FR0-SB. With optical excitation, the increase in electron density or negative charge is shown in purple while the decrease in electron density is shown in yellow. Overall electron density migrates from the yellow regions to the blue regions upon excitation. We notice a decrease in electron density at the diethyl amine side (left) and a net increase in negative charge on the imine nitrogen, which favors proton abstraction. The optimized ground state structure and its SCF electron density was obtained at the PBE/6-31G* level of theory while the excited state CI electron density was obtained using the same functional and basis set with the TD-DFT formalism.

The relative ratio of the areas under the emission bands for the protonated **FR0-PSB** divided by **FR0-SB** in ethanol is 1.45. We have also estimated the relative ratio of quantum yields between **FR0-SB** and **FR0-PSB** as 3.3 (see **Figure 2.7** and **Figure 2.8**). Therefore, one can deduce a relative population ratio of 4.8 between **FR0-PSB** and **FR0-SB** in ethanol. Since **FR0-SB** emission at 460 nm is associated with a lifetime of 89 ps, we surmise that the protonation step is associated with a lifetime of ~18 ps. However, the observed rise in the fluorescence at 650 nm was 197 ps; the large difference can be attributed to the presence of an intermediate(s) between the initial proton transfer and the final protonated species in solution.

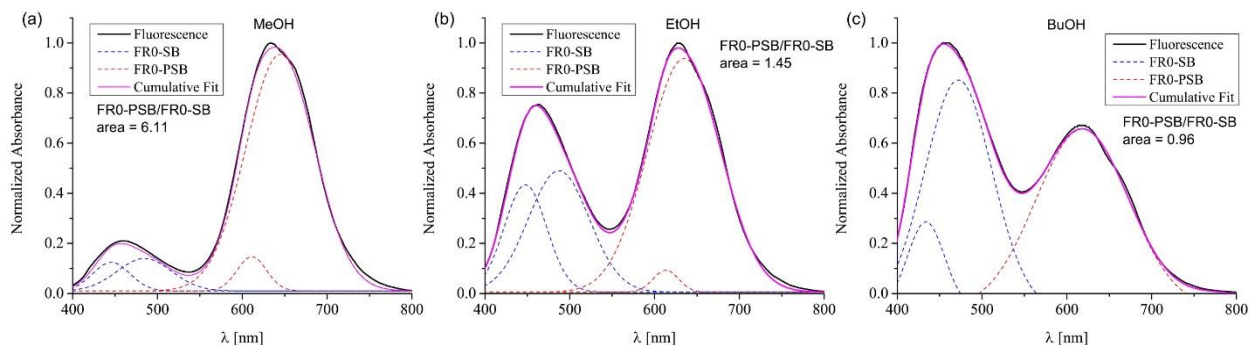


Figure 2.7 Fluorescence spectra of FR0-SB in (a) MeOH, (b) EtOH, and (c) BuOH with multiple Gaussians fit used to estimate the relative emission between the protonated FR0-PSB to the nonprotonated FR0-SB.

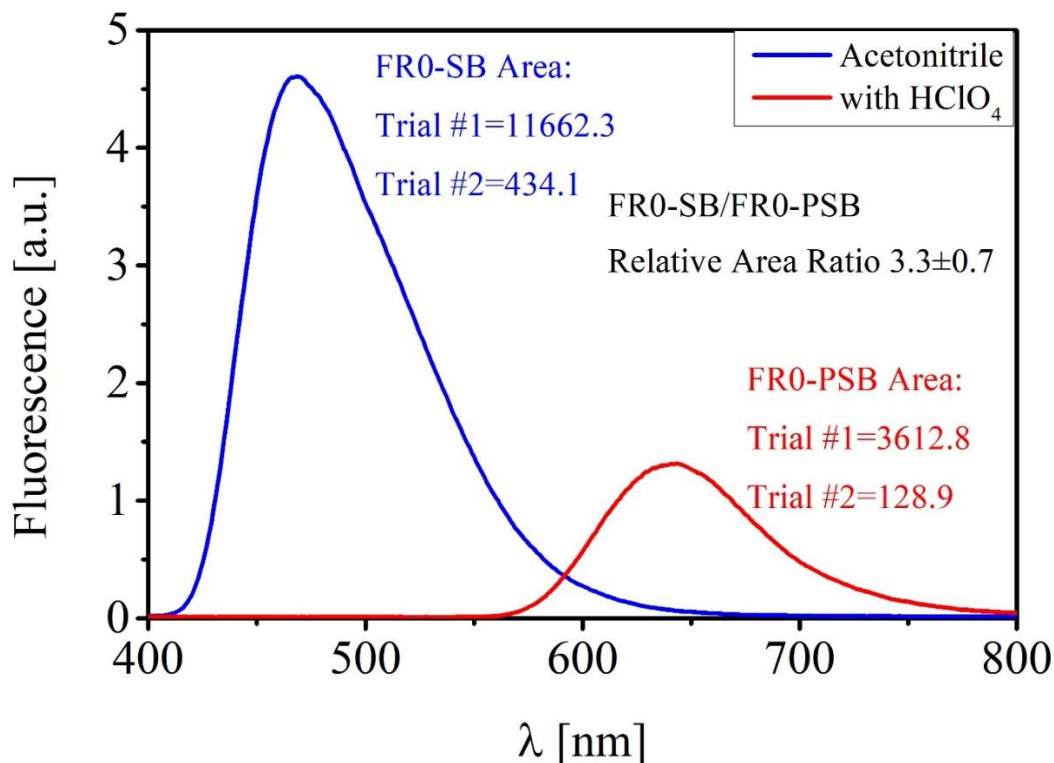


Figure 2.8 Estimation of the relative fluorescence quantum yield between **FR0-SB** and **FR0-PSB**. The fluorescence spectrum in acetonitrile was obtained and then the sample was acidified with diluted HClO_4 in acetonitrile to produce the protonated iminium (**FR0-PSB**). Acidification was carried out until no emission was observed from **FR0-SB**. Each sample was excited at the absorption maxima. The experiments were repeated (two trials) in samples with different concentration. The measured quantum yield from both trials was in close agreement.

The early dynamics can be further investigated using transient absorption as shown in **Figure 2.9**. Upon excitation at 400 nm, a decrease in absorption (positive signal) around 500 nm ($20,000\text{ cm}^{-1}$) was observed initially, which is attributed to excited state absorption (ESA) of **FR0-SB**. The ESA signal decays quickly (arrow **A** in **Figure 2.9a**) and is accompanied by a transient negative signal centered at 588 nm ($17,000\text{ cm}^{-1}$, arrow **B**) that gives rise to another negative signal initially centered at 630 nm ($15,870\text{ cm}^{-1}$, arrow **C**) and shifts to lower energy over time. The negative signal at 630 nm persists longer than 500 ps and is assigned as the stimulated emission (SE) from **FR0-PSB**. The transient signal at 588 nm is ascribed to the SE from an intermediate species that forms during the course of the intermolecular proton transfer. The intermediate is thought to be a caged complex between **FR0-SB** and the solvent molecule with a partial transfer of the proton (*vide infra*) prior to the full proton transfer process that is observed in the intermolecular proton transfer of photoacids.^{69,85}

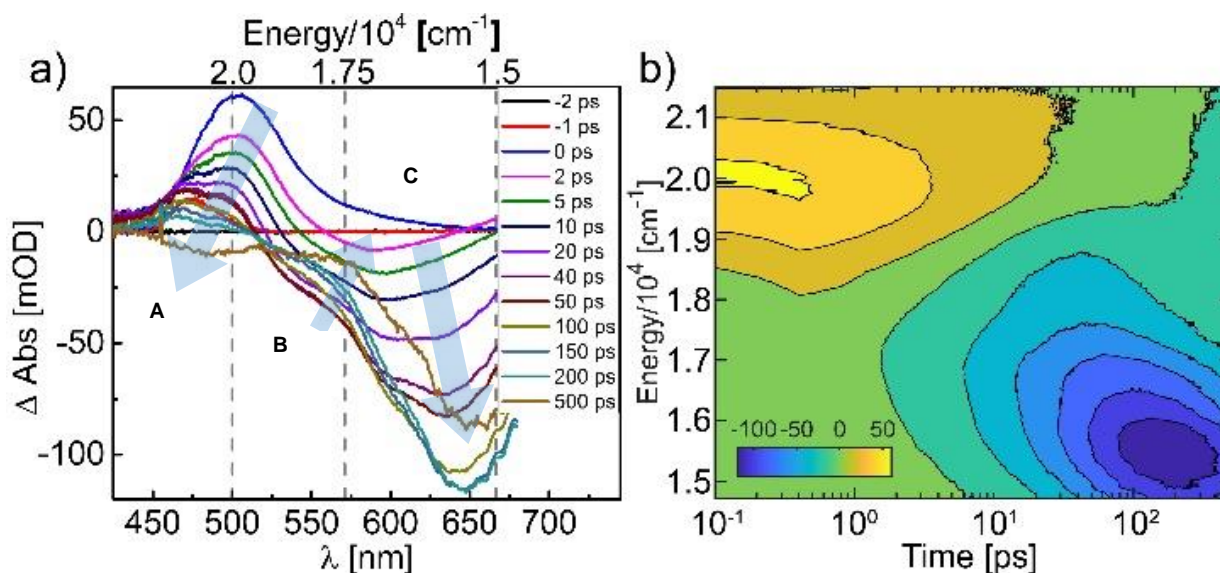


Figure 2.9 (a) Transient absorption spectra of FR0-SB at various time intervals after excitation in EtOH. Labeled arrows show the steps during the ESPT process. (b) Energy progression during the proton transfer process.

Transient absorption in the absence of a proton transfer event, such as in ACN, shows that ESA and SE appear soon after excitation (**Figure 2.10**) since both correspond to the non-protonated form. Both ESA and SE signals are long lived and can be fit to a biexponential decay with a long component of about 2.1 ns corresponding to the lifetime of the excited state and a short 26 to 30 ps component that is ascribed to conformational changes of the molecule upon excitation. The 26 ps decay component is also observed when exciting **FR0-PSB**, confirming its nature as an intramolecular mode from **FR0-SB** regardless of its protonation status (**Figure 2.11**).

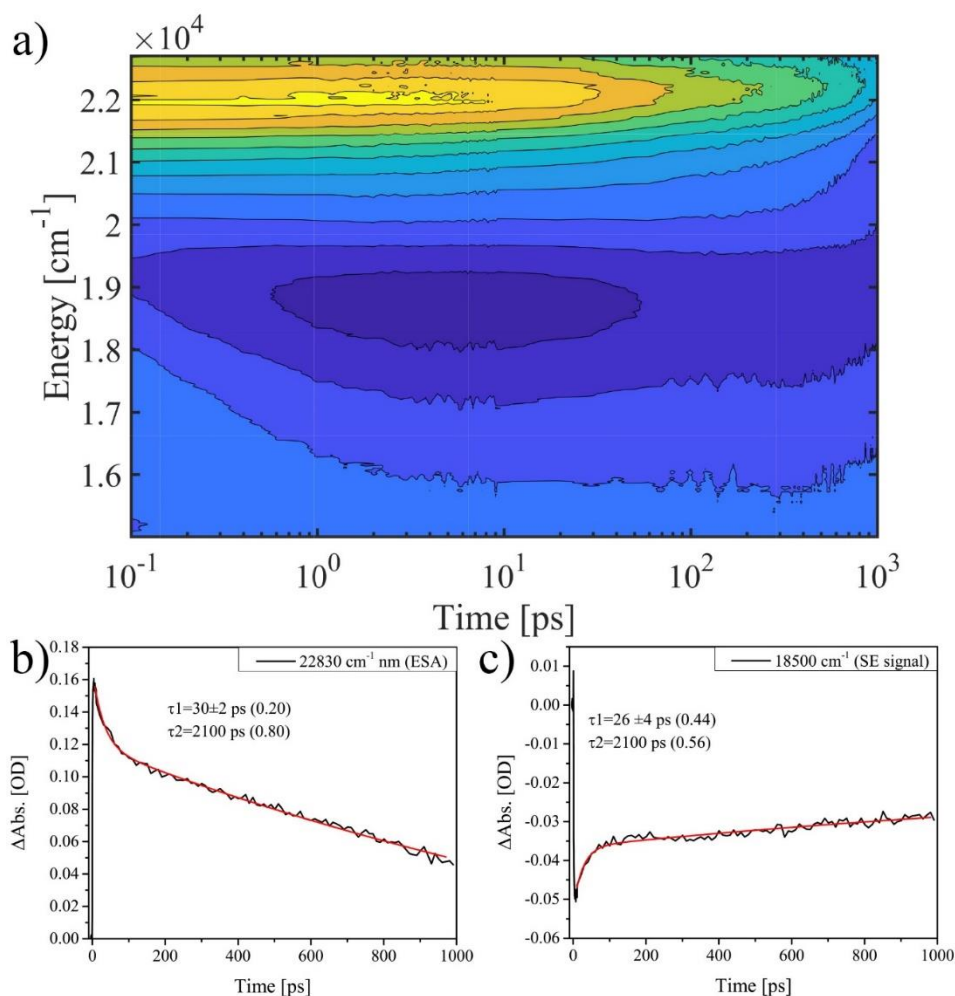


Figure 2.10 Transient absorption data of FR0-SB in acetonitrile. (a) Energy progression in ACN showing the long-lived ESA (b) and SE (c) signals from the non-protonated form along with biexponential fits at certain frequencies corresponding to each signal.

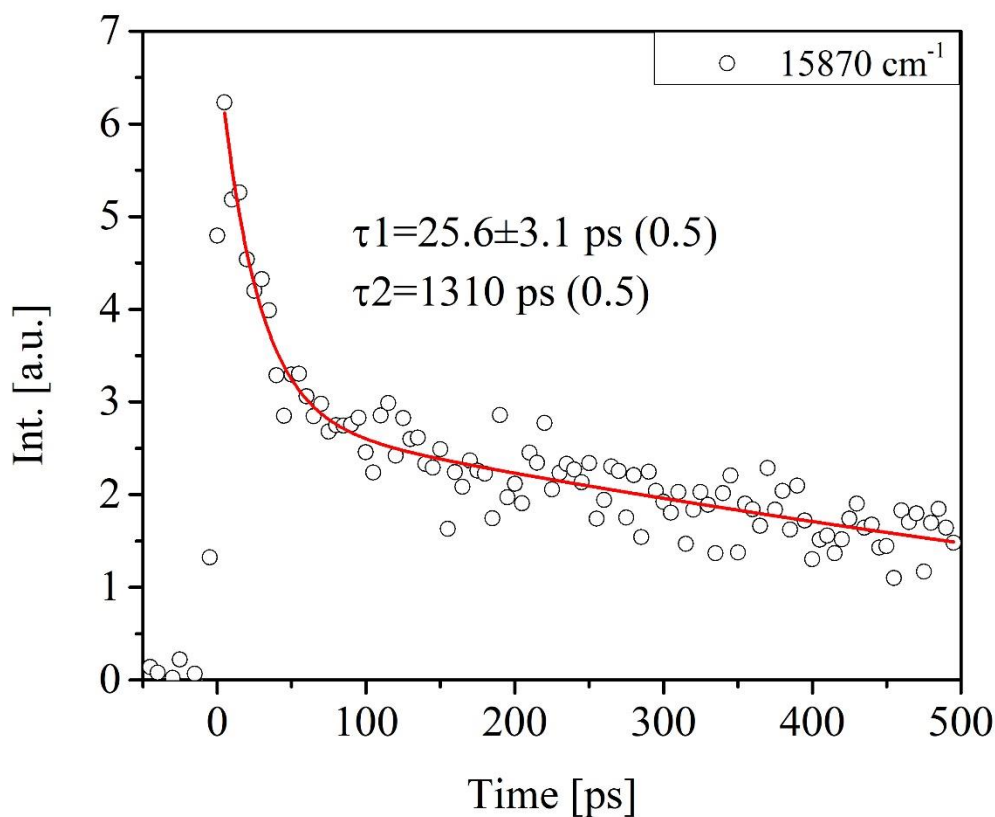


Figure 2.11 Stimulated emission decay of FR0-PSB in ethanol (acidified with HClO₄). Two decay components can be observed, a fast component corresponding to an intramolecular response from FR0-SB and a slow component corresponding to the excited state lifetime.

A more complete description of the experimental transient absorption data in EtOH is best obtained using a four-level sequential global analysis model.⁹¹ The results are summed up in a pictorial model shown in **Figure 2.12**. As stated previously, excitation in ACN (**I** → **III**, **Figure 2.12**) leads to a long-lived excited state (2.11 ns), while proton transfer in EtOH drastically reduces the excited state lifetime of **III** in the protic solvent (89 ps in EtOH). The model shows that the first component, which is the ESA of **FR0-SB** centered around 500 nm (20,000 cm⁻¹), decays with a 15.8 ps time constant (see **III** → **IV**, **Figure 2.12**), which is in agreement with the previously deduced ~18 ps from steady state spectra and the TCSPC measured lifetime.

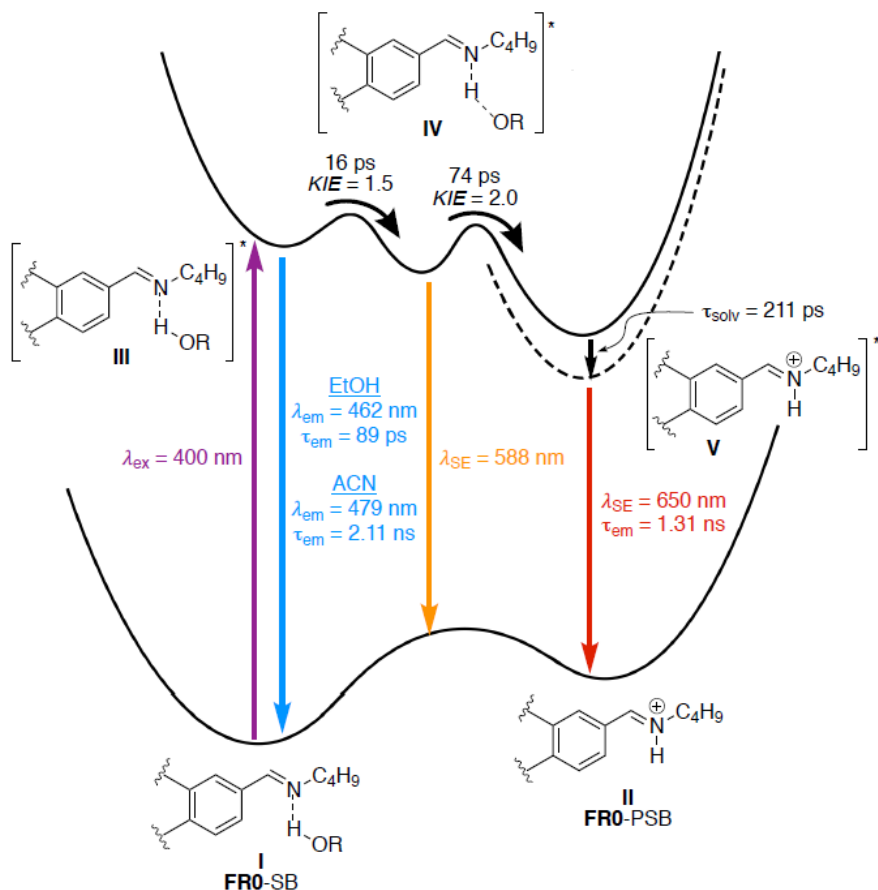


Figure 2.12 Pictorial model for the observed intermolecular ESPT dynamics in EtOH along with the associated time constants for the steps as obtained from global analysis (black) and the TCSPC data (colored).

This timescale is in agreement with the average dielectric relaxation of EtOH (16 ps).⁹⁸ This decay is accompanied with a rise in the second component featuring a broad SE signal centered at 588 nm ($17,000\text{ cm}^{-1}$), presumably the partially protonated state depicted as **IV**, decaying with a 73.9 ps time constant to yield the excited PSB form of **FR0** (**V**). It is worth noting that the partially protonated state **IV** is not emissive and is only observed by stimulated emission. Based on these time constants, we infer that the dielectric relaxation of the solvent is coupled with the formation of an intermediate species prior to the full proton transfer step. Characterized by the **FR0**-PSB SE feature with maxima around 630-660 nm ($15,870 - 15,150\text{ cm}^{-1}$), the final step is

best described with two components that we stipulate as solvation of the protonated form **V**. This step occurs on a 211 ps time scale, which is in agreement with the observed rise time in the TCSPC data at 650 nm (197 ps, see Figure S2b). The last component is long lived and decays with a 1.15 ns time constant, a value that is in agreement with the protonated **FR0-SB** lifetime (1.31 ns) that was previously determined using TCSPC (**Figure 2.5Error! Reference source not found.**).

Similar photophysical behavior is observed when **FR0-SB** is dissolved in MeOH (**Figure 2.13**). The global analysis model shows that the ESA signal from the non-protonated form decays to form the partially-transferred proton complex on a 2.9 ps timescale, also in agreement with the average dielectric solvation time of MeOH (5 ps).⁹⁸ The protonated **FR0-SB** is formed on a 27.1 ps timescale according to the global analysis model.

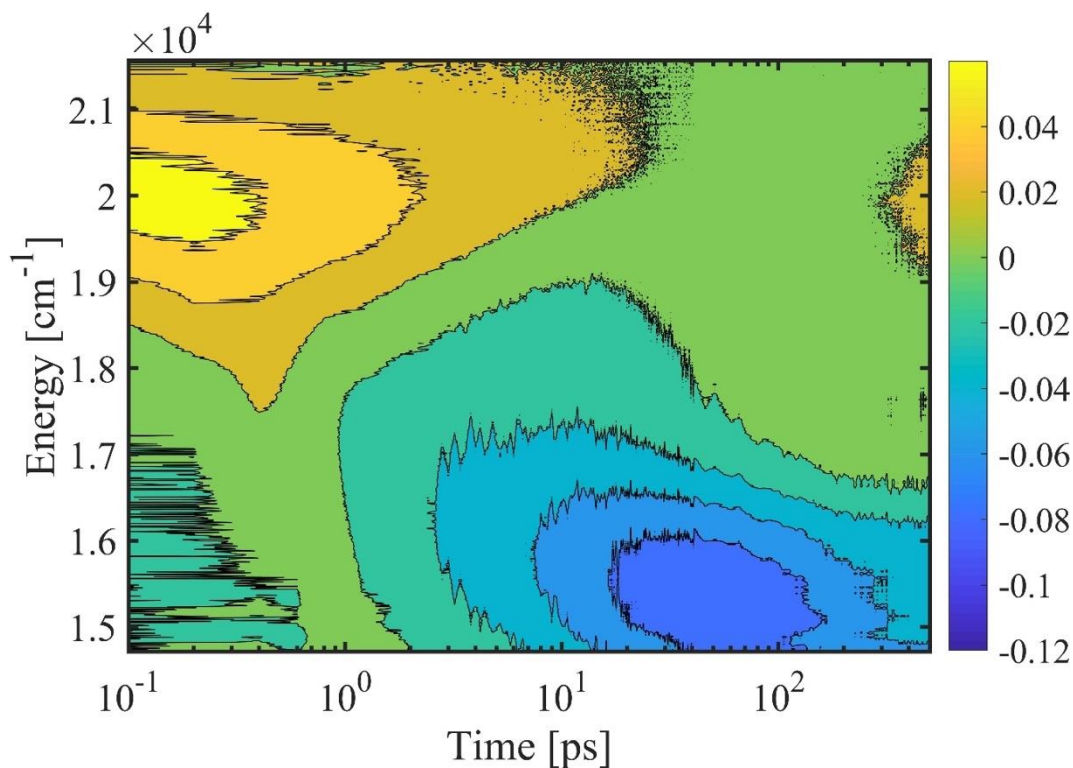


Figure 2.13 Transient absorption of FR0-SB in methanol. The plot shows the energy progression during the course of proton transfer from MeOH to FR0-SB.

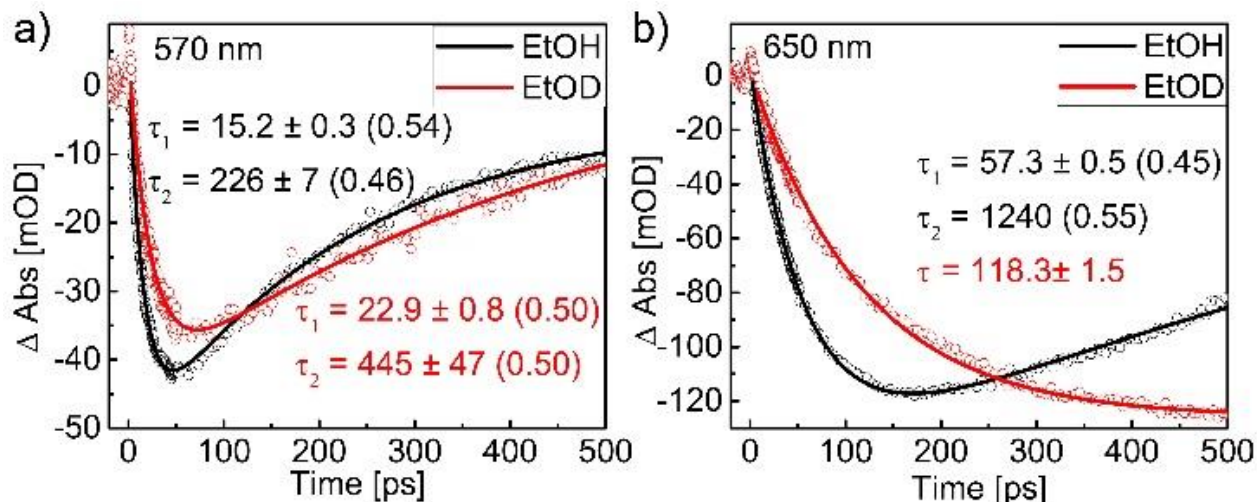


Figure 2.14 Transient absorption traces at (a) 570 nm where SE from the intermediate formation is observed, and (b) 650 nm where SE from the protonated FR0-SB can be seen while dissolved in EtOH (black) and EtOD (red). Biexponential decay constants are given in the inset along with the pre-exponential factors in parentheses. An isotope effect of 1.5 is observed during the formation of the partially-transferred proton intermediate while an isotope effect of 2 is observed during the final protonated form formation. Note, as the result of its apparent long-lived nature, lifetime of the 650 nm decay for the EtOD experiment could not be determined.

The global analysis deduced pathway was further confirmed using the transient absorption traces at selected wavelengths of **FR0-SB** in EtOH and EtOD (**Figure 2.14**). The formation of the intermediate, observed through the SE signal at 570 nm (**Figure 2.14a**), is coupled to dielectric solvent relaxation and occurs with a 15.2 ps time constant, in close agreement with the intermediate formation time as determined by the global analysis model (15.8 ps).

The second trace at 650 nm, which is the SE from the protonated **FR0-SB**, appears with a 57.3 ps time constant and is ascribed to the dissociation of the intermediate to form **FR0-PSB** (**Figure 2.14b**). It is more accurately measured by the global analysis, which gives a 73.9 ps time constant. Analysis of the transient absorption for the decay of each species in EtOH and EtOD (ethanol- d_6) provides KIE for each individual step. The initial 1.5 KIE is supportive of a hydrogen-bonded complex with partial transfer of the proton to the imine. The faster decay of the first transient intermediate in comparison to the second step suggests that the second measured KIE is

independent of the first, as one would not expect a population of the transient species to accumulate. The second, greater KIE (2.0) is suggestive of the actual bond breaking event that leads to the fully protonated species (see **Figure 2.12**). A greater isotope effect is observed in MeOD (methanol-d₄) as shown in **Figure 2.15**.

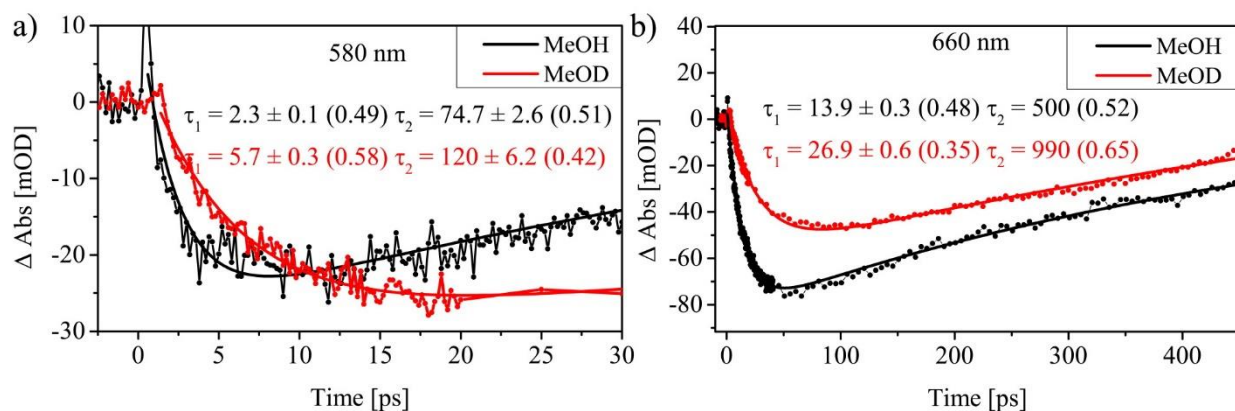


Figure 2.15 Transient absorption traces of FR0-SB in fully deuterated methanol. TA traces at (a) 580 nm where SE from the intermediate formation is observed, and (b) 660 nm where SE from the protonated FR0-SB can be seen while dissolved in MeOH (black) and fully deuterated methanol (red). Biexponential decay constants are given in the inset with the pre-exponential factors in parentheses. An isotope effect of 2 is observed during the formation of the intermediate as well as in the formation of the final protonated form

2.4 Conclusion

A modular molecular system (imine formation via the reaction of an aldehyde with an amine), with flexibility to easily probe structural and electronic factors in future studies, shows a remarkable ability to increase its basicity upon photoexcitation. The ability to electively stimulate proton abstraction with light during reactions will find itself useful in an array of disciplines. By way of possible applications, super photobase proton abstraction is important to protein conformational changes, selective functionalization of unactivated C-H bonds, and potentially assisting in water splitting. Furthermore, the large apparent Stokes shift and strong fluorescence will be useful for imaging and displays. The variety and expansive nature of potential applications for super photobases indicates their importance for further studies.

Chapter 3 Intramolecular Response of Cyanine Dyes

The optically populated excited state wave packet propagates along multidimensional intramolecular coordinates soon after photoexcitation. This action occurs alongside an intermolecular response from the surrounding solvent. Disentangling the multidimensional convoluted signal enables the possibility to separate and understand the initial intramolecular relaxation pathways over the excited state potential energy surface. This chapter discusses how one can track the initial excited state dynamics by measuring the fluorescence yield from the first excited state as a function of time delay between two color femtosecond pulses for several cyanine dyes, having different electronic configurations. We find that when the high frequency pulse precedes the low frequency one and for timescales up to 200 fs, the excited state can be depleted through stimulated emission with efficiency that is dependent on the molecular electronic structure. A similar observation at even shorter times was made by scanning the chirp (frequencies ordering) of a femtosecond pulse. These changes reflect the rate at which the nuclear coordinates of the excited state leave the Franck-Condon (FC) region and progress towards achieving equilibrium. Through functional group substitution, we explore these dynamic changes as a function of dipolar change following photoexcitation. We show that with proper knowledge and control over the phase of the excitation pulses, we can extract the relative energy relaxation rates through which the early intramolecular modes are populated at the FC geometry soon after excitation

This chapter has been reproduced from *Phys. Chem. Chem. Phys.* **2017**, *19*, 14085-14095 with permission from PCCP owner societies.

3.1 Introduction and Background

The molecular dynamics following photoexcitation are determined during the first hundreds of femtoseconds. Upon formation, the excited state wave packet is no longer considered in equilibrium with either the nuclear degrees of freedom or the surrounding solvent. This nascent excited state wave packet determines the ensued dynamics towards the equilibrium. Achieving this equilibrium requires involvement from both intra- and inter-molecular modes through multidimensional coordinates which can occur within tens of femtoseconds as in the barrierless electron transfer or takes up to nanoseconds where diffusional solvent transport are crucial for this equilibrium.^{8,99-101} In general, dynamics that take longer than 100 fs are well understood and assigned whereas the early dynamical steps, soon after the absorption of a photon and up to 100 fs are highly obscured by multiple convoluted signals,¹⁰²⁻¹⁰⁵ with an interplay between intra- and inter-molecular interactions and their corresponding energy fluctuations. So far, ultrafast multidimensional spectroscopic techniques and four-wave mixing methods have been successfully implemented to achieve an understanding about the early timescale processes.^{21,106} However, their implementation requires precise control over a sequence of multiple pulses and a rigorous theoretical treatment to understand the detected signals and how they relate to molecular dynamics.¹⁰⁷ In our current work, we show that single beam pulses with well-defined phase can be used to extract early dynamical information that is not easily obtained by other methods. Single shaped-pulse approaches have the additional advantage that they may be used on single nanoparticles or molecules.⁴⁷

Cyanines are a class of polymethine dyes that consist of an odd number of conjugated $2p_z$ orbitals. Their structure resembles carotenoids and protonated Schiff bases (PSB's), making them an ideal system to model and understand the excited state dynamics of conjugated polyene systems

in general. Moreover, cyanines have potential applications in photodynamic therapy,¹⁰⁸ solar energy conversion,¹⁰⁹ and bioimaging.¹¹⁰ Generally, they are positively charged compounds with an alternating and delocalized electron density between the polymethine two ends.¹¹¹⁻¹¹³ Cyanines have an optically active S_0 - S_1 transition in the visible or near-infrared region, that is highly dependent on the backbone length.¹¹⁴

The ground state electronic structure of cyanine dyes can be viewed as a combination of three configurations: two degenerate resonance structures wherein the positive charge is localized at either end of the conjugated chain and a charge centered configuration.¹¹⁵ These three resonance structures are considered to roughly contribute with an equal amount to the wave function, hence the charge remains delocalized and the polymethine structure is represented with minimal bond length alteration (BLA).¹¹⁶ The S_0 - S_1 , $\pi \rightarrow \pi^*$, optical transition occurs without a significant change in the permanent dipole moment and hence can be described by invoking a nonpolar solvation response.^{112,117} Upon the addition of an electron donating group to the central carbon of the backbone, cyanine dyes exhibit an electronic configuration where the positive charge predominantly remains at this central position to form what is termed as a bis-dipolar configuration.¹¹⁸ In addition, this configuration exhibits an additional symmetric ground state resonance structure that does not contribute to the asymmetric excited state structure.¹¹⁹ Therefore, optical excitation of substituted cyanines is accompanied by a significant change in the dipole moment. This instant change in the dipole moment caused by photoexcitation triggers a polar solvation response,^{38,119} causing the reorientation of solvent molecules. The progress of the molecular relaxation soon after photoexcitation proceeds simultaneously through intra- and inter-molecular modes as illustrated in the schematic representation in **Figure 3.1**.

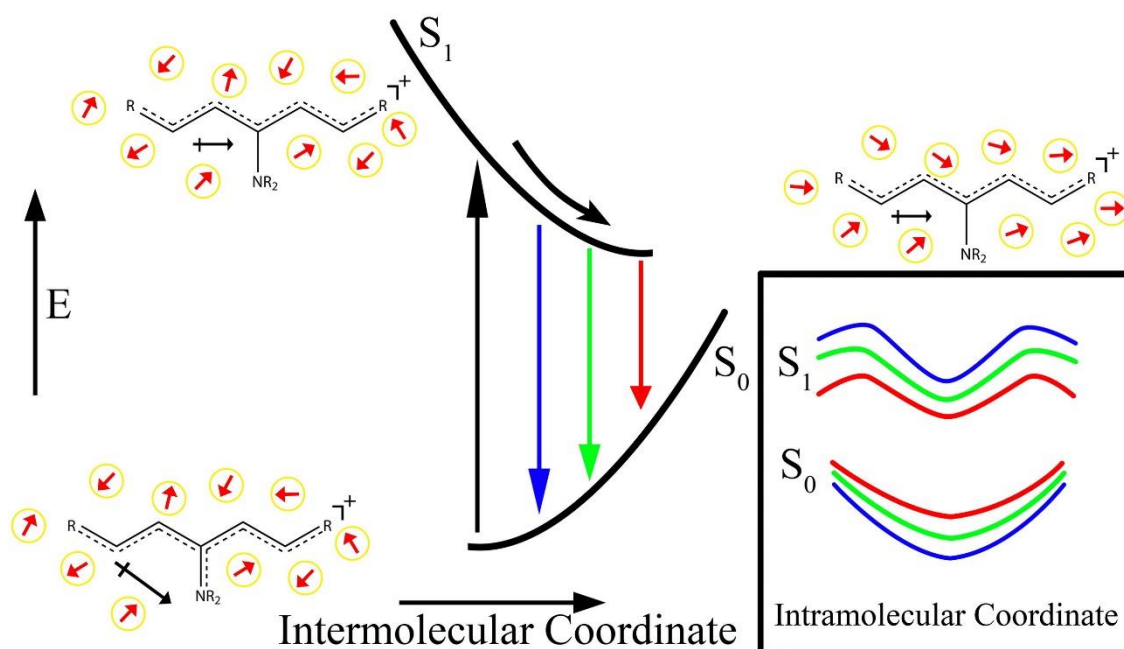


Figure 3.1 Schematic representation for the intermolecular solvation potentials of a cyanine dye where the surrounding solvent responds to the change in the cyanine dipole moment associated with photoexcitation. Relaxation across the intermolecular coordinate is coupled with changes in the multidimensional intramolecular coordinate.

The Dantus research group has been taking advantage of the ability to manipulate the arrival times of the spectral components in a broadband femtosecond pulse to control nonlinear optical processes and develop novel spectroscopic methods.^{33,57} By controlling chirp the molecular dynamics can be probed directly using a single shaped pulse,^{37-38,120-121} this approach can serve to learn about ultrafast processes soon after photoexcitation. As demonstrated in this work for a set of cyanine dyes with rational variations in their structure and their optical properties. Pulse shaping in general has been implemented in multidimensional spectroscopy to provide versatility in tailoring and controlling the pulses at the sample position.^{52,122-123} It also provides the ability to suppress undesired signal pathways.¹²⁴

3.2 Experimental Methods

3.2.1 Synthesis

The experiments were carried out using the cyanine dyes shown in **Figure 3.2**. IR806 (Sigma-Aldrich) was used as purchased without further purification. The other cyanine dyes were synthesized according to a published procedure¹²⁵ starting from IR806 with rational variation of the substituent at the cyanine *meso*- position. That is the central carbon across the polymethine chain.

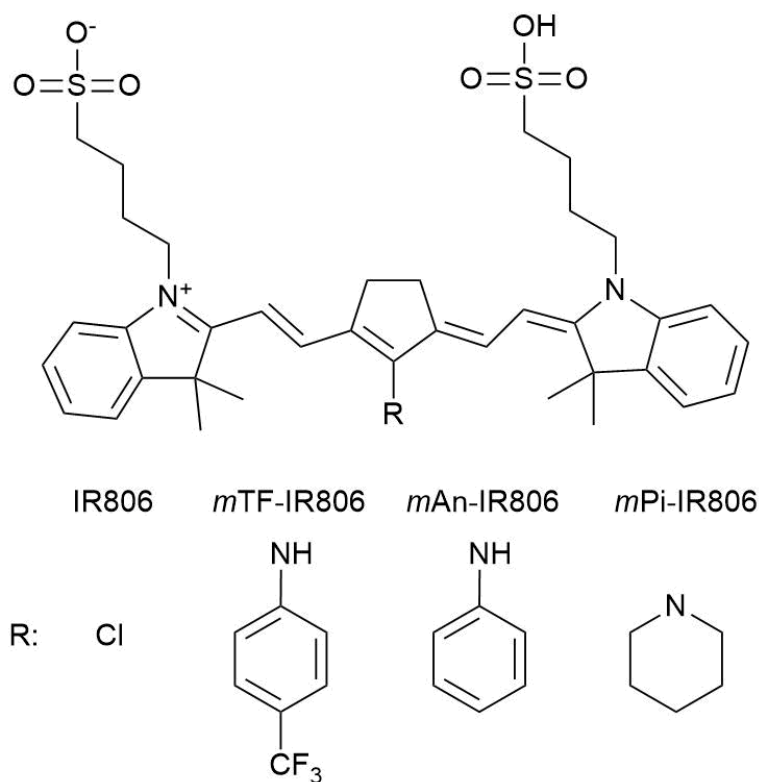


Figure 3.2 Chemical structures of the prepared cyanine dyes.

meso-Trifluoromethylaniline IR806 (*m*TF-IR806): IR806 (0.1 mmol, 1 eq.) was stirred in DMF at 80 °C. Then 4-(trifluoromethyl)aniline (1 mmol, 10 eq.) was added and the mixture was kept under stirring for 8 h. After DMF evaporation the crude mixture was purified using chromatography on silica gel with DCM/MeOH (99:1 – 95:5). Dark blue solid was obtained in a

~20% yield. δ_{H} (500 MHz, Methanol- d_4) 7.77 (2 H, d, J 13.3), 7.72 (2 H, d, J 8.3), 7.48 (2 H, d, J 8.3), 7.31 (4 H, t, J 7.5), 7.18 (2 H, d, J 7.9), 7.11 (2 H, t, J 7.4), 5.85 (2 H, d, J 13.4), 4.61 (1 H, s), 4.04 (4 H, t, J 6.9), 2.90 (4 H, s), 2.86 (4 H, t, J 7.0), 1.98 – 1.86 (8 H, m), 1.39 (12 H, s).

meso-Aniline IR806 (*mAn*-IR806): IR806 (0.02 mmol, 1 eq.) was stirred in DMF at room temperature. Then aniline (0.1 mmol, 5 eq.) was added and the mixture was kept under stirring for 12 h. Dark blue solid was obtained in a ~90% yield. δ_{H} (500 MHz, Methanol- d_4) 7.77 (2 H, d, J 13.0), 7.52 (2 H, t, J 7.8), 7.48 – 7.40 (4 H, m), 7.35 – 7.21 (4 H, m), 7.11 (2 H, d, J 8.1), 7.07 (2 H, t, J 7.5), 5.73 (2 H, d, J 13.1), 3.98 (4 H, t, J 6.6), 2.86 (8 H, d, J 5.8), 1.96 – 1.85 (8 H, m), 1.37 (12 H, s).

meso-Piperidine IR806 (*mPi*-IR806): IR806 (0.02 mmol, 1 eq.) was stirred in DMF at room temperature. Then piperidine (0.1 mmol, 5 eq.) was added and the mixture was kept under stirring for 16 h. After DMF evaporation, dark blue solid was obtained in a ~90% yield. δ_{H} (500 MHz, DMSO- d_6) 7.67 (2 H, d, J 13.1), 7.48 (2 H, d, J 7.4), 7.32 (2 H, t, J 7.7), 7.23 (2 H, d, J 7.9), 7.10 (2 H, t, J 7.5), 5.77 (2 H, d, J 13.2), 3.99 (4 H, t, J 7.8), 3.01 (4 H, t, J 5.6), 2.47 (4 H, t, J 7.2), 1.79 – 1.73 (4 H, m), 1.74 – 1.66 (4 H, m), 1.67 – 1.60 (4 H, m), 1.60 (12 H, s), 1.58 – 1.53 (2 H, m).

3.2.2 Steady State Spectroscopy

UV-Visible absorbance spectra were recorded using an ATI/Unicam UV2 model for IR806 while dissolved in methanol (MeOH) and the remaining substituted cyanine dyes while dissolved in *n*-propanol (PrOH). PrOH has been used with the substituted dyes to have absorption spectra that are red shifted compared to MeOH, which provides better overlap with the excitation laser in the later experiments. Fluorescence spectra for all the dyes while dissolved in the aforementioned solvents were obtained using a Hitachi FL-4500 fluorescence spectrometer.

3.2.3 Laser Experiments

The laser excitation and fluorescence detection experiments were carried out using IR806 dissolved in MeOH, while the remaining dyes were dissolved in PrOH. The starting concentration was 50 μM and further dilutions were made, if necessary, to achieve an optical density value of 0.3 with the excitation laser. The experimental setup consists of a regeneratively amplified Ti:Sapphire laser (Spitfire, Spectra-Physics, Santa Clara, CA) producing femtosecond pulses at a repetition rate of 1 kHz. The pulses were compressed and shaped after the amplifier with a pulse shaper (MIIPS-HD, Biophotonic Solutions Inc., East Lansing, MI) using the Multiphoton Intrapulse Interference Phase Scan (MIIPS) method.^{30,126} The laser pulse-to-pulse stability was ensured with a fidelity value of 0.9.¹²⁷ IR806 and *mTF*-IR806 were excited using near-Gaussian pulses centered at 800 nm with 25.9 nm fwhm bandwidth. The pulse bandwidth corresponds to a pulse duration of 37 fs (when transform-limited, TL). While *mAn*-IR806 and *mPi*-IR806 were excited using near-Gaussian pulses centered at 790 nm with a pulse duration of 35 fs (when TL). In all experiments, unfocused 25 μJ pulses were sent onto a cuvette having a 2 mm path length. Fluorescence signal was detected at a right angle from the excitation axis near the entrance of the cuvette window using a multimode optical fiber connected with a compact spectrometer (USB4000, Ocean Optics). The stimulated emission signal was detected along the laser propagation axis after the cuvette.

The pulses were compressed to TL at the sample location and were further shaped while detecting the fluorescence signal simultaneously. Using the pulse shaper, chirp scan was carried out by applying a chirp phase mask of the form $\phi(\omega) = 0.5\phi''(\omega - \omega_0)^2$, where ϕ'' is the quadratic phase or the chirp value. The chirp value was scanned from negative to positive 20,000 fs^2 . Chirp on the TL pulse stretches it to longer durations according to $\tau / \tau_{TL} = \sqrt{1 + (4 \ln 2)^2 (\phi'' / \tau_{TL}^2)^2}$. In the

case of negative chirp, the high frequency components precede the lower ones; whereas the arrival order is reversed with the positive chirp.

Time delay scans were carried out using the pulse shaper by advancing or delaying the frequencies higher than the laser central frequency. The scan can be viewed as a two-color pump-probe while the fluorescence signal is being detected simultaneously.

3.2.4 Computational Methods

To investigate the structural changes that are accompanied with the substitution of IR806, ground state geometry optimization for all the cyanine dyes was carried out by density functional theory (DFT) using the 6-311+G(3d,p) basis set. A modified hybrid generalized gradient approximation (GGA) functional of Perdew, Burke and Ernzerhof (PBE α) was used.¹²⁸ α , which corresponds to the Hartree-Fock exchange contribution, was tuned to 0.456. The exchange term using this linear combination was found to provide reasonable DFT results in relative agreement with CCSD(T) in terms of the cyanine BLA.¹²⁹ Atomic charges were computed for the optimized ground state geometry using the natural bond orbital (NBO) analysis.¹³⁰ Excited state energies were calculated by the time-dependent DFT (TDDFT) formalism using the 6-311+G(3d,p) basis set to model the experimentally observed blue shift in the absorption maxima of the cyanines as a function of different substituents. When TDDFT was employed, both of the ground state geometry optimization and the vertical excitation were carried out using the PBE functional.¹³¹ Using this functional, reasonable vertical excitation energies for the cyanine dyes can be obtained.¹³²⁻¹³³ All ground state geometry optimizations were followed by frequency calculations to ensure the absence of imaginary eigenvalues and confirm the minimum structure. Solvent effects were incorporated using the Integral Equation Formalism Polarizable Continuum Model (IEF-PCM),¹³⁴ wherein equilibrium solvation was used in the ground state optimization and non-equilibrium

solvation with linear response was used in the excited state calculation. MeOH was used with IR806 while PrOH was used with the other dyes.

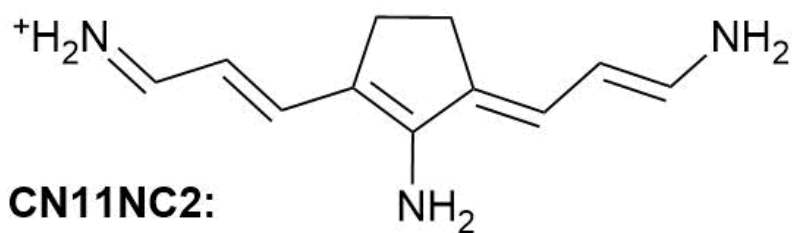
To understand the role of the substituent on the intramolecular response of cyanines, the minimum energy path (MEP) on the excited state potential energy surfaces of simpler cyanine dyes was modeled using the complete active space self-consistent field (CASSCF) with 6-31G(d) as a basis set. The ground state geometry was obtained at the same level of theory with no symmetry constraints. The MEP on the first excited state potential was followed from the Franck-Condon (FC) region up to the emissive excited state minima, state averaging both the ground and the excited state with equal weights. The absence of imaginary frequencies was ensured at both the ground state geometry and the excited state minima. Dynamic electron correlation was accounted for at selected nuclear configurations over the CASSCF MEP using the multireference second order perturbation theory (CASPT2) with 6-31G(d) as a basis set. CASPT2 was employed without correlating the core electrons on the heavy atoms while also including an IPEA shift of 0.25 Hartree in the evaluation of the zeroth order Hamiltonian.¹³⁵ Moreover, the excited state potential energy surfaces for the substituted cyanines was scanned using constrained optimization over the two dihedral angles that represent twisting and pyramidalization of the substituent using CASSCF gradients followed by evaluating the energies using CASPT2. The cyanine models were chosen with the same polymethine backbone length, that is 9 carbons between the two terminal nitrogens. The central three carbons were also locked using a cyclopentene ring. Three cases were considered: (i) unsubstituted (CN11), (ii) amine substituent (CN11N), (iii) dimethyl amine substituent (CN11NC2). The chemical structures for the three dyes are shown in Scheme. 2. For the unsubstituted dye CN11, (12,11) was chosen as the active space, which contains all the conjugated p_z orbitals, whereas (14,12) was considered as an active space for the substituted dyes

to include the substituent nitrogen p_z orbital. All DFT and TDDFT calculations were performed using Gaussian 09 program.¹³⁶ CASSCF and CASPT2 calculations were carried out using Molpro 2012.1.¹³⁷⁻¹⁴¹

CN11:



CN11N:



CN11NC2:

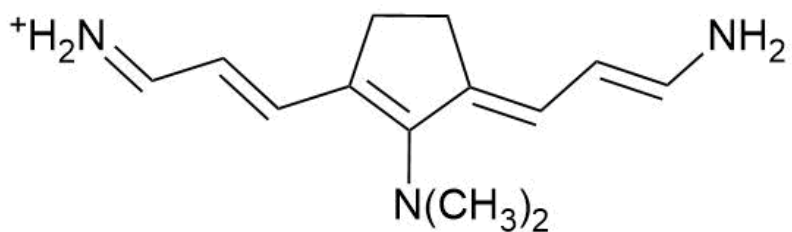


Figure 3.3 The chemical structures for the three model cyanine dyes used in the CASSCF calculations.

3.3 Results

3.3.1 Steady State Spectroscopy

The first excited state transition of the cyanine dye IR806, in which IR806 is presented with the minimal BLA as well as an electronic configuration that is delocalized over the conjugated polymethine backbone, occurs without a significant change in the permanent dipole moment. This $\pi \rightarrow \pi^*$ transition to the S_1 state results in a sharp absorption spectrum featuring a vibronic shoulder at higher energies as shown in **Figure 3.4a**. The fluorescence spectrum for IR806 exhibits slight departure from the mirror image symmetry as can be seen in the same figure.

The remaining cyanine dyes share an identical polymethine structure with IR806, yet differ in terms of the *meso*- substituent. Due to this electron donating substituent, they acquire extra contribution from the charge-centered configuration, which permits a polar solvation response. The absorption spectra for all the polar solvated dyes (**Figure 3.4b-d**) are blue shifted with respect to the nonpolar IR806 and are essentially broader, lacking the cyanine vibronic feature observed for IR806. Interestingly, all the polar solvated cyanines show an additional S_2 absorption peak that is emissive.¹⁴²⁻¹⁴³ The absorption maxima, fluorescence maxima, Stokes shifts and full width at half maxima (fwhm) for the absorption and the fluorescence spectra of all the dyes are given in **Table 3.1**.

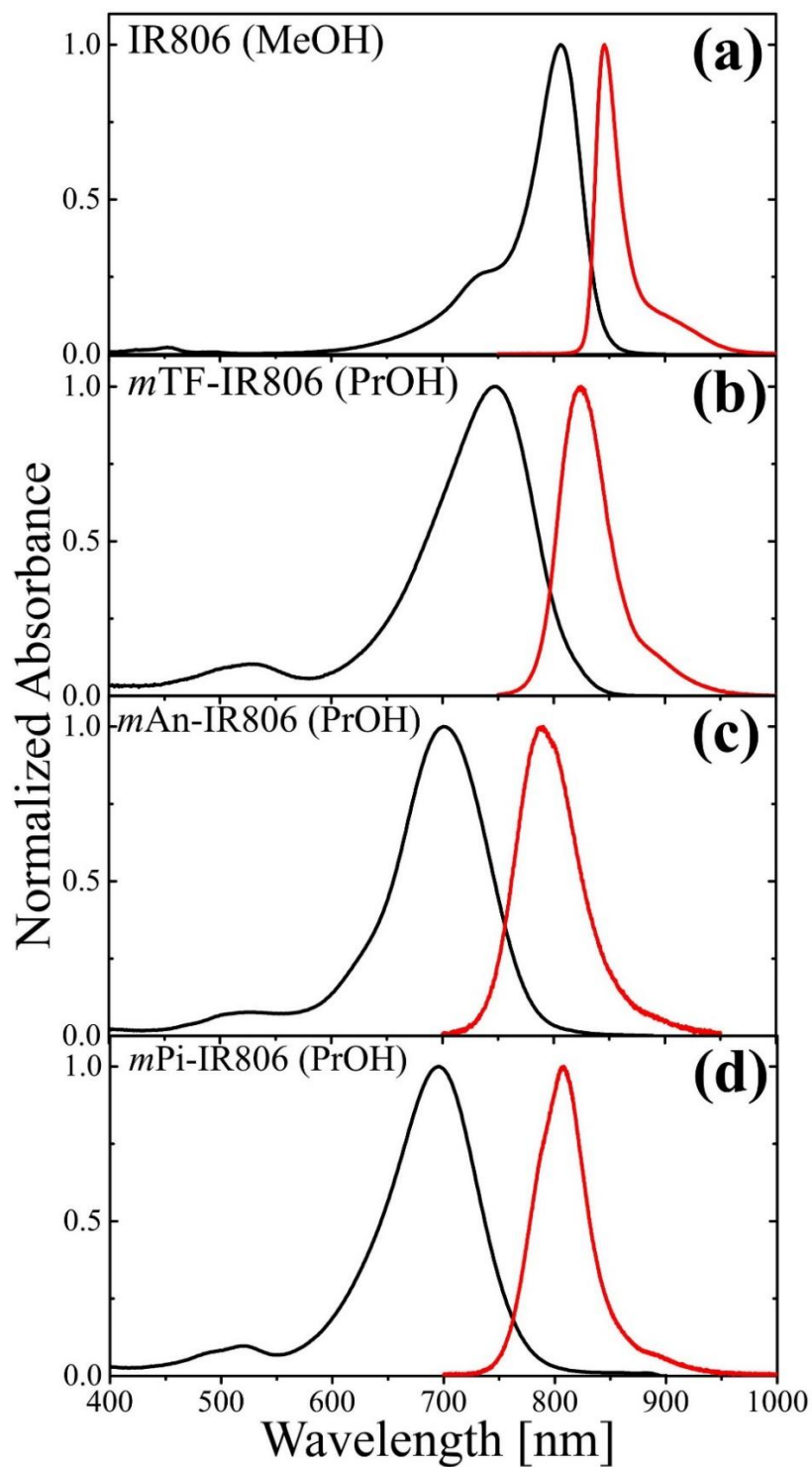


Figure 3.4 Steady state absorption (black) and fluorescence (red) spectra for the cyanine dyes (a) IR806, (b) mTF-IR806, (c) mAn-IR806, and (d) mPi-IR806. The used solvent with each dye is indicated in parentheses.

Table 3.1 Absorption maxima, fluorescence maxima, Stokes shifts and fwhm of the absorption and the emission spectra of the first excited state (S1) for IR806, mTF-IR806, mAn-IR806, and mPi-IR806. S1-S0 Stokes shift measured as the difference between the absorption and fluorescence spectra maxima

	IR806 (MeOH)	<i>m</i>TF-IR806 (PrOH)	<i>m</i>An-IR806 (PrOH)	<i>m</i>Pi-IR806 (PrOH)
Abs. max (cm⁻¹)	12407 (806 nm)	13369 (748 nm)	14265 (701 nm)	14368 (696 nm)
Fl. Max (cm⁻¹)	11825 (845 nm)	12127 (825 nm)	12652 (790 nm)	12377 (807 nm)
S₁-S₀ Stokes Shift (cm⁻¹)	582	1242	1613	1991
Abs. fwhm (cm⁻¹)	778	1908	1857	1935
Fl. fwhm (cm⁻¹)	489	740	1018	834

3.3.2 Chirp and Time Delay Measurements

The total fluorescence signals from each cyanine dye as a function of linear chirp are shown in **Figure 3.5**. The fluorescence signal is normalized with respect to the signal obtained using TL pulses. The stretched pulse duration is shown on the top axis to elucidate the timescales at which changes are observed in the chirp trace. In all cases, the typical first excited state chirp response is obtained.^{37,48} a reduced fluorescence yield while using negatively chirped pulses. The high to low frequencies ordering allows the excited state population to be depleted via stimulated emission before intramolecular vibrational redistribution and fluorescence occur.³⁷ The stimulated emission traces which inversely correlate with the fluorescence traces are shown in **Figure 3.6**.

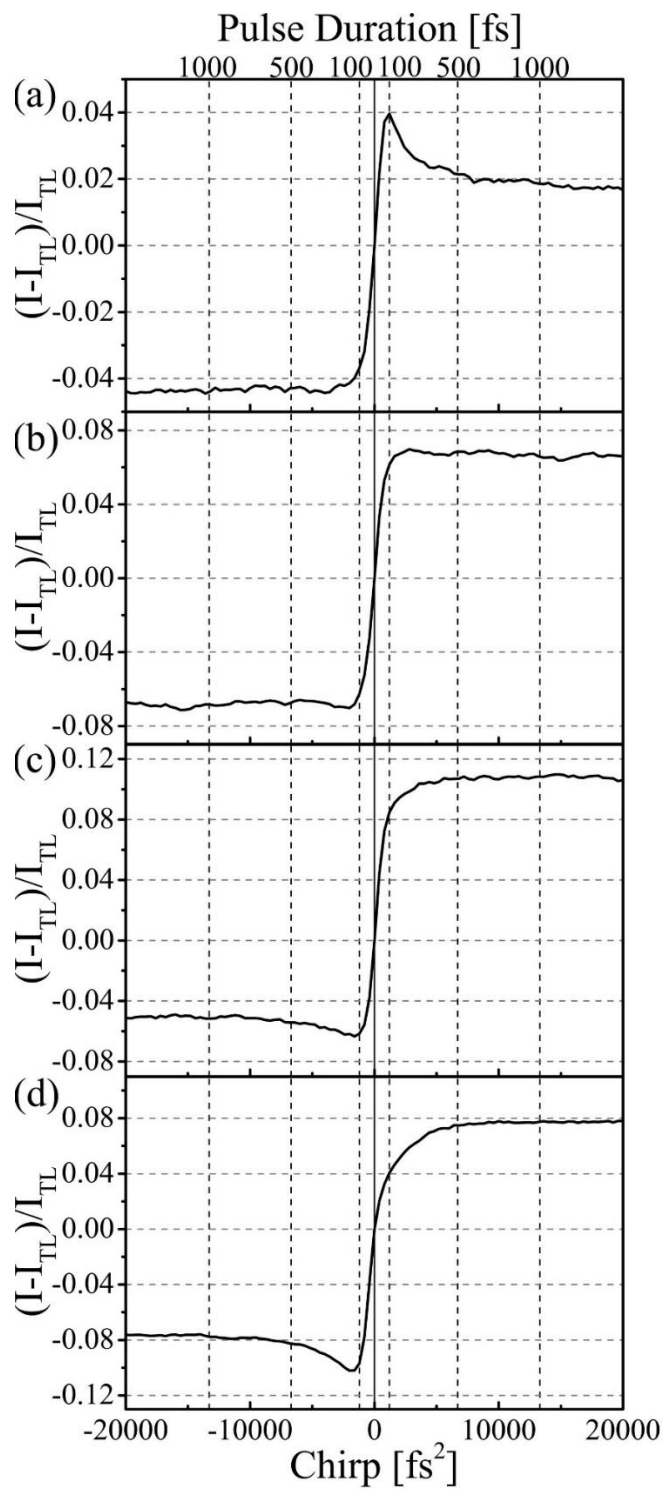


Figure 3.5 Total fluorescence signal as a function of linear chirp for (a) IR806, (b) mTF-IR806, (c) mAn-IR806, and (d) mPi-IR806. Top axis shows the duration of the chirped pulse.

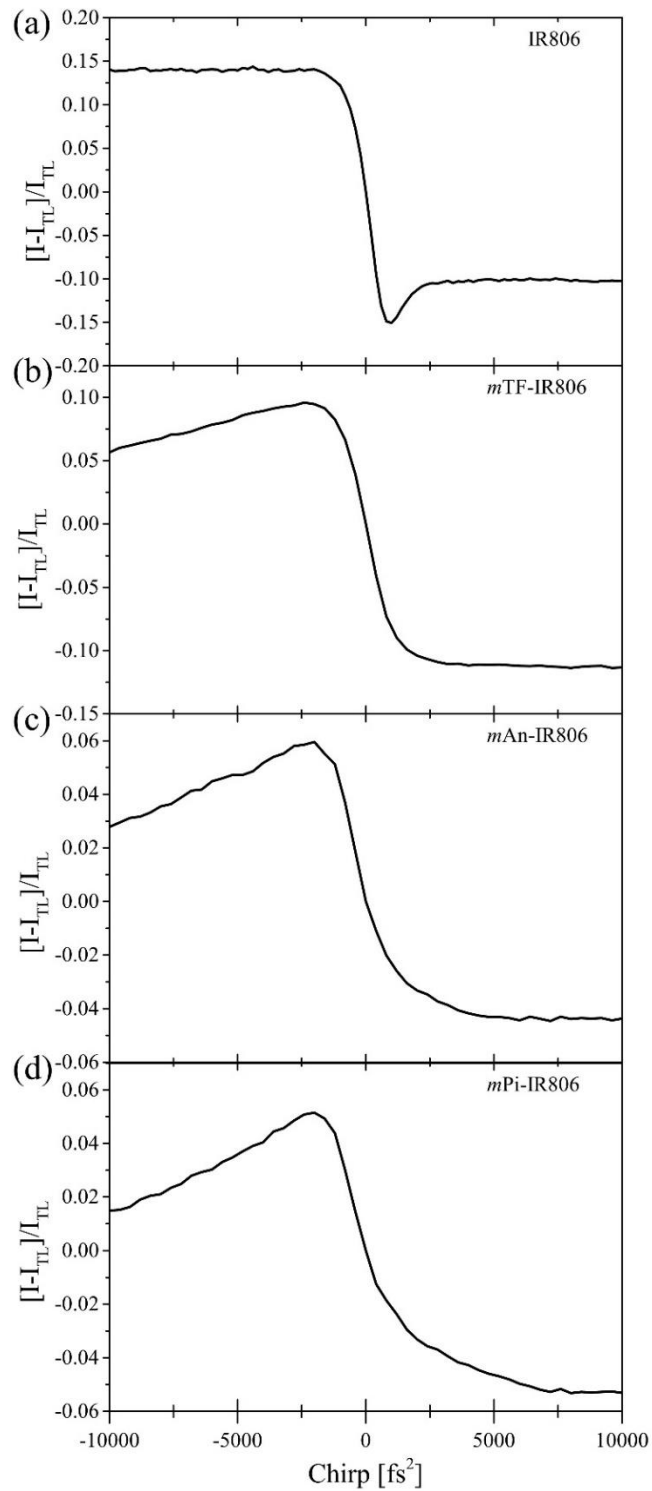


Figure 3.6 Stimulated emission signal as a function of linear chirp for (a) IR806, (b) mTF-IR806, (c) mAn-IR806, and (d) mPi-IR806. The traces are inversely correlated with fluorescence signal as a function of linear chirp.

Previous studies showed that the maximum fluorescence depletion, which occurs at a small negative chirp value, is unaffected by the solvent and its temperature,³⁸ whereas the effect of positive chirp was observed to change as a function intermolecular changes via solvent and temperature. Changes on both sides of the chirp trace were detected as a result of the appearance of new species with different dynamics, such as the formation of a triplet state.¹²⁰ Here we see that IR806 chirp response (**Figure 3.5a**) has a constant fluorescence depletion on the negative chirp side, a chirp response that resembles the nonpolar cyanine dye IR125.³⁸ The positive chirp side shows a sudden increase in the fluorescence signal that reaches a maximum value at 1200 fs² (~100 fs), then it starts to gradually decrease and becomes constant at large positive chirp values (~10,000 fs²), this is also consistent with IR125.³⁸

The remaining cyanine dyes show a gradual change in the chirp response (**Figure 3.5b-d**) according to the following order: *mTF-IR806*, *mAn-IR806*, then *mPi-IR806*, which is correlated with the electron donation strength of the substituent. On the negative chirp side, a maximum fluorescence depletion point starts to appear at small chirp values. The chirp values correspond to durations of about 100-200 fs, such fast time-scales primarily reflect intramolecular modes in the molecule. This maximum depletion occurs when the energy relaxation on the excited state potential energy surface matches the frequency sweep of the chirped pulse. On the positive side of the chirp trace, the sudden increase in the fluorescence signal becomes absent. Instead, a gradual increase in the fluorescence signal is observed as a function of increasing chirp value. These changes on the positive side reflect variations in the intermolecular response for the molecules. For instance, *mPi-IR806* which has the strongest electron donation substituent and is expected to be have with the largest change in dipole moment upon excitation, shows the slowest gradual increase in fluorescence to achieve a constant fluorescence signal.

Pump-probe traces with different frequency pulses were generated using the pulse shaper are shown in **Figure 3.7**. Using these traces, the timescale that is associated with the changes in the molecular response is directly probed, rather than the duration of the chirped pulse. **Figure 3.7a** shows the response when the high frequency pulse precedes the lower one, which resembles the negative chirp case. Using this arrival order, the excited state population responsible for fluorescence is depleted compared to what is obtained using TL pulses. **Figure 3.7b** shows the reversed frequencies ordering, that is the low frequency pulse is followed by the higher frequency one (similar to positive chirp). The total fluorescence is normalized with respect to the asymptotic yield at time delays longer than 500 fs. Each trace in **Figure 3.7** resembles one side of the chirp traces in **Figure 3.5** and shows the same trend across the dyes when compared carefully.

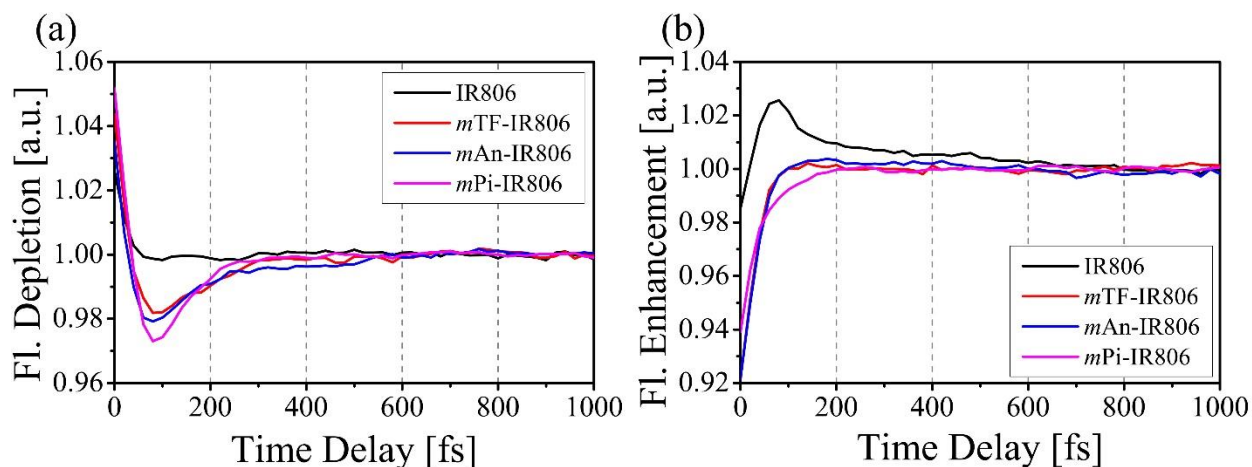


Figure 3.7 Total fluorescence signal using two color pump-probe pulses for the four cyanine dyes when (a) the high frequency pulse precedes the lower frequency one and when (b) the arrival order is reversed.

3.4 Quantum Chemical Calculations & Discussion

Quantum chemical calculations has been applied to explore the electronic properties and potential energy surfaces of the dyes studied experimentally above, and how these properties depend on the substituent on the central carbon. The steady state spectroscopy for the cyanine dyes studied here reveals a difference between the substituted dyes and unsubstituted IR806 (**Figure 3.4**). DFT calculations can provide a connection between the cyanine structures and the observed optical properties. The optical properties of cyanine dyes are highly dependent on the BLA,¹⁴⁴ which is the difference between the lengths of single and double bonds along the polymethine backbone. This difference reflects the proximity in which each electronic configuration contributes to the equilibrated ground state structure. For instance, a cyanine with equal contribution between its two configurations, where in each one the charge is localized at either end of the cyanine, is considered with zero BLA and known as the “cyanine limit”. The linear and nonlinear molecular polarizability, and so the molecular optical response, are directly related to the BLA value.¹⁴⁴ At this cyanine limit, the first and third order polarizabilities are maximized while the optical transition energy is minimized and considerably sharp.¹⁴⁵ Therefore an increase in the optical transition energy along with broadening in the absorption spectra are expected with the increase of BLA for cyanines with the same backbone length, For this purpose, the bond lengths between two adjacent atoms along the polymethine backbone for the optimized ground state structures are shown in **Figure 3.8**. The central carbon is represented with the atomic index 0 while the terminal nitrogens are indexed as 5 and -5. IR806 clearly represents the minimum BLA compared to the other substituted dyes. BLA increases as the electron donation strength for the *meso*- substituent increases. The substituted dyes show higher relative increase in the lengths of the two bonds around the central carbon; this is with respect to the other C-C bonds across the cyanine backbone. This

indicates an increase in the charge-centered resonance structure for the cyanine dye (bis-dipolar),¹¹⁸ which is further confirmed by the increased positive charge on the central carbon as shown later in **Table 3.2**. It was also noticed that with the increased bis-dipolar character, the conjugated backbone slightly departs from planarity, which can be seen as a change in the dihedral angles along the polymethine carbons. This departure from planar structure can be seen in the average dihedral angles along the carbons with indices: 0 to 3, 0 to -3, 1 to 4, and -1 to -4 (**Table 3.2**).

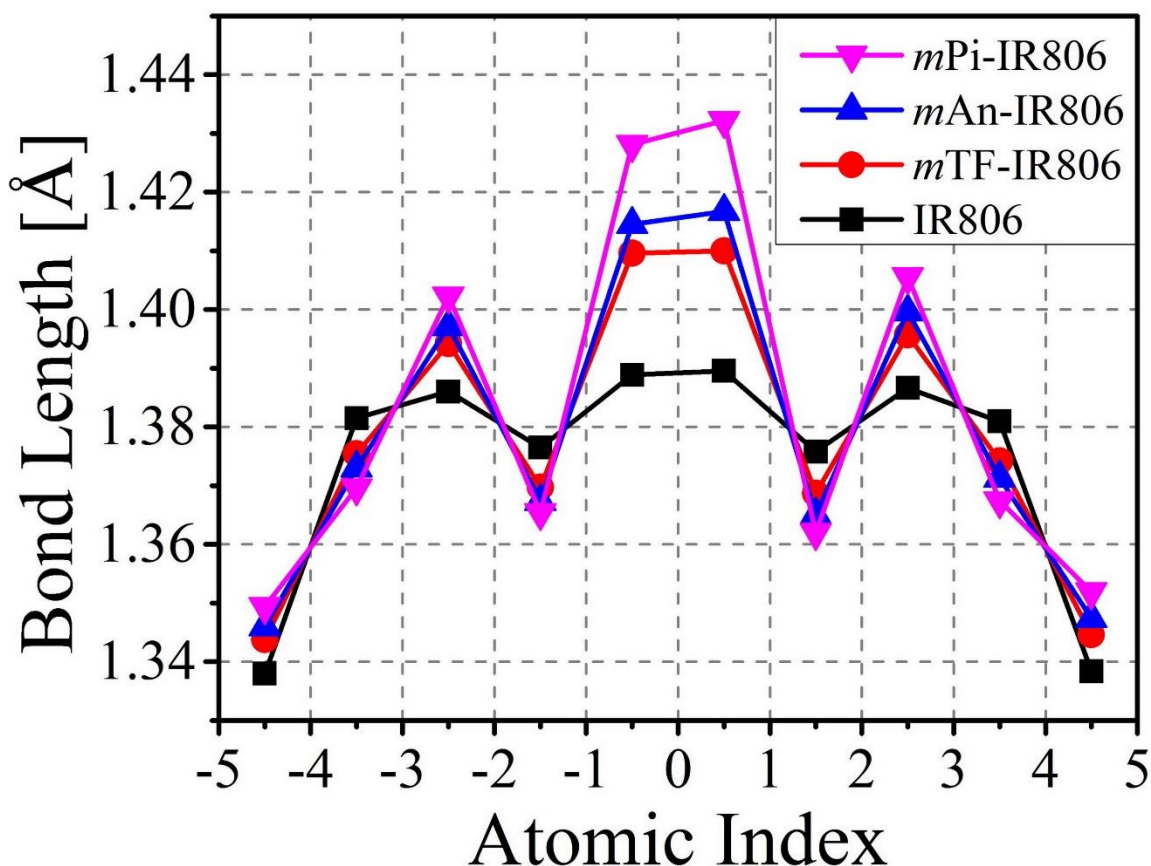


Figure 3.8 Bond length across the conjugated polymethine chain for the optimized ground state structures of the four cyanine dyes. Terminal nitrogens are indexed as -5 and 5.

To address the observed blue shift in the absorption spectra as the substituent electron donation strength increases, the vertical excitation energies on the optimized structures was carried

out using TDDFT. Typically, vertical excitation energies for the cyanine dyes are poorly described by TDDFT due to the multireference nature for these dyes and their highly delocalized electronic transition, but TDDFT often describes other features of these excitations (such as the shape of the excited PES) reasonably well.¹⁴⁶⁻¹⁴⁸ Several functionals have been found to perform better than others for prediction of the vertical excitation energy of the $\pi \rightarrow \pi^*$ excitation of the cyanine dyes, including the PBE functional used in this work.^{132,149} The TDDFT vertical excitation energies are calculated at the PBE/6-311+G(3d,p) level and reported in **Table 3.2** along with the associated error in comparison with the experimental absorption maxima. It is worth noting that the error was slightly larger when employing state-specific PCM solvation rather than the current shown linear response PCM solvation. The calculated excitation energies overestimate the experimental value in all cases. Interestingly, the associated error in the calculated excitation energies for the substituted dyes is smaller than the unsubstituted IR806, which might be attributed to the relative locality of the excitation in the substituted cyanines. The substituted cyanines clearly show the increase in the vertical excitation energies as a function of substituent electron donation strength, as seen experimentally.

Table 3.2 The cyanine dyes' TDDFT vertical excitation energies, error relative to the experimental absorption maxima, NBO charge on the central carbon, and the average dihedral angles for the ground state structures

	TDDFT ΔE (cm^{-1})	error (cm^{-1})	Charge on central C (e) (PBE α)	Average dihedral angle (PBE α)
IR806	14749	2342 (0.29 eV)	0.057	179.60
<i>m</i> TF-IR806	14430	1061 (0.13 eV)	0.387	177.18
<i>m</i> An-IR806	14599	333 (0.04 eV)	0.410	176.82
<i>m</i> Pi-IR806	15105	738 (0.09 eV)	0.463	176.47

In the time resolved experiments, the molecular response on the positive side of the chirp trace (**Figure 3.5**) and time delay scan, in which the low frequency components of the pulse precede the higher ones (**Figure 3.7b**), can be correlated with the intermolecular response.³⁸ In the case of nonpolar response, IR806, the fluorescence signal rises sharply at small chirp and short time delay values. The sudden increase in the signal followed by a gradual decrease has been observed in the chirp scan for indocyanine green (ICG or IR125) when dissolved in ethylene glycol at low temperatures.³⁸ Similarly in the time delay scan when ICG was in the pocket of human serum albumin protein.¹²⁰ The gradual increase in the fluorescence signal observed for positive chirp is a pattern that was observed with the polar solvated cyanine IR144.³⁷ The gradual change across the cyanines studied here, reflects the difference in their polar solvation response. In the time delay traces for instance, *m*TF-IR806 requires about 120 fs to reach a stable fluorescence signal, whereas in the case of *m*Pi-IR806, which has a stronger polar solvation character, it takes about 240 fs to reach a constant signal. The polar solvation response in substituted cyanine dyes is attributed to the larger change in the dipole moment upon excitation compared to their unsubstituted counterparts.^{38,119} This change can be illustrated using the electron density difference

between the excited state TDDFT density and the ground state DFT density as shown in **Figure 3.9** for IR806 and *m*Pi-IR806 plotted at the same isovalue scale. Upon excitation, the electronic density migrates from the yellow to the blue regions. In the case of IR806, the density migration is delocalized over the conjugated system, which is the typical behavior for $\pi \rightarrow \pi^*$ transitions. Also, charge migration between the two opposing poles of the chlorine atom can be observed. This change in the chlorine electronic density occurs because of the increased density on the polymethine central carbon. *m*Pi-IR806 also shows the same delocalized change in the conjugated system electronic density upon excitation. However, density migration from the central carbon to the substituted piperidine is also observed, which can be viewed as a small charge transfer from the polymethine backbone to the substituent. This small charge transfer causes the dipole moment to change instantly upon excitation, triggering the polar solvation response for the substituted cyanines. This change in the dipole moment upon excitation is validated in our TDDFT/DFT calculations where $\mu_{S1} - \mu_{S0}$ for *m*Pi-IR806 was larger (-0.76 Debye) compared to IR806 (-0.54 Debye).

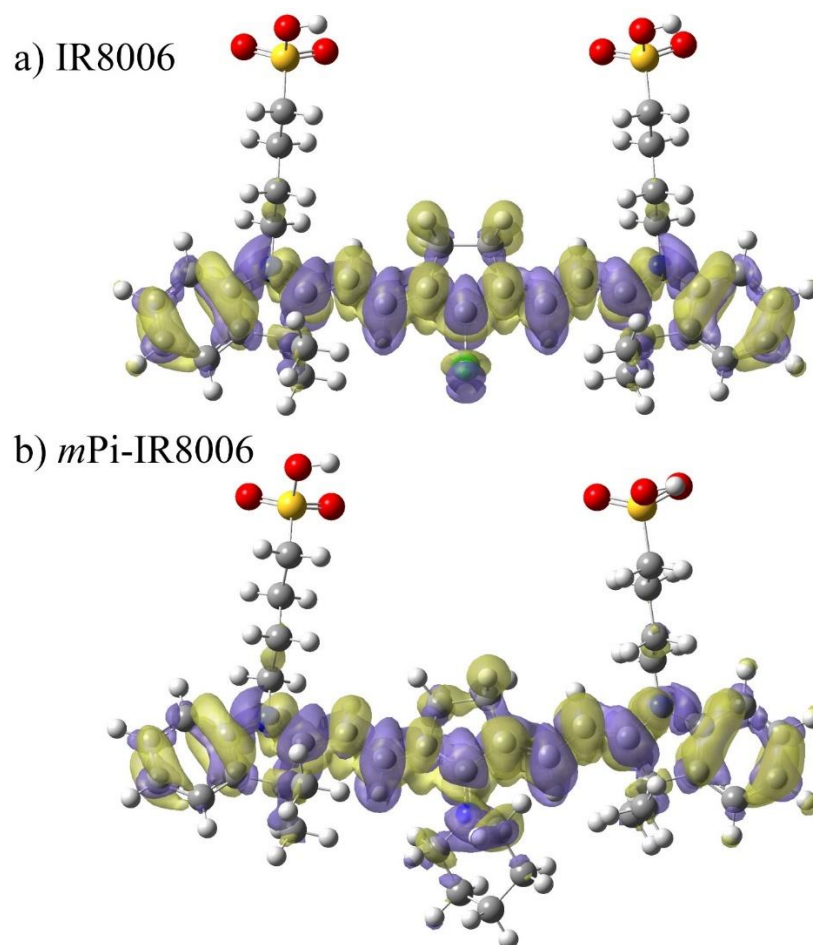


Figure 3.9 Electron density difference between the ground and first excited states for (a) IR806 and (b) *m*Pi-IR806. Upon excitation, the electron density migrates from the yellow to the blue regions.

The excited state dynamics of cyanine dyes has been investigated extensively experimentally¹⁵⁰⁻¹⁵³ and theoretically,¹⁵⁴⁻¹⁵⁵ their behavior is analogous to the dynamics of the isoelectronic PSB's and carotenoids.¹⁵⁶⁻¹⁵⁹ The cyanine dyes tend to exist in the all-trans form while in the ground state. Upon photoexcitation, two modes are excited sequentially. The initial stretching across the conjugated system from the FC region to the emissive planar minima, followed by a torsional motion mode across one of the bonds in the polyene backbone. In the case of short cyanines, this torsional motion is coupled and barrierless, leading to a twisted intramolecular charge transfer state (TICT), that is neighboring a conical intersection (CI) with the

ground state. For longer cyanine dyes, a significant barrier separates the near-planar geometry from the twisted conformers. Beyond this twisting barrier, the nuclear coordinates descend steeply towards the TICT and the CI as well. It has been noticed that the barrier to twisting is smallest around the central carbon.¹⁵⁴ Moreover, this energy barrier is lower for the case of *meso*-substituted cyanine dyes compared to their unsubstituted counterparts.¹⁶⁰

In the cyanines considered in this work, the bonds around the central carbon are locked by a cyclopentene ring, which prevents twisting around the central carbon within the polymethine backbone. The changes that are observed in the time resolved experiments (**Figure 3.5** & **Figure 3.7**) when using negative chirp arise from stimulated emission occurring while the excited state wave packet is within the FC region before escaping towards the emissive minima. Therefore, we seek to understand the potential energy surface from the FC region to the emissive minima of the unsubstituted cyanine in comparison to its substituted counterparts. This is also to assess which dye is associated with the largest change in energy during the course of relaxation on the excited state potential. For this purpose, we have modeled the excited state potential energy surfaces of the three cyanines shown in **Figure 3.3**. The CASSCF ground state structure was planar only in the case of the unsubstituted CN11, while the substituted dyes were slightly twisted across their polymethine backbones. The amine substituents of both CN11N & CN11NC2 are in a planar sp^2 configuration, which implies electron donation from the substituent and the double bond character between the substituent nitrogen and the cyanine backbone. When following the minimum energy path on the excited state potential to the emissive excited state minima for each dye as shown in **Figure 3.10**, one can clearly see that the largest energy change is associated with CN11NC2, which is the dye with the strongest bis-dipolar character.

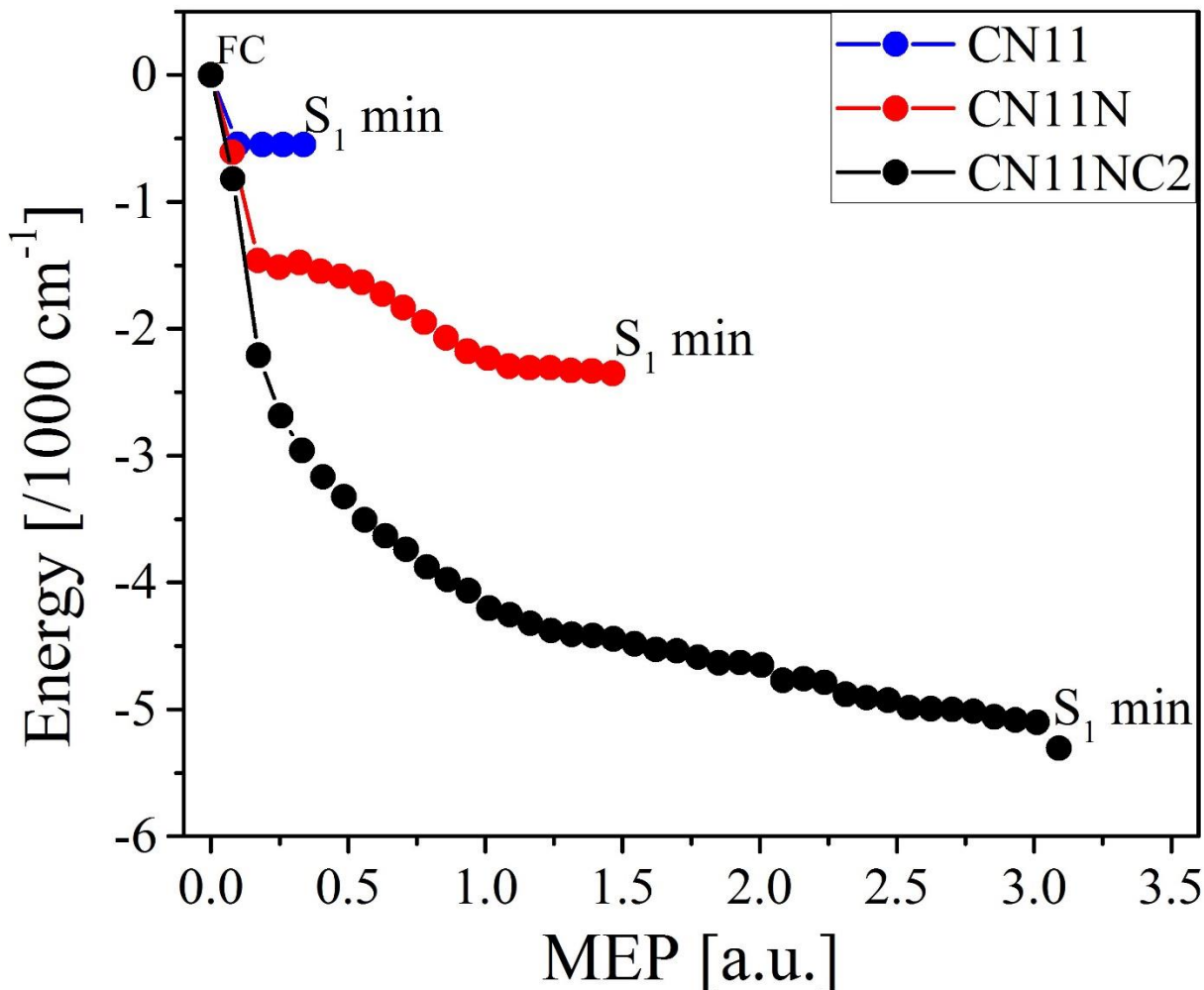


Figure 3.10 The minimum energy path on the first excited state potential from the FC region up to the S₁ minima using CASSCF for the three cyanine models.

The geometric changes associated with this excited state energy relaxation are depicted in **Figure 3.11** for the CASSCF S₁ minimum energy paths of the two substituted cyanines; specifically, the dihedrals that describe substituent twisting and pyramidalization are presented. Symmetric twisting of θ_1 and θ_2 reflect twisting, while the difference, $\theta_2 - \theta_1$, reflects pyramidalization. At the FC geometry, energy relaxation proceeds with the typical stretching mode across the cyanine backbone, similar to the unsubstituted cyanine CN11 and consistent with what is known about long cyanines.¹⁵⁴ However, this mode is coupled with the twisting of the substituent

while the amine group remains planar. At some twisting point (~ 8 degrees for CN11N, ~ 35 degrees for CN11NC2) the amine substituent undergoes pyramidalization, in which the substituent electron donation begins to diminish. The final twisting angle was larger for the case of CN11NC2, which explains the largest energy change of that dye during the course of excited state relaxation. It is worth noting that during the substituent twisting and pyramidalization, the cyanine backbone also gradually twists towards a near-planar geometry.

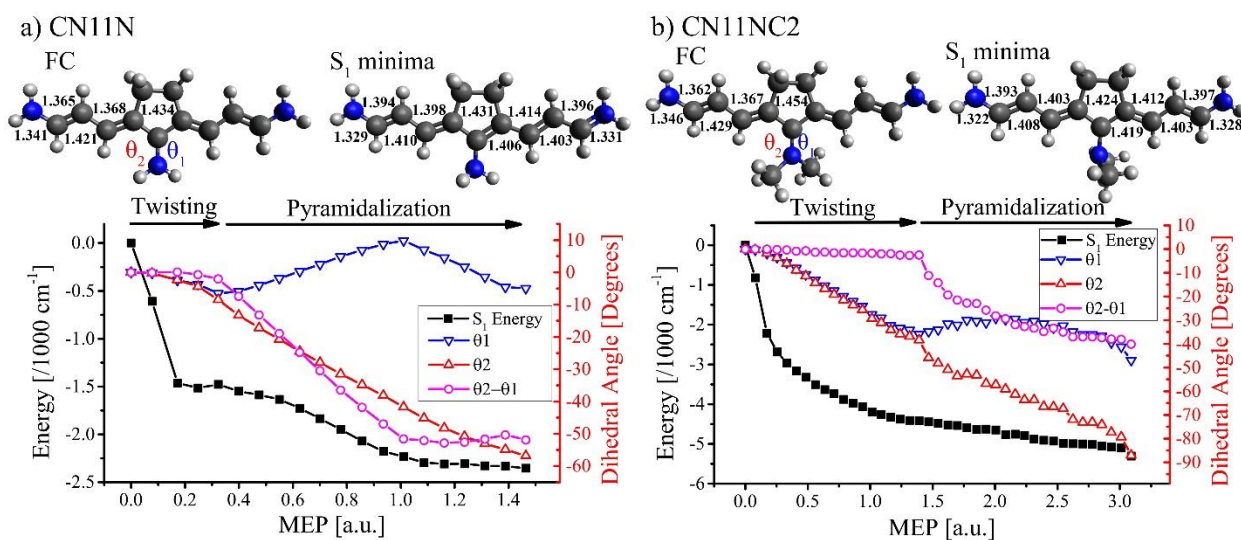


Figure 3.11 CASSCF MEP on the S_1 potential (filled black) for (a) CN11N and (b) CN11NC2 from the FC region to the emissive S_1 minima. Right y axis shows the change in the dihedral angles (open colored) compared to the FC geometry.

CASPT2 calculation were carried out to validate the above CASSCF potential energy surfaces. It was found that the CASPT2 minimum energy path is somewhat different than that predicted by CASSCF (Fig. S2 in †ESI), but like CASSCF, CASPT2 predicts that the cyanines with the most bis-dipolar character exhibit the largest energy relaxation in the excited state. This can be seen in **Figure 3.12**, which shows two dimensional PESs computed at the CASPT2 level. The two dihedral angles (θ_1 and θ_2) defining the twisting and pyramidalization angles of the substituent were constrained, and the remaining coordinates were optimized at the CASSCF level

of theory. Both the CASSCF energies and the CASPT2 energies are computed at these CASSCF optimized structures. The twisting and pyramidalization angles are reported relative to the substituent position at the FC geometry (the 0,0 angles). The CASSCF potentials show that twisting and pyramidalization are both initially favorable, with a stronger driving force for twisting in CN11NC2. On the other hand, the CASPT2 potentials predict that twisting of the planar substituent by more than 10 degrees is energetically unfavorable, while direct pyramidalization of the untwisted species is energetically downhill. Overall, the relative energy change with the dimethyl amine substituted cyanine (CN11NC2) was larger than CN11N during the course of energy relaxation on the excited state potential in both the CASSCF and CASPT2 cases. This larger energy relaxation on the excited state potential for the substituted cyanines implies that the initial wave packet that is prepared at the FC region would escape faster towards the minima compared to the unsubstituted cyanine. **Table 3.3** summarizes the energies at the FC region and the S₁ minima using CASSCF and CASPT2//CASSCF for the three cyanines. The CASPT2 S₁ minima of CN11N and CN11NC2 represent a different geometry than the CASSCF S₁ minima, which were estimated from the CASPT2//CASSCF potentials in **Figure 3.12**.

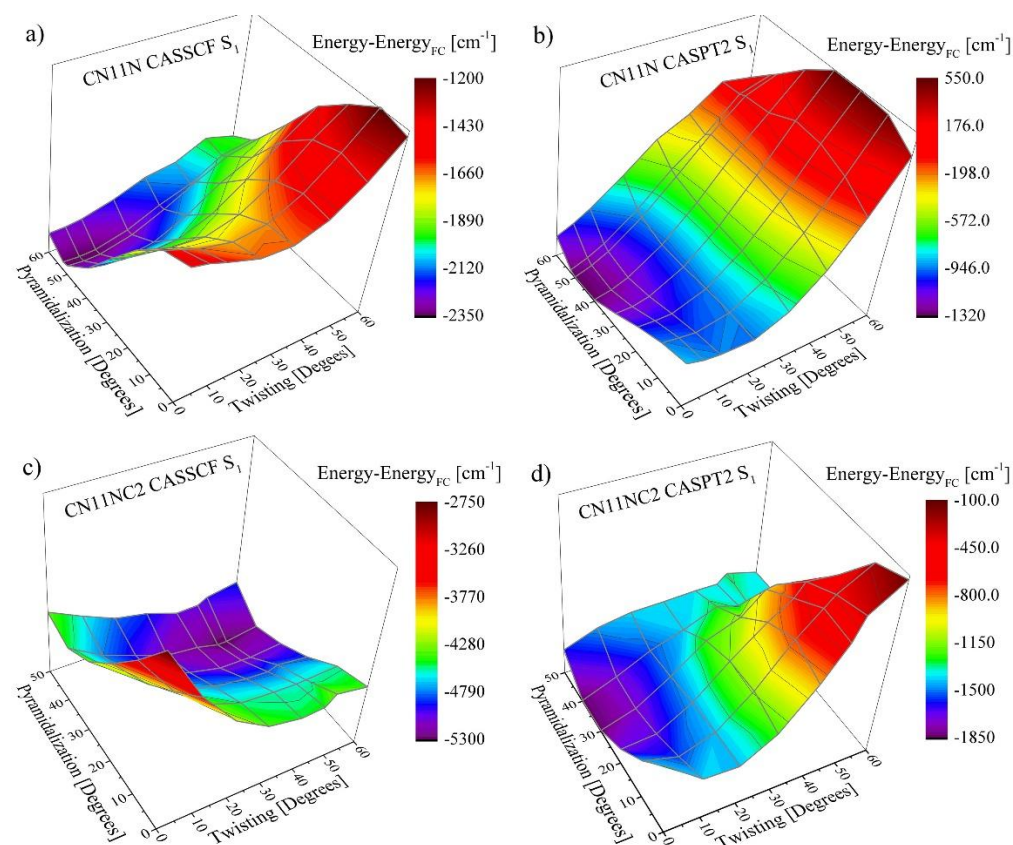


Figure 3.12 Optimized S1 CASSCF and CASPT2//CASSCF potential for (a & b) CN11N and (c & d) CN11NC2 as a function of the two dihedral angles that represent the substituent. The dihedral angles are measured as departure from the FC geometry dihedral angles.

Table 3.3 Ground and excited state energies at the FC and S1 minima for the three cyanine models

	CASSCF		CASPT2//CASSCF	
	S ₀ (cm ⁻¹)	S ₁ (cm ⁻¹)	S ₀ (cm ⁻¹)	S ₁ (cm ⁻¹)
CN11 (FC region)	0	17,665	0	19,600
CN11 (S ₁ minima)	565	17,100	240	19,035
CN11N (FC region)	0	23,150	0	22,825
CN11N (S ₁ minima)	2,580	20,810	1,325	21,505*
CN11NC2 (FC region)	0	24,760	0	23,710
CN11NC2 (S ₁ minima)	3,645	19,445	2,655	21,870*

*CN11N and CN11NC2 CASPT2//CASSCF minima are different than the CASSCF minima. The minima were obtained from the potentials in Figure 3.12

In the time resolved experiments, differences between the four dyes are greatest for small negative chirp values (**Figure 3.5**), and in pump-probe experiments when the high frequency pulse precedes the low frequency pulse (**Figure 3.7a**). IR806 shows a constant fluorescence depletion signal, while the remaining substituted dyes show a relatively higher depletion region at time scales shorter than 200 fs. The relative early time depletion increases according to the following order $m\text{TF-IR806} < m\text{An-IR806} < m\text{Pi-IR806}$, which correlates with their increased bis-dipolar character. This fluorescence depletion is accompanied with an enhanced stimulated emission (**Figure 3.6**),³⁷ which reflects an optimum condition between the excited state wave packet and the frequencies ordering in the interacting field. The fact that this feature is sharper and occurs with higher efficiency (more fluorescence depletion) implies that these conditions are only met for a short period of time after the wave packet preparation at the FC region. We take this to imply that the wave packet, in the case of substituted cyanines, leaves the FC geometry at a faster rate compared to the unsubstituted IR806. Between all the substituted dyes, this rate is the fastest for $m\text{Pi-IR806}$, which has the steepest fluorescence depletion region. This also implies that the initial intramolecular motion at the FC geometry is steeper in terms of energy relaxation. Such faster energy relaxation is feasible with the substituted cyanines as multiple intramolecular modes gets populated at the FC geometry in which the excited state energy dissipates at a faster time scale. This larger energy relaxation is evident in the calculated excited state potentials of the substituted CN11NC2 and CN11N compared to the unsubstituted CN11, see **Figure 3.10** and **Figure 3.12**.

3.5 Conclusion

Using single beam shaped pulses, we were able to provide an insight about the initial excited state dynamics primarily arising from intermolecular modes, starting from the FC region.

The optical properties of cyanine dyes are highly influenced by the electron donation strength of the amine group substituent at the central carbon across the polymethine backbone. These changes affect the initial excited state relaxation dynamics through which multiple intramolecular modes get populated at the FC geometry soon after photoexcitation. Two color pump probe and chirped femtosecond pulses were used to measure the relative rates of the excited state energy relaxation across several cyanine dyes with different electronic configurations. The wave packet motion out of the FC region, which is fastest for the cyanine that is substituted with the strongest electron donation group, led to a sharp feature in the fluorescence depletion experiments. Theoretical calculations confirmed the steepness of the excited state potential of substituted cyanines along the twisting and pyramidalization coordinates of the substituent.

Chapter 4 Cyanine Dynamics Inside Protein Pocket

Differences in the excited state dynamics of molecules and photo-activated drugs either in solution or confined inside protein pockets or large biological macromolecules occur within the first few hundred femtoseconds. Shaped femtosecond laser pulses are used to probe the behavior of indocyanine green (ICG), the only Food and Drug administration (FDA) approved near-infrared dye and photodynamic therapy agent, while free in solution and while confined inside the pocket of the human serum albumin (HSA) protein. Experimental findings indicate that the HSA pocket hinders torsional motion and thus mitigates the triplet state formation in ICG. Low frequency vibrational motion of ICG is observed more clearly when it is bound to the HSA protein.

This chapter has been reproduced from *Phys. Chem. Chem. Phys.* **2015**, *17*, 5872-5877 with permission from PCCP owner societies.

4.1 Introduction and Background

A considerable amount of effort has been and is being made by both experimentalists and theoreticians on better understanding and modeling the early time dynamics of solvated molecules soon after photo-excitation, where the environment surrounding the molecules plays a major role in the ensuing molecular dynamics.^{42,103,119,161-164} Understanding the quantum behavior of biomolecules is of even greater importance, given their paramount role in proper functioning of living beings.¹⁶⁵ Biological cavities formed primarily within protein pockets serve to direct and control the behavior of host molecules, their chemical reactivity and photochemical behavior. Studying probe-molecules confined by protein pockets can provide insight in to the interaction between host-molecules, intrinsic chromophores and drugs.¹⁶⁶⁻¹⁶⁹ Furthermore, such understanding can be used to recognize the basis of pharmacokinetics and pharmacodynamics of protein-carried drugs,¹⁷⁰⁻¹⁷¹ wherein the chemical and physical properties of such confined molecules can differ drastically from those free in solution.¹⁶⁷ Development of effective protein fluorescent labels having specific targets,¹⁷² and understanding the chemical behavior of the labeling ligand during the early stages of photoexcitation can be useful in gaining information about the ligand behavior inside the protein and in probing the stages of protein folding and different protein conformations as well.¹⁷³⁻¹⁷⁴ One such case of special interest is how rhodopsin controls vision upon being excited by a photon. The absorption of photons trigger the isomerization of the bound 11-*cis*-retinal to produce the all-*trans* retinal, in turn initiating the process of vision.¹⁷⁵ Here we focus on indocyanine green (ICG) docked inside the pocket of human serum albumin (HSA) protein as a model system for studying the behavior of molecules confined in biological pockets.

Human serum albumin (HSA) protein is especially interesting as it is the most abundant protein in plasma and constitutes about half of human blood proteins. HSA plays a crucial role in the delivery and transport of many molecules and biomolecules such as fatty acids, drugs, metal ions and steroids within the body.¹⁷⁶ HSA consists of 585 amino acids forming a monomeric globular shape, which can be further divided into three α -helical domains.¹⁷⁷⁻¹⁷⁸ Ligands bind with HSA either to the hydrophobic pocket of site IIA which is dominated by strong hydrophobic interactions, or to the polar cationic pocket of site IIIA which involves dipole-dipole, van der Waals and hydrogen bonding type of weak interactions.^{166-168,179}

Indocyanine green (ICG) is a tricyanocyanine dye and is the only near-infrared FDA approved dye¹⁸⁰ that is widely used in a variety of medical applications such as cardio-circulatory measurements, liver function tests, ophthalmological imaging and sentinel lymph node mapping in cancer patients.¹⁸¹⁻¹⁸⁶ The spectroscopic properties of ICG have already been well investigated¹⁸⁷⁻¹⁹⁰ and several photoisomerization mechanisms were sought for ICG that address multiphoton processes to produce triplet state, photodegraded species and *cis* isomers.¹⁹¹⁻¹⁹³ Being a tricyanocyanine dye, ICG aggregation and photophysical behavior is highly dependent on the environment¹⁸⁸ and the molecule tends to exist in an all-*trans* form while in the ground state.^{34, 35} Moreover, the low fluorescence quantum yield for ICG in water ($\phi_F = 0.027$)¹⁸⁸ can be attributed to the excited state *trans-cis* isomerization,¹⁹⁴⁻¹⁹⁵ large triplet state formation cross section¹⁸⁹ and several other photoreactions.¹⁹¹⁻¹⁹³ The main medical use of ICG arises from its ability to bind with albumin¹⁹⁶⁻¹⁹⁷ and is therefore extensively used in the labeling of HSA.¹⁹⁸⁻¹⁹⁹ ICG has a binding constant of $5.7 \times 10^5 \text{ M}^{-1}$ to HSA²⁰⁰ and results in a bathochromic shift (red shift) of the ICG absorbance (**Figure 4.1**) which in turn increases the fluorescence quantum yield ($\phi_F = 0.040$).¹⁸⁸

Moreover, ICG exhibits higher degree of photostability when forming J-aggregates, in non-polar solvents and in blood plasma.²⁰¹

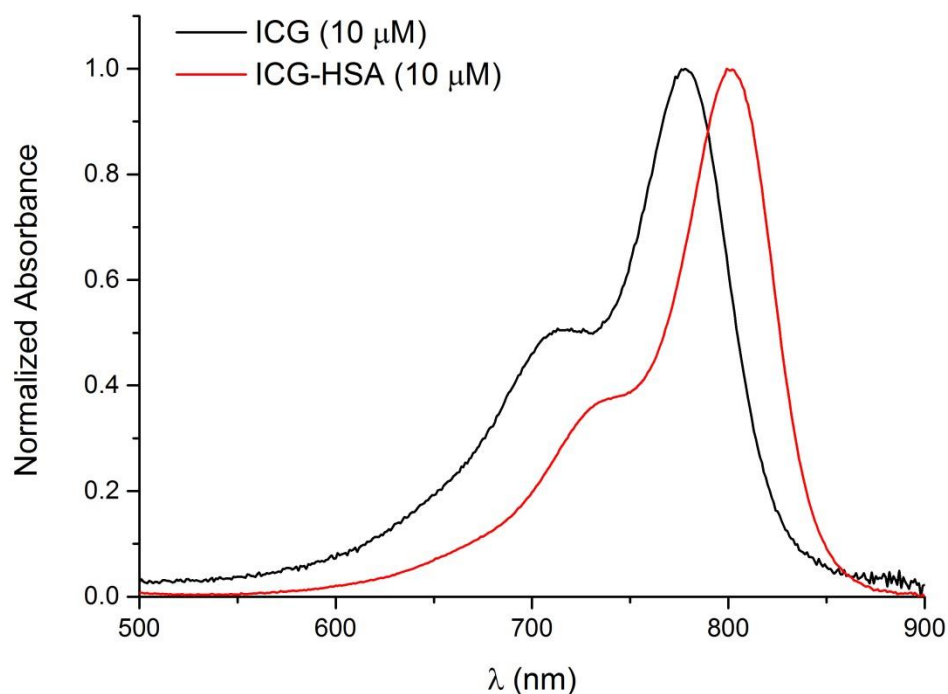


Figure 4.1 Normalized ICG (black) and ICG-HSA (red) absorbance spectra showing ICG red shift after binding inside HSA site IIA pocket.

The asymmetric response of fluorescence intensity with chirped pulses was first reported by Shank et. al.⁴⁸ Fluorescence depletion for negatively chirped pulses was explained by an intrapulse pump-dump of the electronic population since the arrival order of frequencies is from high to low and therefore this depletion was used in controlling the population transfer in multilevel systems as well.^{58,202-203} Various interpretations for the molecular response with chirped pulses were proposed, Cao and coworkers²⁰⁴ proposed an intrapulse three-level model, while Fainberg introduced non-Markovian relaxation in to the existing theory.²⁰⁵⁻²⁰⁶ More recently results from our research group showed that negative chirp is sensitive to intramolecular dynamics

while positive chirp is sensitive to intermolecular dynamics.³⁸ When comparing a solution of IR144 in ethylene glycol, we noted that the negative chirp data was unaffected by temperature and a clear maximum depletion occurred at -2500 fs^2 corresponding to a pulse duration of 200 fs.³⁸ Maximum depletion depends on the optimum pulse duration and frequency sweep to dump population from the excited state. This occurs on a short timescale and is primarily dependent on the intramolecular potential energy surfaces. For positive chirps, however, temperature affected the chirp value when maximum fluorescence is achieved. The chirp values for maximum fluorescence ranged from 5,000 to 10,000 fs^2 , corresponding to dynamics occurring in the 0.5-1 ps timescales, which are associated with solvation dynamics.³⁸ Temperature affects viscosity and intermolecular dynamics associated with solvation. These changes are observed for positive chirps. Here we used chirped femtosecond laser pulses to probe the early stages of excited state dynamical behavior of ICG molecules while free in solution and while confined inside HSA protein pocket. We also varied the repetition rate of the laser in order to probe the formation and dynamics of excited triplet states. In addition to using chirped pulses, we also performed pump probe measurement to directly determine the timescales.

4.2 Experimental Methods

The experimental setup (**Figure 4.2**) has been described previously,³⁷⁻³⁸ wherein 38 fs pulses (when TL) were produced from a regeneratively amplified Ti:Sapphire laser. The pulses were compressed and shaped using a MIIPS-HD (Biophotonic Solutions Inc.) phase and amplitude pulse shaper placed after the amplifier using the multiphoton intrapulse interference phase scan (MIIPS) approach.^{30,126} Unfocused 90 μJ laser pulses centered at 800 nm at a repetition rate of 1 kHz or 200 Hz were used, with a peak intensity at the sample of $5 \times 10^9 \text{ W/cm}^2$ when transform limited. Chirped pulses having the phase function $\varphi(\omega) = 0.5\varphi''(\omega - \omega_0)^2$ were generated using the pulse shaper where φ'' is the quadratic phase. A typical chirp scan consisted of scanning the chirp from negative to positive $30,000 \text{ fs}^2$. Quadratic phase on a 38 fs TL pulse stretches it to longer durations according to $t / t_{TL} = 1 + 4 \ln 2 (\varphi'' / t_{TL}^2)$. The high frequency components (blue part of the pulse) arrive before the low frequency ones (red part of the pulse) for a negatively chirped pulse, while the order of arrival is reversed for a positively chirped pulse (**Figure 4.2c**), depending upon the magnitude of chirp or how “stretched” the pulse is. Dynamical information can be obtained by correlating the value of chirp to the pulse duration; for instance, a chirp value of 1000 fs^2 can be used to observe processes occurring at around 100 fs; the temporal stretching is determined by the formula given above. Repeated sets of measurements were taken over different days and compared and checked for reproducibility.

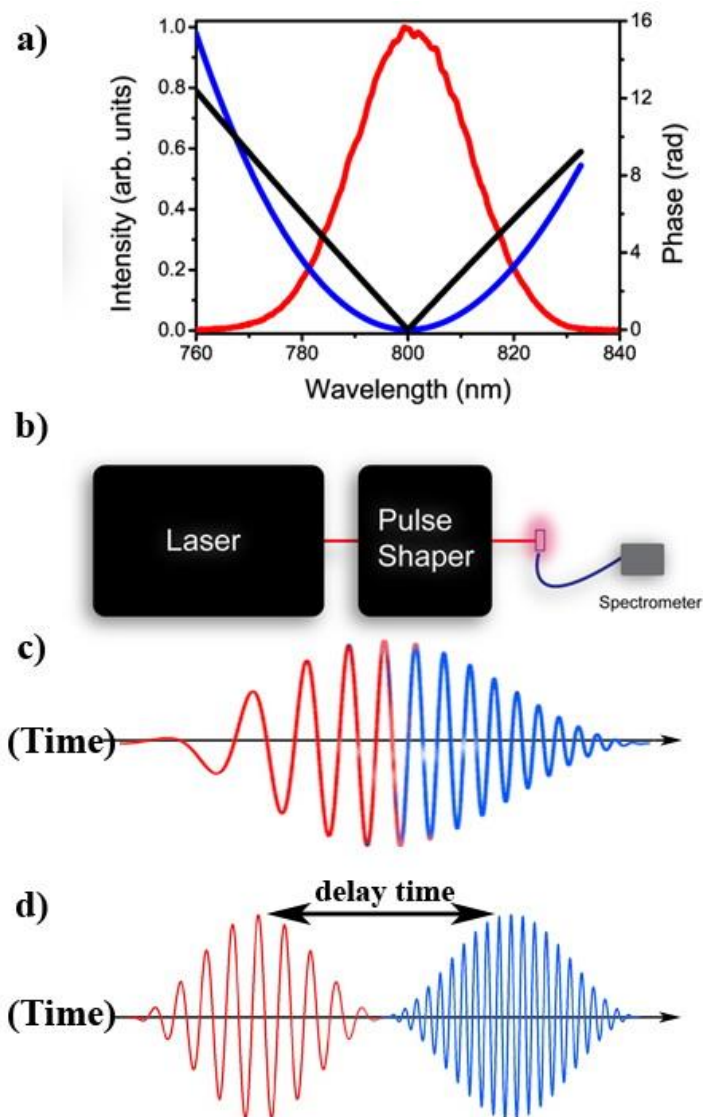


Figure 4.2 (a) TL pulse spectrum (red) with positive chirp phase mask (blue) and positive delay time phase mask (black). (b) Experimental setup, note the laser was not focused on the cuvette. (c) Schematic representation of a positively chirped pulse in the time domain, and of a (d) pump-probe type pair of pulses with positive delay time having frequency arrival ordering such that the red portion of the pulse arrives before the blue portion

Delay time phase masks (**Figure 4.2a**) were introduced using the shaper by delaying the red half (greater than 800 nm) of the pulse with respect to the blue half (smaller than 800 nm) by changing the slope of a linear phase. Delay scans were performed from negative to positive 1 ps in 20 fs steps. For negative time delays the pump pulse, consisting of the high frequency

components arrives before the low frequency ones, while for positive delays the lower frequency pulse precedes the higher frequency one (**Figure 4.2d**). Integrated fluorescence signal was simultaneously detected at right angles using a compact spectrometer while ensuring that the collected signal is associated to the proper range for either ICG or ICG-HSA since ICG-HSA fluorescence occurs in a red shifted region compared to free ICG. Indocyanine green (Sigma-Aldrich, I2633) and human serum albumin protein (Sigma-Aldrich, A3782) were used as purchased without any further purification. 10 μM indocyanine green (ICG) and 1:1 10 μM indocyanine green with human serum albumin (ICG-HSA) solutions were freshly prepared and used immediately. All solutions were prepared under atmospheric conditions unless noted otherwise in the results section. Solutions were prepared in 10 mM, pH=7 sodium phosphate buffer prepared using Milli-Q water and proper amounts of monosodium and disodium phosphate. Solutions were placed inside a 2 mm cuvette to minimize any possible phase distortion since accurate measurements are required while delivering dispersion free pulses with the exact desired delay times.

UV-visible (ATI/Unicam UV2) absorbance spectra for ICG and ICG-HSA were used to confirm ICG binding within the protein pocket (**Figure 4.1**) and checking for ICG aggregation at the working concentration. Molecular docking was performed to simulate ICG conformation within the HSA pocket and to also determine the most favored binding site. The crystal structure of HSA was obtained from the protein data bank (PDB: 1AO6),¹⁷⁷ and the ICG 3D structure was created using ChemBio3D. HSA was loaded using AutoDock Tools,²⁰⁷ water and multiple protein crystals were removed, polar hydrogen atoms were added, grid box size and position were assigned to contain all the protein and ICG rotatable bonds were identified using AutoDock Tools. The files were saved in proper formats and were docked using AutoDock Vina²⁰⁸ which utilizes the

Lamarckian Genetic Algorithm (LGA) based on the adaptive local method search and provides 10 conformers having the lowest binding energy. AutoDock Tools was used to visualize the docked ICG conformers; finally, the ICG conformer with the lowest energy was further studied using a box of smaller grid size containing the docked position and was chosen to be visualized.

4.3 Results and Discussion

4.3.1 Molecular Modeling & Docking

Molecular docking was performed for ICG molecule with HSA using AutoDock Vina to reveal the most favorable binding mode for ICG within HSA pocket and the most probable conformer while in the ground state. After visualizing the 10 most probable binding conformers and determining the one with the highest binding affinity, it was concluded that ICG is more likely to bind within the hydrophobic region of HSA (site IIA), presumably due to the hydrophobic nature of the majority of ICG molecule. Further docking was carried out in a smaller grid box which contained only site IIA of HSA pocket to identify the most favored ICG conformer inside that specific binding pocket. Visualization of the results for the conformer with the highest affinity is presented in **Figure 4.3**. Note that ICG inside the HSA pocket is mostly in a *trans* configuration. The relatively tight configuration implies that the pocket provides some steric hindrance that may affect the photoisomerization behavior of ICG.

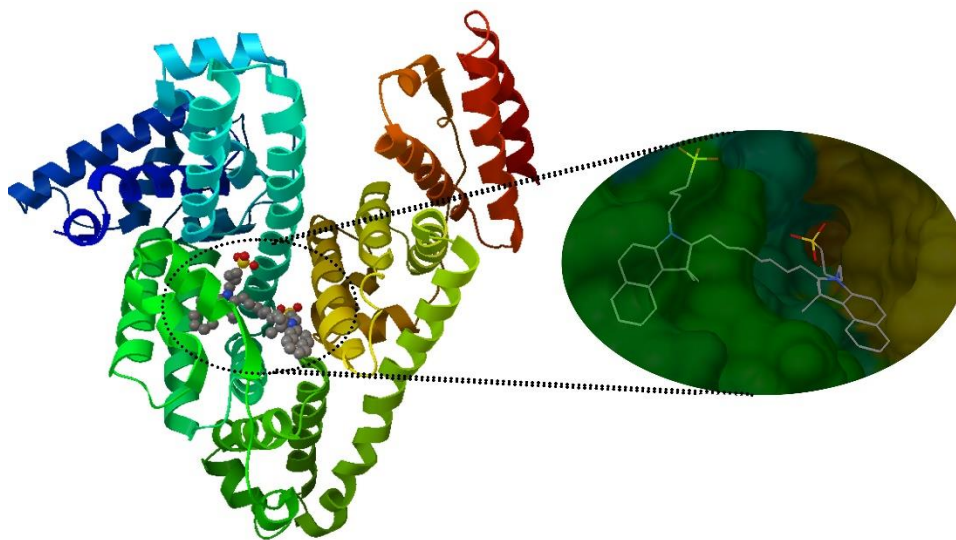


Figure 4.3 Molecular modeling showing the most favored binding site of ICG within site IIA of the HSA protein. HSA was colored according to its chains and ICG elements were colored in grey (C), blue (N), yellow (S) and red (O).

4.3.2 Fluorescence Behavior with Shaped Laser Pulses

Steady state absorption and fluorescence of ICG has been extensively discussed elsewhere;¹⁸⁸ here we investigate the use of shaped femtosecond pulses to probe the excited state dynamics of ICG and ICG-HSA especially during the first few hundreds femtoseconds after excitation.

Integrated fluorescence intensity from ICG and ICG-HSA solution as a function of spectral chirp (φ) at repetition rates of 1 kHz (black) and 200 Hz (red) are shown in **Figure 4.4**. The integrated intensity was collected for several measurements, compared without any normalization then finally averaged and normalized on a scale from 0 to 1. Notable differences were observed (**Figure 4.4a**) in the fluorescence response ‘chirp effect’ curve for ICG at different repetition rates. At 200 Hz, a typical ‘chirp effect’ response is observed with fluorescence depletion for negatively chirped pulses followed by a rapid rise for positively chirped pulses. However, when operating at 1 kHz an additional fluorescence intensity decrease feature is observed around -5000 fs^2 which gets sharper upon approaching TL pulses. The rate of fluorescence increase for positive chirp is considerably slower when data is obtained at 1 kHz. Identical chirp effect curves are obtained for ICG-HSA (**Figure 4.4b**) when collecting the fluorescence as a function of chirp at the two different repetition rates. From these experiments we learn that at 1 kHz ICG accumulates a transient species that is not present for ICG-HSA.

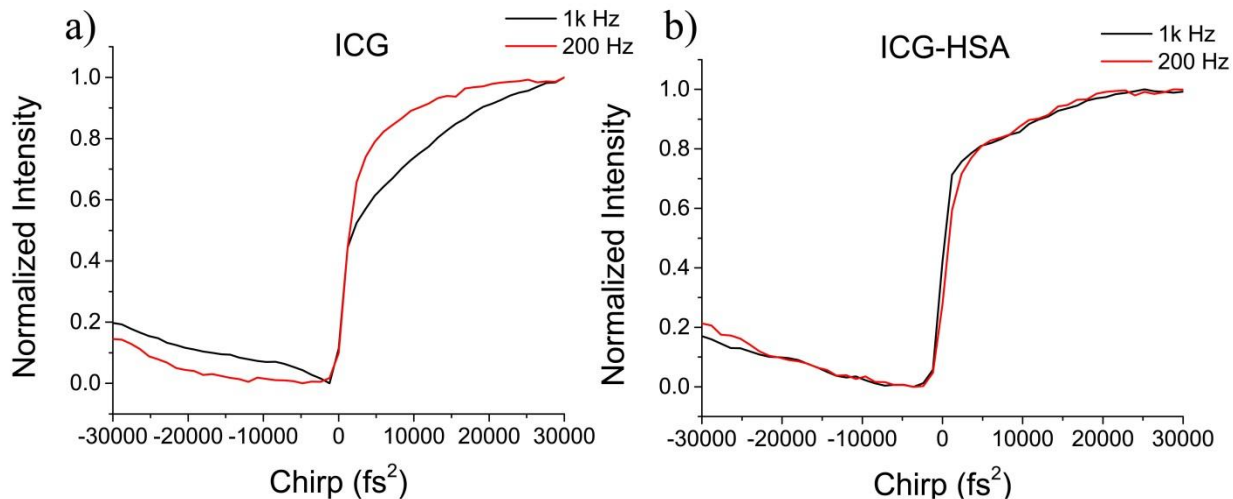


Figure 4.4 Normalized integrated fluorescence intensity as a function of spectral chirped for (a) ICG solution and (b) ICG-HSA solution at different repetition rates.

When comparing ICG and ICG-HSA results at 200 Hz, no difference in the dynamical behavior is observed when the data is normalized from 0 to 1 (**Figure 4.5a**), confirming the absence of a transient species. When the data was normalized according to the fluorescence intensity for TL pulses (**Figure 4.5b**), the fluorescence of ICG-HSA is less intense for positive chirps than that of free ICG.

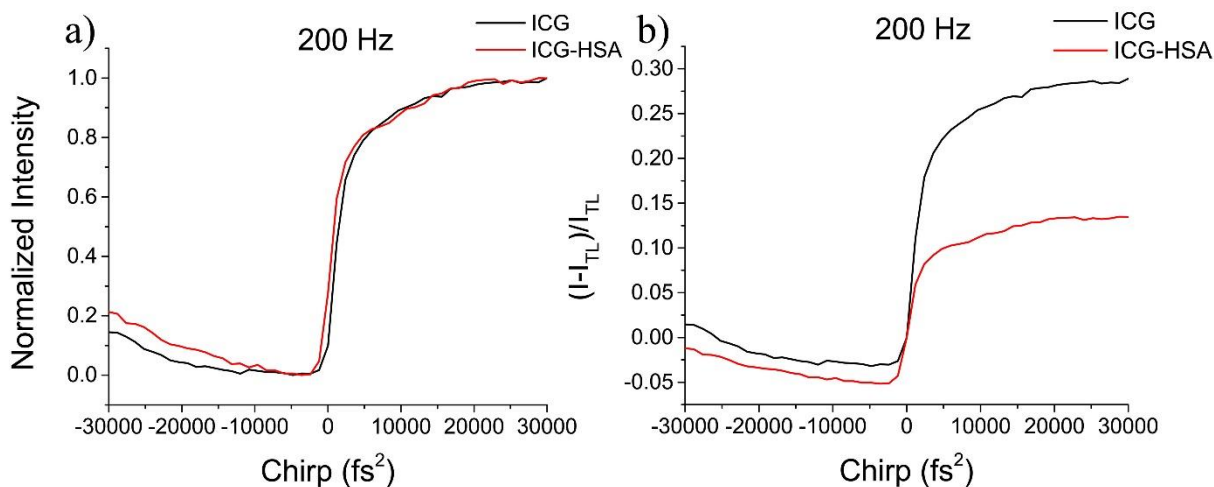


Figure 4.5 Integrated fluorescence intensity as a function of spectral chirp at a repetition rate of 200 Hz for ICG (black) and ICG-HSA (red) normalized (a) from 0 to 1 and (b) according to integrated fluorescence using TL pulses.

Differences in the response to chirp due to the laser repetition rate are attributed to the photo-dynamical behavior for free ICG molecules in solution. Several single and multi-photon photoisomerization pathways have been proposed to address the non-radiative behavior of ICG.¹⁹¹⁻¹⁹³ They can be summarized as excited state *trans-cis* isomerization, triplet state formation through intersystem crossing and formation of photo degradation products. ICG *cis* photo-isomer and triplet state have a lifetime of ~ 1 ms,¹⁹¹ and thus can accumulate and be observed when the pulse repetition rate is 1 kHz, because consecutive pulse arrive at the sample every 1 ms. We confirmed the presence of triplet state by removing O₂, which acts as a triplet state quencher, from the sample by bubbling Argon (Ar) in the solution and recording the chirp scans in the oxygen depleted samples. The fluorescence spectra for ICG solution bubbled with Ar as a function of chirp at 1 kHz (**Figure 4.6**) clearly shows a sharper decrease in the fluorescence intensity for negatively chirped pulses and slower rise for positively chirped pulses as compared to the air saturated solution. The accumulation of triplet ICG changes the observed behavior given that the signal

arises from a different molecular species. Note that for ICG-HSA no such behavior was observed, even in the absence of oxygen using Ar bubbled solution (**Figure 4.7**). We conclude from this observation that the HSA protein pocket prevents the formation of the triplet state of ICG.

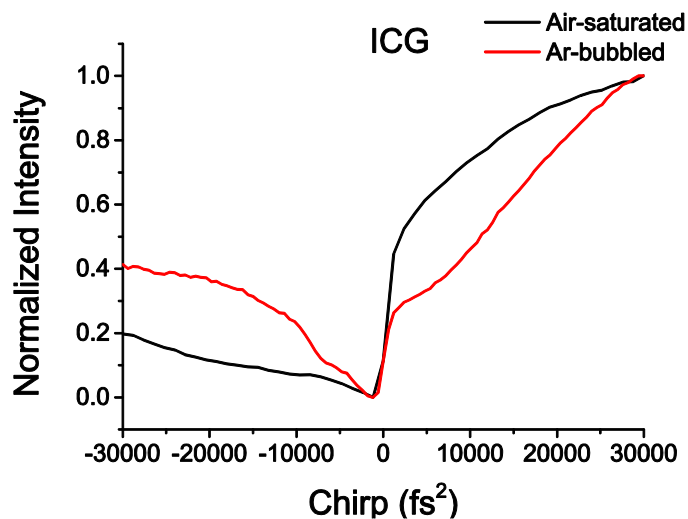


Figure 4.6 Normalized integrated fluorescence intensity as a function of chirp for ICG solution in the presence and absence of O₂ at 1 kHz repetition rate.

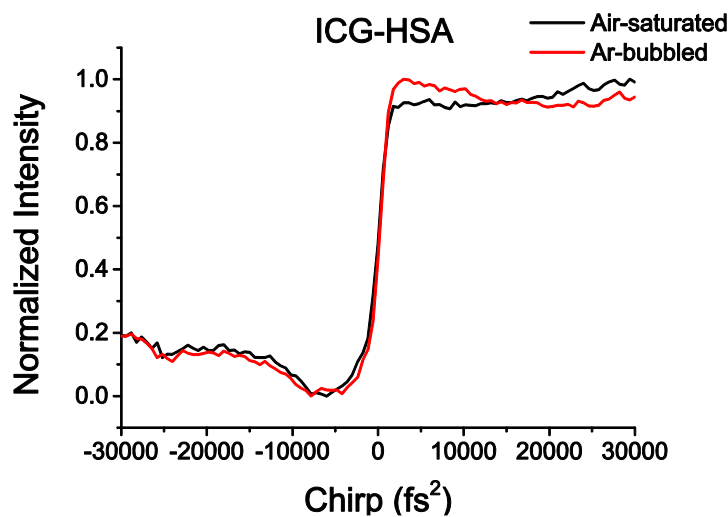


Figure 4.7 Normalized integrated fluorescence intensity as a function of chirp for ICG-HSA solution in the presence and absence of O₂ at 1 kHz repetition rate.

To get an even clearer picture and better understanding about the time scale of the relevant processes occurring during the chirp scan we performed pump probe type measurements as

described in the experimental section on the same solutions. The detected fluorescence intensity normalized from 0 to 1 for both ICG and ICG-HSA at different repetition rates are shown in **Figure 4.8a** and **b** respectively. For negative delay times, lower fluorescence intensity was observed and this can be explained by stimulated depletion of the electronic population from the first excited state, while for positive delays, the order of arrival of the spectral parts of the pulse is reversed and is considered not suitable for dumping the electronic population back to the ground state.

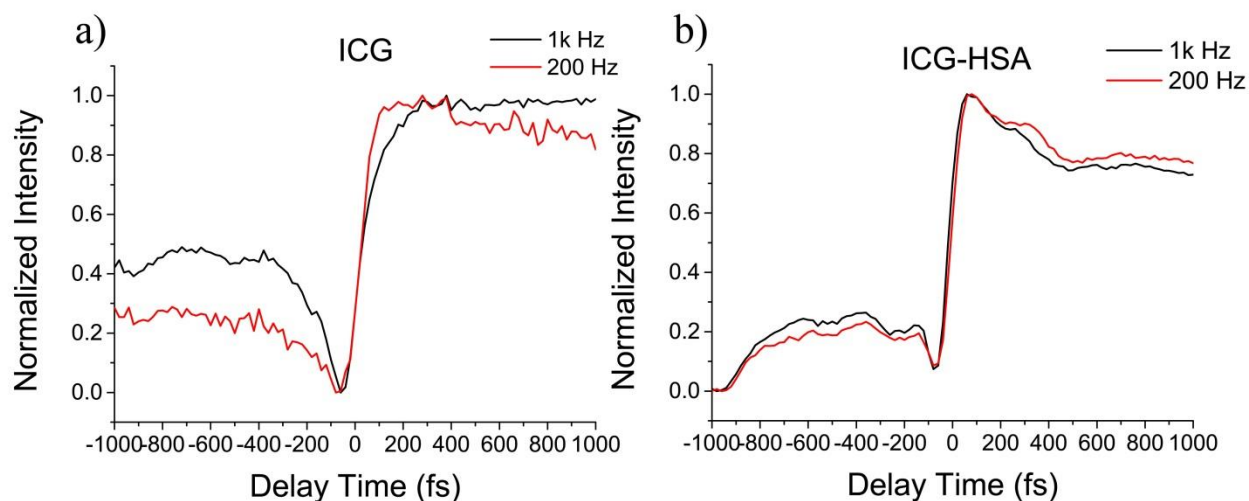


Figure 4.8 Normalized integrated fluorescence intensity as a function of delay time between the pump and probe pulses for (a) ICG solution and (b) ICG-HSA solution at repetition rates of 1 kHz (black) and 200 Hz (red).

We find that for ICG (**Figure 4.8a**) at 1 kHz repetition rate compared with 200 Hz, there was a clear feature at negative delay times in fluorescence intensity from -400 fs to -50 fs. Additionally, with positive delay times, fluorescence intensity increases more slowly for 1 kHz data. When ICG is confined inside the HSA pocket no difference can be seen between the 1 kHz and 200 Hz time-resolved curves (**Figure 4.8b**). The time resolved data again point to the accumulation of triplet-state ICG when the experiments is performed at 1 kHz, and we also confirm that the HSA pocket prevents the formation of triplet-state HSA.

The fluorescence intensity as a function of delay time (**Figure 4.8b**) for ICG-HSA reveals ~ 290 fs vibrational oscillations in the negative delay portion of the transient and ~ 175 fs vibrational oscillations in the positive delay portion. These oscillations are not observed for free ICG. Fitting the vibrational oscillations observed for ICG-HSA to a cosine function in the form $A + a \cos(2\pi\omega t + \phi) + bt$ (**Figure 4.9**) yields a vibrational frequency of $115 \pm 15 \text{ cm}^{-1}$ and $190 \pm 15 \text{ cm}^{-1}$ for the negative and positive delay times respectively. These values are slightly different from previously reported vibrational frequency of ICG in methanol (146 cm^{-1} for the ground-state bleach and 138 cm^{-1} for the excited state stimulated emission).²⁰⁹ While our experiments are carried out in aqueous solutions, and our signal to noise is low, the significant differences can be attributed to the presence of ICG inside the HSA binding pocket.

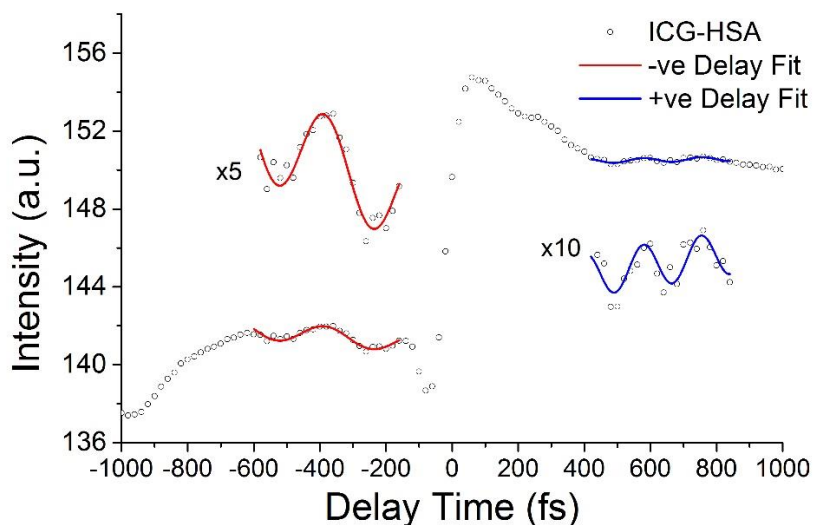


Figure 4.9 Integrated fluorescence intensity as a function of delay time between pump and probe pulses for ICG-HSA. The ~ 290 fs oscillations in the negative delay time side and the ~ 175 fs oscillations in the positive delay time were fitted using a cosine function with $115 \pm 15 \text{ cm}^{-1}$ and $190 \pm 15 \text{ cm}^{-1}$ oscillation respectively and are vertically zoomed in the insets.

4.4 Conclusion

The early, sub-picosecond, excited state dynamics of indocyanine green in aqueous solution as well as within the hydrophobic pocket of human serum albumin were studied using both chirped femtosecond laser pulses and pump-probe time-resolved measurements. In general, the behavior of indocyanine green in solution is similar to that of other cyanine dyes.³⁸ When aqueous solution experiments are carried out at high repetition rates it becomes clear that a new molecular species accumulates and different photodynamic behavior is observed. The differences are assigned to the accumulation of triplet state. We confirmed the nature of the triplet state by carrying out experiments in the absence of oxygen, an effective triplet quencher. When the probe molecule is inside the protein pocket, no triplet state formation and accumulation is detected. Time resolved experiments confirm the chirped pulse experiments and reveal coherent vibrational oscillations when the probe molecule is inside the protein pocket.

Chapter 5 Controlling Energy Transfer in Cyanines

Fast population transfer from higher to lower excited states occurs via internal conversion (IC) and is the basis of Kasha's rule, which states that spontaneous emission takes place from the lowest excited state of the same multiplicity. Photonic control over IC is of interest because it would allow direct influence over intramolecular nonradiative decay processes occurring in condensed phase. In this chapter the S_2 and S_1 fluorescence yield for different cyanine dyes in solution as a function of linear chirp are tracked. For the cyanine dyes with polar solvation response IR144 and *meso*-piperidine substituted IR806, increased S_2 emission was observed when using TL pulses, whereas chirped pulses led to increased S_1 emission. The non-polar solvated cyanine IR806, on the other hand, did not show S_2 emission. A theoretical model, based on a non-perturbative solution of the equation of motion for the density matrix, is offered to explain and simulate the anomalous chirp dependence. Our findings, which depend on pulse properties beyond peak intensity, offer a photonic method to control S_2 population thereby opening the door for the exploration of photochemical processes initiated from higher excited states.

This chapter has been adapted with permission from (*J. Phys. Chem. A* **2016**, *120*, 1876-1858)
Copyright © 2016, American Chemical Society.

5.1 Introduction and Background

Kasha's rule is one of the fundamental phenomena governing the photochemistry and photophysics of molecules in condensed phase. It states that following excitation to higher electronic excited states, spontaneous emission occurs from the lowest electronic excited state, independent of the photon energy used during the excitation process.²¹⁰ The basis for this rule is that the rates of nonradiative processes such as, internal conversion (IC), intersystem crossing (ISC) and vibrational relaxation from higher excited states are much faster than the spontaneous radiative decay rate of that excited state.²¹¹ Some compounds, such as azulenes, aromatic acenes, thioketones, and polyenes have been observed to violate Kasha's rule and exhibit fluorescence from higher excited states simultaneously along with the fluorescence from the lowest excited state.²¹¹

Photonic control of intramolecular nonradiative decay pathways opens up the possibility of utilizing higher excited states to manipulate the final product distribution of photo-induced reactions,²¹² design optoelectronic switches²¹³ and utilize more efficient charge transfer events.²¹⁴ It has been reported that by controlling the properties of the molecular environment, such as pH and viscosity, the dual emission behavior noted above was affected due to changes in the excited state intramolecular proton/charge transfer.²¹⁵⁻²¹⁶ Structural changes such as the carbon substitution position of organometallic complexes play a key role in changing non-radiative MLCT state that leads to the production of dual emissive states.²¹⁷ Here, as part of our efforts toward understanding and controlling laser-matter interactions,⁴⁴ we explore photonic control over Kasha's rule with the goal of significantly enhancing emission from a higher (S_2) electronic state.

Cyanines are a class of polymethine dyes structurally related to protonated Schiff bases, carotenoids, and other conjugated polyenes. Some are approved for photodynamic therapy and

bioimaging;²¹⁸ their backbone consists of an odd number of conjugated $2p_z$ orbitals that results in a S_0 - S_1 transition in the visible or near-IR region. The large S_2 - S_1 energy gap ranges from 0.6 to 1 eV, and leads to comparatively weak coupling between the two excited states and a slowing of the IC rates according to the energy gap law, which states that IC rate decreases exponentially with increasing energy separation.¹⁴³ Cyanine dyes exhibit dual fluorescence when excited directly to the S_2 state.²¹⁹⁻²²² The fluorescence quantum yield and lifetime of the S_2 state for cyanine dyes has been shown to increase with solvent viscosity.²²³

The broad and essentially featureless absorption spectra of polyatomic molecules in condensed phase poses a challenge for photonic control strategies especially when compared to the spectra of isolated small molecules for which energy levels are sharp and well defined. Spectral broadening due to spectral congestion and inhomogeneous and homogeneous broadening prevent one from mapping potential energy surfaces and finding gateways responsible for IC, ISC and barriers to isomerization. Linear chirp, one of the simplest forms of pulse shaping and results in a carrier frequency sweep from higher to lower frequencies (positive chirp) or the reverse sweep (negative chirp), has been used previously to control population and hence fluorescence yields of large molecules in solution.^{42,48} Chirped pulses have also been used to control the yield of a desired photoproduct^{51,224} and population transfer in fluorescent proteins.²²⁵ The chirp dependence of molecular fluorescence from S_1 states has been explained theoretically.^{37,48,203,206,226-227} Control with more complex pulse shapes resulting from closed loop optimization have been used to control processes related to solar energy capture, suppression of radiationless transitions, and photoisomerization; the effect of shaped pulses on the yields of photoproducts has been demonstrated experimentally²²⁸⁻²³⁴ and theoretically.^{155,235-237} These efforts have been reviewed in the past.^{44,238-239} While some of the work referenced here include excitation to S_2 ,^{155,228} robust

control of S_2 to S_1 IC using shaped pulses has not been reported. Here we explore control of S_2 fluorescence yield using chirp following direct S_2 excitation. In our experiments, we monitor fluorescence from both S_2 and S_1 states, as a function of chirp for different cyanine dyes.

5.2 Experimental Methods

5.2.1 Laser and pulse shaper

The experimental setup shown in **Figure 5.1** uses a non-collinear optical parametric amplifier (NOPA, Spectra-Physics Spirit NOPA-3H) as a source of tunable femtosecond pulses. The NOPA is pumped by an amplified direct diode-pumped Yb laser (Spectra-Physics Spirit 1040-4) which delivers 1040 nm pulses at a 100 kHz repetition rate with pulse energy of 40 μ J. The NOPA has a built-in third harmonic generator that is used to pump the white-light continuum seed pulses in order to generate visible wavelengths tunable from 500-750nm. For the current experiments, we used pulses centered at 517, 540 and 545 nm. The NOPA pulses were compressed and shaped using a femtoJock (Biophotonic Solutions Inc. USA) phase and amplitude pulse shaper using the MIIPS method.²⁹⁻³⁰ The pulse durations ranged from 13 to 16 fs depending on the excitation wavelength.

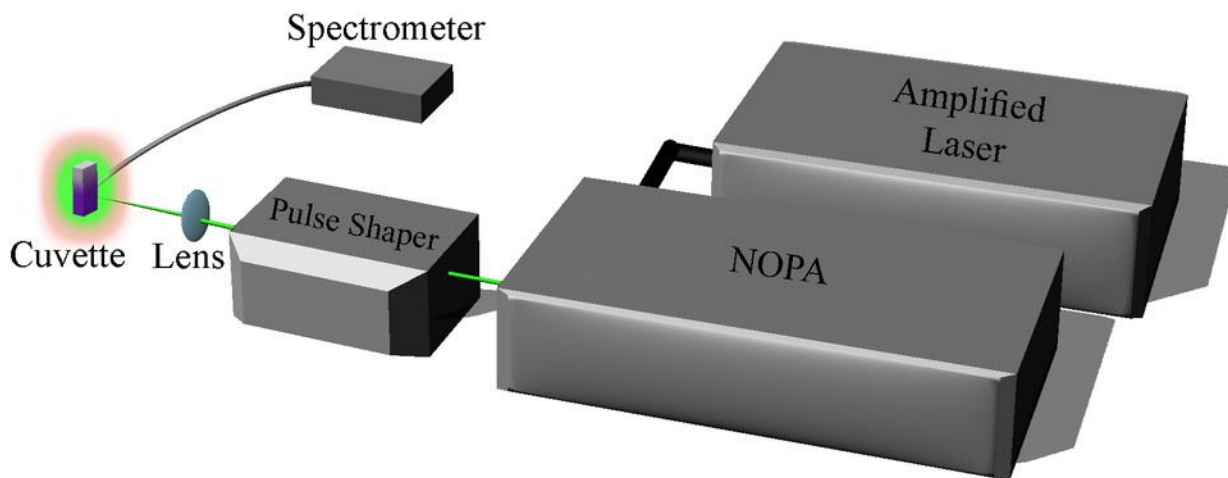


Figure 5.1 Experimental Setup. The output of the NOPA was phase and amplitude shaped using MIIPS femtoJock pulse shaper and then was focused on the cyanine dye in a 2 mm path length cuvette, the fluorescence signal was detected directly at a right angle using a fiber-coupled compact spectrometer.

5.2.2 Fluorescence Excitation and Detection

The compressed pulses were focused with a 10 cm focal length lens onto a cuvette having a 2 mm path length. Second order dispersion caused by the cuvette wall on the incident side of the beam was accounted for when compressing the pulses using the MIIPS scan procedure with the pulse shaper. Solvent introduced dispersion, which is about 60 fs²/mm at our working wavelength,²⁴⁰ was minimized by collecting the signal at a right angle near the entrance cuvette window with a multimode optical fiber, with 25 degree acceptance angle, placed in contact with the cuvette. Chirp phase masks of the form $\phi(\omega) = 0.5\phi''(\omega - \omega_0)^2$, where ϕ'' is the quadratic phase, were applied using the pulse shaper. The chirp scan was conducted by varying the quadratic phase from negative to positive 5000 fs². Quadratic phase on the TL pulse stretches it to longer durations according to $\tau / \tau_{TL} = \sqrt{1 + (4 \ln 2)^2 (\phi'' / \tau_{TL}^2)^2}$. Laser fluence dependence measurements were carried out by changing the amplitude mask in the pulse shaper while ensuring retention of the desired phase mask. Chirp scan experiments were conducted with pulse energies of 31 nJ ~ 1.1 mJ/cm² laser fluence for IR144 and 18 nJ ~ 0.65 mJ/cm² for *meso*-piperidine-IR806 (*mPi*-IR806), while simultaneously detecting the fluorescence from S₁ and S₂ excited state. The fluorescence collected by the optical fiber was detected using a compact spectrometer (Ocean Optics USB4000).

5.2.3 Samples

The experiments were carried out on three cyanine dyes: 50 μM IR144 (Exciton) dissolved in methanol, 50 μM IR806 (Sigma-Aldrich) dissolved in methanol, and 50 μM *mPi*-IR806 dissolved in propanol. The chemical structures of the cyanine dyes studied here IR806, IR144 and *mPi*-IR806 are shown in **Figure 5.2**. *mPi*-IR806 was prepared using a published procedure¹²⁵ using IR806

(0.02 mmol) and piperidine (0.1 mmol), which were stirred at room temperature in DMF for 16 hrs. NMR shifts confirming the identity of *mPi*-IR806 are provided in Chapter 3.

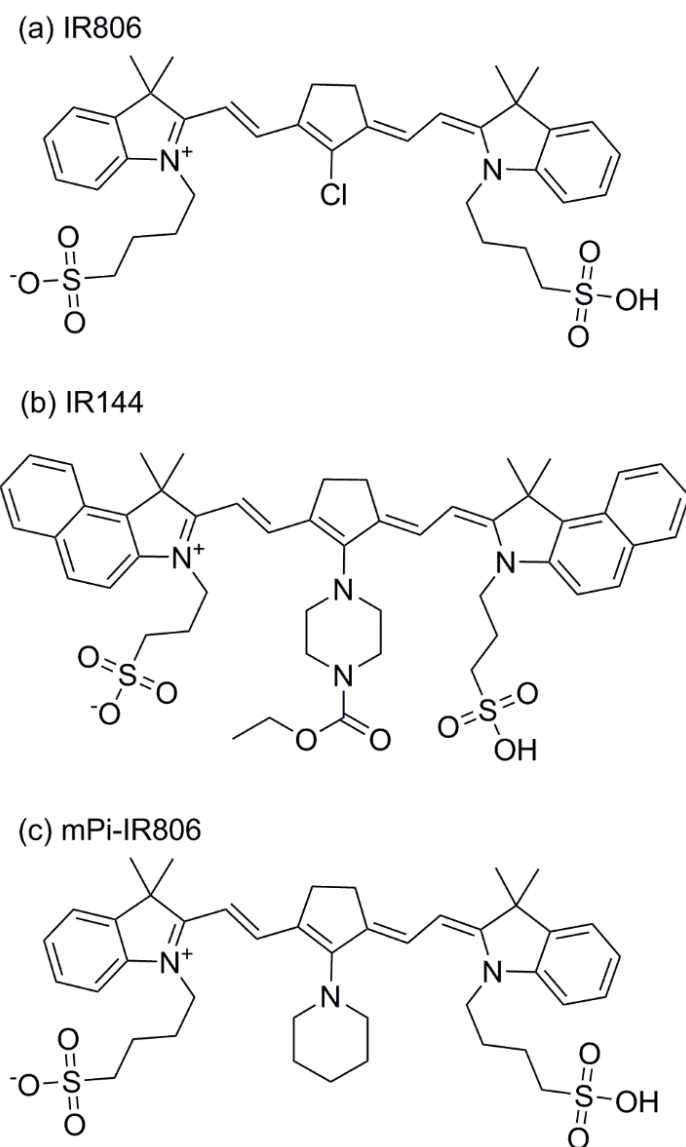


Figure 5.2 Chemical structures of (a) IR806, (b) IR144 and (c) *mPi*-IR806.

5.3 Results

5.3.1 Steady State Spectroscopy

As in many other symmetrical cyanine dyes, the $\pi \rightarrow \pi^*$ transition in IR806 occurs without a significant change in the permanent dipole moment.^{112,119,241-242} In IR144 and *mPi*-IR806, however, there is a significant change in the permanent dipole moment associated with the optical excitation due to the addition of the 1-piperazinecarboxylate and piperidine groups, respectively, in conjugation with the main polyene backbone. This coupling contributes in producing a symmetrical ground state resonance structure that does not contribute to the antisymmetric excited state structure, resulting in a dipole moment change upon S_1 electronic excitation and triggering a polar solvation response.¹¹⁹

The steady state absorption spectra of IR806, IR144 (both dissolved in MeOH) and *mPi*-IR806 (dissolved in PrOH) are shown in **Figure 5.3a**. The spectrum from the non-polar solvated dye IR806 has in addition to a maxima at 806 nm, a shoulder at ca. 735 nm, a feature that is very common in the absorption spectra of cyanine dyes.^{112,241-242} The polar solvated dyes, IR144 and *mPi*-IR806, lack the vibronic feature and possess wider absorption spectra, with $\lambda_{\max} = 740$ nm and 696 nm, respectively. Both, IR144 and *mPi*-IR806 absorption spectra show small peaks with $\lambda_{\max} = 540$ nm and 521 nm with cross sections of ca. 1.7×10^{-18} cm² and 3.6×10^{-18} cm², respectively. The absorption maxima, fluorescence maxima, Stokes shifts and FWHM of the absorption and the fluorescence spectra from the S_1 state of the three dyes are presented in **Table 5.1**.

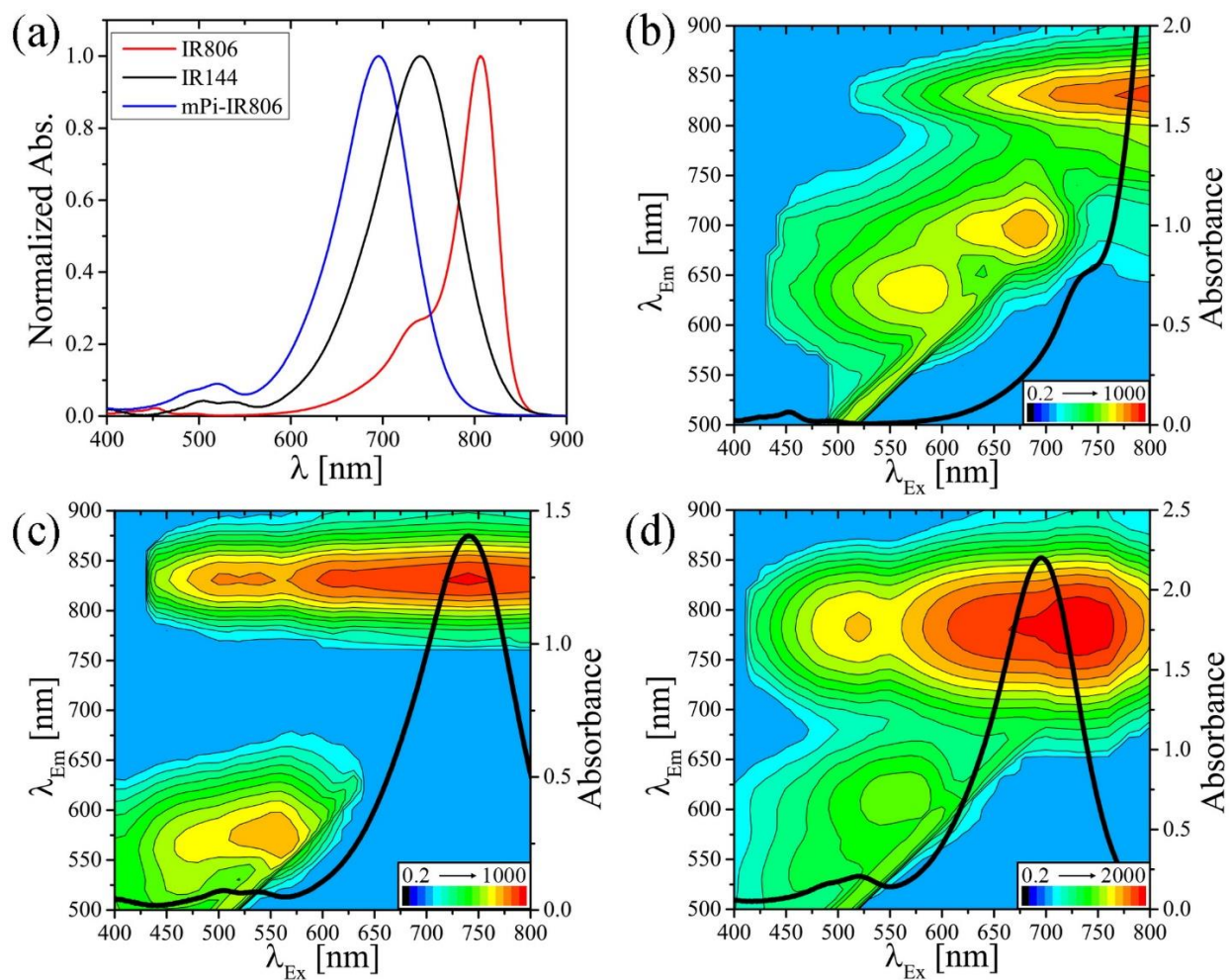


Figure 5.3 (a) Absorption spectra for the three cyanine-dyes in scheme 1. Two-dimensional fluorescence excitation–emission spectra for (b) IR806, (c) IR144 and (d) *mPi*-IR806. Contour lines are plotted on a logarithmic scale. The absorption spectrum (black line) for each dye is superimposed on the excitation axis.

Table 5.1 Absorption maxima, fluorescence maxima, Stokes shifts and FWHM of the absorption and the emission spectra of the S₁ state for IR806, IR144 and *m*Pi-IR806. S₁-S₀ Stokes shift measured as the difference between the absorption and fluorescence spectra maxima.

	IR806 (Methanol)	IR144 (Methanol)	<i>m</i>Pi-IR806 (Propanol)
Abs. max (cm⁻¹)	12407 (806 nm)	13514 (740 nm)	14368 (696 nm)
Fl. Max (cm⁻¹)	11825 (845 nm)	11862 (843 nm)	12723 (786 nm)
S₁-S₀ Stokes Shift (cm⁻¹)	582	1652	1645
Abs. FWHM (cm⁻¹)	778	1988	1935
Fl. FWHM (cm⁻¹)	489	974	981

Two-dimensional fluorescence excitation–emission spectra for the three dyes help discern the presence of emission bands at higher energies as shown in **Figure 5.3b-d**. The absorption spectrum for each dye is superimposed on the excitation axis. The higher energy emission bands originate from the higher S₂ state or a structurally rearranged intramolecular charge transfer (CT) state within the S₁ manifold.²⁴³ For IR806, higher energy emissions with maxima at 700 nm and 637 nm originate from the blue edge of the vibronic absorption band of the S₁ state and not from the S₂ state. This observation was further confirmed from fluorescence excitation spectra obtained when detecting these high-energy emissions (**Figure 5.4**), and has been observed to occur from nonpolar solvated cyanines.²⁴⁴ The assignment was further confirmed by the observed reduced fluorescence yield observed as a function of increased solvent viscosity (**Figure 5.5**).

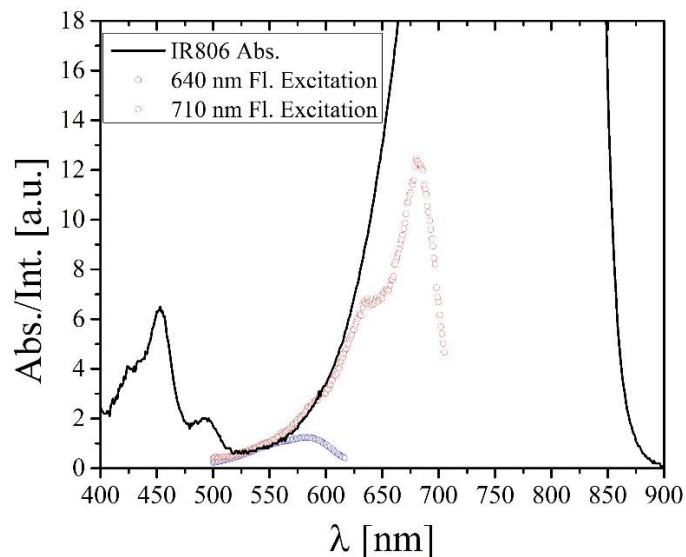


Figure 5.4 Absorption spectrum for IR806 along with the excitation spectra for the emission with maxima at 637 nm (determined with detection at 640 nm) and the emission with maxima at 700 nm (determined with detection at 710 nm).

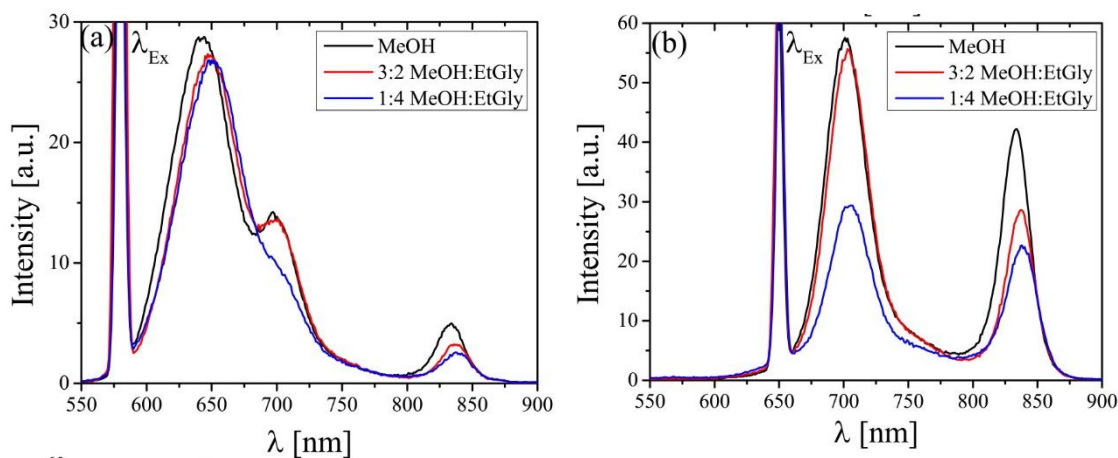


Figure 5.5 IR806 fluorescence from both TICT's and the S_1 state bottom was depleted while increasing the solvent viscosity, indicating that the nature of these emissions as twisting along the polyene conjugation backbone from the planar Franck-Condon region to the S_1 bottom within the S_1 surface. MeOH: methanol. EtGly: ethylene glycol.

The spectroscopy and photophysics of the S_1 excited state of the cyanine dye IR144 have been discussed in the literature.^{119,245-247} However, little is known about the dynamics of higher excited state(s) of this dye and its close analogue *m*Pi-IR806. The two-dimensional excitation-

fluorescence spectra (**Figure 5.3c-d**) for the two dyes reveal higher emission bands that arise mainly from absorption bands with $\lambda_{\text{max}} = 540$ nm and 521 nm for IR144 and *m*Pi-IR806, respectively. Correlation between the S_2 absorption and excitation spectra was observed for the emissions with maxima at ca. 588 nm for IR144 and ca. 557 nm for *m*Pi-IR806 (**Figure 5.6**). Unlike IR806, the high-energy emission bands from IR144 and *m*Pi-IR806 were found to increase with solvent viscosity (**Figure 5.7**), in agreement with previous studies on cyanines S_2 fluorescence that attributed this finding to the need for out-of-planar motion to couple S_2 to S_1 energy transfer.²²³

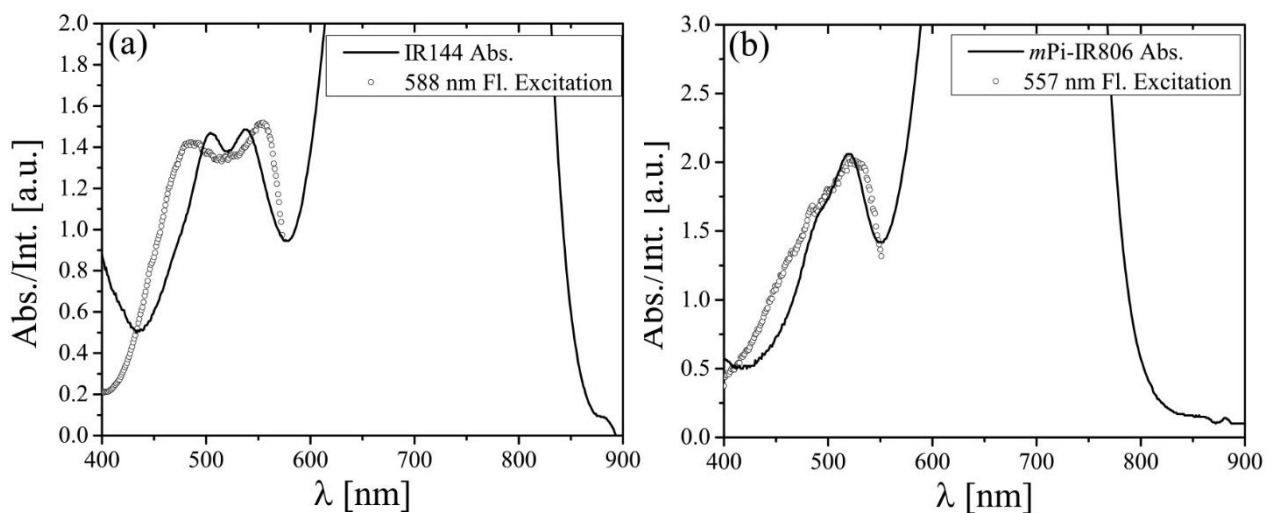


Figure 5.6 (a) IR144 and (b) *m*Pi-IR806 absorption spectra along with the excitation spectra for S_2 fluorescence with maxima at 588 nm and 557 nm, respectively.

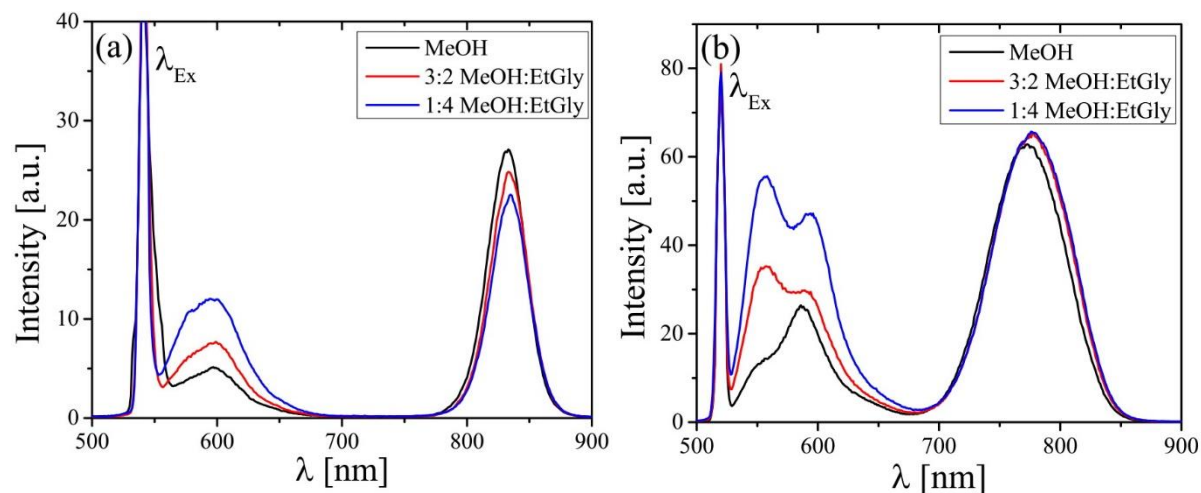


Figure 5.7 (a) IR144 and (b) *mPi*-IR806 fluorescence spectra showing an increase in the S_2 fluorescence yield while increasing the solvent viscosity. MeOH: methanol. EtGly: ethylene glycol.

Lifetime measurements using TCSPC of the S_1 fluorescence along with the S_2 fluorescence for IR144 and *mPi*-IR806 using 540 nm and 505 nm excitation, respectively, are shown in **Figure 5.8**. IR144 S_1 state has a decay time constant of 577 ps, which is close to the known life time of IR144 when excited directly to the S_1 state.^{246,248} A fast (<45 ps, instrument limited) rise corresponds to IC from the higher excited state. Emission from the higher energy state ($\lambda=588$ nm) has two components; a fast instrument limited <45 ps rate corresponding to IC and a slower 187 ps decay, corresponding to the S_2 - S_0 fluorescence life time. For *mPi*-IR806, the S_1 state has a fluorescence decay time constant of 975 ps, along with a 215 ps rise corresponds to IC from the higher excited state. Detection of the S_2 fluorescence at $\lambda=557$ nm has two components; a fast instrument limited 85 ps rate corresponding to IC and a slower 270 ps decay, corresponding to the S_2 - S_0 fluorescence life time. The slower IC rise in the S_1 emission for *mPi*-IR806 compared to the S_2 fast decay component can be explained by the presence of CT emission with maxima at 614 nm occurring between S_2 and S_1 . This CT emission was found to have decay constants that are different from S_1 and S_2 decay constants (**Figure 5.9** and **Table 5.2**).

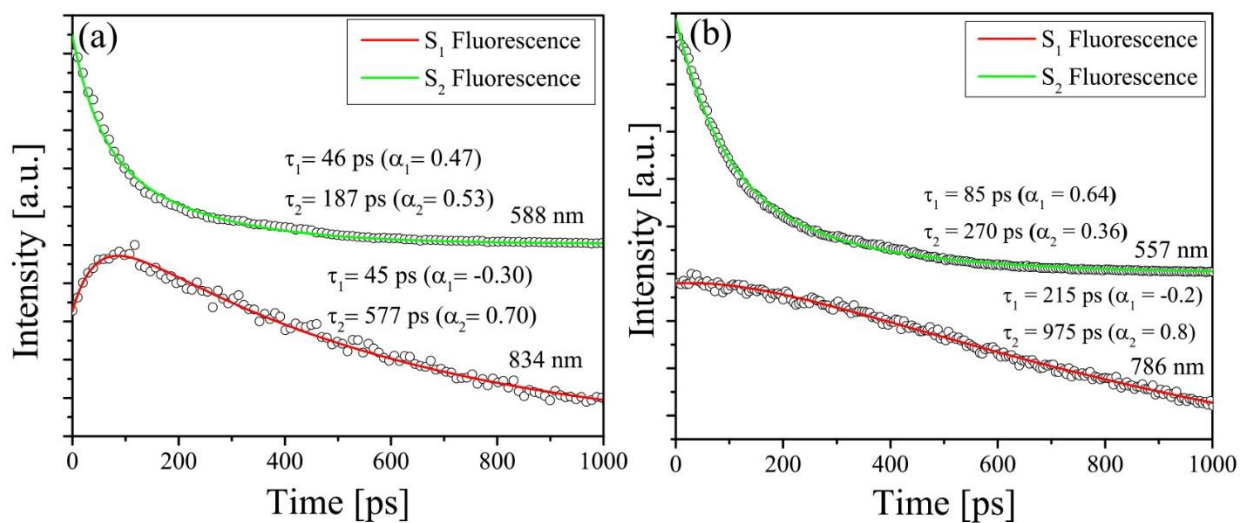


Figure 5.8 TCSPC decay curves along with biexponential fit constants for the S₁ (red) and S₂ (green) fluorescence for (a) IR144 when excited at 540 nm and (b) *mPi*-IR806 when excited at 505 nm.

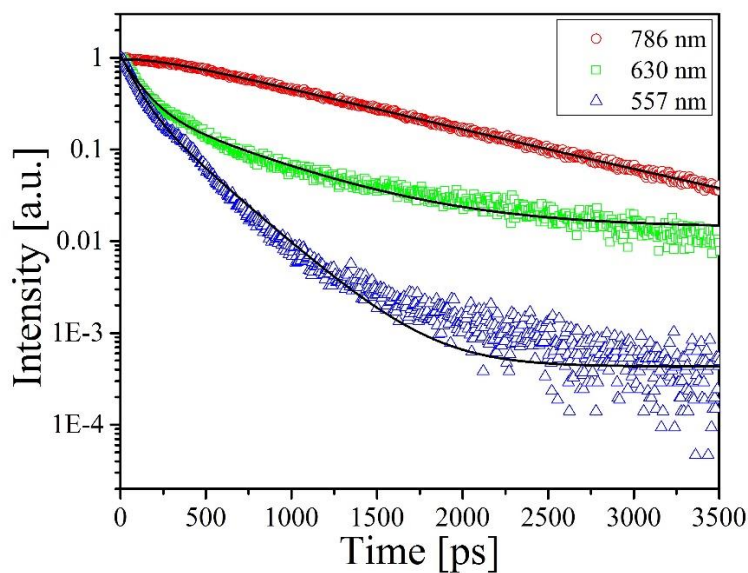


Figure 5.9 Fluorescence lifetime decay curves for *mPi*-IR806 upon excitation at 505 nm showing three different emissions at different wavelengths.

Table 5.2 Fitting parameters for the lifetime decay curves of *mPi-IR806*.

	$\tau_1 (\alpha_1)$ in ps	$\tau_2 (\alpha_2)$ in ps
557 nm	85 (0.64)	270 (0.36)
630 nm	110 (0.72)	590 (0.28)
786 nm	215 (-0.2)	975 (0.8)

5.3.2 Chirp studies on the S_2 state of IR144 and *mPi-IR806*

Fluorescence yield dependence on chirp experiments on IR144 were carried out using 16 fs laser pulses centered at 545 nm that match the S_2 absorption profile of IR144 to excite the sample while simultaneously detecting the resolved fluorescence signal from the S_1 and S_2 states using the same spectrometer. The same approach was followed with *mPi-IR806* using 13 fs pulses centered at 517 nm matching the S_2 absorption profile. The fluorescence spectra for IR144 using the aforementioned laser spectrum produced two peaks with maxima at 588 nm and 843 nm that are from S_2 and S_1 states, respectively (**Figure 5.10a**). While the *mPi-IR806* fluorescence peak maxima were at 558 nm and 786 nm, which are from S_2 and S_1 states, respectively (**Figure 5.10b**). It is worth noting that using the 517 nm-centered pulses, *mPi-IR806* fluorescence with maxima at 558 nm was mainly from the S_2 state without much involvement of the emission at 614 nm (see **Figure 5.3d**).

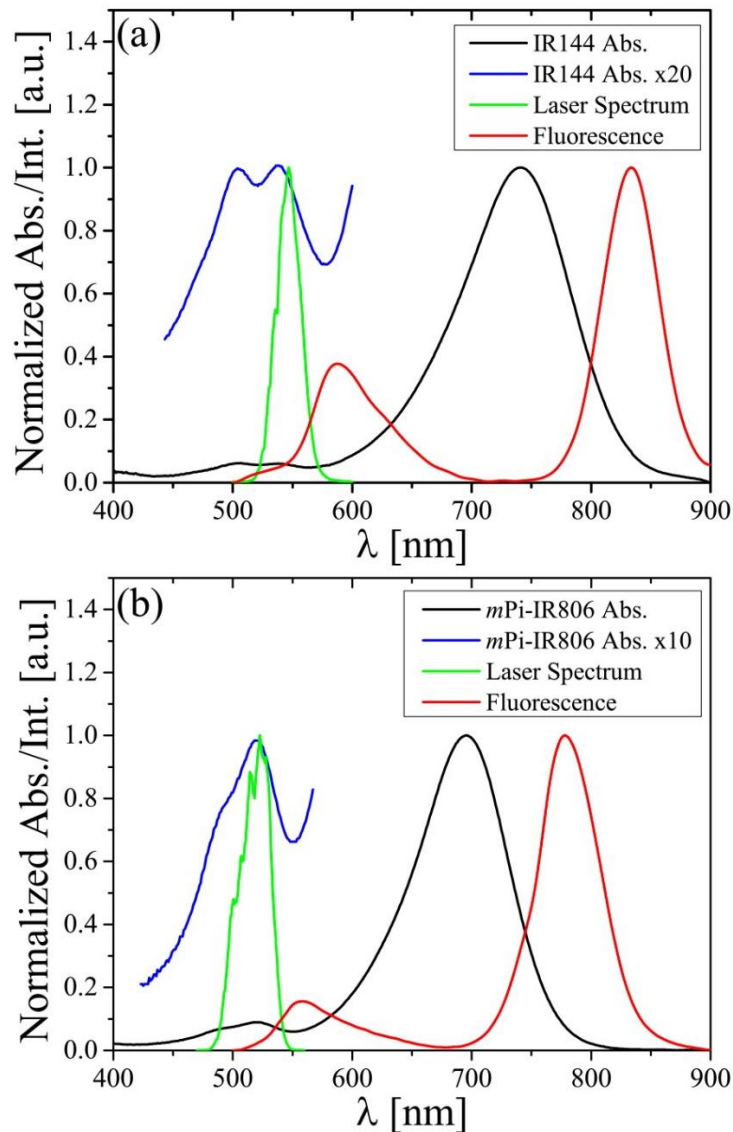


Figure 5.10 (a) IR144 and (b) *mPi*-IR806 fluorescence spectra using direct excitation to the S_2 state for each dye.

The observed fluorescence yields from S_2 and S_1 were found to be dependent on chirp as shown in **Figure 5.11**. No spectral shifts were observed as a function of chirp (**Figure 5.11** inset). The enhancement of the S_2 fluorescence yield observed for TL pulses corresponds to a concomitant depletion of emission from the S_1 state. The anomalous S_2 fluorescence as a function of chirp was found to differ drastically from the typical ‘chirp effect’ dependence in general and in particular

when exciting the IR144 S_1 state.^{37-38,48,120} By typical chirp effect we refer to the observation of reduced fluorescence yield when using negatively chirped pulses; the reduced yield caused by stimulated emission induced by the redder frequencies following the bluer frequencies. In a typical chirp experiment, maximum fluorescence yield is observed for positively chirped pulses. Clearly, S_2 excitation with chirped pulses does not agree with previous findings and leads to anomalous chirp dependence.

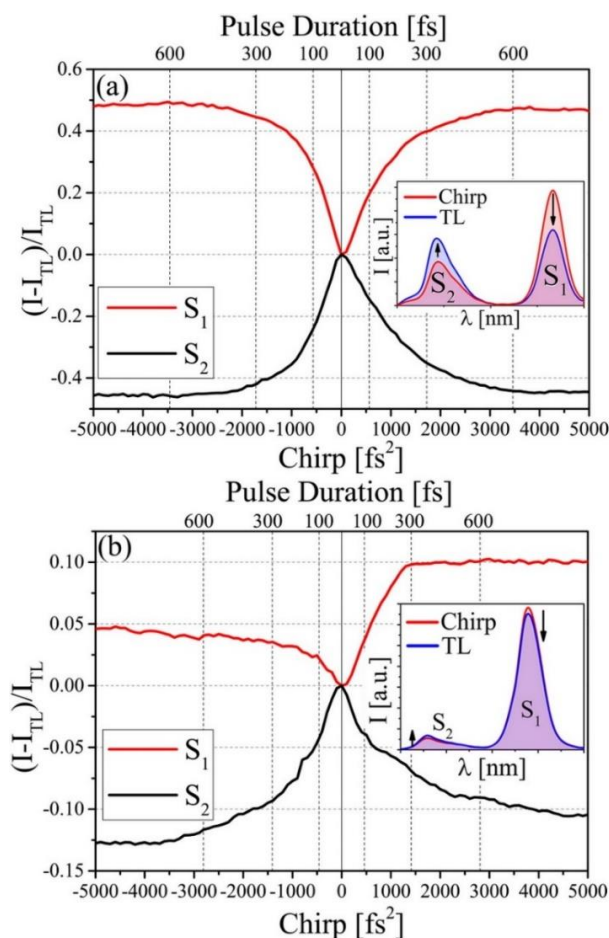


Figure 5.11 Integrated fluorescence intensity from S_1 (red) and S_2 (black) states as a function of linear chirp for (a) IR144 and (b) *mPi*-IR806, top axis shows the corresponding chirped pulse duration. TL pulses lead to greater S_2 fluorescence, while chirped pulses lead to greater S_1 fluorescence. A greater degree of asymmetry between positive and negative chirp values is observed for *mPi*-IR806. Inset: S_1 and S_2 emission spectra when excited by TL (blue) and chirped (red) pulses.

Chirps greater than 3000 fs² reduce S₂ fluorescence by about 42% and 13% compared to what is obtained using TL pulses for IR144 and *m*Pi-IR806, respectively. The chirp dependence is asymmetric, with greater depletion for negative values especially for *m*Pi-IR806. The asymmetry is observed at laser fluence higher than ~0.5 mJ/cm² (see **Figure 5.12b** and **d**). Lower emission from the resonant state (here S₂) would be expected with negatively chirped pulses, which deplete the excited state population before intramolecular vibrational redistribution and fluorescence occurs by tracking the excited-state wavepacket's motion from the Franck–Condon geometry to lower energy.³⁷ The degree of symmetry with respect to chirp is important because it establishes that the dynamics are sensitive to the order in which different frequencies arrive. An asymmetric response can be observed when dynamics occur on a similar timescale to the excitation laser pulse.²⁴⁹ The slightly asymmetric S₂ fluorescence dependence observed implies that wavepacket motion out of the FC region occurs on a timescale comparable with the pulse duration.

From the results in **Figure 5.11**, we find that the fluorescence yield from the S₂ state is greater when excited using TL pulses and lower for chirped pulses. What is unexpected and surprising is that the yield of S₁ fluorescence does not mimic the yield of S₂ fluorescence, given that most of the S₁ population is attained via IC from S₂. When comparing the chirp dependence of the S₂ and S₁ states in **Figure 5.11** for IR144, it can be seen that changes in the fluorescence yields from the two states are anti-correlated; *i.e.* TL pulses maximize S₂ and minimize S₁ population. In other words, the S₂ fluorescence enhancement occurs at the expense of IC to S₁. The same is observed for *m*Pi-IR806 when comparing the fluorescence yield from both states using TL and positive chirp. Differences between IR144 and *m*Pi-IR806 arise from the fact that excitation is not exclusive to the S₂ state. Therefore, the chirp trace for the S₁ fluorescence of *m*Pi-IR806 is a result of two components; (i) direct S₁ excitation evidenced by the depleted fluorescence on the

negative side, (ii) IC from S_2 evidenced by the fluorescence depletion using TL pulses. In both cases, the excitation pulse, which prepares the initial wave-packet on the S_2 surface, controls IC to the lower excited state.

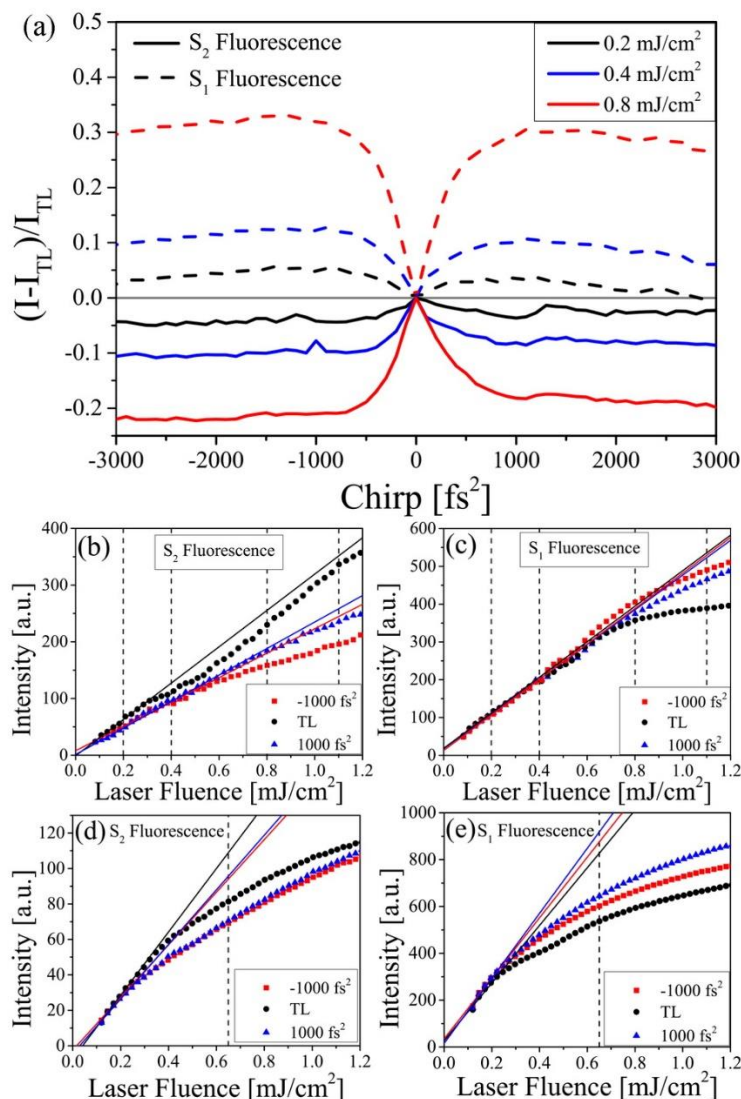


Figure 5.12 (a) IR144 S_2 (solid lines) and S_1 (dashed lines) fluorescence yield as a function of chirp at various laser fluence values. Fluorescence intensity dependence as a function of laser fluence for IR144 from (b) S_2 and (a) S_1 states using TL (black), negatively (red) and positively (blue) chirped 1000 fs^2 pulses. Fluorescence intensity dependence as a function of laser fluence for *mPi*-IR806 from (d) S_2 and (e) S_1 states using TL (black), negatively (red) and positively (blue) chirped 1000 fs^2 pulses. The vertical lines indicate the laser fluence values at which the chirp scans were carried out. Linear fitting for the fluorescence yield at low laser fluence ($0.1\text{-}0.25 \text{ mJ/cm}^2$) is shown as a guide to discern where nonlinear fluence dependence becomes important.

Fluorescence yield experiments were repeated for IR144 at lower laser fluences, as shown in **Figure 5.12a**. The chirp dependence found at lower fluences, where fluorescence yield is linear with laser intensity, is similar to what was found at higher fluences and shown in **Figure 5.11a**. Fluorescence yield as a function of laser fluence was recorded using TL, negatively and positively (1000 fs^2) chirped pulses for IR144 (**Figure 5.12b** and **c**) and *m*Pi-IR806 (**Figure 5.12d** and **e**). For both molecules, linear dependence of fluorescence intensity is observed at lower laser fluence for both S_1 and S_2 states. Note that for all laser fluences and for both molecules S_2 fluorescence is greater for TL pulses compared to chirped ones. Conversely, S_1 fluorescence is greater for chirped pulses as opposed to TL pulses. These differences only increase with intensity.

No S_2 fluorescence was observed for IR806. This absence may be related to the non-polar solvation nature of this cyanine dye. Nevertheless, we see the absence of S_2 fluorescence to serve as an important control, albeit negative, for our research. The S_1 fluorescence yield as a function of chirp for IR806 (**Figure 5.13**) shows minimum fluorescence yield for negative chirps and maximum for positive chirps, what we have earlier termed typical chirp dependence. We ascribe this behavior to the non-polar nature of the S_1 state in IR806.

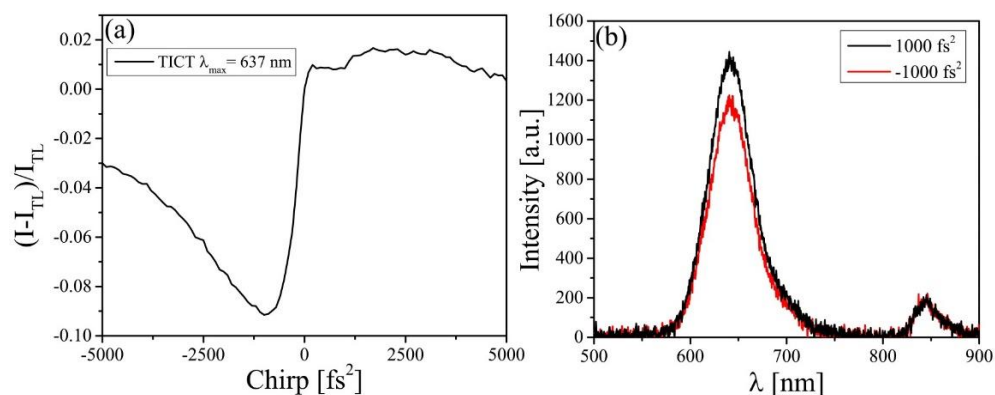


Figure 5.13 (a) Total fluorescence intensity for the emission with maxima at 637 nm as a function of chirp on the 540 nm centered pulses. (b) IR806 emission when excited using 540 nm centered pulses at different chirp values showing that the change is only associated with 637 nm emission.

5.3.3 Theoretical Modeling

A full simulation of the present experiment, including *ab initio* calculation of the relevant ground and excited states in the presence of solvent and the intense laser fields, are presently out of our reach. There is sufficient information about the S_1 and S_0 potential energy surfaces to determine that initial dynamics following excitation in S_1 is along the so-called bond-length alternation (BLA) coordinates.^{151,154} In the longer cyanines ($n \geq 5$), a significant barrier on the S_1 surface divides planar and twisted conformations of the polyene backbone. Beyond the barrier, the system descends steeply along torsional gradients. A CI between S_1 and S_0 is responsible for nonradiative decay from S_1 . For IR144 and *m*IR806 the large S_1 - S_0 Stokes shift and the significant increase in S_2 - S_0 fluorescence with increased viscosity leads to expect S_2 has a more planar geometry than S_1 . A simplified schematic representation of the three singlet states inspired by Jortner's gap law strong coupling case,²⁵⁰ for S_2 emission from molecules with internal conversion is shown in **Figure 5.14**. In addition, we depict an effective model with the minimum number of energy levels that can help explain our findings.

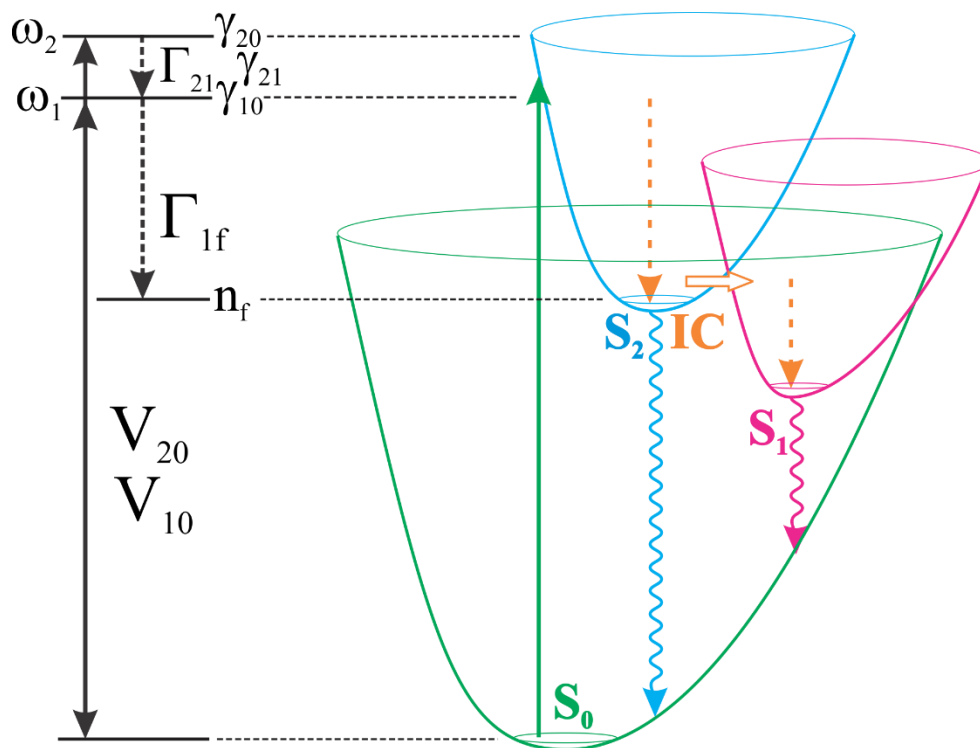


Figure 5.14 Simplified schematic of S_0 , S_1 , and S_2 energy levels considered in our model. (Left) Four level model used for our calculations, consists of the ground state and 3 levels in the S_2 excited state. ω_0 is the laser frequency, ω_1 and ω_2 are frequencies of the two levels in S_2 that interact with the laser. n_f is the population reaching the bottom of S_2 , note this state is outside the laser spectrum, V is the transition dipole dependent laser interaction, Γ is the relaxation rate, γ is the dephasing rate. (Right) Schematic representation of the three lower singlet states of cyanine molecules plotted as a function of spatial coordinates involving twisting from the planar ground state configuration and bond lengthening. Internal conversion (IC) to S_1 requires twisting. The IC from S_1 to S_0 expected at a torsion angle of 90° is not indicated.

The relevant energy levels consist of a ground state level and three levels representing the S_2 state. The upper two levels (ω_1 and ω_2) are consistent with the S_2 absorption spectrum features while the lowest energy level (n_f) corresponding to the bottom of the S_2 state, which fluoresces at wavelengths far from the excitation laser and is therefore dark to the excitation laser pulse. The laser frequency ω_0 was set to interact with the higher two levels ω_1 and ω_2 while both levels were set to relax irreversibly. Our goal is first to solve for the population in (n_f) as a function of chirp.

Then, because S_1 is populated via IC only from the upper levels but not from the lowest level, consistent with the observation of S_2 fluorescence, the total excited population from the ground state ends as population in either S_2 or S_1 . Therefore, S_1 population equals $(1-S_2)$ which has an inverse dependence on chirp compared to S_2 . Our experiments are performed in a regime where fluorescence from S_2 has very slight saturation for TL or chirped pulse excitation (**Figure 5.12**), therefore, our model should be able to take into account nonlinear optical laser-molecule interactions. We used a non-perturbative solution of the equation of motion for the density matrix (eq 5.1 and eq 5.2)²⁵¹ to describe the system in the presence of the field

$$\frac{d\rho_{aa}}{dt} = -\frac{i}{\hbar} \sum_v (V_{av}\rho_{va} - \rho_{av}V_{av}) + \sum_{Eb>Ea} \Gamma_{ab}\rho_{bb} - \sum_{Eb>Ea} \Gamma_{ba}\rho_{aa} \quad (5.1)$$

$$\frac{d\rho_{ab}}{dt} = -i(\omega_a - \omega_b)\rho_{ab} - \frac{i}{\hbar} \sum_v (V_{av}\rho_{vb} - \rho_{av}V_{vb}) - \gamma_{ab}\rho_{ab} \quad (5.2)$$

where V is the transition dipole, a and b represent the levels in the model, ρ_{aa} and ρ_{ab} are the diagonal and the off diagonal elements of the density matrix which represent the populations and coherences between the levels, respectively. The coherence-dephasing rate is $\gamma_{ab} = 1/2(\Gamma_a + \Gamma_b)$, where Γ_a and Γ_b are the relaxation rates. The dipole moment matrix interaction with the chirped pulses is represented by eq 5.3.

$$V_{ab}(t) = \mu_{ab}E_0 \sqrt{\frac{\tau_0^2}{\tau_0^2 - i\phi''}} \exp\left[-\frac{1}{2} \frac{t^2}{\tau_0^2 - i\phi''}\right] \quad (5.3)$$

where μ_{ab} is the dipole moment matrix element, τ_0 is the TL pulse duration and ϕ'' is the chirp value.

When solving the system of differential equations numerically for the population in the lowest level (n_f), the best match with the experimental observations was found when we set ω_1

to be resonant with the laser frequency while ω_2 was set to the vertical transition frequency obtained from Lorentzian peak deconvolution of the experimental S_2 absorption band. The transition dipole moment matrix element μ_{ab} for each level was set as the square root of the relative strength of each deconvoluted peak from the S_2 absorption band, given that the absorbance is directly proportional to the square of the transition dipole moment. The relaxation time $\tau_2 = 1/\Gamma_{21}$ from ω_2 to ω_1 consistent with our simulation was found to occur on a very fast time scale of about 10 fs and 5 fs for IR144 and *mPi*-IR806, respectively. Such value is in close proximity to reported IR144 three-pulse photon-echo peak shift component from the S_1 state that arise due to backbone stretching intramolecular vibrations.²⁴⁵ The other relaxation component $\tau_1 = 1/\Gamma_{1f}$, which is from ω_1 to the final emitting level n_f was about 100 fs and 500 fs for IR144 and *mPi*-IR806, respectively. These slower dynamics presumably involve torsion. Results from the simulations for the dependence of the final S_2 population and the S_1 population calculated as $S_1=1-S_2$, are shown for IR144 (**Figure 5.15a**) and *mPi*-IR806 (**Figure 5.15b**). The calculated S_1 population for *mPi*-IR806 as $S_1=1-S_2$ only represents IC from S_2 , therefore we have also added S_1 population via direct S_1 excitation to match the experimental results. Direct S_1 population was carried out using a similar previous model that describes the S_1 chirp effect.³⁷ The S_1 level calculations were performed for a three level model consisting of one ground level representing the ground state and two excited levels representing high-energy vibrational levels in the S_1 state. The laser field was set to interact equally with the two excited levels and the high level was set to relax on a 10 fs timescale to the lower level. The model was successful in reproducing the typical S_1 chirp effect as population depletion using negatively chirped pulses. The final *mPi*-IR806 S_1 population trace shown in **Figure 5.15b** is a linear combination of 25% from direct S_1 interaction and 75% via IC from S_2 .

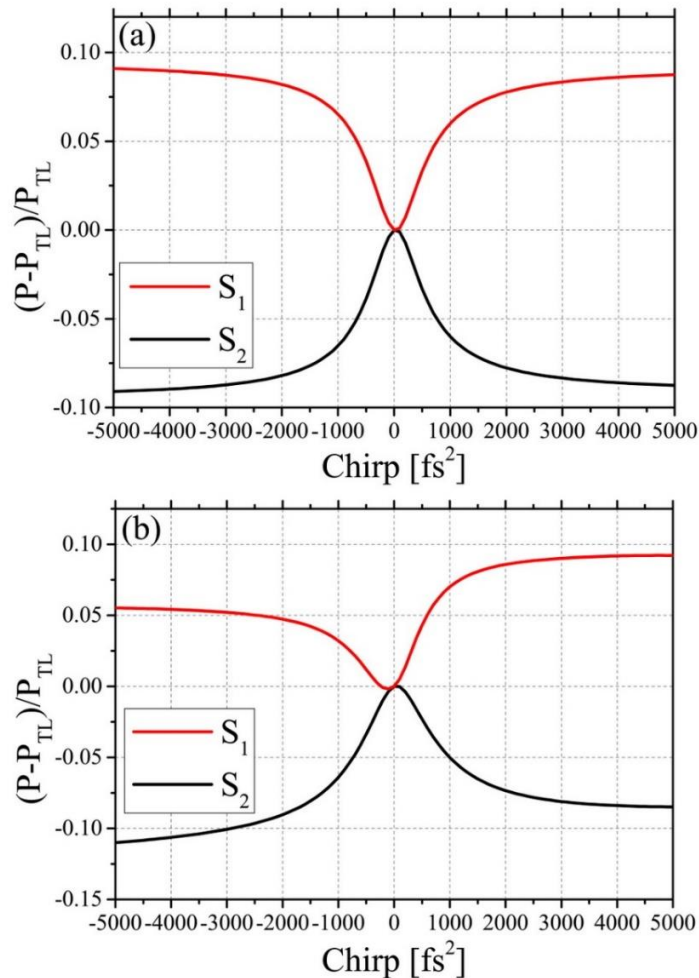


Figure 5.15 Theoretical simulations for S_2 state (black) and S_1 state (red) population as a function chirp for (a) IR144 and (b) mPi-IR806.

From the reduced theoretical model, we find a set of conditions consistent with our experimental findings. TL pulses result in a larger population in the bottom of the S_2 potential than chirped pulses. This would imply that IC from S_2 to S_1 , presumably through a conical intersection, occurs before the wave-packet reaches the lowest point on the potential energy surface of S_2 . This observation is consistent with the presence of S_2 fluorescence.

5.4 Discussion

Interpretation of our experimental findings requires we establish what is known, and limit the number of processes to be considered to the fewest possible. The higher energy emission from the polar solvated dyes (IR144 and *m*Pi-IR806) originates from the S_2 state. Based on the hundreds of picoseconds fluorescence lifetimes of the S_2 state for IR144 and *m*Pi-IR806, we surmise that population that reaches the bottom of the S_2 potential, which is displaced in energy and in space from the FC region, is trapped by a barrier; *i.e.* IC to S_1 slows dramatically. The barrier is likely to be the known polyene conjugation-length dependent transition state barrier, similar to that on the S_1 potential energy surface, which separates the planar FC region from that of twisted conformations, where a conical intersection with the ground state, S_0 , is located.^{151,252-253} However, this barrier is located on the S_2 surface and separates the FC from the conical intersection with the S_1 surface. These observations are further confirmed by enhanced S_2 emission as a function of increased solvent viscosity for both IR144 and *m*Pi-IR806. The observed enhancement of S_2 fluorescence for TL pulses becomes more pronounced as laser intensity increases. Our findings imply that chirped pulses create wave packets that more efficiently cross to S_1 , this process in dynamic competition with energy relaxation, which brings the population to the bottom of the S_2 potential well, where IC to S_1 is inefficient. From our theory and numerical calculations, we find that IC must take place before energy relaxation, and dephasing must be very fast, <20 fs (TL pulse duration) and competes with vibrational relaxation and wave packet motion.

Two possible mechanisms for our experimental findings are considered. First, we suggest a mechanism based purely on first-order wave packet preparation. It is likely that TL pulse excitation creates a compact wave packet that is less efficient at crossing from S_2 to S_1 at short times than a diffuse wave packet, which better access the region where the S_2 and S_1 potential

surfaces interact. Second, because TL pulse excitation is likely to drive more strongly double quantum excitations to a higher state S_n , cycling between the S_n and S_2 states would be expected to confine wave packets near to the S_2 planar minimum and suppress IC.²⁵⁴⁻²⁵⁸ Similarly, TL pulse excitation strongly drives cycling between the S_2 and S_0 surfaces and limits IC accordingly.

The first mechanism is consistent with our observations because to some extent they are independent of laser intensity. We find that the fluorescence yield of S_2 is lower for chirped pulses than for TL pulses at all laser intensities, and fluorescence yield of S_1 is higher for chirped than for TL pulses (see **Figure 5.12**). The theory model offered here did not take into account calculation of FC factors of IC for wave packets created by TL or chirped pulses. The second mechanisms, whereby the laser strongly couples two or more states, is consistent with our finding that laser intensity caused a greater difference in the final state populations. While there is no reason *a priori* why excitation to higher excited states would preferentially end in S_2 rather than S_1 , laser driven transitions between two states have been considered as means to alter vibrational relaxation dynamics²⁵⁹ and to potentially cause population dependent dynamics.²⁶⁰

The exact photophysical process that leads to the observed control over IC is difficult to determine given the complexity of the systems. The Hamiltonian of each system has multiple dimensions and the existence of a conical intersection between S_1 and S_2 has not been determined. Our observations, however, show photonic control over the higher excited state fluorescence in cyanine dyes. It is likely that the actual mechanism involves both of the proposed mechanisms. The degree of control exerted over S_2 population can be harnessed to explore the role of higher excited states in photochemical processes such as photosynthesis, especially in carotenoids where the first optically active state is a higher excited state that undergoes rapid IC to S_1 .²⁶¹

5.5 Conclusion

Control over internal conversion from S_2 to S_1 of the cyanine dyes IR144 and *m*Pi-IR806 has been achieved by phase control over the excitation pulses that prepare the initial population in the upper excited state. We found anomalous chirp dependence, whereby TL pulses cause a greater population in the excited state than chirped pulses. Furthermore, we find internal conversion to S_1 is not proportional to the total initial population but instead it is inversely proportional. The experimental results were successfully simulated using the equation of motion for the density matrix for a four level system. Under strong field interaction, TL pulses were more efficient in directing the population to the bottom of S_2 from which direct fluorescence occurs rather than IC to the S_1 state.

Chapter 6 Role of High-Order Dispersion on the Ionization of Molecules

While the interaction of atoms in strong fields is well understood, the same cannot be said about molecules. We consider how dissociative ionization of molecules depends on the quality of the femtosecond laser pulses, in particular, the presence of third- and fourth-order dispersion. We find that high-order dispersion (HOD) unexpectedly results in order-of-magnitude enhanced ion yields, along with the factor of three greater kinetic energy release compared to transform-limited pulses with equal peak intensities. The magnitude of these effects is not caused by increased pulse duration. We evaluate the role of pulse pedestals produced by HOD and other pulse shaping approaches, for a number of molecules including acetylene, methanol, methylene chloride, acetonitrile, toluene and *o*-nitrotoluene, and discuss our findings in terms of processes such as pre-alignment, pre-ionization, and bond softening. We conclude, based on the quasi-symmetric temporal dependence of the observed enhancements that cascade ionization is likely responsible for the large accumulation of charge prior to the ejection of energetic fragments along the laser polarization axis.

This chapter has been adapted with permission from (*J. Phys. Chem. A* **2016**, *120*, 8529-8536)
Copyright © 2016, American Chemical Society.

6.1 Introduction and Background

Ultrashort intense femtosecond pulses with peak intensities higher than 10^{13} W/cm² have associated field-strength of ~ 1 V/Å. Their interaction with matter, while simpler to understand for atoms, is much more complex for molecules.²⁶²⁻²⁶⁹ Molecules produce multiply charged species, change their molecular structure through: deformation, isomerization, and the migration of atoms between different sites within the charged molecule.²⁷⁰⁻²⁷⁶ Understanding and controlling these chemical processes with ultrafast laser pulses has been an ongoing dream in the field since the 1980's.^{44,266-267,277-279}

Strong field ionization is largely determined by the peak intensity and the duration of the laser field. Within a few cycles, the electric field is able to overcome molecular bonds and cause dissociation. Efficient proton elimination with high excess energy from molecules is often observed.^{272,280} A number of models have been considered to explain dissociative ionization of molecules under intense fields. One such model posits that the process is ruled by stretching of C-H bonds.²⁸¹ As the duration of pulse increases, bond-lengths reach a critical internuclear distance from which ionization cross section is greater. Another model proposes hydrocarbons ionize to a high-charge state and dissociate in a concerted Coulombic explosion.²⁷² At the leading edge of the pulse, C-H bonds stretch and the molecule is ionized multiple times. After this event, the skeleton of the molecule Coulomb explodes and forms highly charged fragments. Both of these models depend on pulse duration to explain the dissociative ionization processes.

With the advent of pulse shapers capable of preparing well-defined laser pulses, in terms of phase, amplitude, and polarization,¹¹ understanding dissociative ionization in greater detail has become possible. Here we explore if the presence of low-intensity pedestals in the pulse, caused by high-

order dispersion (HOD), influence the strong-field dissociative ionization of molecules. We focus on HOD because of its natural prevalence in ultrafast laser systems.

The electric field distribution in time domain for a broadband laser pulse with an angular frequency ω can be expressed as:

$$E(t) \equiv \int_{-\infty}^{\infty} E(\omega) e^{-i\omega t} d\omega \quad (6.1)$$

$$E(t) \equiv \int_{-\infty}^{\infty} E(\omega) e^{-i\omega t} d\omega \quad (6.2)$$

where

$$E(\omega) = e^{-\frac{1}{2}(\omega-\omega_0)^2 \tau_0^2} e^{i\varphi(\omega)} \quad (6.3)$$

in which $\tau_0 = \frac{\tau_{FWHM}}{2\sqrt{\ln(2)}}$, τ_{FWHM} is the pulse duration at FWHM. The term $\varphi(\omega)$ is known as the phase

of the pulse and can be expanded as:

$$\varphi(\omega) = \varphi^{(0)} + \frac{\varphi^{(1)}(\omega - \omega_0)}{1} + \frac{\varphi^{(2)}(\omega - \omega_0)^2}{2!} + \frac{\varphi^{(3)}(\omega - \omega_0)^3}{3!} + \frac{\varphi^{(4)}(\omega - \omega_0)^4}{4!} + \dots \quad (6.4)$$

The first term $\varphi^{(0)}$ corresponds to a time delay for all the frequencies; the second term $\varphi^{(2)}$ corresponds to the second order dispersion (SOD), also known as chirp. Chirp causes a temporal broadening of the pulse and a change in the arrival order of frequencies in accordance with the phase sign. Using chirp to control the fragmentation of a dissociative event has been studied extensively during the past twenty years.^{224,282-283} Work from this group showed that there is a trend applies to substantially all molecules; sixteen different molecules were studied, and the extent of fragmentation was dictated by the pulse duration.²⁶⁶ Terms higher than $\varphi^{(2)}$ are referred to as high-order dispersion. For instance, third order dispersion (TOD) causes the appearance of a pedestal before (when negative) or after (when positive) the main pulse, and fourth order

dispersion (FOD) causes the appearance of a symmetrical pedestal on both sides of the main pulse. While a great deal of research has been conducted using chirped pulses, few reports explore the role of high-order dispersion in dissociative ionization. The effect of negative TOD on the dissociation of H_2^+ was an increase in ion yields due to pre-alignment caused by the pre-pulse pedestal.⁵⁹ Whereas negative TOD was found to suppress the nonsequential ionization of the anion SF_6^- .²⁸⁴

In this chapter we explore whether the pulse pedestal resulting from HOD influences the dissociative ionization of large molecules. Our interest stems from the fact that HOD is technically challenging to measure and eliminate. Therefore, if an effect is found, it is likely relevant to previous and future experiments with intense femtosecond laser pulses. Moreover, it can help understand the interaction between molecules and intense laser fields.

6.2 Experimental Methods

The experimental setup used here consists of a regeneratively amplified Ti:sapphire laser (Spitfire, Spectra Physics, Santa Clara, CA) producing femtosecond pulses at 1 kHz repetition rate. The near-Gaussian pulses were centered at 800 nm and had a 25.8 nm bandwidth FWHM. The pulses were compressed and shaped after the amplifier using a pulse shaper (MIIPS-HD, Biophotonic Solutions Inc., East Lansing, MI) utilizing the Multiphoton Intrapulse Interference Phase Scan (MIIPS) method.^{30,126} The pulse bandwidth corresponds to 36 fs (FWHM) when compressed to transform-limited (TL). The shaper was also used to introduce TOD and FOD phase masks. Amplitude correction was implemented by increasing the transmission value for the HOD pulses relative to the TL pulses without changing the laser spectrum. This was used to ensure the peak intensity for the phase shaped pulses was the same as that for the TL pulses. The amplitude mask value is based on the theoretical change in the pulse peak intensity while introducing the HOD phase. This was verified experimentally based on the total SHG signal that is obtained from TL, HOD phase only, and amplitude corrected HOD pulses which are also compared to the theoretical SHG signal based on the laser spectrum. High fidelity (pulse-to-pulse stability) of the laser and the absence of pre/post pulses were ensured and confirmed via the fidelity assessment procedure.^{127,285}

The experiments were carried out using a Wiley-McLaren time-of-flight mass spectrometer (TOF-MS) having a 0.5 m long field free drift region. The MS chamber was maintained under high vacuum with a base pressure of $6-8 \times 10^{-9}$ Torr. The samples were outgassed by repeated freeze-thaw cycles under vacuum. After outgassing, the samples were introduced into the vacuum chamber via a leak valve and the pressure was maintained at 5×10^{-6} Torr. Laser pulses were focused onto the effusive sample using a 300 mm achromatic lens. The experiments were carried out at pulse energies corresponding to peak intensities of 1.7, 3.4, 5.1, and 6.8×10^{14} W/cm². The

pulses were linearly polarized in parallel to the TOF-MS and the ion detection axis. The ion extraction plates were 1 cm apart and the DC extraction field between the repeller and the extractor was set at 320 V/cm, while the extractor was kept at 1880 V. The extractor plate consisted of a 0.9 mm wide slit that is perpendicular to the laser propagation axis to ensure ion extraction from the central part of the focused beam and mitigate volume ionization effects.²⁸⁶⁻²⁸⁸ The zero-voltage ground plate was a 16 mm diameter circular wire grid placed 1 cm away from the extractor plate. Ions were detected using a 500 MHz digital oscilloscope coupled with dual microchannel plates (MCP's) in Chevron configuration. The MCP's were located at the end of the field-free drift region of the TOF-MS. For each peak intensity value, the resulting ions from one thousand laser shots were collected and averaged. The data acquisition program collected the averaged signal for each of the different phases being evaluated in close succession, in order to prevent the influence of long-term drifts in the signal. This procedure, evaluating multiple different phases, was repeated to obtain 500 averages for each phase.

The effect of high-order dispersion on a femtosecond pulse is relatively subtle and not easy to characterize. We recorded interferometric autocorrelations (AC) for the four types of pulses considered in this research; they are TL, $-3 \times 10^4 \text{ fs}^3$ TOD, $3 \times 10^4 \text{ fs}^3$ TOD, and $3 \times 10^6 \text{ fs}^4$ FOD as shown in **Figure 6.1**. For the case of TOD pulses, a cross-correlation with a TL pulse is presented. The cross correlation measurement (TL vs TOD pulses) are carried out by the pulse shaper and a method called multiple independent comb shaping (MICS).²⁸⁹ The cross-correlation reveals the asymmetric temporal profile for the pulses and confirms the pedestals for positive and negative TOD has mirror image symmetry (**Figure 6.2**). HOD introduces a small pedestal, and some pulse broadening. The retrieved pulse durations (FWHM) are 36, 48, and 64 fs for each

phase, respectively. For all our experiments, the peak intensity of the pulses, with or without HOD, was kept constant.

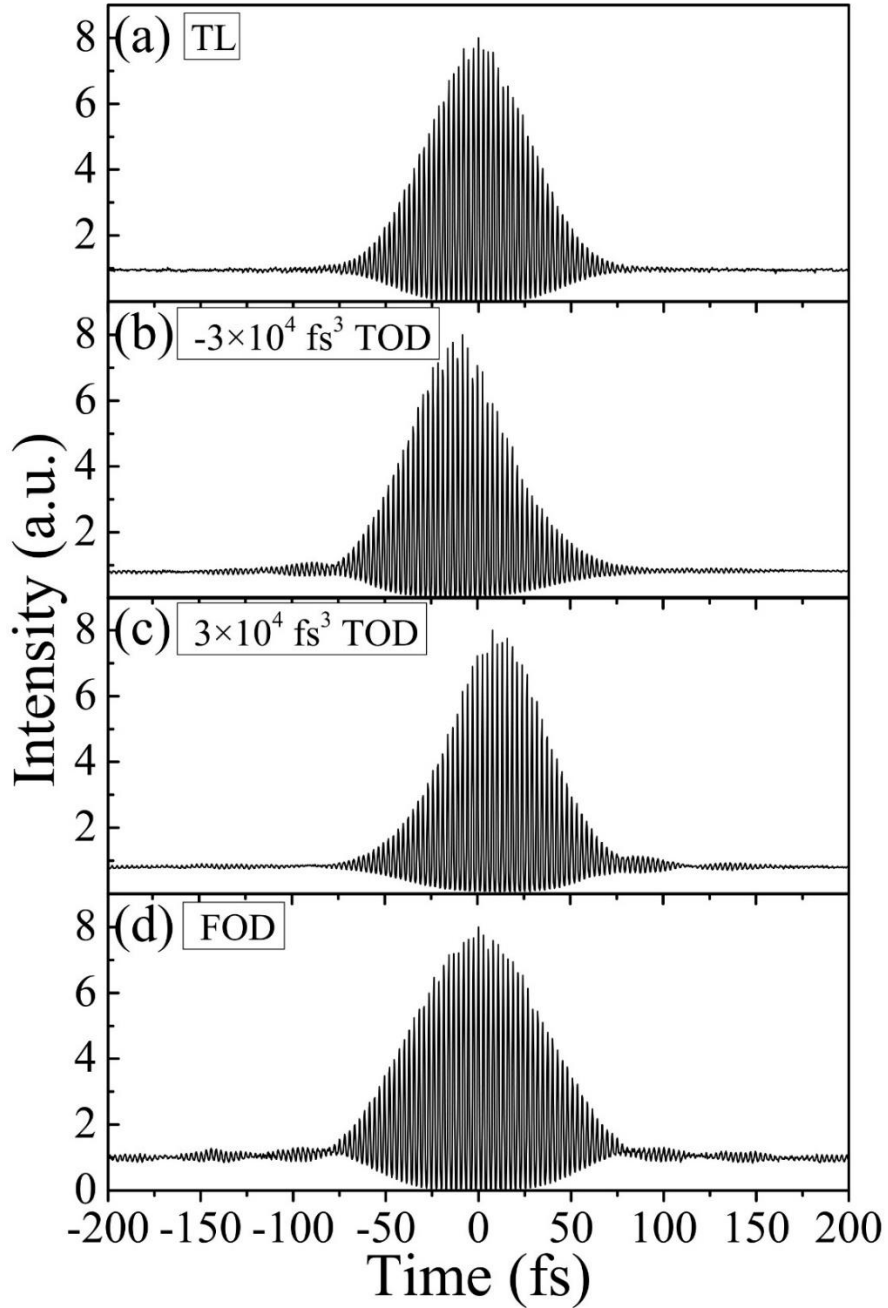


Figure 6.1 Interferrometric AC for (a) TL, (b) $-3 \times 10^4 \text{ fs}^3$ TOD, (c) $3 \times 10^4 \text{ fs}^3$ TOD, and (d) $3 \times 10^6 \text{ fs}^4$ FOD pulses. The TOD traces are cross-correlations with TL pulses to show the asymmetric time profiles.

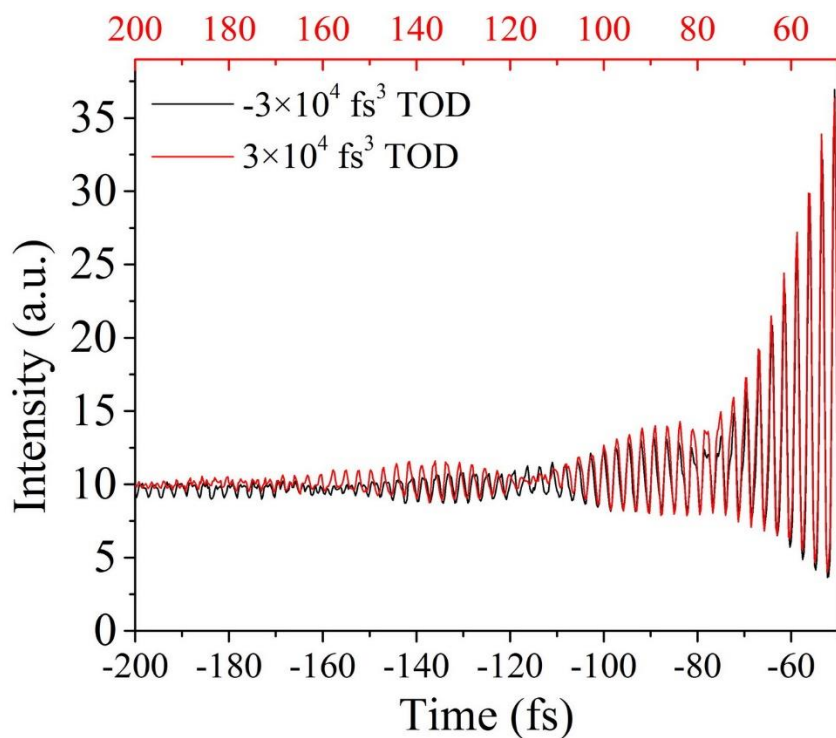


Figure 6.2 Cross-correlation for $-3 \times 10^4 \text{ fs}^3$ TOD (black, bottom axis) and $3 \times 10^4 \text{ fs}^3$ TOD (red, top axis) with a TL pulse.

The pedestals seem to be negligible in the autocorrelations shown in **Figure 6.1**. For this reason, we plot calculated pulse profiles in logarithmic scale in **Figure 6.3**. FOD causes a time-symmetric pedestal, while TOD causes a leading (negative) or following (positive) pedestal. The intensity of these pedestals is about 1-2 orders of magnitude smaller than the main pulse and extends for about 200 fs. In strong field laser experiments, where the peak intensity can exceed $1 \times 10^{15} \text{ W/cm}^2$ (as shown in **Figure 6.3**), these pedestals cannot be ignored. Our experiments track the dissociative ionization process observed for a number of molecules including acetylene, methanol, methylene chloride, acetonitrile, toluene and *o*-nitrotoluene; comparing results for TL pulses and pulses with HOD. Our presentation begins by describing in detail results for toluene and *o*-nitrotoluene; we then generalize to the other molecules.

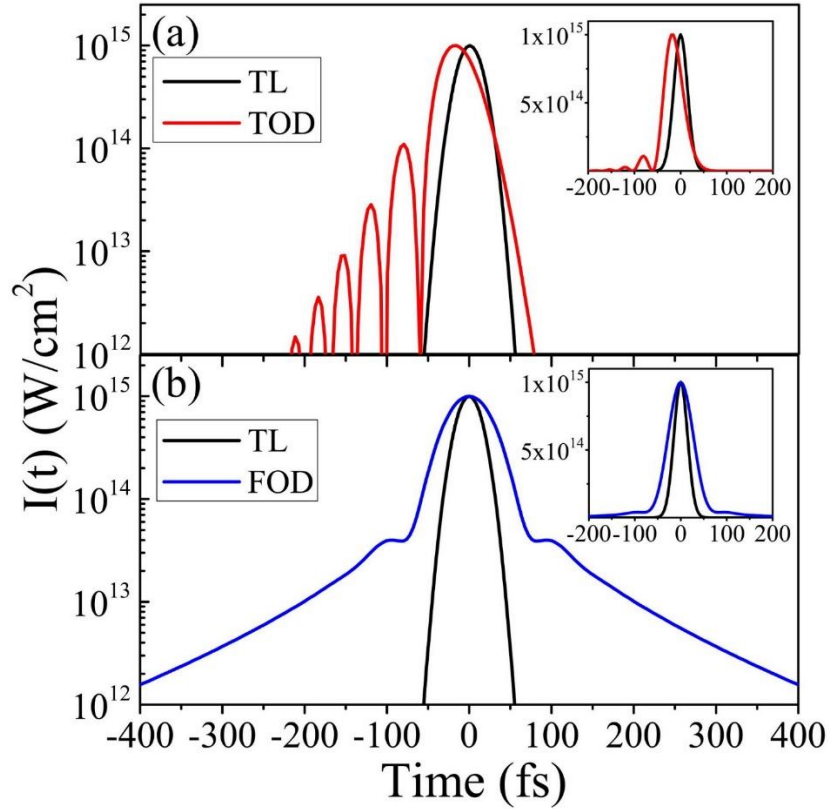


Figure 6.3 Theoretical simulation for the intensity of TL pulses compared to that of (a) $-3 \times 10^4 \text{ fs}^3$ TOD and (b) $3 \times 10^6 \text{ fs}^4$ FOD pulses. The insets show same pulses on a linear scale. Positive TOD (not shown) resembles the negative TOD shown in (a) except that the pedestal appears after the main pulse.

6.3 Results

The mass spectrum from toluene using TL pulses at 6.8×10^{14} W/cm² is shown in **Figure 6.4** (*o*-nitrotoluene mass spectrum is shown in **Figure 6.5**). Both are in good agreement with previous studies.^{266,290-291} The strong non-resonant fragmentation of both molecules produces shorter hydrocarbons along with multiply charged ions. Coulomb explosion products can be identified in the spectrum because of their structure; ions traveling towards the detector arrive at earlier times compared to backward moving ions. When comparing the two compounds, *o*-nitrotoluene, which is more polarizable than toluene and has an ionization potential that is larger by 0.4 eV,²⁹² produces larger amounts of fragment ions relative to that of the molecular ion.²⁶⁶

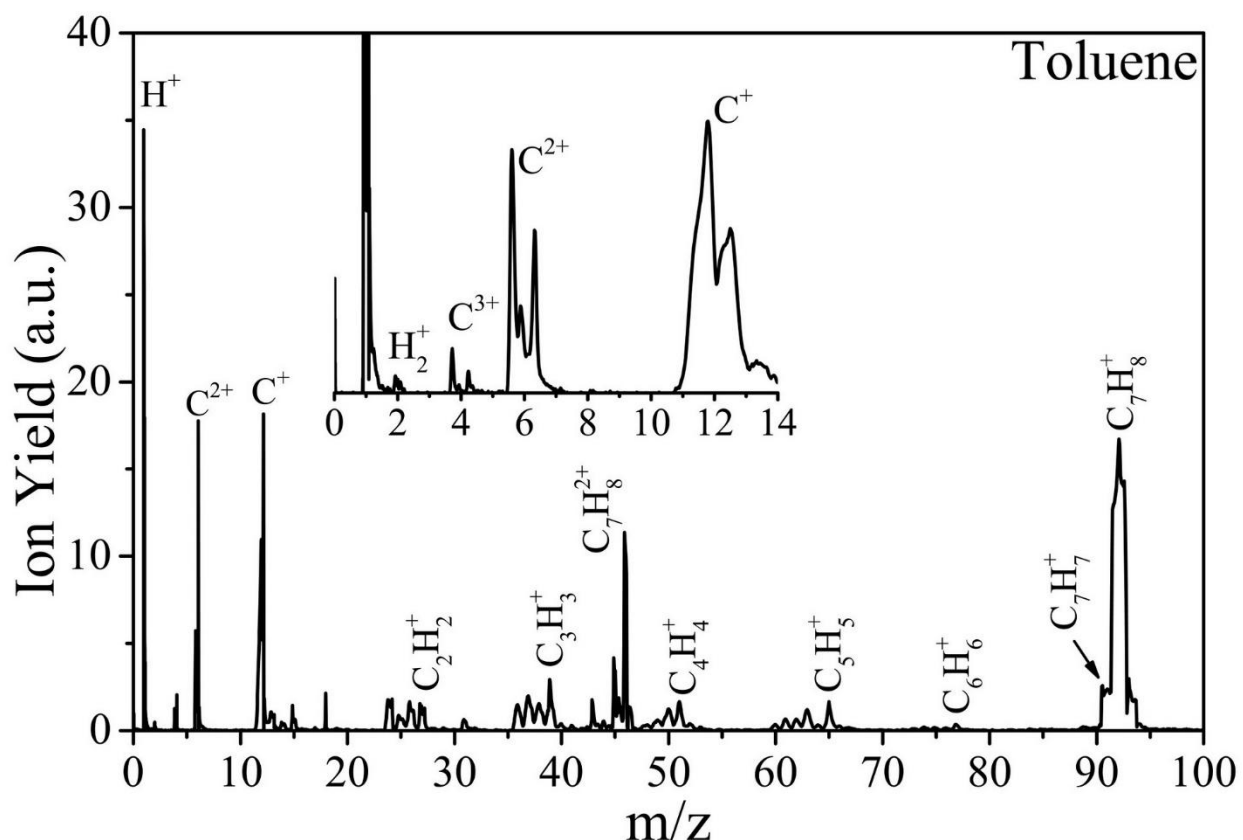


Figure 6.4 TOF mass spectrum for toluene. The inset in the spectrum shows magnified region over the small m/z fragments.

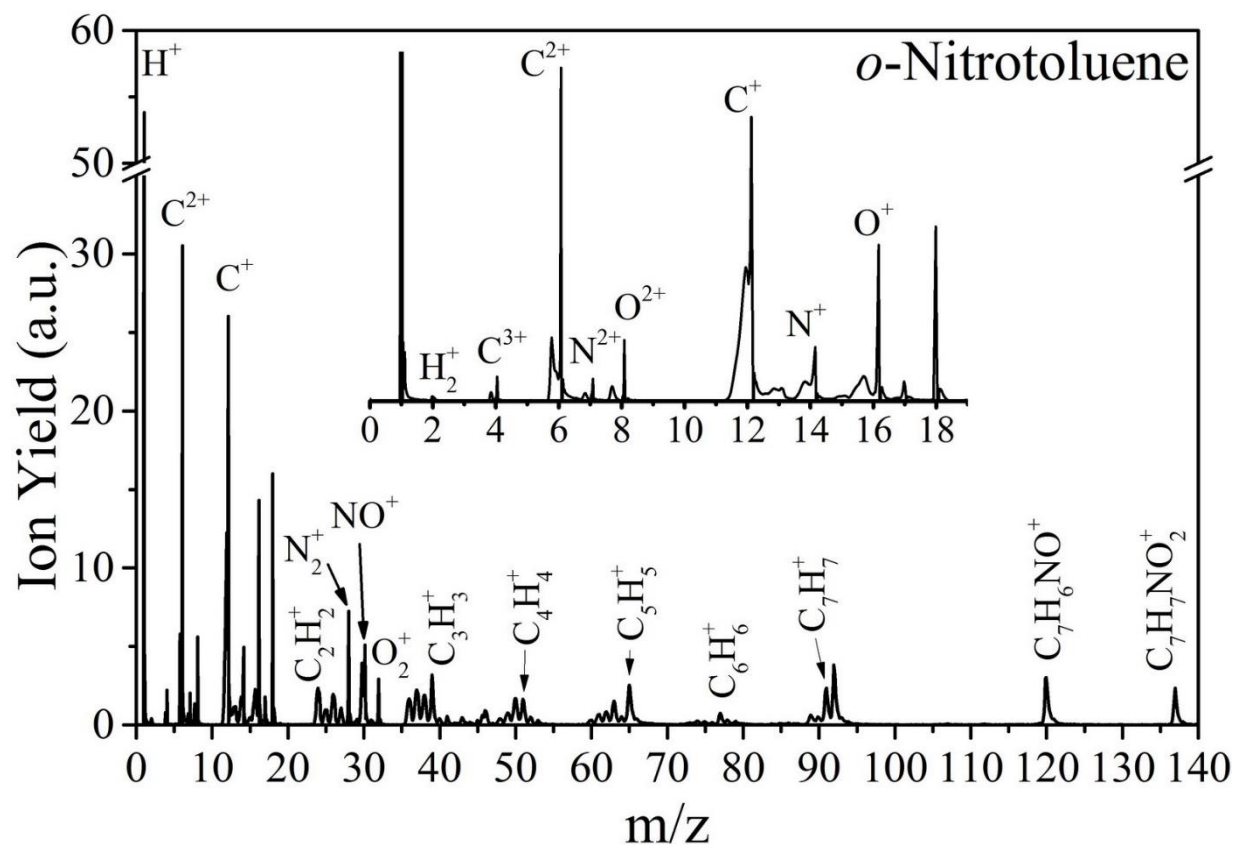


Figure 6.5 TOF mass spectrum for *o*-nitrotoluene. The inset shows magnified region over the small m/z fragments.

The main results are depicted in logarithmic spider plots in **Figure 6.6** for toluene and **Figure 6.7** for *o*-nitrotoluene. Based on this plotting scheme,²⁹³ where ion yields are normalized to yields obtained from TL pulses at the given intensity, the mass spectrum using TL pulses is represented as a unity circle. This allows one to determine the relative associated changes in the ion yields when using HOD pulses. Each of the spider plots represents the variations in the relative yield at a particular peak intensity.

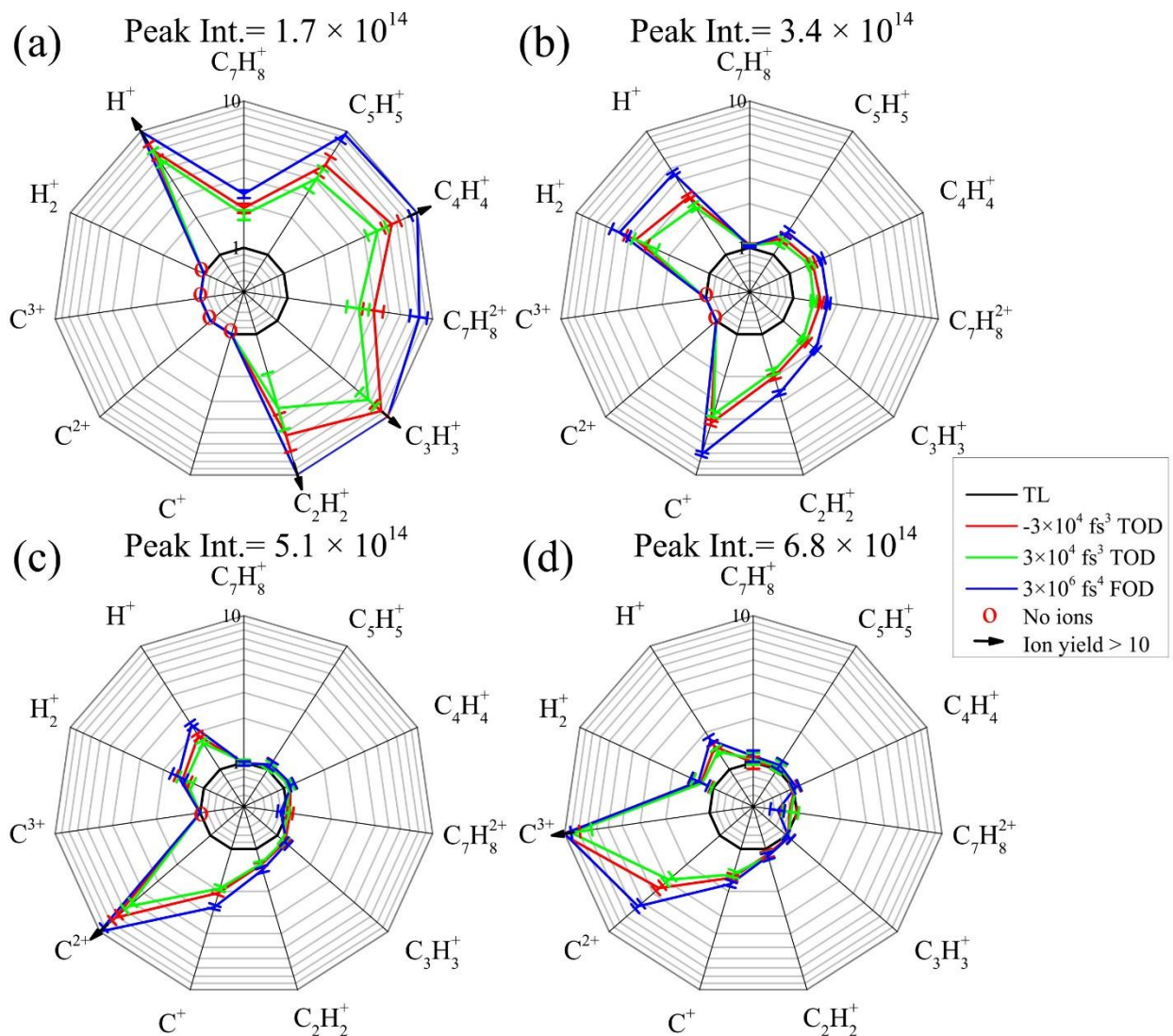


Figure 6.6 Spider plots on a logarithmic scale for the observed toluene fragment ions using FOD (blue), negative (red), and positive (green) TOD pulses compared to TL (black) pulses at (a) 1.7 , (b) 3.4 , (c) 5.1 , and (d) 6.8×10^{14} W/cm^2 peak intensity. The ion yield enhancements indicated by the black arrows using FOD are: in (a) for $\text{C}_4\text{H}_4^+ = 12.5 \pm 1.0$, $\text{C}_3\text{H}_3^+ = 18.4 \pm 1.6$, $\text{C}_2\text{H}_2^+ = 14.6 \pm 1.9$, and $\text{H}^+ = 20 \pm 2$. In (c) for $\text{C}^{2+} = 13.7 \pm 0.8$. In (d) for $\text{C}^{3+} = 16 \pm 1$.

At the lowest peak intensity (**Figure 6.5a**), one can clearly see yield enhancements resulting from HOD for all of the observed fragment ions, which are the H^+ ion and the heavy fragments. Note that at the lowest intensities some ions are not observed and those are marked by red dots. Comparing between negative (pre-pedestal) and positive (post-pedestal) TOD, slightly higher enhancement is observed for pulses with a pre-pedestal. In the case of FOD, symmetrical

pedestal, the ion yields were much higher than TL or TOD pulses. With respect to TL, FOD enhancement of several ions, exceeds an order of magnitude; which is represented by the small black arrows in **Figure 6.6a**. At higher peak intensities **Figure 6.6b-d**, the same trend is observed. The highest overall enhancement occurs when using FOD pulses, whereas negative TOD produces slightly more ions compared to positive TOD. The general enhancement pattern at different peak intensities can be summarized as follows: i. At any peak intensity the ions yield increases in the following order: TL < positive TOD < negative TOD < FOD. ii. At low peak intensity, the heavy fragments and H⁺ experience the greatest increase in yield. iii. At higher peak intensities, the lower m/z fragments (C⁺, C²⁺, C³⁺) are enhanced.

Similar behavior was observed for *o*-nitrotoluene as shown in the Spider plots in **Figure 6.7**. The general trend in the ion yields enhancement is similar to toluene. The highest observed ion yields were observed when using FOD pulses as well. Slight enhancement is observed for negative relative to positive TOD. The observed HOD enhancements are slightly lower than those noted in the case of toluene.

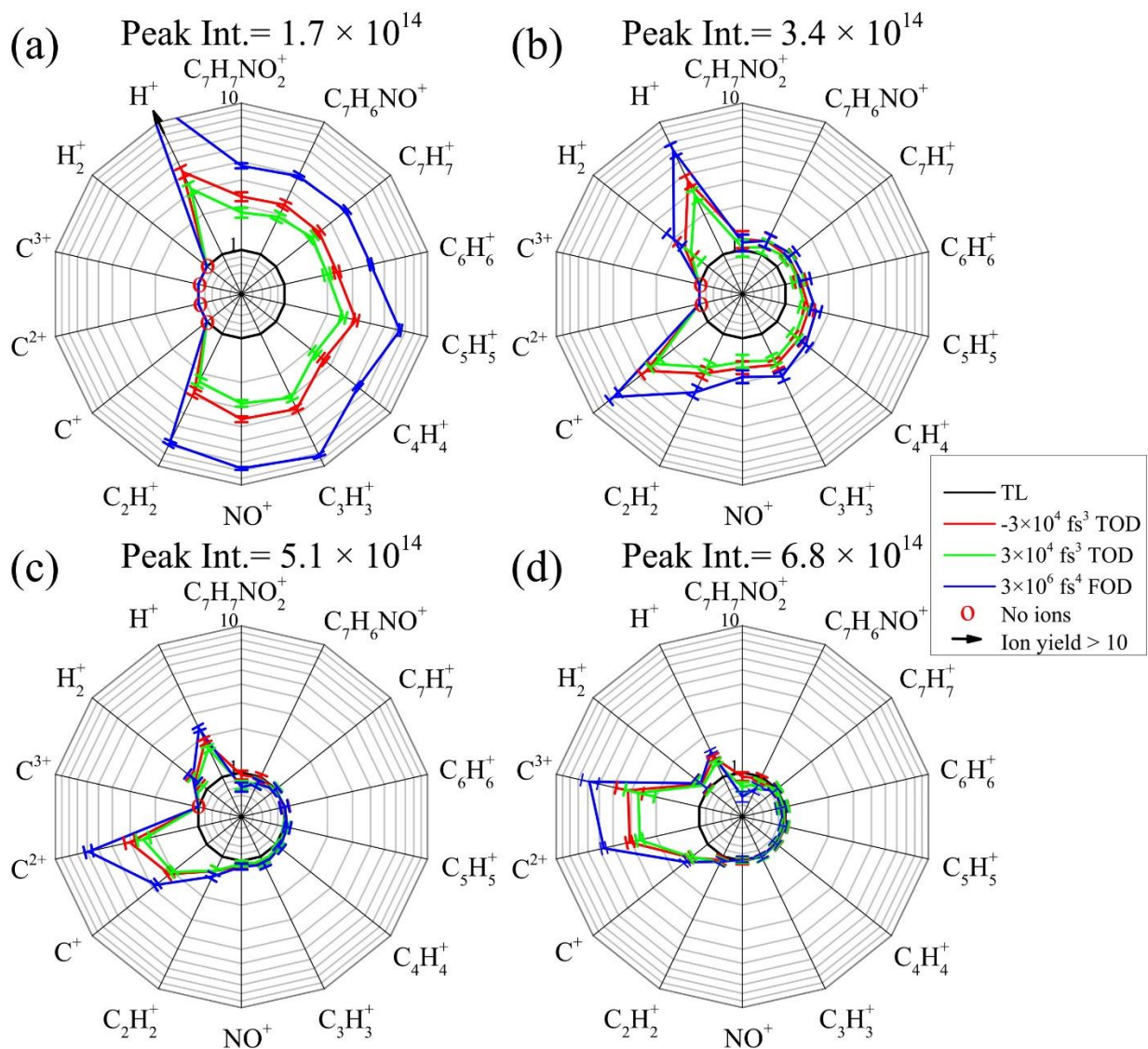


Figure 6.7 Spider plots on a logarithmic scale for the observed *o*-nitrotoluene fragment ions using FOD (blue), negative (red) and positive (green), TOD pulses compared to TL (black) pulses at (a) 1.7, (b) 3.4, (c) 5.1, and (d) 6.8×10^{14} W/cm² peak intensity. The ion yield enhancements indicated by the black arrows using FOD in (a) for $H^+ = 15.9 \pm 1.0$.

Similar experiments were carried out on a number of different molecules. The dissociative ionization of acetylene, methanol, methylene chloride, and acetonitrile showed, in general, similar ion yields enhancement as described for the larger molecules. Here we only show in detail results for acetylene in **Figure 6.8**. As for the other molecules, at low intensity factor-of-ten enhancement is observed for the parent ion. At higher intensities, the over an order-of-magnitude enhancement

is observed for C^{2+} , and, in the case of acetylene, for the doubly charged acetylene ion. Formation of acetylene dication, at mass-to-charge 13 is distinguished from the CH^+ fragment ion, based on the appearance of a small peak at mass-to-charge 13.5 corresponding to ^{13}C containing doubly charged acetylene ions with an intensity pattern that matches the relative natural abundance of the carbon isotope. Double ionization of acetylene requires ~ 32 eV, and its ground state is stable.²⁹⁴ Dissociative enhancement associated with HOD occurs with the smaller molecules at slightly higher intensities compared to the larger ones. Moreover, the proton ion yield enhancement (compared to TL at any given peak intensity) was also smaller and was found to increase in the following order: methylene chloride < acetonitrile < acetylene < methanol.

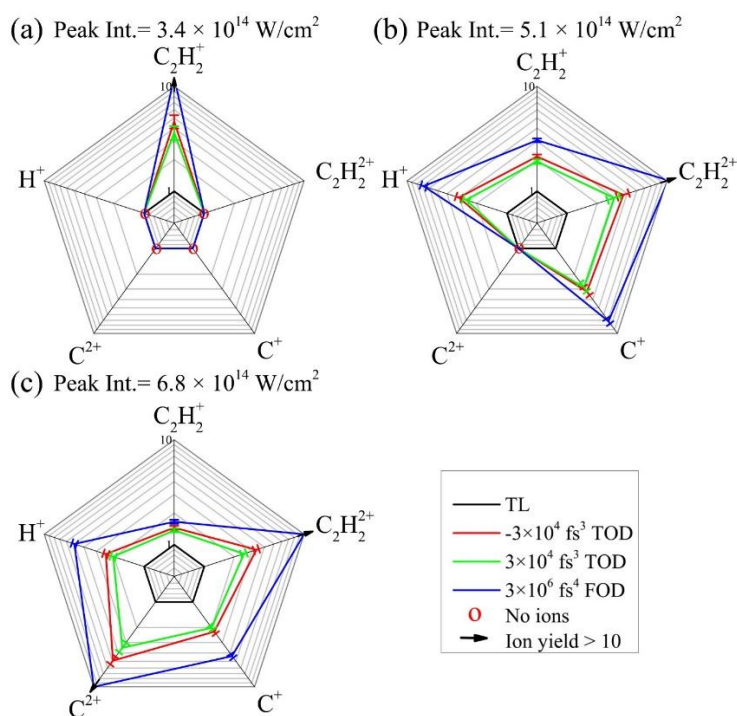


Figure 6.8 Spider plots on a logarithmic scale for the observed acetylene fragment ions using FOD (blue), negative (red), and positive (green) TOD pulses compared to TL (black) pulses at (a) 3.4 , (b) 5.1 , and (c) 6.8×10^{14} W/cm² peak intensity. The ion yield enhancements indicated by the black arrows using FOD are: in (a) for $C_2H_2^{2+} = 12.2 \pm 0.8$. In (b) for $C_2H_2^{2+} = 10.2 \pm 0.9$. In (c) for $C_2H_2^{2+} = 12.2 \pm 0.7$, and for $C^{2+} = 16.5 \pm 1.2$.

Kinetic energy release (KER) following dissociative ionization was obtained from the measured peak profiles for the light fragments, which appear as multiple separate components due to the fact that the forward Coulomb exploded fragments reach the detector at an earlier time compared to the backward ones (see Figure 3). From such peak profiles, the KER can be calculated according to the equation:²⁹⁵

$$KER(eV) = 9.65 \times 10^{-7} \frac{\Delta t^2 n^2 F^2}{8m} \quad (6.5)$$

where Δt is the separation time between the forward and backward peaks in nanoseconds, n is the charge, F is the DC extraction field in V/cm, and m is the atomic mass number. The KER distributions are obtained from the forward ion peaks in **Figure 6.9**, in order to circumvent the limited angular acceptance in the ion spectrometer over the energetic fragments. The calculated KER distributions was obtained at 6.8×10^{14} W/cm² for the forward peaks of H⁺, C³⁺, and C²⁺ from toluene and *o*-nitrotoluene while using vertically polarized beam (parallel to the flight tube and the detection axis). HOD increases the total ion yields as well as the KER distribution. This is observed both, regarding the cutoff KER and the most probable KER. A similar behavior is observed for C³⁺ and C²⁺.

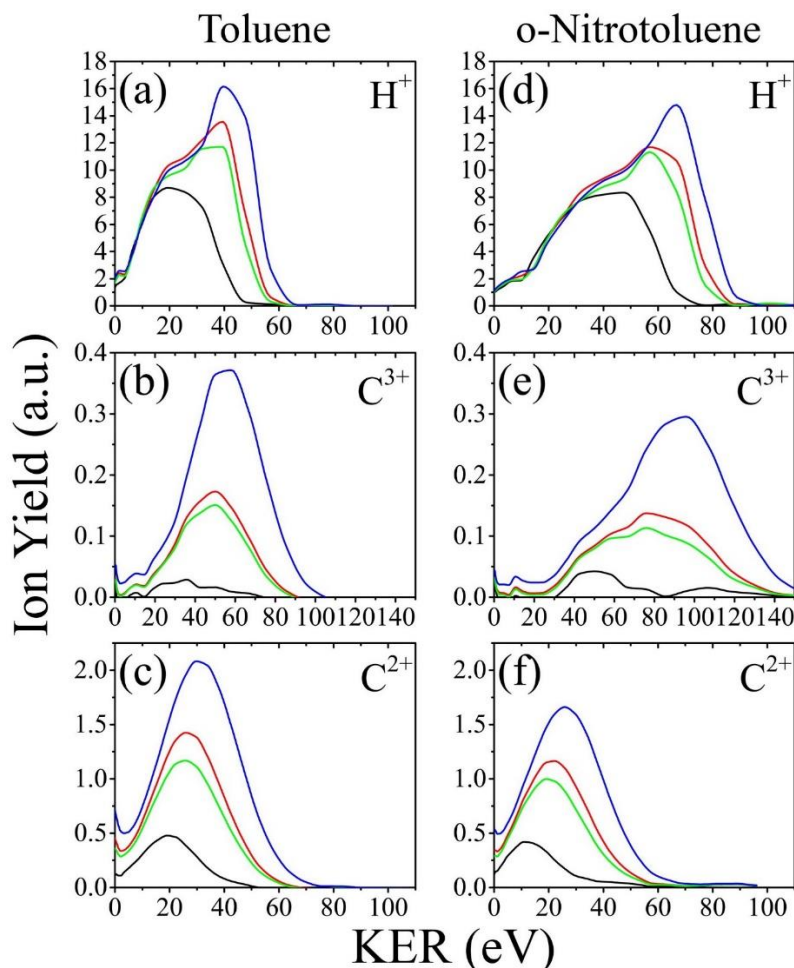


Figure 6.9 KER from (a-c) toluene and (d-f) *o*-nitrotoluene using TL (black), positive (green) and negative (red) TOD, and FOD (blue) pulses at 6.8×10^{14} W/cm² peak intensity.

Similar increase in the KER of H⁺, C²⁺, and C⁺ was found for acetylene (**Figure 6.10**), and for the other smaller molecules. The increase in KER associated with the presence of HOD indicates greater accumulation of charge prior to Coulomb explosion. The increase in both of the total amount of fragments and their KER indicates a significant role for the pedestal in the dissociation mechanism. The KER cut-off values from acetylene and the other small molecules were smaller than those observed for the larger molecules. The KER increase appears to depend on the number of charges that can be accumulated prior to Coulomb explosion, as discussed below.

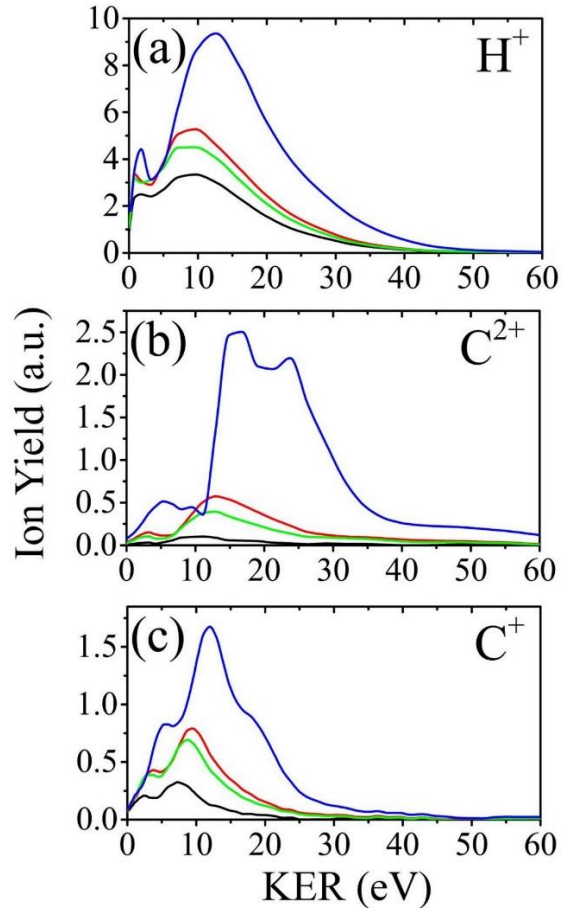


Figure 6.10 KER from acetylene using TL (black), positive (green) and negative (red) TOD, and FOD (blue) pulses at $6.8 \times 10^{14} \text{ W/cm}^2$ peak intensity.

6.4 Discussion

To understand the underlying mechanism behind the observed yield and KER enhancements reported for pulses with HOD, we draw from previous findings in the strong field ionization literature. Ionization processes are highly dependent on the relative orientation of the molecule and the laser polarization axis.²⁹⁶ Pulses with negative TOD have been implemented to increase the dissociation yield of H_2^+ ⁵⁹ by means of using the pedestal to induce nonadiabatic alignment of the molecule. Such a mechanism is feasible in the case of small diatomic molecules, where the rotational constant supports fast rotation within the timescale of the pedestal. In the current work with large molecules, the rotational constants are associated with a rotational motion that is two orders of magnitude slower. Therefore, it is unlikely that significant alignment is induced by the pre-pedestal. Moreover, one would expect to have a greater difference between negative and positive TOD, whereas only slight enhancement was observed in the favor of negative TOD.

It has been shown that when the molecular bonds get stretched to a certain critical internuclear distance "bond softening", ionization cross section reaches a peak rate that is orders of magnitude larger than at the equilibrium internuclear distance.²⁹⁷ This process is also known as enhanced ionization and is attributed mainly to the nonadiabatic electron density localization near the nuclei after bond stretching. The enhanced ionization mechanism has been used to explain the ejection of energetic H^+ from polyatomic hydrocarbons due to the accumulation of a highly charged parent ion.²⁷² With increasing molecular size, bond softening can occur at multiple C-H bonds simultaneously, leading to a highly charged state with strong Coulomb repulsion forces. The highly charged state mechanism, in which all the H^+ fragments are ejected at once in a concerted fashion, has been demonstrated in the framework of time-dependent Hartree-Fock²⁹⁸ and time-dependent density functional theories.²⁹⁹⁻³⁰⁰ In our current work, the ejection of energetic H^+ can

be explained to take place following a similar mechanism, which is supported by the increased KER values with accordance to the molecular size.

TOD and FOD pulses are associated with the presence of pedestals along with a slight increase in the pulse duration. An increase in the yield of energetic H^+ ejection from molecules has been observed to occur at constant intensity with longer pulse durations.²⁸¹ The observation was attributed to the necessity to populate the precursor's highly charged states through which multiple C-H stretching and softening can occur, followed by the concerted Coulomb explosion. However, the currently observed enhancement, both in terms of yield and kinetic energy, is attributed mainly to the pulse pedestals. We confirm this assertion by plotting changes in the ion yields when employing TL pulses with durations that are similar to that of the TOD and FOD. Such changes were much smaller than those found for TOD and FOD pulses (**Figure 6.11**).

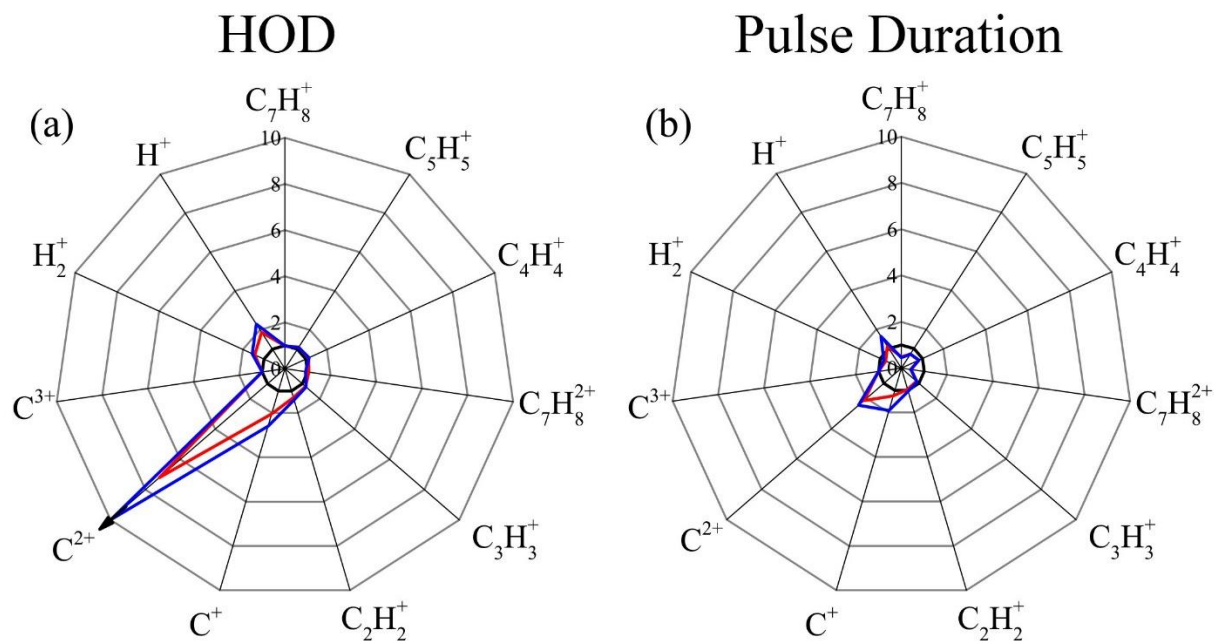


Figure 6.11 (a) Ion yield enhancement from toluene at $5.1 \times 10^{14} \text{ W/cm}^2$ normalized with respect to the yield of 36 fs TL pulses (black unity circle at 1) when using negative TOD (red) and FOD (blue). (b) The same normalized comparison with respect to 36 fs TL pulses when using 48 fs TL pulses (red) and 64 fs TL pulses (blue).

The higher KER values are consistent with HOD pedestals leading to highly charged precursors prior to Coulomb explosion. Here we suggest that pre-ionization is important to reach higher charge densities. To evaluate this hypothesis, we recorded the ion yields from toluene and *o*-nitrotoluene as a function of laser peak intensity using TL pulses as shown in **Figure 6.12**. For both molecules, it can be seen that molecular ionization starts at 10^{14} W/cm² and saturates soon after. Pre-ionization is also expected to enhanced electron density localization near the nuclei.

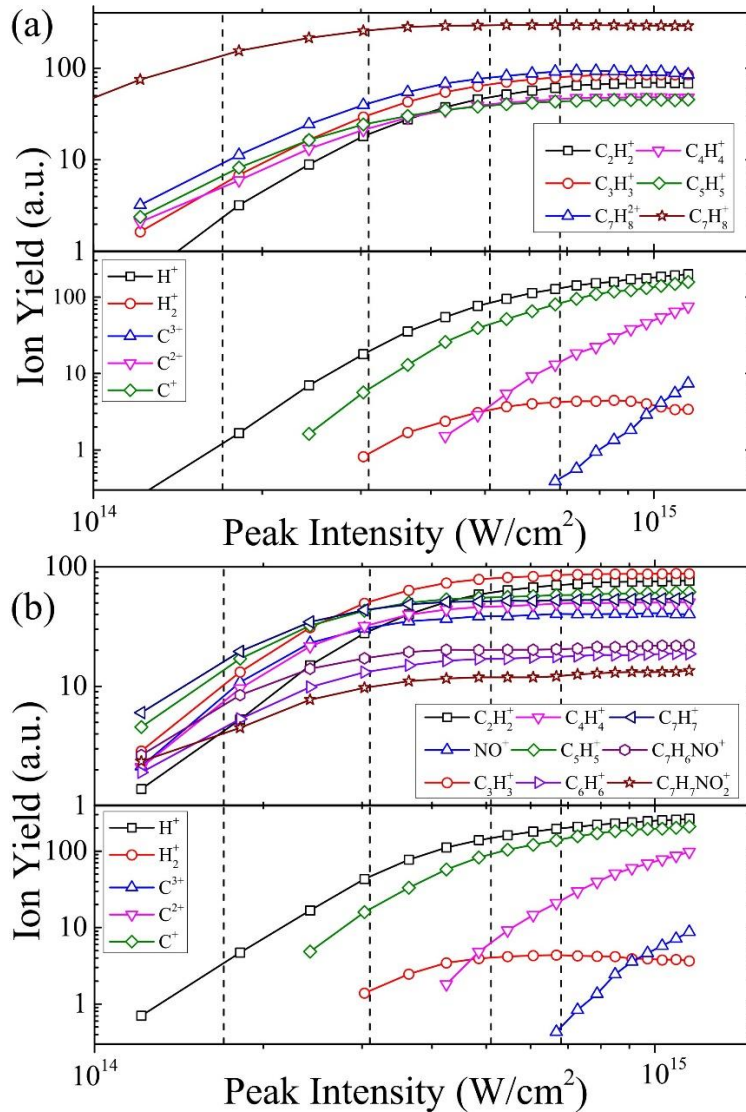


Figure 6.12 Ion yield as a function of peak intensity for (a) toluene and (b) *o*-nitrotoluene on a double-log scale. Vertical lines indicate the peak intensities at which the HOD pulses were used.

Taking pre-alignment, bond softening, and pre-ionization into account, we were surprised that we do not see larger differences between negative and positive TOD. We expected a greater difference. In the search for that difference, we carried out pump-probe experiments by generating a weak long pulse (~100-200 fs) and a stronger (~10 times more intense) short pulse (50 fs). However, the ion yield differences were slightly higher when the long pulse precedes the short one, which is similar to the negative TOD enhancement compared to positive TOD. We also evaluated fifth-order dispersion pulses that closely matched the pedestal of the FOD pulses and again failed to see large differences between positive and negative fifth order dispersion. Our findings show that FOD, which is time symmetric, produced the highest ion yields and KER values. From which it can be surmised that even a lagging pedestal is effective. Therefore, we propose our results require we consider a process known as cascaded ionization.³⁰¹⁻³⁰² We envision that at the intensities being studied, a number of electrons move in response to the field, the cascaded hopping of electrons within these large molecules leads to the creation of highly charged ions such as C^{3+} , and their emission along the polarization direction of the laser pulses.

6.5 Conclusion

The dissociative ionization of a number of molecules including acetylene, methanol, methylene chloride, acetonitrile, toluene and *o*-nitrotoluene following interaction with intense laser pulses in the presence and absence of high order dispersion have been explored in this chapter. We find that both third- and fourth-order dispersion leads to an order of magnitude increases in the yield of fragment ions and that these enhancements are accompanied by a factor of three increase in the kinetic energy release of these ions; a factor of two increase for the smaller molecules. Comparison between pulses with pre- and post-pedestals found relatively small differences, implying that mechanisms such as pre-alignment, pre-ionization, and bond softening appear to play a relatively small role in explaining our results. We invoke a cascaded ionization process, in which multiple electrons hop within the molecule causing highly charged species. Once the electron cloud forms, it creates a localized plasma that is highly susceptible to the laser field and hence to the trailing pulse pedestal. This explanation is consistent with the detection of highly charged species such as C^{3+} emitted along the laser polarization axis, the minuscule difference between pre- and post-pedestal pulses, and the molecular size dependence. We have found that the effects are greater for larger molecules. Future work will focus on molecular properties that enhance our findings. Similarly, we will explore the use of differently shaped pulses that may best take advantage of cascaded ionization. In particular, we are eager to explore stretched square pulses that offer fast initial ionization and maintain the field intensity constant until the end of the pulse.³⁰³ Through collaborations, we hope to explore time-dependent theoretical simulation of our results and coincidence measurements that will further clarify the processes leading to high-energy highly charged particles.

Chapter 7 Summary and Future Outlook

The work presented in this thesis is a continuation of an endless effort from the Dantus research group to use femtosecond laser pulses to understand control laser-matter interaction. The work that is described here in particular focuses on mainly on how to use shaped pulses to understand and control excited state dynamics of molecules. Chapter 2 focused on unraveling the dynamical steps that are associated in ESPT from protic solvents to a Schiff base known as FR0-SB. The use of single beam shaped pulses to reveal dynamical information for cyanine dyes with various substituents as well as the effect of protein pocket on the dynamics of cyanines are described in Chapters 3 and 4. Lastly, shaped femtosecond pulses have been used to control energy transfer and the population of higher excited state in cyanines in Chapter 5 as well as the ionization yield and KER of polyatomic molecules using pulses with HOD.

In the following subsection a future perspective is given for two major areas that have been investigated in this thesis.

7.1 Photobases and Proton Transfer Dynamics

The amount of literature that is known about photobases is still scarce and limited relative to what is known about photoacids. With the given photobase in hand, further steady-state and time-resolved studies can be carried out to address proton transfer dynamics from non-alcoholic solvents as the studies presented here were limited to small alcohols.

The kinetic and steric factors can also be addressed and how would they be related to the observed proton transfer dynamics as in the studied alcohols, mainly MeOH and EtOH, the time-resolved intermediate formation was limited by the dielectric solvent relaxation constant and this was also reflected in the observed final equilibrium between the protonated and nonprotonated forms of FR0-SB after excitation. However, early results show large differences in ESPT when comparing *n*-propanol with *iso*-propanol, which hints towards the importance of steric factors in abstracting the proton and solvating the negatively charged alkoxide moiety without further geminate recombination.

Further studies can be also carried out on similar Schiff bases that are bound inside specifically designed protein systems in which the protons are placed at targeted amino acids allowing ESPT to occur from those protons while shielding the photobase environment.

7.2 Controlling Energy Transfer in Cyanines

In this thesis a powerful control scheme is proposed in Chapter 5 in which excitation to higher excited state can couple the system between the higher excited state and the ground state in which internal conversion to lower excited state.

In the demonstrated control the S_2 state was populated directly with a one photon transition using shaped pulses. Further studies could make use of using lower frequency photons to reach the excited state using a multiphoton transition while modulating the phase of the excitation pulse, in a particular the use of sinusoidal and pi-step phases which were demonstrated as strong tools to specifically enhance targeted multiphoton transitions. Early unpublished results from our group on the same molecular system (IR144) while using infrared pulses that are centered around 1070 nm with a sinusoidal phase demonstrate the applicability of this approach to modulate the relative emissions between S_2 and S_1 states.

The control scheme can be also applied to molecular systems in which the reaction can be initiated from a higher excited state with better efficiency than a lower excited state. Such as energy transfer from the S_2 state in carotenoids to the chlorophyll Qx band in light harvesting complexes. Or in specifically designed dual chromophores that can trigger a fluorophore release from a higher excited state.³⁰⁴

APPENDIX

List of Publications

- (1) Ghanbarpour, A.; **Nairat, M.**; Nosrati, M.; Santos, E. M.; Vasileiou, C.; Dantus, M.; Borhan, B.; Geiger, J. H., Mimicking microbial rhodopsin isomerization in a single crystal. *J. Am. Chem. Soc.* **2018**, *submitted*.
- (2) Ekanayake, N.; **Nairat, M.**; Weingartz, N. P.; Michie, M. J.; Levine, B. G.; Dantus, M., Substituent effects on H_3^+ formation via H_2 roaming mechanisms under strong-field photodissociation of organic molecules. *J. Chem. Phys.* **2018**, *in press*.
- (3) Ekanayake, N.; Severt, T.; **Nairat, M.**; Weingartz, N.; Farris, B.; Kaderiya, B.; Feizollah, P.; Jochim, B.; Ziaee, F.; Borne, K.; P., K. R.; Carnes, K. D.; Rolles, D.; Rudenko, A.; Levine, B. G.; Jackson, J. E.; Ben-Itzhak, I.; Dantus, M., H_2 roaming chemistry and the formation of H_3^+ from organic molecules in strong laser fields. *Nat. Commun.* **2018**, *9*, 5168.
- (4) Sheng, W.*; **Nairat, M.***; Pawlaczyk, P. D.; Mroccka, E.; Farris, B.; Pines, E.; Geiger, J. H.; Borhan, B.; Dantus, M., Ultrafast Dynamics of a “Super” Photobase. *Angew. Chem. Int. Ed.* **2018**, *57*, 14742-14746. **equal contribution*
- (5) Rasskazov, G.; **Nairat, M.**; Magoulas, I.; Lozovoy, V. V.; Piecuch, P.; Dantus, M., Femtosecond real-time probing of reactions MMXVII: The predissociation of sodium iodide in the A 0+ state. *Chem. Phys. Lett.* **2017**, *683*, 121-127.
- (6) **Nairat, M.**; Webb, M.; Esch, M. P.; Lozovoy, V. V.; Levine, B. G.; Dantus, M., Time-resolved signatures across the intramolecular response in substituted cyanine dyes. *Phys. Chem. Chem. Phys.* **2017**, *19*, 14085-14095.
- (7) Lozovoy, V. V.; **Nairat, M.**; Dantus, M., Binary-phase compression of stretched pulses. *J. Opt.* **2017**, *19*, 105506.
- (8) Ekanayake, N.; **Nairat, M.**; Kaderiya, B.; Feizollah, P.; Jochim, B.; Severt, T.; Berry, B.; Pandiri, K. R.; Carnes, K. D.; Pathak, S.; Rolles, D.; Rudenko, A.; Ben-Itzhak, I.; Mancuso, C. A.; Fales, B. S.; Jackson, J. E.; Levine, B. G.; Dantus, M., Mechanisms and time-resolved dynamics for trihydrogen cation (H_3^+) formation from organic molecules in strong laser fields. *Sci. Rep.* **2017**, *7*, 4703.
- (9) **Nairat, M.**; Lozovoy, V. V.; Dantus, M., Order of Magnitude Dissociative Ionization Enhancement Observed for Pulses with High Order Dispersion. *J. Phys Chem. A* **2016**, *120*, 8529-8536.
- (10) **Nairat, M.**; Konar, A.; Lozovoy, V. V.; Beck, W. F.; Blanchard, G. J.; Dantus, M., Controlling S_2 Population in Cyanine Dyes Using Shaped Femtosecond Pulses. *J. Phys. Chem. A* **2016**, *120*, 1876-1885.

(11) **Nairat, M.**; Konar, A.; Kaniecki, M.; Lozovoy, V. V.; Dantus, M., Investigating the Role of Human Serum Albumin Protein Pocket on the Excited State Dynamics of Indocyanine Green Using Shaped Femtosecond Laser Pulses. *Phys. Chem. Chem. Phys.* **2015**, *17*, 5872-5877.

BIBLIOGRAPHY

BIBLIOGRAPHY

- (1) Dantus, M.; Rosker, M. J.; Zewail, A. H., Real-time femtosecond probing of “transition states” in chemical reactions. *J. Chem. Phys.* **1987**, *87*, 2395-2397.
- (2) Shank, C. V., Investigation of Ultrafast Phenomena in the Femtosecond Time Domain. *Science* **1986**, *233*, 1276-1280.
- (3) Zewail, A. H., Femtochemistry: Atomic-Scale Dynamics of the Chemical Bond. *The Journal of Physical Chemistry A* **2000**, *104*, 5660-5694.
- (4) Rosker, M. J.; Dantus, M.; Zewail, A. H., Femtosecond real-time probing of reactions. I. The technique. *J. Chem. Phys.* **1988**, *89*, 6113-6127.
- (5) Stolow, A., FEMTOSECOND TIME-RESOLVED PHOTOELECTRON SPECTROSCOPY OF POLYATOMIC MOLECULES. *Annual Review of Physical Chemistry* **2003**, *54*, 89-119.
- (6) Nibbering, E. T. J.; Fidler, H.; Pines, E., ULTRAFAST CHEMISTRY: Using Time-Resolved Vibrational Spectroscopy for Interrogation of Structural Dynamics. *Annual Review of Physical Chemistry* **2004**, *56*, 337-367.
- (7) Berera, R.; van Grondelle, R.; Kennis, J. T. M., Ultrafast transient absorption spectroscopy: principles and application to photosynthetic systems. *Photosynthesis research* **2009**, *101*, 105-118.
- (8) Rosspeintner, A.; Lang, B.; Vauthey, E., Ultrafast Photochemistry in Liquids. *Annu. Rev. Phys. Chem.* **2013**, *64*, 247-271.
- (9) Ultrafast Processes in Chemistry. *Chemical Reviews* **2017**, *117*, 10621-11124.
- (10) Brumer, P.; Shapiro, M., Control of unimolecular reactions using coherent light. *Chemical Physics Letters* **1986**, *126*, 541-546.
- (11) Weiner, A. M., Femtosecond Pulse Shaping Using Spatial Light Modulators. *Rev. Sci. Instrum.* **2000**, *71*, 1929-1960.
- (12) Rose, T. S.; Rosker, M. J.; Zewail, A. H., Femtosecond real-time observation of wave packet oscillations (resonance) in dissociation reactions. *J. Chem. Phys.* **1988**, *88*, 6672-6673.
- (13) Dantus, M.; Bowman, R. M.; Zewail, A. H., Femtosecond Laser Observations of Molecular Vibration and Rotation. *Nature* **1990**, *343*, 737.

- (14) Diels, J.-C.; Rudolph, W., Measurement Techniques of Femtosecond Spectroscopy. In *Ultrashort Laser Pulse Phenomena (Second Edition)*, Diels, J.-C.; Rudolph, W., Eds. Academic Press: Burlington, 2006; pp 491-530.
- (15) Sundström, V., Femtobiology. *Annual Review of Physical Chemistry* **2008**, *59*, 53-77.
- (16) Cerullo, G.; Manzoni, C.; Lüer, L.; Polli, D., Time-resolved methods in biophysics. 4. Broadband pump-probe spectroscopy system with sub-20 fs temporal resolution for the study of energy transfer processes in photosynthesis. *Photochemical & Photobiological Sciences* **2007**, *6*, 135-144.
- (17) Dantus, M.; Zewail, A., Introduction: Femtochemistry. *Chemical Reviews* **2004**, *104*, 1717-2124.
- (18) Joo, T.; Jia, Y.; Yu, J. Y.; Lang, M. J.; Fleming, G. R., Third-order nonlinear time domain probes of solvation dynamics. *The Journal of Chemical Physics* **1996**, *104*, 6089-6108.
- (19) Ruckebusch, C.; Sliwa, M.; Pernot, P.; de Juan, A.; Tauler, R., Comprehensive data analysis of femtosecond transient absorption spectra: A review. *Journal of Photochemistry and Photobiology C: Photochemistry Reviews* **2012**, *13*, 1-27.
- (20) Mukamel, S., *Principles of Nonlinear Optical Spectroscopy*. Oxford University Press: New York, 1995.
- (21) Nuernberger, P.; Ruetzel, S.; Brixner, T., Multidimensional Electronic Spectroscopy of Photochemical Reactions. *Angew. Chem. Int. Ed.* **2015**, *54*, 11368-11386.
- (22) Antoine, M.; Sébastien, W.; Béatrice, C., A newcomer's guide to ultrashort pulse shaping and characterization. *Journal of Physics B: Atomic, Molecular and Optical Physics* **2010**, *43*, 103001.
- (23) Weiner, A. M., Femtosecond pulse shaping using spatial light modulators. *Rev. Sci. Instr.* **2000**, *71*, 1929-1960.
- (24) Trebino, R.; DeLong, K. W.; Fittinghoff, D. N.; Sweetser, J. N.; Krumbügel, M. A.; Richman, B. A.; Kane, D. J., Measuring ultrashort laser pulses in the time-frequency domain using frequency-resolved optical gating. *Review of Scientific Instruments* **1997**, *68*, 3277-3295.
- (25) Iaconis, C.; Walmsley, I. A., Spectral phase interferometry for direct electric-field reconstruction of ultrashort optical pulses. *Opt. Lett.* **1998**, *23*, 792-794.
- (26) Yelin, D.; Meshulach, D.; Silberberg, Y., Adaptive femtosecond pulse compression. *Opt. Lett.* **1997**, *22*, 1793-1795.

- (27) Meshulach, D.; Yelin, D.; Silberberg, Y., Adaptive real-time femtosecond pulse shaping. *J. Opt. Soc. Am. B* **1998**, *15*, 1615-1619.
- (28) Bardeen, C. J.; Yakovlev, V. V.; Wilson, K. R.; Carpenter, S. D.; Weber, P. M.; Warren, W. S., Feedback quantum control of molecular electronic population transfer. *Chemical Physics Letters* **1997**, *280*, 151-158.
- (29) Lozovoy, V. V.; Pastirk, I.; Dantus, M., Multiphoton Intrapulse Interference. IV. Ultrashort Laser Pulse Spectral Phase Characterization and Compensation. *Opt. Lett.* **2004**, *29*, 775-7.
- (30) Coello, Y.; Lozovoy, V. V.; Gunaratne, T. C.; Xu, B.; Borukhovich, I.; Tseng, C.-h.; Weinacht, T.; Dantus, M., Interference Without an Interferometer: a Different Approach to Measuring, Compressing, and Shaping Ultrashort Laser Pulses. *J. Opt. Soc. Am. B* **2008**, *25*, A140-A150.
- (31) Lozovoy, V. V.; Xu, B.; Coello, Y.; Dantus, M., Direct measurement of spectral phase for ultrashort laser pulses. *Opt. Express* **2008**, *16*, 592-597.
- (32) Dela Cruz, J. M.; Lozovoy, V. V.; Dantus, M., Coherent control improves biomedical imaging with ultrashort shaped pulses. *Journal of Photochemistry and Photobiology A: Chemistry* **2006**, *180*, 307-313.
- (33) Lozovoy, V. V.; Pastirk, I.; Walowicz, K. A.; Dantus, M., Multiphoton intrapulse interference. II. Control of two- and three-photon laser induced fluorescence with shaped pulses. *J. Chem. Phys.* **2003**, *118*, 3187-3196.
- (34) Walowicz, K. A.; Pastirk, I.; Lozovoy, V. V.; Dantus, M., Multiphoton Intrapulse Interference. 1. Control of Multiphoton Processes in Condensed Phases. *J. Phys. Chem. A* **2002**, *106*, 9369-9373.
- (35) Dela Cruz, J. M.; Lozovoy, V. V.; Dantus, M., Quantitative Mass Spectrometric Identification of Isomers Applying Coherent Laser Control. *The Journal of Physical Chemistry A* **2005**, *109*, 8447-8450.
- (36) Li, H.; Harris, D. A.; Xu, B.; Wrzesinski, P. J.; Lozovoy, V. V.; Dantus, M., Standoff and arms-length detection of chemicals with single-beam coherent anti-Stokes Raman scattering. *Applied Optics* **2009**, *48*, B17-B22.
- (37) Konar, A.; Lozovoy, V. V.; Dantus, M., Solvation Stokes-Shift Dynamics Studied by Chirped Femtosecond Laser Pulses. *J. Phys. Chem. Lett.* **2012**, *3*, 2458-2464.
- (38) Konar, A.; Lozovoy, V. V.; Dantus, M., Solvent Environment Revealed by Positively Chirped Pulses. *J. Phys. Chem. Lett.* **2014**, *5*, 924-928.

- (39) Weiner, A. M.; Leaird, D. E.; Wiederrecht, G. P.; Nelson, K. A., Femtosecond Pulse Sequences Used for Optical Manipulation of Molecular Motion. *Science* **1990**, *247*, 1317-1319.
- (40) Heritage, J. P.; Weiner, A. M.; Thurston, R. N., Picosecond pulse shaping by spectral phase and amplitude manipulation. *Opt. Lett.* **1985**, *10*, 609-11.
- (41) Grumstrup, E. M.; Shim, S.-H.; Montgomery, M. A.; Damrauer, N. H.; Zanni, M. T., Facile collection of two-dimensional electronic spectra using femtosecond pulse-shaping technology. *Opt. Express* **2007**, *15*, 16681-16689.
- (42) Nibbering, E. T. J.; Wiersma, D. A.; Duppen, K., Ultrafast nonlinear spectroscopy with chirped optical pulses. *Phys. Rev. Lett.* **1992**, *68*, 514-517.
- (43) Gordon, R. J.; Rice, S. A., ACTIVE CONTROL OF THE DYNAMICS OF ATOMS AND MOLECULES. *Annual Review of Physical Chemistry* **1997**, *48*, 601-641.
- (44) Dantus, M.; Lozovoy, V. V., Experimental Coherent Laser Control of Physicochemical Processes. *Chem. Rev.* **2004**, *104*, 1813-1860.
- (45) Brinks, D.; Stefani, F. D.; Kulzer, F.; Hildner, R.; Taminiau, T. H.; Avlasevich, Y.; Mullen, K.; van Hulst, N. F., Visualizing and controlling vibrational wave packets of single molecules. *Nature* **2010**, *465*, 905-908.
- (46) Hildner, R.; Brinks, D.; Nieder, J. B.; Cogdell, R. J.; van Hulst, N. F., Quantum Coherent Energy Transfer over Varying Pathways in Single Light-Harvesting Complexes. *Science* **2013**, *340*, 1448-1451.
- (47) Brinks, D.; Hildner, R.; van Dijk, E. M. H. P.; Stefani, F. D.; Nieder, J. B.; Hernando, J.; van Hulst, N. F., Ultrafast dynamics of single molecules. *Chem. Soc. Rev.* **2014**, *43*, 2476-2491.
- (48) Cerullo, G.; Bardeen, C. J.; Wang, Q.; Shank, C. V., High-Power Femtosecond Chirped Pulse Excitation of Molecules in Solution. *Chem. Phys. Lett.* **1996**, *262*, 362-368.
- (49) Malkmus, S.; Dürr, R.; Sobotta, C.; Pulvermacher, H.; Zinth, W.; Braun, M., Chirp Dependence of Wave Packet Motion in Oxazine 1. *The Journal of Physical Chemistry A* **2005**, *109*, 10488-10492.
- (50) Ruetzel, S.; Diekmann, M.; Nuernberger, P.; Walter, C.; Engels, B.; Brixner, T., Multidimensional spectroscopy of photoreactivity. *Proceedings of the National Academy of Sciences* **2014**, *111*, 4764-4769.
- (51) Consani, C.; Ruetzel, S.; Nuernberger, P.; Brixner, T., Quantum Control Spectroscopy of Competing Reaction Pathways in a Molecular Switch. *J. Phys. Chem. A* **2014**, *118*, 11364-11372.

- (52) Shim, S.-H.; Zanni, M. T., How to turn your pump-probe instrument into a multidimensional spectrometer: 2D IR and Vis spectroscopies via pulse shaping. *Phys. Chem. Chem. Phys.* **2009**, *11*, 748-761.
- (53) Meshulach, D.; Silberberg, Y., Coherent quantum control of multiphoton transitions by shaped ultrashort optical pulses. *Physical Review A* **1999**, *60*, 1287-1292.
- (54) Meshulach, D.; Silberberg, Y., Coherent quantum control of two-photon transitions by a femtosecond laser pulse. *Nature* **1998**, *396*, 239.
- (55) Zhu, L.; Kleiman, V.; Li, X.; Lu, S. P.; Trentelman, K.; Gordon, R. J., Coherent Laser Control of the Product Distribution Obtained in the Photoexcitation of HI. *Science* **1995**, *270*, 77-80.
- (56) Judson, R. S.; Rabitz, H., Teaching lasers to control molecules. *Phys. Rev. Lett.* **1992**, *68*, 1500-1503.
- (57) Walowicz, K. A.; Pastirk, I.; Lozovoy, V. V.; Dantus, M., Multiphoton Intrapulse Interference. 1. Control of Multiphoton Processes in Condensed Phases. *J. Phys. Chem. A* **2002**, *106*, 9369-9373.
- (58) Cao, J. S.; Bardeen, C. J.; Wilson, K. R., Molecular "pi pulse" for total inversion of electronic state population. *Phys. Rev. Lett.* **1998**, *80*, 1406-1409.
- (59) Lev, U.; Graham, L.; Madsen, C. B.; Ben-Itzhak, I.; Bruner, B. D.; Esry, B. D.; Frostig, H.; Heber, O.; Natan, A.; Prabhudesai, V. S.; Schwalm, D.; Silberberg, Y.; Strasser, D.; Williams, I. D.; Zajfman, D., Quantum Control of Photodissociation using Intense, Femtosecond Pulses Shaped with Third Order Dispersion. *J. Phys. B At. Mol. Opt. Phys.* **2015**, *48*, 201001.
- (60) Li, H.; Harris, D. A.; Xu, B.; Wrzesinski, P. J.; Lozovoy, V. V.; Dantus, M., Coherent mode-selective Raman excitation towards standoff detection. *Opt. Express* **2008**, *16*, 5499-5504.
- (61) James T. Hynes; Klinman, P. J. P.; Limbach, H.-H.; Schowen, R. L., Hydrogen-Transfer Reactions. Wiley-VCH Verlag GmbH & Co. KGaA: 2007.
- (62) Förster, T., Die pH-Abhängigkeit der Fluoreszenz von Naphthalinderivaten. *Z. Elektrochem.* **1950**, *54*, 531-535.
- (63) Ireland, J. F.; Wyatt, P. A. H., Acid-Base Properties of Electronically Excited States of Organic Molecules. *Adv. Phys. Org. Chem.* **1976**, *12*, 131-221.
- (64) Arnaut, L. G.; Formosinho, S. J., Excited-state proton transfer reactions I. Fundamentals and intermolecular reactions. *J. Photochem. Photobiol. A: Chemistry* **1993**, *75*, 1-20.

(65) Douhal, A.; Lahmani, F.; Zewail, A. H., Proton-transfer reaction dynamics. *Chem. Phys.* **1996**, *207*, 477-498.

(66) Pines, E.; Pines, D., Proton Dissociation and Solute-Solvent Interactions Following Electronic Excitation of Photoacids. In *Ultrafast Hydrogen Bonding Dynamics and Proton Transfer Processes in the Condensed Phase*, Elsaesser, T.; Bakker, H. J., Eds. Springer Netherlands: Dordrecht, 2002; pp 155-184.

(67) Tolbert, L. M.; Solntsev, K. M., Excited-State Proton Transfer: From Constrained Systems to “Super” Photoacids to Superfast Proton Transfer. *Acc. Chem. Res.* **2002**, *35*, 19-27.

(68) Agmon, N., Elementary Steps in Excited-State Proton Transfer. *J. Phys. Chem. A* **2005**, *109*, 13-35.

(69) Kumpulainen, T.; Lang, B.; Rosspeintner, A.; Vauthey, E., Ultrafast Elementary Photochemical Processes of Organic Molecules in Liquid Solution. *Chem. Rev.* **2017**, *117*, 10826-10939.

(70) Abbruzzetti, S.; Crema, E.; Masino, L.; Veccli, A.; Viappiani, C.; Small, J. R.; Libertini, L. J.; Small, E. W., Fast Events in Protein Folding: Structural Volume Changes Accompanying the Early Events in the N²¹⁹²I Transition of Apomyoglobin Induced by Ultrafast pH Jump. *Biophys. J.* **2000**, *78*, 405-415.

(71) Wan, P.; Shukla, D., Utility of acid-base behavior of excited states of organic molecules. *Chem. Rev.* **1993**, *93*, 571-584.

(72) Shen, J.-Y.; Chao, W.-C.; Liu, C.; Pan, H.-A.; Yang, H.-C.; Chen, C.-L.; Lan, Y.-K.; Lin, L.-J.; Wang, J.-S.; Lu, J.-F.; Chun-Wei Chou, S.; Tang, K.-C.; Chou, P.-T., Probing water micro-solvation in proteins by water catalysed proton-transfer tautomerism. *Nat. Commun.* **2013**, *4*, 2611.

(73) Peretz-Soroka, H.; Pevzner, A.; Davidi, G.; Naddaka, V.; Kwiat, M.; Huppert, D.; Patolsky, F., Manipulating and Monitoring On-Surface Biological Reactions by Light-Triggered Local pH Alterations. *Nano Lett.* **2015**, *15*, 4758-4768.

(74) Kwon, J. E.; Park, S. Y., Advanced Organic Optoelectronic Materials: Harnessing Excited-State Intramolecular Proton Transfer (ESIPT) Process. *Adv. Mater.* **2011**, *23*, 3615-3642.

(75) White, W.; Sanborn, C. D.; Fabian, D. M.; Ardo, S., Conversion of Visible Light into Ionic Power Using Photoacid-Dye-Sensitized Bipolar Ion-Exchange Membranes. *Joule* **2018**, *2*, 94-109.

(76) Piatkevich, K. D.; Malashkevich, V. N.; Almo, S. C.; Verkhusha, V. V., Engineering ESPT Pathways Based on Structural Analysis of LSSmKate Red Fluorescent Proteins with Large Stokes Shift. *J. Am. Chem. Soc.* **2010**, *132*, 10762-10770.

- (77) Das, A.; Ayad, S.; Hanson, K., Enantioselective Protonation of Silyl Enol Ether Using Excited State Proton Transfer Dyes. *Org. Lett.* **2016**, *18*, 5416-5419.
- (78) Ryan, E. T.; Xiang, T.; Johnston, K. P.; Fox, M. A., Absorption and Fluorescence Studies of Acridine in Subcritical and Supercritical Water. *J. Phys. Chem. A* **1997**, *101*, 1827-1835.
- (79) Favaro, G.; Mazzucato, U.; Masetti, F., Excited state reactivity of aza aromatics. I. Basicity of 3-styrylpyridines in the first excited singlet state. *J. Phys. Chem.* **1973**, *77*, 601-604.
- (80) Yatsushashi, T.; Inoue, H., Molecular Mechanism of Radiationless Deactivation of Aminoanthraquinones through Intermolecular Hydrogen-Bonding Interaction with Alcohols and Hydroperoxides. *J. Phys. Chem. A* **1997**, *101*, 8166-8173.
- (81) Jiménez-Sánchez, A.; Santillan, R., A photochromic–acidochromic HCl fluorescent probe. An unexpected chloride-directed recognition. *Analyst* **2016**, *141*, 4108-4120.
- (82) Munitz, N.; Avital, Y.; Pines, D.; Nibbering, E. T. J.; Pines, E., Cation-Enhanced Deprotonation of Water by a Strong Photobase. *Isr. J. Chem.* **2009**, *49*, 261-272.
- (83) Akulov, K.; Simkovitch, R.; Erez, Y.; Gepshtein, R.; Schwartz, T.; Huppert, D., Acid Effect on Photobase Properties of Curcumin. *J. Phys. Chem. A* **2014**, *118*, 2470-2479.
- (84) Vogt, B. S.; Schulman, S. G., Reversible proton transfer in photoexcited xanthone. *Chem. Phys. Lett.* **1983**, *97*, 450-453.
- (85) Simkovitch, R.; Akulov, K.; Shomer, S.; Roth, M. E.; Shabat, D.; Schwartz, T.; Huppert, D., Comprehensive Study of Ultrafast Excited-State Proton Transfer in Water and D₂O Providing the Missing RO \cdots H⁺ Ion-Pair Fingerprint. *J. Phys. Chem. A* **2014**, *118*, 4425-4443.
- (86) Suyama, K.; Shirai, M., Photobase generators: Recent progress and application trend in polymer systems. *Prog. Polym. Sci.* **2009**, *34*, 194-209.
- (87) Solntsev, K. M.; Huppert, D.; Agmon, N.; Tolbert, L. M., Photochemistry of “Super” Photoacids. 2. Excited-State Proton Transfer in Methanol/Water Mixtures. *J. Phys. Chem. A* **2000**, *104*, 4658-4669.
- (88) Carmeli, I.; Huppert, D.; Tolbert, L. M.; Haubrich, J. E., Ultrafast excited-state proton transfer from dicyano-naphthol. *Chem. Phys. Lett.* **1996**, *260*, 109-114.
- (89) Huppert, D.; Tolbert, L. M.; Linares-Samaniego, S., Ultrafast Excited-State Proton Transfer from Cyano-Substituted 2-Naphthols. *J. Phys. Chem. A* **1997**, *101*, 4602-4605.

- (90) Kucherak, O. A.; Didier, P.; Mély, Y.; Klymchenko, A. S., Fluorene Analogues of Prodan with Superior Fluorescence Brightness and Solvatochromism. *J. Phys. Chem. Lett.* **2010**, *1*, 616-620.
- (91) Snellenburg, J. J.; Laptенок, S.; Seger, R.; Mullen, K. M.; van Stokkum, I. H. M., Glotaran: A Java-Based Graphical User Interface for the R Package TIMP. *J. Stat. Soft.* **2012**, *49*, 22.
- (92) Weller, A., Quantitative Untersuchungen der Fluoreszenzumwandlung bei Naphtholen. *Z. Elektrochem.* **1952**, *56*, 662-668.
- (93) Marciniak, B.; Kozubek, H.; Paszyc, S., Estimation of pKa* in the first excited singlet state. A physical chemistry experiment that explores acid-base properties in the excited state. *J. Chem. Edu.* **1992**, *69*, 247.
- (94) Driscoll, E. W.; Hunt, J. R.; Dawlaty, J. M., Photobasicity in Quinolines: Origin and Tunability via the Substituents' Hammett Parameters. *J. Phys. Chem. Lett.* **2016**, *7*, 2093-2099.
- (95) Maitani, Y.; Nakagaki, M.; Nagai, T., Determination of the acid dissociation constants in ethanol-water mixtures and partition coefficients for diclofenac. *Int. J. Pharm.* **1991**, *74*, 105-114.
- (96) Goodhue, L. D.; Hixon, R. M., Electron-Sharing Ability of Organic Radicals. VII. Dissociation Constants of a Series of Organic Acids and Amines in Water, Methanol and Ethanol. *J. Am. Chem. Soc.* **1934**, *56*, 1329-1333.
- (97) Kütt, A.; Leito, I.; Kaljurand, I.; Sooväli, L.; Vlasov, V. M.; Yagupolskii, L. M.; Koppel, I. A., A Comprehensive Self-Consistent Spectrophotometric Acidity Scale of Neutral Brønsted Acids in Acetonitrile. *J. Org. Chem.* **2006**, *71*, 2829-2838.
- (98) Horng, M. L.; Gardecki, J. A.; Papazyan, A.; Maroncelli, M., Subpicosecond Measurements of Polar Solvation Dynamics: Coumarin 153 Revisited. *J. Phys. Chem.* **1995**, *99*, 17311-17337.
- (99) Kumar, P. V.; Maroncelli, M., Polar solvation dynamics of polyatomic solutes: Simulation studies in acetonitrile and methanol. *J. Chem. Phys.* **1995**, *103*, 3038-3060.
- (100) W. P. de Boeij; M. S. Pshenichnikov; Wiersma, D. A., Ultrafast Solvation Dynamics Explored by Femtosecond Photon Echo Spectroscopies. *Annu. Rev. Phys. Chem.* **1998**, *49*, 99-123.
- (101) Glasbeek, M.; Zhang, H., Femtosecond Studies of Solvation and Intramolecular Configurational Dynamics of Fluorophores in Liquid Solution. *Chem. Rev.* **2004**, *104*, 1929-1954.

- (102) Rosenthal, S. J.; Xie, X.; Du, M.; Fleming, G. R., Femtosecond solvation dynamics in acetonitrile: Observation of the inertial contribution to the solvent response. *J. Chem. Phys.* **1991**, *95*, 4715-4718.
- (103) Jimenez, R.; Fleming, G. R.; Kumar, P. V.; Maroncelli, M., Femtosecond solvation dynamics of water. *Nature* **1994**, *369*, 471-473.
- (104) Jumper, C. C.; Arpin, P. C.; Turner, D. B.; McClure, S. D.; Rafiq, S.; Dean, J. C.; Cina, J. A.; Kovac, P. A.; Mirkovic, T.; Scholes, G. D., Broad-Band Pump–Probe Spectroscopy Quantifies Ultrafast Solvation Dynamics of Proteins and Molecules. *J. Phys. Chem. Lett.* **2016**, *7*, 4722-4731.
- (105) Kumpulainen, T.; Lang, B.; Rosspeintner, A.; Vauthey, E., Ultrafast Elementary Photochemical Processes of Organic Molecules in Liquid Solution. *Chem. Rev.* **2016**.
- (106) Jonas, D. M., Two-Dimensional Femtosecond Spectroscopy. *Annu. Rev. Phys. Chem.* **2003**, *54*, 425-463.
- (107) Mukamel, S., Multidimensional Femtosecond Correlation Spectroscopies of Electronic and Vibrational Excitations. *Annu. Rev. Phys. Chem.* **2000**, *51*, 691-729.
- (108) Delaey, E.; van Laar, F.; De Vos, D.; Kamuhabwa, A.; Jacobs, P.; de Witte, P., A comparative study of the photosensitizing characteristics of some cyanine dyes. *J. Photochem. Photobiol. B* **2000**, *55*, 27-36.
- (109) Zhao, Y.; Meek, G. A.; Levine, B. G.; Lunt, R. R., Near-Infrared Harvesting Transparent Luminescent Solar Concentrators. *Adv. Optical Mater.* **2014**, *2*, 606-611.
- (110) Fang, C.; Wang, K.; Zeng, C.; Chi, C.; Shang, W.; Ye, J.; Mao, Y.; Fan, Y.; Yang, J.; Xiang, N.; Zeng, N.; Zhu, W.; Fang, C.; Tian, J., Illuminating necrosis: From mechanistic exploration to preclinical application using fluorescence molecular imaging with indocyanine green. *Sci. Rep.* **2016**, *6*, 21013.
- (111) Mishra, A.; Behera, R. K.; Behera, P. K.; Mishra, B. K.; Behera, G. B., Cyanines during the 1990s: A Review. *Chem. Rev.* **2000**, *100*, 1973-2012.
- (112) Bricks, J. L.; Kachkovskii, A. D.; Slominskii, Y. L.; Gerasov, A. O.; Popov, S. V., Molecular design of near infrared polymethine dyes: A review. *Dyes Pigments* **2015**, *121*, 238-255.
- (113) Das, D. K.; Makhal, K.; Bandyopadhyay, S. N.; Goswami, D., Direct Observation of Coherent Oscillations in Solution due to Microheterogeneous Environment. *Sci. Rep.* **2014**, *4*, 6097.

- (114) Voiciuk, V.; Redeckas, K.; Derevyanko, N. A.; Kulinich, A. V.; Barkauskas, M.; Vengris, M.; Sirutkaitis, V.; Ishchenko, A. A., Study of photophysical properties of a series of polymethine dyes by femtosecond laser photolysis. *Dyes Pigments* **2014**, *109*, 120-126.
- (115) Terenziani, F.; Przhonska, O. V.; Webster, S.; Padilha, L. A.; Slominsky, Y. L.; Davydenko, I. G.; Gerasov, A. O.; Kovtun, Y. P.; Shandura, M. P.; Kachkovski, A. D.; Hagan, D. J.; Van Stryland, E. W.; Painelli, A., Essential-State Model for Polymethine Dyes: Symmetry Breaking and Optical Spectra. *J. Phys. Chem. Lett.* **2010**, *1*, 1800-1804.
- (116) Marder, S. R.; Gorman, C. B.; Tiemann, B. G.; Perry, J. W.; Bourhill, G.; Mansour, K., Relation Between Bond-Length Alternation and Second Electronic Hyperpolarizability of Conjugated Organic Molecules. *Science* **1993**, *261*, 186-189.
- (117) Berg, M., Viscoelastic Continuum Model of Nonpolar Solvation. 1. Implications for Multiple Time Scales in Liquid Dynamics. *J. Phys. Chem. A* **1998**, *102*, 17-30.
- (118) Pascal, S.; Haefele, A.; Monnereau, C.; Charaf-Eddin, A.; Jacquemin, D.; Le Guennic, B.; Andraud, C.; Maury, O., Expanding the Polymethine Paradigm: Evidence for the Contribution of a Bis-Dipolar Electronic Structure. *J. Phys. Chem. B* **2014**, *118*, 4038-4047.
- (119) Yu, A.; Tolbert, C. A.; Farrow, D. A.; Jonas, D. M., Solvatochromism and Solvation Dynamics of Structurally Related Cyanine Dyes. *J. Phys. Chem. A* **2002**, *106*, 9407-9419.
- (120) Nairat, M.; Konar, A.; Kaniecki, M.; Lozovoy, V. V.; Dantus, M., Investigating the Role of Human Serum Albumin Protein Pocket on the Excited State Dynamics of Indocyanine Green Using Shaped Femtosecond Laser Pulses. *Phys. Chem. Chem. Phys.* **2015**, *17*, 5872-5877.
- (121) Konar, A.; Lozovoy, V. V.; Dantus, M., Stimulated Emission Enhancement Using Shaped Pulses. *J. Phys. Chem. A* **2016**, *120*, 2002-2008.
- (122) Harel, E.; Fidler, A. F.; Engel, G. S., Single-Shot Gradient-Assisted Photon Echo Electronic Spectroscopy. *J. Phys. Chem. A* **2011**, *115*, 3787-3796.
- (123) Rodriguez, Y.; Frei, F.; Cannizzo, A.; Feurer, T., Pulse-shaping assisted multidimensional coherent electronic spectroscopy. *J. Chem. Phys.* **2015**, *142*, 212451.
- (124) Marroux, H. J. B.; Orr-Ewing, A. J., Distinguishing Population and Coherence Transfer Pathways in a Metal Dicarbonyl Complex Using Pulse-Shaped Two-Dimensional Infrared Spectroscopy. *J. Phys. Chem. B* **2016**, *120*, 4125-4130.
- (125) Strekowski, L.; Lipowska, M.; Patonay, G., Substitution reactions of a nucleofugal group in heptamethine cyanine dyes. Synthesis of an isothiocyanato derivative for labeling of proteins with a near-infrared chromophore. *J. Org. Chem.* **1992**, *57*, 4578-4580.

- (126) Xu, B.; Gunn, J. M.; Cruz, J. M. D.; Lozovoy, V. V.; Dantus, M., Quantitative Investigation of the Multiphoton Intrapulse Interference Phase Scan Method for Simultaneous Phase Measurement and Compensation of Femtosecond Laser Pulses. *J. Opt. Soc. Am. B* **2006**, *23*, 750-759.
- (127) Rasskazov, G.; Lozovoy, V. V.; Dantus, M., Spectral Amplitude and Phase Noise Characterization of Titanium-Sapphire Lasers. *Opt. Express* **2015**, *23*, 23597-23602.
- (128) Perdew, J. P.; Ernzerhof, M.; Burke, K., Rationale for mixing exact exchange with density functional approximations. *J. Chem. Phys.* **1996**, *105*, 9982-9985.
- (129) Giesecking, R. L.; Ravva, M. K.; Coropceanu, V.; Brédas, J.-L., Benchmarking Density Functional Theory Approaches for the Description of Symmetry Breaking in Long Polymethine Dyes. *J. Phys. Chem. C* **2016**, *120*, 9975-9984.
- (130) NBO 6.0. Glendening, J. K. Badenhoop, A. E. Reed, J. E. Carpenter, J. A. Bohmann, C. M. Morales, C. R. Landis, and F. Weinhold, Theoretical Chemistry Institute, University of Wisconsin, Madison (2013).
- (131) Perdew, J. P.; Burke, K.; Ernzerhof, M., Generalized Gradient Approximation Made Simple. *Phys. Rev. Lett.* **1996**, *77*, 3865-3868.
- (132) Jacquemin, D.; Zhao, Y.; Valero, R.; Adamo, C.; Ciofini, I.; Truhlar, D. G., Verdict: Time-Dependent Density Functional Theory “Not Guilty” of Large Errors for Cyanines. *J. Chem. Theory Comput.* **2012**, *8*, 1255-1259.
- (133) Karaca, S.; Elmacı, N., A computational study on the excited state properties of a cationic cyanine dye: TTBC. *Comp. Theor. Chem.* **2011**, *964*, 160-168.
- (134) Cancès, E.; Mennucci, B.; Tomasi, J., A new integral equation formalism for the polarizable continuum model: Theoretical background and applications to isotropic and anisotropic dielectrics. *J. Chem. Phys.* **1997**, *107*, 3032-3041.
- (135) Ghigo, G.; Roos, B. O.; Malmqvist, P.-Å., A modified definition of the zeroth-order Hamiltonian in multiconfigurational perturbation theory (CASPT2). *Chem. Phys. Lett.* **2004**, *396*, 142-149.
- (136) Frisch, M. J.; Trucks, G. W.; Schlegel, H. B.; Scuseria, G. E.; Robb, M. A.; Cheeseman, J. R.; Scalmani, G.; Barone, V.; Mennucci, B.; Petersson, G. A.; Nakatsuji, H.; Caricato, M.; Li, X.; Hratchian, H. P.; Izmaylov, A. F.; Bloino, J.; Zheng, G.; Sonnenberg, J. L.; Hada, M.; Ehara, M.; Toyota, K.; Fukuda, R.; Hasegawa, J.; Ishida, M.; Nakajima, T.; Honda, Y.; Kitao, O.; Nakai, H.; Vreven, T.; Montgomery Jr., J. A.; Peralta, J. E.; Ogliaro, F.; Bearpark, M. J.; Heyd, J.; Brothers, E. N.; Kudin, K. N.; Staroverov, V. N.; Kobayashi, R.; Normand, J.; Raghavachari, K.; Rendell,

A. P.; Burant, J. C.; Iyengar, S. S.; Tomasi, J.; Cossi, M.; Rega, N.; Millam, N. J.; Klene, M.; Knox, J. E.; Cross, J. B.; Bakken, V.; Adamo, C.; Jaramillo, J.; Gomperts, R.; Stratmann, R. E.; Yazyev, O.; Austin, A. J.; Cammi, R.; Pomelli, C.; Ochterski, J. W.; Martin, R. L.; Morokuma, K.; Zakrzewski, V. G.; Voth, G. A.; Salvador, P.; Dannenberg, J. J.; Dapprich, S.; Daniels, A. D.; Farkas, Ö.; Foresman, J. B.; Ortiz, J. V.; Cioslowski, J.; Fox, D. J. *Gaussian 09*, Gaussian, Inc.: Wallingford, CT, USA, 2009.

(137) Werner, H.-J.; Knowles, P. J.; Knizia, G.; Manby, F. R.; Schütz, M., Molpro: a general-purpose quantum chemistry program package. *Wiley Interdiscip. Rev. Comput. Mol. Sci.* **2012**, *2*, 242-253.

(138) H.-J. Werner, P. J. K., G. Knizia, F. R. Manby, M. Schütz, P. Celani, W. Györffy, D. Kats, T. Korona, R. Lindh, A. Mitrushenkov, G. Rauhut, K. R. Shamasundar, T. B. Adler, R. D. Amos, A. Bernhardsson, A. Berning, D. L. Cooper, M. J. O. Deegan, A. J. Dobbyn, F. Eckert, E. Goll, C. Hampel, A. Hesselmann, G. Hetzer, T. Hrenar, G. Jansen, C. Köppl, Y. Liu, A. W. Lloyd, R. A. Mata, A. J. May, S. J. McNicholas, W. Meyer, M. E. Mura, A. Nicklaß, D. P. O'Neill, P. Palmieri, D. Peng, K. Pflüger, R. Pitzer, M. Reiher, T. Shiozaki, H. Stoll, A. J. Stone, R. Tarroni, T. Thorsteinsson, M. Wang *MOLPRO, version 2012.1, a package of ab initio programs*.

(139) Werner, H. J.; Knowles, P. J., A second order multiconfiguration SCF procedure with optimum convergence. *J. Chem. Phys.* **1985**, *82*, 5053-5063.

(140) Busch, T.; Esposti, A. D.; Werner, H. J., Analytical energy gradients for multiconfiguration self-consistent field wave functions with frozen core orbitals. *J. Chem. Phys.* **1991**, *94*, 6708-6715.

(141) Celani, P.; Werner, H.-J., Multireference perturbation theory for large restricted and selected active space reference wave functions. *J. Chem. Phys.* **2000**, *112*, 5546-5557.

(142) Nairat, M.; Konar, A.; Lozovoy, V. V.; Beck, W. F.; Blanchard, G. J.; Dantus, M., Controlling S2 Population in Cyanine Dyes Using Shaped Femtosecond Pulses. *J. Phys. Chem. A* **2016**, *120*, 1876-1885.

(143) Guarín, C. A.; Villabona-Monsalve, J. P.; López-Arteaga, R.; Peon, J., Dynamics of the Higher Lying Excited States of Cyanine Dyes. An Ultrafast Fluorescence Study. *J. Phys. Chem. B* **2013**, *117*, 7352-7362.

(144) Marder, S. R.; Gorman, C. B.; Meyers, F.; Perry, J. W.; Bourhill, G.; Brédas, J.-L.; Pierce, B. M., A Unified Description of Linear and Nonlinear Polarization in Organic Polymethine Dyes. *Science* **1994**, *265*, 632-635.

(145) Ohira, S.; Hales, J. M.; Thorley, K. J.; Anderson, H. L.; Perry, J. W.; Brédas, J.-L., A New Class of Cyanine-like Dyes with Large Bond-Length Alternation. *J. Am. Chem. Soc.* **2009**, *131*, 6099-6101.

- (146) Jacquemin, D.; Perpète, E. A.; Ciofini, I.; Adamo, C.; Valero, R.; Zhao, Y.; Truhlar, D. G., On the Performances of the M06 Family of Density Functionals for Electronic Excitation Energies. *J. Chem. Theory Comput.* **2010**, *6*, 2071-2085.
- (147) Le Guennic, B.; Jacquemin, D., Taking Up the Cyanine Challenge with Quantum Tools. *Acc. Chem. Res.* **2015**, *48*, 530-537.
- (148) Zhekova, H.; Krykunov, M.; Autschbach, J.; Ziegler, T., Applications of Time Dependent and Time Independent Density Functional Theory to the First π to π^* Transition in Cyanine Dyes. *J. Chem. Theory Comput.* **2014**, *10*, 3299-3307.
- (149) Send, R.; Valsson, O.; Filippi, C., Electronic Excitations of Simple Cyanine Dyes: Reconciling Density Functional and Wave Function Methods. *J. Chem. Theory Comput.* **2011**, *7*, 444-455.
- (150) Wei, Z.; Nakamura, T.; Takeuchi, S.; Tahara, T., Tracking of the Nuclear Wavepacket Motion in Cyanine Photoisomerization by Ultrafast Pump–Dump–Probe Spectroscopy. *J. Am. Chem. Soc.* **2011**, *133*, 8205-8210.
- (151) Bishop, M. M.; Roscioli, J. D.; Ghosh, S.; Mueller, J. J.; Shepherd, N. C.; Beck, W. F., Vibrationally Coherent Preparation of the Transition State for Photoisomerization of the Cyanine Dye Cy5 in Water. *J. Phys. Chem. B* **2015**, *119*, 6905-6915.
- (152) Weigel, A.; Pfaffe, M.; Sajadi, M.; Mahrwald, R.; Improta, R.; Barone, V.; Polli, D.; Cerullo, G.; Ernstring, N. P.; Santoro, F., Barrierless photoisomerisation of the "simplest cyanine": Joining computational and femtosecond optical spectroscopies to trace the full reaction path. *Phys. Chem. Chem. Phys.* **2012**, *14*, 13350-13364.
- (153) Dietzek, B.; Pascher, T.; Yartsev, A., Tracking Ultrafast Excited-State Bond-Twisting Motion in Solution Close to the Franck–Condon Point. *J. Phys. Chem. B* **2007**, *111*, 6034-6041.
- (154) Sanchez-Galvez, A.; Hunt, P.; Robb, M. A.; Olivucci, M.; Vreven, T.; Schlegel, H. B., Ultrafast Radiationless Deactivation of Organic Dyes: Evidence for a Two-State Two-Mode Pathway in Polymethine Cyanines. *J. Am. Chem. Soc.* **2000**, *122*, 2911-2924.
- (155) Hunt, P. A.; Robb, M. A., Systematic Control of Photochemistry: The Dynamics of Photoisomerization of a Model Cyanine Dye. *J. Am. Chem. Soc.* **2005**, *127*, 5720-5726.
- (156) Peteanu, L. A.; Schoenlein, R. W.; Wang, Q.; Mathies, R. A.; Shank, C. V., The first step in vision occurs in femtoseconds: complete blue and red spectral studies. *Proc. Natl. Acad. Sci. USA* **1993**, *90*, 11762-11766.

- (157) Rivalta, I.; Nenov, A.; Garavelli, M., Modelling retinal chromophores photoisomerization: from minimal models in vacuo to ultimate bidimensional spectroscopy in rhodopsins. *Phys. Chem. Chem. Phys.* **2014**, *16*, 16865-16879.
- (158) Garavelli, M.; Vreven, T.; Celani, P.; Bernardi, F.; Robb, M. A.; Olivucci, M., Photoisomerization Path for a Realistic Retinal Chromophore Model: The Nonatetraeniminium Cation. *J. Am. Chem. Soc.* **1998**, *120*, 1285-1288.
- (159) Ghosh, S.; Roscioli, J. D.; Bishop, M. M.; Gurchiek, J. K.; LaFountain, A. M.; Frank, H. A.; Beck, W. F., Torsional Dynamics and Intramolecular Charge Transfer in the S₂ (11Bu⁺) Excited State of Peridinin: A Mechanism for Enhanced Mid-Visible Light Harvesting. *J. Phys. Chem. Lett.* **2016**, *7*, 3621-3626.
- (160) Cao, J.; Hu, C.; Sun, W.; Xu, Q.; Fan, J.; Song, F.; Sun, S.; Peng, X., The mechanism of different sensitivity of meso-substituted and unsubstituted cyanine dyes in rotation-restricted environments for biomedical imaging applications. *RSC Advances* **2014**, *4*, 13385-13394.
- (161) de Boeij, W. P.; Pshenichnikov, M. S.; Wiersma, D. A., Ultrafast Solvation Dynamics Explored by Femtosecond Photon Echo Spectroscopies. *Annu. Rev. Phys. Chem.* **1998**, *49*, 99-123.
- (162) Fleming, G. R.; Cho, M., Chromophore-Solvent Dynamics. *Annu. Rev. Phys. Chem.* **1996**, *47*, 109-134.
- (163) Mukamel, S., MULTIDIMENSIONAL FEMTOSECOND CORRELATION SPECTROSCOPIES OF ELECTRONIC AND VIBRATIONAL EXCITATIONS. *Ann. Rev. Phys. Chem.* **2000**, *51*, 691-729.
- (164) Nandi, N.; Bhattacharyya, K.; Bagchi, B., Dielectric Relaxation and Solvation Dynamics of Water in Complex Chemical and Biological Systems. *Chem. Rev.* **2000**, *100*, 2013-2046.
- (165) Mishra, S., *Biomolecules*. Discovery Publishing House: New Delhi, 2003.
- (166) Zhong, D.; Douhal, A.; Zewail, A. H., Femtosecond studies of protein–ligand hydrophobic binding and dynamics: Human serum albumin. *Proc. Natl. Acad. Sci.* **2000**, *97*, 14056-14061.
- (167) Martín, C.; Gil, M.; Cohen, B.; Douhal, A., Ultrafast Photodynamics of Drugs in Nanocavities: Cyclodextrins and Human Serum Albumin Protein. *Langmuir* **2012**, *28*, 6746-6759.
- (168) Martin, C.; Cohen, B.; Gaamoussi, I.; Ijjaali, M.; Douhal, A., Ultrafast Dynamics of C30 in Solution and within CDs and HSA Protein. *J. Phys. Chem. B* **2014**, *118*, 5760-5771.
- (169) Gellman, S. H., ed., *Chem. Rev.* **1997**, *97*, 1231-1734.

- (170) Kragh-Hansen, U., Molecular aspects of ligand binding to serum albumin. *Pharmacol. Rev.* **1981**, *33*, 17-53.
- (171) Peters, T., Jr., Serum albumin. *Adv. Protein Chem.* **1985**, *37*, 161-245.
- (172) Gonçalves, M. S. T., Fluorescent Labeling of Biomolecules with Organic Probes. *Chem. Rev.* **2008**, *109*, 190-212.
- (173) Mataga, N.; Chosrowjan, H.; Taniguchi, S., Investigations into the dynamics and mechanisms of ultrafast photoinduced reactions taking place in photoresponsive protein nanospaces (PNS). *J. Photochem. Photobiol. C* **2004**, *5*, 155-168.
- (174) Royer, C. A., Probing Protein Folding and Conformational Transitions with Fluorescence. *Chem. Rev.* **2006**, *106*, 1769-1784.
- (175) Wald, G., Molecular Basis of Visual Excitation. *Science* **1968**, *162*, 230-239.
- (176) Peters, T., Jr., *All about Albumin: Biochemistry, Genetics, and Medical Applications*. Academic Press: San Diego, 1996.
- (177) Sugio, S.; Kashima, A.; Mochizuki, S.; Noda, M.; Kobayashi, K., Crystal structure of human serum albumin at 2.5 Å resolution. *Protein Eng.* **1999**, *12*, 439-446.
- (178) He, X. M.; Carter, D. C., Atomic structure and chemistry of human serum albumin. *Nature* **1992**, *358*, 209-215.
- (179) Il'ichev, Y. V.; Perry, J. L.; Simon, J. D., Interaction of Ochratoxin A with Human Serum Albumin. Preferential Binding of the Dianion and pH Effects. *J. Phys. Chem. B* **2002**, *106*, 452-459.
- (180) Bongsu, J.; Vullev, V. I.; Anvari, B., Revisiting Indocyanine Green: Effects of Serum and Physiological Temperature on Absorption and Fluorescence Characteristics. *IEEE J. Quantum Electron.* **2014**, *20*, 149-157.
- (181) Frangioni, J. V., In vivo near-infrared fluorescence imaging. *Curr. Opin. Chem. Biol.* **2003**, *7*, 626-634.
- (182) Yannuzzi, L. A., Indocyanine Green Angiography: A Perspective on Use in the Clinical Setting. *Am. J. Ophthalmol.* **2011**, *151*, 745-751.
- (183) Nimura, H.; Narimiya, N.; Mitsumori, N.; Yamazaki, Y.; Yanaga, K.; Urashima, M., Infrared ray electronic endoscopy combined with indocyanine green injection for detection of sentinel nodes of patients with gastric cancer. *Brit. J. Surg.* **2004**, *91*, 575-579.

- (184) Schaafsma, B. E.; Mieog, J. S. D.; Hutteman, M.; van der Vorst, J. R.; Kuppen, P. J. K.; Löwik, C. W. G. M.; Frangioni, J. V.; van de Velde, C. J. H.; Vahrmeijer, A. L., The clinical use of indocyanine green as a near-infrared fluorescent contrast agent for image-guided oncologic surgery. *J. Surg. Onc.* **2011**, *104*, 323-332.
- (185) van der Vorst, J. R.; Schaafsma, B. E.; Verbeek, F. P. R.; Swijnenburg, R. J.; Hutteman, M.; Liefers, G. J.; van de Velde, C. J. H.; Frangioni, J. V.; Vahrmeijer, A. L., Dose optimization for near-infrared fluorescence sentinel lymph node mapping in patients with melanoma. *Brit. J. Derm.* **2013**, *168*, 93-98.
- (186) Desmettre, T.; Devoisselle, J. M.; Mordon, S., Fluorescence Properties and Metabolic Features of Indocyanine Green (ICG) as Related to Angiography. *Surv. Ophthalmol.* **2000**, *45*, 15-27.
- (187) Landsman, M. L.; Kwant, G.; Mook, G. A.; Zijlstra, W. G., Light-absorbing properties, stability, and spectral stabilization of indocyanine green. *J. Appl. Physiol.* **1976**, *40*, 575-83.
- (188) Philip, R.; Penzkofer, A.; Bäumlner, W.; Szeimies, R. M.; Abels, C., Absorption and fluorescence spectroscopic investigation of indocyanine green. *J. Photochem. Photobiol. A* **1996**, *96*, 137-148.
- (189) Reindl, S.; Penzkofer, A.; Gong, S. H.; Landthaler, M.; Szeimies, R. M.; Abels, C.; Bäumlner, W., Quantum yield of triplet formation for indocyanine green. *J. Photochem. Photobiol. A* **1997**, *105*, 65-68.
- (190) Rotermond, F.; Weigand, R.; Holzer, W.; Wittmann, M.; Penzkofer, A., Fluorescence spectroscopic analysis of indocyanine green J aggregates in water. *J. Photochem. Photobiol. A* **1997**, *110*, 75-78.
- (191) Gratz, H.; Penzkofer, A.; Abels, C.; Szeimies, R. M.; Landthaler, M.; Bäumlner, W., Photoisomerisation, triplet formation, and photo-degradation dynamics of indocyanine green solutions. *J. Photochem. Photobiol. A* **1999**, *128*, 101-109.
- (192) Fuyuki, M.; Furuta, K.; Wada, A., Multiphoton processes in photoreactions of indocyanine green in ethanol. *J. Photochem. Photobiol. A* **2013**, *252*, 152-158.
- (193) Fuyuki, M.; Furuta, K.; Wada, A., Vibronic relaxation dynamics at intermediate state of two-pump excitation: Photoisomerization of indocyanine green in ethanol. *RSC Adv.* **2013**, *3*, 7313-7320.
- (194) Sudeep, P. K.; Takechi, K.; Kamat, P. V., Harvesting Photons in the Infrared. Electron Injection from Excited Tricarbocyanine Dye (IR-125) into TiO₂ and Ag@TiO₂ Core-Shell Nanoparticles. *J. Phys. Chem. C* **2006**, *111*, 488-494.

- (195) Meyer, Y. H.; Pittman, M.; Plaza, P., Transient absorption of symmetrical carbocyanines. *J. Photochem. Photobiol. A* **1998**, *114*, 1-21.
- (196) Muckle, T. J., Plasma proteins binding of indocyanine green. *Biochem. Med.* **1976**, *15*, 17-21.
- (197) Colyer, C., Noncovalent labeling of proteins in capillary electrophoresis with laser-induced fluorescence detection. *Cell Biochem. Biophys.* **2000**, *33*, 323-37.
- (198) Moody, E. D.; Viskari, P. J.; Colyer, C. L., Non-covalent labeling of human serum albumin with indocyanine green: a study by capillary electrophoresis with diode laser-induced fluorescence detection. *J. Chromatogr. B* **1999**, *729*, 55-64.
- (199) McCorquodale, E. M.; Colyer, C. L., Indocyanine green as a noncovalent, pseudofluorogenic label for protein determination by capillary electrophoresis. *Electrophoresis* **2001**, *22*, 2403-2408.
- (200) Berezin, M. Y.; Guo, K.; Akers, W.; Livingston, J.; Solomon, M.; Lee, H.; Liang, K.; Agee, A.; Achilefu, S., Rational Approach To Select Small Peptide Molecular Probes Labeled with Fluorescent Cyanine Dyes for in Vivo Optical Imaging. *Biochem.* **2011**, *50*, 2691-2700.
- (201) Holzer, W.; Mauerer, M.; Penzkofer, A.; Szeimies, R. M.; Abels, C.; Landthaler, M.; Bäumler, W., Photostability and thermal stability of indocyanine green. *J. Photochem. Photobiol. B* **1998**, *47*, 155-164.
- (202) Bardeen, C. J.; Yakovlev, V. V.; Wilson, K. R.; Carpenter, S. D.; Weber, P. M.; Warren, W. S., Feedback quantum control of molecular electronic population transfer. *Chem. Phys. Lett.* **1997**, *280*, 151-158.
- (203) Bardeen, C. J.; Cao, J.; Brown, F. L. H.; Wilson, K. R., Using Time-dependent Rate Equations to Describe Chirped Pulse Excitation in Condensed Phases. *Chem. Phys. Lett.* **1999**, *302*, 405-410.
- (204) Cao, J.; Che, J.; Wilson, K. R., Intrapulse Dynamical Effects in Multiphoton Processes: Theoretical Analysis. *J. Phys Chem. A* **1998**, *102*, 4284-4290.
- (205) Fainberg, B. D.; Gorbunov, V. A., Coherent Population Transfer in Molecules Coupled with a Dissipative Environment by an Intense Ultrashort Chirped Pulse. *J. Chem. Phys.* **2002**, *117*, 7222-7232.
- (206) Fainberg, B. D.; Gorbunov, V. A., Coherent population transfer in molecules coupled with a dissipative environment by intense ultrashort chirped pulse. II. A simple model. *J. Chem. Phys.* **2004**, *121*, 8748-8754.

- (207) Sanner, M. F., Python: a programming language for software integration and development. *J. Mol. Graph. Model.* **1999**, *17*, 57-61.
- (208) Trott, O.; Olson, A. J., AutoDock Vina: Improving the speed and accuracy of docking with a new scoring function, efficient optimization, and multithreading. *J. Comput. Chem.* **2010**, *31*, 455-461.
- (209) Park, J.-S.; Joo, T., Nuclear dynamics in electronic ground and excited states probed by spectrally resolved four wave mixing. *J. Chem. Phys.* **2002**, *116*, 10801-10808.
- (210) Kasha, M., Characterization of Electronic Transitions in Complex Molecules. *Discuss. Faraday Soc.* **1950**, *9*, 14-19.
- (211) Itoh, T., Fluorescence and Phosphorescence from Higher Excited States of Organic Molecules. *Chem. Rev.* **2012**, *112*, 4541-4568.
- (212) Petersson, J.; Eklund, M.; Davidsson, J.; Hammarström, L., Variation of Excitation Energy Influences the Product Distribution of a Two-Step Electron Transfer: S₂ vs S₁ Electron Transfer in a Zn(II)porphyrin–Viologen Complex. *J. Am. Chem. Soc.* **2009**, *131*, 7940-7941.
- (213) Wallin, S.; Monnereau, C.; Blart, E.; Gankou, J.-R.; Odobel, F.; Hammarström, L., State-Selective Electron Transfer in an Unsymmetric Acceptor–Zn(II)porphyrin–Acceptor Triad: Toward a Controlled Directionality of Electron Transfer from the Porphyrin S₂ and S₁ States as a Basis for a Molecular Switch. *J. Phys. Chem. A* **2010**, *114*, 1709-1721.
- (214) Bouit, P.-A.; Spänig, F.; Kuzmanich, G.; Krokos, E.; Oelsner, C.; Garcia-Garibay, M. A.; Delgado, J. L.; Martín, N.; Guldi, D. M., Efficient Utilization of Higher-Lying Excited States to Trigger Charge-Transfer Events. *Chem.-Eur. J.* **2010**, *16*, 9638-9645.
- (215) Yushchenko, D. A.; Shvadchak, V. V.; Klymchenko, A. S.; Duportail, G.; Pivovarenko, V. G.; Mély, Y., Modulation of Excited-State Intramolecular Proton Transfer by Viscosity in Protic Media. *J. Phys. Chem. A* **2007**, *111*, 10435-10438.
- (216) Rajendiran, N.; Balasubramanian, T., Dual Fluorescence of N-phenylanthranilic Acid: Effect of Solvents, pH and β -cyclodextrin. *Spectrochim. Acta A* **2007**, *68*, 867-876.
- (217) Glazer, E. C.; Magde, D.; Tor, Y., Dual Emission from a Family of Conjugated Dinuclear RuII Complexes. *J. Am. Chem. Soc.* **2005**, *127*, 4190-4192.
- (218) Luo, S.; Zhang, E.; Su, Y.; Cheng, T.; Shi, C., A Review of NIR Dyes in Cancer Targeting and Imaging. *Biomaterials* **2011**, *32*, 7127-7138.

- (219) Müller, A.; Pflüger, E., Laser-Fashspectroscopy of Cryptocyanine. *Chem. Phys. Lett.* **1968**, *2*, 155-159.
- (220) Tashiro, H.; Yajima, T., Direct Measurement of Blue Fluorescence Lifetimes in Polymethine Dyes Using a Picosecond Laser. *Chem. Phys. Lett.* **1976**, *42*, 553-557.
- (221) Rěhák, V.; Novák, A.; Titz, M., S₂ → S₀ Fluorescence of cryptocyanine solutions. *Chem. Phys. Lett.* **1977**, *52*, 39-42.
- (222) Das, D. K.; Makhal, K.; Singhal, S.; Goswami, D., Polarization Induced Control of Multiple Fluorescence from a Molecule. *Chem. Phys. Lett.* **2013**, *579*, 45-50.
- (223) Kasatani, K.; Sato, H., Viscosity-Dependent Decay Dynamics of the S₂ State of Cyanine Dyes with 3, 5, and 7 Methine Units by Picosecond Fluorescence Lifetime Measurements. *Bull. Chem. Soc. Jpn.* **1996**, *69*, 3455-3460.
- (224) Pastirk, I.; Brown, E. J.; Zhang, Q.; Dantus, M., Quantum Control of the Yield of a Chemical Reaction. *J. Chem. Phys.* **1998**, *108*, 4375-4378.
- (225) Bardeen, C. J.; Yakovlev, V. V.; Squier, J. A.; Wilson, K. R., Quantum Control of Population Transfer in Green Fluorescent Protein by Using Chirped Femtosecond Pulses. *J. Am. Chem. Soc.* **1998**, *120*, 13023-13027.
- (226) Fainberg, B. D., Nonperturbative Analytic Approach to the Interaction of Intense Ultrashort Chirped Pulses with Molecules in Solution: Picture of “Moving” Potentials. *J. Chem. Phys.* **1998**, *109*, 4523-4532.
- (227) Hashimoto, N. T.; Misawa, K.; Lang, R., Three-level Picture for Chirp-dependent Fluorescence Yields under Femtosecond Optical Pulse Irradiation. *Appl. Phys. Lett.* **2003**, *82*, 2749-2751.
- (228) Herek, J. L.; Wohlleben, W.; Cogdell, R. J.; Zeidler, D.; Motzkus, M., Quantum control of energy flow in light harvesting. *Nature* **2002**, *417*, 533-535.
- (229) Vogt, G.; Krampert, G.; Niklaus, P.; Nuernberger, P.; Gerber, G., Optimal Control of Photoisomerization. *Phys. Rev. Lett.* **2005**, *94*, 068305.
- (230) Prokhorenko, V. I.; Nagy, A. M.; Waschuk, S. A.; Brown, L. S.; Birge, R. R.; Miller, R. J. D., Coherent Control of Retinal Isomerization in Bacteriorhodopsin. *Science* **2006**, *313*, 1257-1261.

- (231) Vogt, G.; Nuernberger, P.; Brixner, T.; Gerber, G., Femtosecond pump–shaped-dump quantum control of retinal isomerization in bacteriorhodopsin. *Chem. Phys. Lett.* **2006**, *433*, 211-215.
- (232) Buckup, T.; Lebold, T.; Weigel, A.; Wohlleben, W.; Motzkus, M., Singlet versus triplet dynamics of β -carotene studied by quantum control spectroscopy. *J. Photochem. Photobiol. A* **2006**, *180*, 314-321.
- (233) Kuroda, D. G.; Singh, C. P.; Peng, Z.; Kleiman, V. D., Mapping Excited-State Dynamics by Coherent Control of a Dendrimer's Photoemission Efficiency. *Science* **2009**, *326*, 263-267.
- (234) Schneider, J.; Wollenhaupt, M.; Winzenburg, A.; Bayer, T.; Kohler, J.; Faust, R.; Baumert, T., Efficient and robust strong-field control of population transfer in sensitizer dyes with designed femtosecond laser pulses. *Phys. Chem. Chem. Phys.* **2011**, *13*, 8733-8746.
- (235) Sukharev, M.; Seideman, T., Optimal Control Approach to Suppression of Radiationless Transitions. *Phys. Rev. Lett.* **2004**, *93*, 093004.
- (236) Abe, M.; Ohtsuki, Y.; Fujimura, Y.; Domcke, W., Optimal control of ultrafast cis-trans photoisomerization of retinal in rhodopsin via a conical intersection. *J. Chem. Phys.* **2005**, *123*, 144508.
- (237) Petersen, J.; Wohlgemuth, M.; Sellner, B.; Bonacic-Koutecky, V.; Lischka, H.; Mitric, R., Laser pulse trains for controlling excited state dynamics of adenine in water. *Phys. Chem. Chem. Phys.* **2012**, *14*, 4687-4694.
- (238) Brixner, T.; Gerber, G., Quantum Control of Gas-Phase and Liquid-Phase Femtochemistry. *ChemPhysChem* **2003**, *4*, 418-438.
- (239) Wohlleben, W.; Buckup, T.; Herek, J. L.; Motzkus, M., Coherent Control for Spectroscopy and Manipulation of Biological Dynamics. *ChemPhysChem* **2005**, *6*, 850-857.
- (240) Devi, P.; Lozovoy, V. V.; Dantus, M., Measurement of Group Velocity Dispersion of Solvents Using 2-cycle Femtosecond Pulses: Experiment and Theory. *AIP Advances* **2011**, *1*, 032166.
- (241) West, W.; Pearce, S., The Dimeric State of Cyanine Dyes. *J. Phys. Chem.* **1965**, *69*, 1894-1903.
- (242) Webster, S.; Padilha, L. A.; Hu, H.; Przhonska, O. V.; Hagan, D. J.; Van Stryland, E. W.; Bondar, M. V.; Davydenko, I. G.; Slominsky, Y. L.; Kachkovski, A. D., Structure and linear spectroscopic properties of near IR polymethine dyes. *J. Lumin.* **2008**, *128*, 1927-1936.

- (243) Grabowski, Z. R.; Rotkiewicz, K.; Rettig, W., Structural Changes Accompanying Intramolecular Electron Transfer: Focus on Twisted Intramolecular Charge-Transfer States and Structures. *Chem. Rev.* **2003**, *103*, 3899-4032.
- (244) Zhang, Z.; Berezin, M. Y.; Kao, J. L. F.; d'Avignon, A.; Bai, M.; Achilefu, S., Near-Infrared Dichromic Fluorescent Carbocyanine Molecules. *Angew. Chem. Int. Ed.* **2008**, *47*, 3584-3587.
- (245) Passino, S. A.; Nagasawa, Y.; Joo, T.; Fleming, G. R., Three-Pulse Echo Peak Shift Studies of Polar Solvation Dynamics. *J. Phys. Chem. A* **1997**, *101*, 725-731.
- (246) Mohanty, J.; Palit, D. K.; Mittal, J. P., Photophysical Properties of Two Infrared Laser dyes - IR-144 and IR-140: A Picosecond Laser Flash Photolysis Study. *Proc. Indian Nat. Sci. Acad. Part A* **2000**, *66*, 303-315.
- (247) Carson, E. A.; Diffey, W. M.; Shelly, K. R.; Lampa-Pastirk, S.; Dillman, K. L.; Schleicher, J. M.; Beck, W. F., Dynamic-Absorption Spectral Contours: Vibrational Phase-Dependent Resolution of Low-Frequency Coherent Wave-Packet Motion of IR144 on the Ground-State and Excited-State $\pi \rightarrow \pi^*$ Surfaces. *J. Phys. Chem. A* **2004**, *108*, 1489-1500.
- (248) Thompson, R. B.; Frisoli, J. K.; Lakowicz, J. R., Phase Fluorometry Using a Continuously Modulated Laser Diode. *Anal. Chem.* **1992**, *64*, 2075-2078.
- (249) Gunaratne, T. C.; Zhu, X.; Lozovoy, V. V.; Dantus, M., Symmetry of Nonlinear Optical Response to Time Inversion of Shaped Femtosecond Pulses as a Clock of Ultrafast Dynamics. *Chem. Phys.* **2007**, *338*, 259-267.
- (250) Freed, K. F.; Jortner, J., Multiphonon Processes in the Nonradiative Decay of Large Molecules. *J. Chem. Phys.* **1970**, *52*, 6272-6291.
- (251) Boyd, R., *Nonlinear Optics*. Academic Press: Burlington, 2008.
- (252) Migani, A.; Olivucci, M., Conical Intersections and Organic Reaction Mechanisms. In *Conical Intersections: Electronic Structure, Dynamics & Spectroscopy*, World Scientific: Singapore, 2004; pp 271-320.
- (253) Ruiz, D. S.; Cembran, A.; Garavelli, M.; Olivucci, M.; Fuß, W., Structure of the Conical Intersections Driving the *cis-trans* Photoisomerization of Conjugated Molecules. *Photochem. Photobiol.* **2002**, *76*, 622-633.
- (254) Pollard, W. T.; Lee, S.-Y.; Mathies, R. A., Wave Packet Theory of Dynamic Absorption Spectra in Femtosecond Pump-probe Experiments. *J. Chem. Phys.* **1990**, *92*, 4012-4029.

- (255) Pollard, W. T.; Mathies, R. A., Analysis of Femtosecond Dynamic Absorption Spectra of Nonstationary States. *Annu. Rev. Phys. Chem.* **1992**, *43*, 497-523.
- (256) Scherer, N. F.; Jonas, D. M.; Fleming, G. R., Femtosecond Wave Packet and Chemical Reaction Dynamics of Iodine in Solution: Tunable Probe Study of Motion Along the Reaction Coordinate. *J. Chem. Phys.* **1993**, *99*, 153-168.
- (257) Jonas, D. M.; Bradforth, S. E.; Passino, S. A.; Fleming, G. R., Femtosecond Wavepacket Spectroscopy: Influence of Temperature, Wavelength, and Pulse Duration. *J. Phys. Chem.* **1995**, *99*, 2594-2608.
- (258) Kim, J.; Mukamel, S.; Scholes, G. D., Two-dimensional Electronic Double-quantum Coherence Spectroscopy. *Acc. Chem. Res.* **2009**, *42*, 1375-1384.
- (259) Weidinger, D.; Engel, M. F.; Gruebele, M., Freezing Vibrational Energy Flow: A Fitness Function for Interchangeable Computational and Experimental Control. *J. Phys. Chem. A* **2009**, *113*, 4184-4191.
- (260) Tomasi, J.; Mennucci, B.; Cammi, R., Quantum Mechanical Continuum Solvation Models. *Chem. Rev.* **2005**, *105*, 2999-3094.
- (261) Polívka, T.; Sundström, V., Ultrafast Dynamics of Carotenoid Excited States—From Solution to Natural and Artificial Systems. *Chem. Rev.* **2004**, *104*, 2021-2072.
- (262) Giusti-Suzor, A.; Mies, F. H.; DiMauro, L. F.; Charron, E.; Yang, B., Dynamics of H₂⁺ in Intense Laser Fields. *J. Phys. B At. Mol. Opt. Phys.* **1995**, *28*, 309-339.
- (263) Yamanouchi, K., The Next Frontier. *Science* **2002**, *295*, 1659-1660.
- (264) Posthumus, J. H., The Dynamics of Small Molecules in Intense Laser Fields. *Rep. Prog. Phys.* **2004**, *67*, 623-665.
- (265) Esry, B. D.; Saylor, A. M.; Wang, P. Q.; Carnes, K. D.; Ben-Itzhak, I., Above Threshold Coulomb Explosion of Molecules in Intense Laser Pulses. *Phys. Rev. Lett.* **2006**, *97*, 013003.
- (266) Lozovoy, V. V.; Zhu, X.; Gunaratne, T. C.; Harris, D. A.; Shane, J. C.; Dantus, M., Control of Molecular Fragmentation Using Shaped Femtosecond Pulses. *J. Phys. Chem. A* **2008**, *112*, 3789-3812.
- (267) Konar, A.; Shu, Y.; Lozovoy, V. V.; Jackson, J. E.; Levine, B. G.; Dantus, M., Polyatomic Molecules under Intense Femtosecond Laser Irradiation. *J. Phys. Chem. A* **2014**, *118*, 11433-11450.

- (268) Smith, B. H.; Compton, R. N., Laser Multiphoton Ionization of Tetrakis(dimethylamino)ethylene. *J. Phys. Chem. A* **2014**, *118*, 7288-7296.
- (269) Gong, X.; Kunitski, M.; Betsch, K. J.; Song, Q.; Schmidt, L. P. H.; Jahnke, T.; Kling, N. G.; Herrwerth, O.; Bergues, B.; Senftleben, A.; Ullrich, J.; Moshhammer, R.; Paulus, G. G.; Ben-Itzhak, I.; Lezius, M.; Kling, M. F.; Zeng, H.; Jones, R. R.; Wu, J., Multielectron Effects in Strong-field Dissociative Ionization of Molecules. *Phys. Rev. A* **2014**, *89*, 043429.
- (270) Hasegawa, H.; Hishikawa, A.; Yamanouchi, K., Coincidence Imaging of Coulomb Explosion of CS₂ in Intense Laser Fields. *Chem. Phys. Lett.* **2001**, *349*, 57-63.
- (271) Comstock, M.; Senekerimyan, V.; Dantus, M., Ultrafast Laser Induced Molecular Alignment and Deformation: Experimental Evidence from Neutral Molecules and from Fragment Ions. *J. Phys. Chem. A* **2003**, *107*, 8271-8281.
- (272) Roither, S.; Xie, X.; Kartashov, D.; Zhang, L.; Schöffler, M.; Xu, H.; Iwasaki, A.; Okino, T.; Yamanouchi, K.; Baltuska, A.; Kitzler, M., High Energy Proton Ejection from Hydrocarbon Molecules Driven by Highly Efficient Field Ionization. *Phys. Rev. Lett.* **2011**, *106*, 163001.
- (273) Xie, X.; Roither, S.; Schöffler, M.; Lötstedt, E.; Kartashov, D.; Zhang, L.; Paulus, G. G.; Iwasaki, A.; Baltuska, A.; Yamanouchi, K.; Kitzler, M., Electronic Predetermination of Ethylene Fragmentation Dynamics. *Phys. Rev. X* **2014**, *4*, 021005.
- (274) Wu, H.; Zhang, S.; Zhang, J.; Yang, Y.; Deng, L.; Jia, T.; Wang, Z.; Sun, Z., Observation of Hydrogen Migration in Cyclohexane under an Intense Femtosecond Laser Field. *J. Phys. Chem. A* **2015**, *119*, 2052-2057.
- (275) Voronova, K.; Mozaffari Easter, C. M.; Covert, K. J.; Bodi, A.; Hemberger, P.; Sztáray, B., Dissociative Photoionization of Diethyl Ether. *J. Phys. Chem. A* **2015**, *119*, 10654-10663.
- (276) Kübel, M.; Siemering, R.; Burger, C.; Kling, N. G.; Li, H.; Alnaser, A. S.; Bergues, B.; Zherebtsov, S.; Azzeer, A. M.; Ben-Itzhak, I.; Moshhammer, R.; de Vivie-Riedle, R.; Kling, M. F., Steering Proton Migration in Hydrocarbons Using Intense Few-Cycle Laser Fields. *Phys. Rev. Lett.* **2016**, *116*, 193001.
- (277) Assion, A.; Baumert, T.; Bergt, M.; Brixner, T.; Kiefer, B.; Seyfried, V.; Strehle, M.; Gerber, G., Control of Chemical Reactions by Feedback-Optimized Phase-Shaped Femtosecond Laser Pulses. *Science* **1998**, *282*, 919-922.
- (278) Alnaser, A. S.; Kübel, M.; Siemering, R.; Bergues, B.; Kling, N. G.; Betsch, K. J.; Deng, Y.; Schmidt, J.; Alahmed, Z. A.; Azzeer, A. M.; Ullrich, J.; Ben-Itzhak, I.; Moshhammer, R.; Kleineberg, U.; Krausz, F.; de Vivie-Riedle, R.; Kling, M. F., Subfemtosecond Steering of

Hydrocarbon Deprotonation through Superposition of Vibrational Modes. *Nat. Commun.* **2014**, *5*, 3800.

(279) Bohinski, T.; Moore Tibbetts, K.; Tarazkar, M.; Romanov, D. A.; Matsika, S.; Levis, R. J., Strong Field Adiabatic Ionization Prepares a Launch State for Coherent Control. *J. Phys. Chem. Lett.* **2014**, *5*, 4305-4309.

(280) Rudenko, A.; Zrost, K.; Feuerstein, B.; de Jesus, V. L. B.; Schröter, C. D.; Moshhammer, R.; Ullrich, J., Correlated Multielectron Dynamics in Ultrafast Laser Pulse Interactions with Atoms. *Phys. Rev. Lett.* **2004**, *93*, 253001.

(281) Xie, X.; Roither, S.; Schöffler, M.; Xu, H.; Bubin, S.; Lötstedt, E.; Erattuphuza, S.; Iwasaki, A.; Kartashov, D.; Varga, K.; G. Paulus, G.; Baltuška, A.; Yamanouchi, K.; Kitzler, M., Role of Proton Dynamics in Efficient Photoionization of Hydrocarbon Molecules. *Phys. Rev. A* **2014**, *89*, 023429.

(282) Itakura, R.; Yamanouchi, K.; Tanabe, T.; Okamoto, T.; Kannari, F., Dissociative Ionization of Ethanol in Chirped Intense Laser Fields. *J. Chem. Phys.* **2003**, *119*, 4179-4186.

(283) Yazawa, H.; Tanabe, T.; Okamoto, T.; Yamanaka, M.; Kannari, F.; Itakura, R.; Yamanouchi, K., Open-loop and Closed-loop Control of Dissociative Ionization of Ethanol in Intense Laser Fields. *J. Chem. Phys.* **2006**, *124*, 204314.

(284) Albeck, Y.; Kandhasamy, D. M.; Strasser, D., Multiple Detachment of the SF₆⁻ Molecular Anion with Shaped Intense Laser Pulses. *J. Phys Chem. A* **2014**, *118*, 388-395.

(285) Lozovoy, V. V.; Rasskazov, G.; Pestov, D.; Dantus, M., Quantifying Noise in Ultrafast Laser Sources and its Effect on Nonlinear Applications. *Opt. Express* **2015**, *23*, 12037-12044.

(286) Walker, M. A.; Hansch, P.; Van Woerkom, L. D., Intensity-Resolved Multiphoton Ionization: Circumventing Spatial Averaging. *Phys. Rev. A* **1998**, *57*, R701-R704.

(287) Hankin, S. M.; Villeneuve, D. M.; Corkum, P. B.; Rayner, D. M., Intense-Field Laser Ionization Rates in Atoms and Molecules. *Phys. Rev. A* **2001**, *64*, 013405.

(288) Wang, P.; Sayler, A. M.; Carnes, K. D.; Esry, B. D.; Ben-Itzhak, I., Disentangling the Volume Effect Through Intensity-Difference Spectra: Application to Laser-Induced Dissociation of H₂⁺. *Opt. Lett.* **2005**, *30*, 664-666.

(289) Pestov, D.; Lozovoy, V. V.; Dantus, M., Multiple Independent Comb Shaping (MICS): Phase-only Generation of Optical Pulse Sequences. *Opt. Express* **2009**, *17*, 14351-14361.

- (290) Kaziannis, S.; Kotsina, N.; Kosmidis, C., Interaction of Toluene with Two-color Asymmetric Laser Fields: Controlling the Directional Emission of Molecular Hydrogen Fragments. *J. Chem. Phys.* **2014**, *141*, 104319.
- (291) Papadopoulou, C. C.; Kaziannis, S.; Kosmidis, C., Probing the Dynamics of Highly Excited Toluene on the fs Timescale. *Phys. Chem. Chem. Phys.* **2015**, *17*, 31727-31734.
- (292) *NIST Chemical Webbook, NIST Standard Reference Database Number 69 - November 1998 Release.*
- (293) Lozovoy, V. V.; Dantus, M., Laser Control of Physicochemical Processes; Experiments and Applications. *Annu. Rep. Prog. Chem. Sect. C: Phys. Chem.* **2006**, *102*, 227-258.
- (294) Thissen, R.; Delwiche, J.; Robbe, J. M.; Duflot, D.; Flament, J. P.; Eland, J. H. D., Dissociations of the Ethyne Dication C₂H₂²⁺. *J. Chem. Phys.* **1993**, *99*, 6590-6599.
- (295) Siozos, P.; Kaziannis, S.; Kosmidis, C., Multielectron Dissociative Ionization of CH₃I Under Strong Picosecond Laser Irradiation. *Int. J. Mass spectrom.* **2003**, *225*, 249-259.
- (296) Jonas, L. H.; Lotte, H.; Jens, H. N.; Henrik, S.; Darko, D.; Lars Bojer, M., Orientation-Dependent Ionization Yields from Strong-Field Ionization of Fixed-in-Space Linear and Asymmetric Top Molecules. *J. Phys. B At. Mol. Opt. Phys.* **2012**, *45*, 015101.
- (297) Seideman, T.; Ivanov, M. Y.; Corkum, P. B., Role of Electron Localization in Intense-Field Molecular Ionization. *Phys. Rev. Lett.* **1995**, *75*, 2819-2822.
- (298) Lötstedt, E.; Kato, T.; Yamanouchi, K., Efficient Ionization of One-Dimensional Acetylene Investigated by Time-Dependent Hartree-Fock Calculations. *Phys. Rev. A* **2012**, *86*, 023401.
- (299) Bubin, S.; Atkinson, M.; Varga, K.; Xie, X.; Roither, S.; Kartashov, D.; Baltuška, A.; Kitzler, M., Strong Laser-Pulse-Driven Ionization and Coulomb Explosion of Hydrocarbon Molecules. *Phys. Rev. A* **2012**, *86*, 043407.
- (300) Russakoff, A.; Bubin, S.; Xie, X.; Erattupuzha, S.; Kitzler, M.; Varga, K., Time-dependent Density-Functional Study of the Alignment-Dependent Ionization of Acetylene and Ethylene by Strong Laser Pulses. *Phys. Rev. A* **2015**, *91*, 023422.
- (301) Pegarkov, A. I., Electron Excitation and 'Cascade' Ionization of Diatomic Molecules with Ultra-Short Pulses of Strong IR Lasers. *Chem. Phys. Lett.* **2001**, *343*, 642-648.
- (302) Sakabe, S.; Nishihara, K.; Nakashima, N.; Kou, J.; Shimizu, S.; Zhakhovskii, V.; Amitani, H.; Sato, F., The Interactions of Ultra-Short High-Intensity Laser Pulses with Large Molecules and Clusters: Experimental and Computational Studies. *Phys. Plasmas* **2001**, *8*, 2517-2524.

(303) Lozovoy, V. V.; Rasskazov, G.; Ryabtsev, A.; Dantus, M., Phase-Only Synthesis of Ultrafast Stretched Square Pulses. *Opt. Express* **2015**, *23*, 27105-27112.

(304) Rodríguez-Romero, J.; Guarín, C. A.; Arroyo-Pieck, A.; Gutiérrez-Arzaluz, L.; López-Arteaga, R.; Cortés-Guzmán, F.; Navarro, P.; Peon, J., Fluorophore Release from a Polymethinic Photoremovable Protecting Group Through a Nonlinear Optical Process. *ChemPhotoChem* **2017**, *1*, 397-407.